



Kunnskap for en bedre verden

DEPARTMENT OF ENERGY AND PROCESS  
ENGINEERING

TEP4905 - INDUSTRIELL PROSESSTEKNIKK, MASTEROPPGAVE

---

# Experimental Investigation of a Cold Thermal Energy Storage System for Industrial Application

---

*Author:*  
Saleh Sakka Amini

Jun, 2021

---

## Acknowledgement

I would like to thank my family and my friends for all the support they provided during these times. Furthermore, I would like to thank Dr. Armin Hafner for making this project possible and for his guidance throughout the project, Ph.D candidate Håkon Selvnes for his guidance through each stage of the process, and finally the Norwegian University of Science and Technology for making this work possible.

---

## Abstract

Global warming is a reality that industries need to understand and work accordingly to limit by reducing their greenhouse gas emissions. Thermal energy consumption across industries varies greatly between peak and off-peak demand throughout the day and throughout the year. Refrigeration is a very energy-demanding process with huge variation in demand between peak hours and off-peak hours. This increases the load on the chillers and increases the capital cost due to the need of purchasing big equipment that can satisfy the varied demand for energy. Cold thermal energy storage (CTES) can be used to minimize the gap between the demand and supply of energy. Phase change materials (PCMs) use latent heat to store thermal energy storage which makes it an effective way of storing energy due to its high energy density. Literature review shows that extensive research has been done on integrating PCMs in buildings for different applications. These can be space cooling and heating, ventilation, and domestic hot water storage tanks. Furthermore, the use of TES for high-temperature applications such as solar energy applications is more spread compared with low-temperature applications. There has been an increased focus on the study of PCM-based CTES systems for small applications such as domestic refrigeration and air conditioning applications. However, there is a lack of study on CTES systems for large-scale industrial applications. This report presents the results of experimental investigations about the performance of a CTES system that is designed to be integrated with an industrial  $\text{NH}_3/\text{CO}_2$  cascade refrigeration system for a meat processing plant for peak shaving purposes. The CTES consists of a sealed tank filled with PCM and a stack of 10 pillow plate heat exchangers with the possibility to change the distance between the plates. The refrigerant used in this experiment was  $\text{CO}_2$ . The experiment consisted of charging and discharging cycles which dictate solidifying and melting the PCM. During these cycles, each of the inlet  $\text{CO}_2$  temperature and flow rate into the plate heat exchangers were varied in order to map out the system performance for two different configurations being 15 mm and 30 mm distance between the plate heat exchangers. The experiment was run using two different PCMs with different properties. The PCMs used were water and RT-9HC having 0 °C melting temperature and -9,7 °C, respectively. The CTES unit filled with water as the PCM had a storage capacity of 12,16 kW and 24,32 kW for the 15 mm and 30 mm configurations, respectively. The CTES unit filled with RT-9HC as the PCM had a storage capacity of 7,27 kW and 14,54 kW for the 15 mm and 30 mm configurations, respectively. Both PCMs proved to be efficient under the right conditions of the refrigerant flow rate and its inlet temperature and can be used for peak shaving purposes. Water can be used as the PCM when the system is to be integrated to provide cooling between 6 °C and 10 °C. This can be utilized for example in fruits and vegetable cooling, or space cooling. The RT-9HC as a PCM can be integrated with a refrigeration system to provide cooling between -4 °C and 4 °C. During discharging, a minimum temperature difference of 6 K between the PCM and the refrigerant is needed for the system to be able to extract more than 70% of the latent heat capacity. For discharging, a flow rate of 7 kg min<sup>-1</sup> seemed to be optimal. The system showed to be temperature sensitive where 1 °C difference in the inlet  $\text{CO}_2$  temperature can have a huge effect on how long the system can hold the maximum heat flow. Findings show that the cumulative discharged energy into the CTES was highest when the inlet  $\text{CO}_2$  temperature into the system was highest.

---

## Sammendrag

Global oppvarming er en realitet som næringer trenger å forstå og arbeide deretter for å begrense ved å redusere klimagassutslippene. Termisk energiforbruk på tvers av næringer varierer sterkt mellom topp- og off-peak-etterspørsel gjennom dagen og gjennom året. Kjøling er en veldig energikrevende prosess med stor variasjon i etterspørsel mellom topp- og lavtider. Dette øker belastningen på kjølere og øker kapitalkostnadene på grunn av behovet for å kjøpe stort utstyr som kan tilfredsstille det varierte energibehovet. Lagring av kald termisk energi (CTES) kan brukes til å minimere gapet mellom etterspørsel og tilbud av energi. Faseendringsmaterialer (PCM) bruker latent varme til å lagre termisk energilagring, noe som gjør det til en effektiv måte å lagre energi på grunn av dens høye energitetthet. Litteraturstudie viser at det er gjort omfattende forskning på integrering av PCM i bygninger for forskjellige applikasjoner. Dette kan være romkjøling og oppvarming, ventilasjon og lagringstanker for varmtvann til husholdninger. Videre er bruken av TES for applikasjoner med høy temperatur som solenergianvendelser mer spredt sammenlignet med applikasjoner med lav temperatur. Det har vært et økt fokus på studien av PCM-baserte CTES-systemer for små applikasjoner som kjøling og klimaanlegg. Imidlertid mangler det studier på CTES-systemer for store industrielle applikasjoner.

Denne rapporten presenterer resultatene av eksperimentelle undersøkelser om ytelsen til et CTES-system som er designet for å integreres med et industrielt  $\text{NH}_3/\text{CO}_2$  kaskadekjølesystem for et kjøttforedlingsanlegg for toppbarberingsformål. CTES består av en forseglet tank fylt med PCM og en stabel med 10 pute plate varmevekslere med mulighet for å endre avstanden mellom platene. Kjølemediet som ble brukt i dette eksperimentet var  $\text{CO}_2$ . Eksperimentet besto av lade- og utladningssykluser som dikterer størkning og smelting av PCM. I løpet av disse syklusene ble hver av innløpet  $\text{CO}_2$  temperatur og strømningshastighet inn i platevarmevekslerne variert for å kartlegge systemytelsen for to forskjellige konfigurasjoner som var 15 mm og 30 mm avstand mellom platevarmevekslerne. Eksperimentet ble kjørt med to forskjellige PCM-er med forskjellige egenskaper. De anvendte PCM-ene var vann og RT-9HC med henholdsvis  $0\text{ }^\circ\text{C}$  og smeltepunkt  $-9,7\text{ }^\circ\text{C}$ . CTES-enheten fylt med vann som PCM hadde en lagringskapasitet på 12,16 kW og 24,32 kW for henholdsvis 15 mm og 30 mm konfigurasjoner. CTES-enheten fylt med RT-9HC som PCM hadde en lagringskapasitet på 7,27 kW og 14,54 kW for henholdsvis 15 mm og 30 mm konfigurasjoner. Begge PCM-ene viste seg å være effektive under de rette forholdene for kjølemediumens strømningshastighet og dens innløpstemperatur og kan brukes til toppbarberingsformål. Vann kan brukes som PCM når systemet skal integreres for å gi kjøling mellom  $6\text{ }^\circ\text{C}$  og  $10\text{ }^\circ\text{C}$ . Dette kan f.eks. brukes i kjøling av frukt og grønnsaker, eller romkjøling. RT-9HC som PCM kan integreres med et kjølesystem for å gi kjøling mellom  $-4\text{ }^\circ\text{C}$  og  $4\text{ }^\circ\text{C}$ . Under tømmingen er det nødvendig med en minimum temperaturforskjell på 6 K mellom PCM og kjølemediet for systemet for å kunne trekke ut mer enn 70 % av den latente varmekapasiteten. For utslipp syntes en strømningshastighet på  $7\text{ kg min}^{-1}$  å være optimal. Systemet viste seg å være temperaturfølsomt der  $1\text{ }^\circ\text{C}$  forskjell i innløpet  $\text{CO}_2$  temperatur kan ha en enorm effekt på hvor lenge systemet kan holde maksimal varmestrøm. Funn viser at den kumulative utladede energien i CTES var høyest når innløpet  $\text{CO}_2$  temperaturen i systemet var høyest.

---

# Contents

<b>List of Figures</b>	<b>vi</b>
<b>List of Tables</b>	<b>ix</b>
<b>1 Introduction</b>	<b>1</b>
<b>2 Literature Review</b>	<b>2</b>
2.1 Refrigeration . . . . .	2
2.1.1 History of Refrigerant . . . . .	4
2.1.2 CO <sub>2</sub> as a Refrigerant . . . . .	4
2.1.3 CO <sub>2</sub> Transcritical Cycle . . . . .	5
2.2 Thermal Energy Storage . . . . .	6
2.2.1 Sensible Heat Storage . . . . .	6
2.2.2 Latent Heat Storage . . . . .	7
2.2.3 Advantages of TES . . . . .	8
2.2.4 Sizing Strategies . . . . .	8
2.3 Phase Change Material . . . . .	9
2.3.1 Organic PCM . . . . .	10
2.3.2 Inorganic PCMs . . . . .	12
2.3.3 Eutectic PCMs . . . . .	14
2.3.4 Measurement of Thermal Properties of PCMs . . . . .	14
2.3.5 Physical and Thermal Properties Enhancement . . . . .	15
2.4 Applications of Cold Thermal Energy Storage . . . . .	16
2.4.1 Air Conditioning(AC) . . . . .	17
2.4.2 Free Cooling . . . . .	20
2.4.3 Refrigeration . . . . .	22
2.4.4 Food Storage and Transport . . . . .	25
2.4.5 Building Applications . . . . .	27
2.4.6 Sub-zero Applications . . . . .	28
2.4.7 Other Applications . . . . .	28
<b>3 Experimental Setup</b>	<b>29</b>
3.1 Components . . . . .	32
3.1.1 Pillow Plates Heat Exchangers . . . . .	32
3.1.2 Liquid Receiver . . . . .	33

---

3.1.3	Evaporator and Condenser . . . . .	34
3.1.4	Glycol Circuit . . . . .	35
3.1.5	Centralised CO <sub>2</sub> System . . . . .	36
3.1.6	Electrical Cabinet . . . . .	36
3.1.7	Sensors . . . . .	36
<b>4</b>	<b>Methods</b>	<b>38</b>
4.1	PCM Used in Experimental Facility . . . . .	38
4.2	CTES Test Rig . . . . .	38
4.3	Charging Mode . . . . .	39
4.4	Discharging Mode . . . . .	42
<b>5</b>	<b>Results</b>	<b>45</b>
5.1	Charging Mode . . . . .	45
5.1.1	Water as PCM . . . . .	45
5.1.2	RT-9HC as PCM . . . . .	51
5.2	Discharging Mode . . . . .	59
5.2.1	Water . . . . .	59
5.2.2	RT-9HC . . . . .	68
<b>6</b>	<b>Discussion</b>	<b>78</b>
6.1	Charging Mode . . . . .	78
6.1.1	Water . . . . .	78
6.1.2	RT-9HC . . . . .	80
6.2	Discharging Mode . . . . .	81
6.2.1	Water . . . . .	81
6.2.2	RT-9HC . . . . .	83
<b>7</b>	<b>Conclusion</b>	<b>84</b>
<b>8</b>	<b>Further Work</b>	<b>86</b>
	<b>Bibliography</b>	<b>87</b>
<b>9</b>	<b>Appendices</b>	<b>95</b>
9.1	Draft of a Conference Paper . . . . .	95
9.2	Safety Document . . . . .	104

---

## List of Figures

1	Carnot Cycle in a P-V diagram . . . . .	2
2	Vapor compression cycle . . . . .	3
3	Carnot cycle vs ideal vapor compression cycle in a temperature-entropy diagram . . . . .	3
4	Isentropic expansion vs isenthalpic expansion in a temperature-entropy diagram . . . . .	4
5	CO <sub>2</sub> pressure enthalpy diagram . . . . .	5
6	CO <sub>2</sub> transcritical cycle shown in figure a and subcritical cycle shown in figure b . . . . .	6
7	Types of thermal energy storage . . . . .	6
8	Sensible heat vs latent heat temperature change . . . . .	8
9	Outcome of different integrating possibilities . . . . .	9
10	Latent heat storage classification . . . . .	10
11	Effect of supercooling on heat storage . . . . .	16
12	CTES system proposed for an HVAC system . . . . .	17
13	Charging and discharging modes . . . . .	18
14	A prototype of thermoelectric system using PCM as TES for space cooling . . . . .	18
15	A schematic diagram of the PCM-AC system . . . . .	19
16	A schematic diagram of the PCM-AC system . . . . .	20
17	Schematic of the integrated free cooling system . . . . .	21
18	System showing airflow during discharging in part a and during charging in part b . . . . .	21
19	Test huts at the University of Auckland campus . . . . .	22
20	PCM-CTES integration methods . . . . .	23
21	The built refrigeration system . . . . .	23
22	PCM integration with the evaporator . . . . .	24
23	a) Refrigeration model b) the design of the novel PCM heat exchanger . . . . .	25
24	Experiment design comparing PCM-based truck and conventional truck . . . . .	26
25	Gel containers for food storage . . . . .	27
26	PCM containers . . . . .	27
27	Cooling vest with integrated fans and PCM material . . . . .	29
28	Diagram of the experimental setup . . . . .	30
29	CTES system with the condenser. . . . .	31
30	CTES system with the evaporator and glycol circuit . . . . .	31
31	CTES system with the liquid receiver . . . . .	32
32	Stack of pillow plates . . . . .	33
33	Liquid receiver . . . . .	34

---

34	Condenser . . . . .	35
35	Liquid receiver . . . . .	35
36	Glycol circuit . . . . .	36
37	Time to complete the charging process for different average inlet CO <sub>2</sub> temperatures with respect to their flow rate for the 15 mm configuration for water . . . . .	46
38	Time to complete the charging process for different average inlet CO <sub>2</sub> temperatures with respect to their flow rate for the 30 mm configuration for water . . . . .	46
39	Pressure drop for different CO <sub>2</sub> inlet temperatures grouped in their respective flow rates for the 15 mm configuration for water . . . . .	47
40	Pressure drop for different CO <sub>2</sub> inlet temperatures grouped in their respective flow rates for the 30 mm configuration for water . . . . .	47
41	Temperature difference between the inlet CO <sub>2</sub> temperature and the average PCM temperature for the 15 mm configuration for water . . . . .	48
42	Temperature difference between the inlet CO <sub>2</sub> temperature and the average PCM temperature for the 30 mm configuration for water . . . . .	49
43	Temperature difference between the inlet CO <sub>2</sub> temperature and outlet CO <sub>2</sub> temperature for the 15 mm configuration for water . . . . .	50
44	Inlet CO <sub>2</sub> temperature during the charging cycle for the 15 mm configuration for water . . . . .	50
45	Temperature difference between the inlet CO <sub>2</sub> temperature and outlet CO <sub>2</sub> temperature for the 30 mm configuration for water . . . . .	51
46	Charging time and pressure drop across the CTES for the different mass flow rates with a fixed inlet CO <sub>2</sub> temperature for the 15 mm configuration for RT-9HC . . .	52
47	Charging time and pressure drop across the CTES for the different mass flow rates with a fixed inlet CO <sub>2</sub> temperature for the 30 mm configuration for RT-9HC . . .	52
48	Charging time vs average inlet CO <sub>2</sub> temperature for the 15 mm configuration for RT-9HC . . . . .	53
49	Charging time vs average inlet CO <sub>2</sub> temperature for the 30 mm configuration for RT-9HC . . . . .	54
50	Pressure drop vs average inlet CO <sub>2</sub> temperature for the 15 mm configurations for RT-9HC . . . . .	54
51	Pressure drop vs average inlet CO <sub>2</sub> temperature for the 15 mm configuration for RT-9HC . . . . .	55
52	Temperature difference between inlet CO <sub>2</sub> temperature and PCM for the 15 mm configuration for RT-9HC . . . . .	56
53	Inlet CO <sub>2</sub> temperature calculated based on the pressure for the 15 mm configuration for RT-9HC . . . . .	56
54	Temperature difference between inlet CO <sub>2</sub> temperature and PCM for the 30 mm configuration for RT-9HC . . . . .	57
55	Inlet CO <sub>2</sub> temperature calculated based on the pressure for the 30 mm configuration for RT-9HC . . . . .	58
56	The average temperature above the bottom, middle, and top plate during C4 charging test for the 15 mm configuration for RT-9HC . . . . .	59

---



---

57	The average PCM temperature above the bottom, middle, and top plate during C4.5 for the 30 mm configuration for RT-9HC . . . . .	59
58	Pressure drop for different average inlet CO <sub>2</sub> temperatures grouped in their respective flow rates for the 15 mm configuration for water . . . . .	60
59	Pressure drop for different average inlet CO <sub>2</sub> temperatures grouped in their respective flow rates for the 30 mm configuration for water . . . . .	61
60	Mean discharge duty of the different mean inlet CO <sub>2</sub> temperatures grouped according to their respective flow rate for the 15 mm configuration for water . . . . .	62
61	Mean discharge duty of the different mean inlet CO <sub>2</sub> temperatures grouped according to their respective flow rate for the 30 mm configuration for water . . . . .	63
62	Heat flow vs time to discharge for the different operating conditions for the 15 mm configuration for water . . . . .	64
63	Heat flow vs time to discharge for the different operating conditions for the 30 mm configuration for water . . . . .	65
64	Cumulative energy discharged throughout the cycle time for the 15 mm configuration for water . . . . .	66
65	Cumulative energy discharged throughout the cycle time for the 30 mm configuration for water . . . . .	66
66	Difference between inlet CO <sub>2</sub> and outlet CO <sub>2</sub> temperature for the 15 mm configuration for water . . . . .	67
67	Difference between inlet CO <sub>2</sub> and outlet CO <sub>2</sub> temperature for the 30 mm configuration for water . . . . .	68
68	Discharging time for the different inlet CO <sub>2</sub> temperature for the 15 mm configurations for RT-9HC . . . . .	70
69	Discharging time for the different inlet CO <sub>2</sub> temperature for the 30 mm configurations for RT-9HC . . . . .	71
70	Mean discharge duty for the different inlet CO <sub>2</sub> temperature for the 15 mm configurations for RT-9HC . . . . .	72
71	Mean discharge duty for the different inlet CO <sub>2</sub> temperature for the 30 mm configurations for RT-9HC . . . . .	72
72	Heat flow during the discharging cycles for the 15 mm configuration for RT-9HC .	73
73	Heat flow during the discharging cycles for the 30 mm configuration for RT-9HC .	74
74	Cumulative energy discharged during the discharging cycles for the 15 mm configuration for RT-9HC . . . . .	75
75	Cumulative energy discharged during the discharging cycles for the 30 mm configuration for RT-9HC . . . . .	75
76	inlet-outlet CO <sub>2</sub> temperature of the 15 mm configuration for RT-9HC . . . . .	76
77	inlet-outlet CO <sub>2</sub> temperature of the 30 mm configuration for RT-9HC . . . . .	76
78	CO <sub>2</sub> path inside the heat exchangers . . . . .	80

---

## List of Tables

1	GWP and ODP for different refrigerants . . . . .	4
2	Properties of different paraffin waxes . . . . .	11
3	Properties of different Non-paraffin . . . . .	12
4	Properties of different salt hydrates . . . . .	13
5	Potential metallic for use as PCMs . . . . .	13
6	Low melting point metals . . . . .	13
7	Organic eutectic materials . . . . .	14
8	inorganic eutectic materials . . . . .	14
9	Properties of water and ice . . . . .	38
10	Properties of RT-9HC solid and liquid phases . . . . .	38
11	Charging mode running parameters with 15 mm and 30 mm distance between the plates for water . . . . .	39
12	15 mm configuration first set of experiment with RT-9HC . . . . .	40
13	Set of charging cycles with fixed inlet CO <sub>2</sub> temperature while varying the mass flow rate for the 15mm distance with RT-9HC . . . . .	40
14	30 mm configuration first set of experiment with RT-9HC . . . . .	41
15	Set of charging cycles with fixed inlet CO <sub>2</sub> temperature while varying the mass flow rate for 30 mm configuration with RT-9HC . . . . .	41
16	Latent heat stored in ice for the two different configurations . . . . .	41
17	Latent heat stored in the solid RT-9HC for both configurations . . . . .	42
18	Discharging mode running parameters with 15 mm and 30 mm distances between the plates for the water . . . . .	42
19	15 mm configuration first set of discharging tests with the RT-9HC . . . . .	43
20	Set of discharging cycles with fixed inlet CO <sub>2</sub> temperature while varying the mass flow rate for the 15mm distance with the RT-9HC . . . . .	43
21	Set of discharging cycles with fixed inlet CO <sub>2</sub> temperature while varying the mass flow rate for the 30mm distance with the RT-9HC . . . . .	43
22	Charging test results for the 15 mm configuration for water . . . . .	45
23	Charging test results for the 30 mm configuration for water . . . . .	45
24	Results of the discharging tests for the 15 mm configurations for water . . . . .	61
25	Results of the discharging tests for the 30 mm configurations for water . . . . .	62
26	Total system performance for water . . . . .	68
27	Results for the initial tests with fixed inlet CO <sub>2</sub> temperature for the 15 mm configuration for RT-9HC . . . . .	69
28	Results for the initial tests with fixed inlet CO <sub>2</sub> temperature for the 30 mm configuration for RT-9HC . . . . .	69

---

29	Results obtained from performing the discharging cycles for the 15 mm configurations for RT-9HC . . . . .	69
30	Results obtained from performing the discharging cycles for the 30 mm configurations for RT-9HC . . . . .	70
31	The total system performance including the subcooling effect for RT-9HC . . . . .	77
32	Mean discharged duty in periods up to 90% of the total discharged energy for the RT-9HC . . . . .	84

---

## Nomenclature

$\Delta h_m$	Heat of fusion per unit mass J/kg
$\rho$	Density kg/m <sup>3</sup>
$a_m$	Fraction melted
$C_p$	Specific heat J/kg k
$L$	Specific latent heat of fusion of substance J/g
$M$	Mass kg
$m$	Mass flow rate kg/s
$T$	Temperature K
$T_f$	Final temperature K
$T_i$	initial temperature K
$T_m$	Melting temperature K
$V$	Volume m <sup>2</sup>
CFC	Chloridefluoridecarbon
CTES	Cold Thermal Energy Storage
GWP	Global Warming Potential
HCFC	Hydrochlorofluorocarbon
HFCs	Hydrofluorocarbons
ODP	Ozone Depletion Potential
PCM	Phase Change Material
RTD	Resistance Temperature Detectors
TES	Thermal Energy Storage

---

# 1 Introduction

The increase in greenhouse gas emissions resulting from growing energy consumption rates is pushing industry to integrate more energy friendly and efficient solutions [1]. Thermal energy consumption is high among different types of industries, and the energy demand for different processes fluctuates throughout the day and throughout the year [2]. This can lead to energy waste and the need for bigger equipment to cover the range of this fluctuation [3]. Integrating thermal energy storage (TES) with these systems is a key factor that can level the difference between the supply and demand of energy. Refrigeration is an energy demanding process with a significant difference in peak and normal time demands. Therefore integrating cold thermal energy storage in refrigeration systems can improve the performance and reliability of the refrigeration systems allowing it to meet peak time demands without increasing the load on the chillers. Cold thermal energy storage uses phase change materials to store the energy during off-peak time and uses this energy later during peak demands leading to saving energy and reducing costs [4]. Literature review shows that a lot of research has been done on the integration of PCMs in building materials for hot and cold applications such as space heating and cooling, ventilation, and domestic hot water storage tanks. Furthermore, the use of PCM-based TES is more spread for high-temperature applications such as solar energy applications compared to low-temperature applications. This can be attributed to the difficulties associated with TES systems for low-temperature applications such as high initial costs and difficult integration strategies. PCM-based CTES systems have gained an increased focus scientifically and commercially, however it is still lacking a proper implementation across the refrigeration industry. This can be due to a lack of study on large scale CTES systems for industrial applications as most of the research done is about the use of CTES in small systems such as domestic refrigeration [5–7].

A CTES unit which uses phase change material as a storage medium for thermal energy is being investigated in this work. The unit is to be integrated in a  $\text{NH}_3/\text{CO}_2$  cascade refrigerant system for food processing plant for peak shaving purposes. The refrigerant used in this setup is  $\text{CO}_2$  due to its potentials in refrigeration cycles, being environmentally friendly, and safe refrigerant [8]. The experiment consists of charging cycle where the latent heat is stored by solidifying the PCM, and discharging cycle where the latent heat is extracted out by melting the PCM. Two different PCMs were experimented with which are water and RT-9HC. The charging and discharging cycles were run multiple times with different parameters to try to figure out how changing these parameters affect the system, and to map the running parameters that lead to optimal performance. These parameters are the flow rate of the refrigerant, the temperature of the refrigerant, and the system geometrical configuration. This report shows how the system performed when changing the previously mentioned parameters among the explanation of the different results. This report first presents a literature review of refrigeration, thermal energy storage, and phase change materials. Second, this report provides a description for the experimental setup followed by the methods and procedures followed in this work. Third, the results of this work are shown followed by a discussion and a conclusion explaining the findings of this work. Finally some suggestions for future work are presented. The appendices contain a draft for a conference paper and the risk assessment documents which were completed for this experiment.

---

## 2 Literature Review

### 2.1 Refrigeration

Refrigeration is the process of cooling down a space or a medium to lower temperatures than its surroundings. Refrigeration has applications across many industries such as industrial refrigerators, air conditioning, and cryogenics. Carnot cycle represents the theoretical ideal refrigeration cycle, meaning that it sets the limit for the efficiency that can be achieved by any engine. Figure 1 below shows the thermodynamic principle followed by refrigeration which is the Carnot cycle. The four stages shown starts with isothermal expansion as heat is transferred from high temperature reservoir at constant temperature, followed by isentropic expansion of the gas, followed by isothermal compression as heat is transferred to low temperature reservoir, and finally an adiabatic compression before the cycle repeats again.

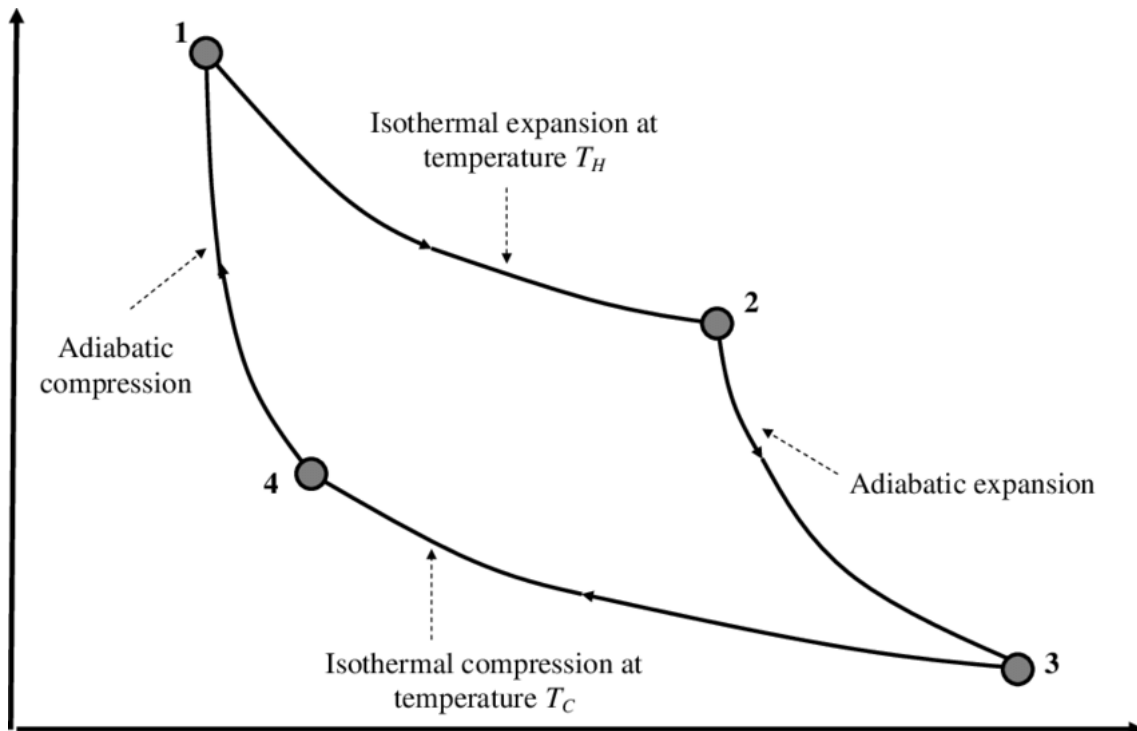


Figure 1: Carnot Cycle in a P-V diagram  
[9]

The vapor compression cycle is a conventional refrigeration cycle. The cycle has the four essential elements for the refrigeration to happen which are as follows: an evaporator, a mechanical compressor, a condenser, and an expansion valve. The refrigerant contained inside the cycle undergoes various changes while it is circulating within these different components. Starting at the evaporator, heat is transferred into the refrigerant transforming it mainly from liquid to vapor due to the refrigerant being in a lower temperature than the heat source. The vapor is then compressed into high pressure and temperature before heading towards the condenser where it releases heat to the surroundings lowering down its temperature and causing the refrigerant to condense into a liquid state. The high pressure refrigerant is then transferred into low pressure and low temperature vapor using an expansion device. The low pressure and low temperature refrigerant flows into the evaporator so the cycle can start again. Figure 2 below shows a simple vapor compression cycle with its essential components using an expansion valve as the expansion device.

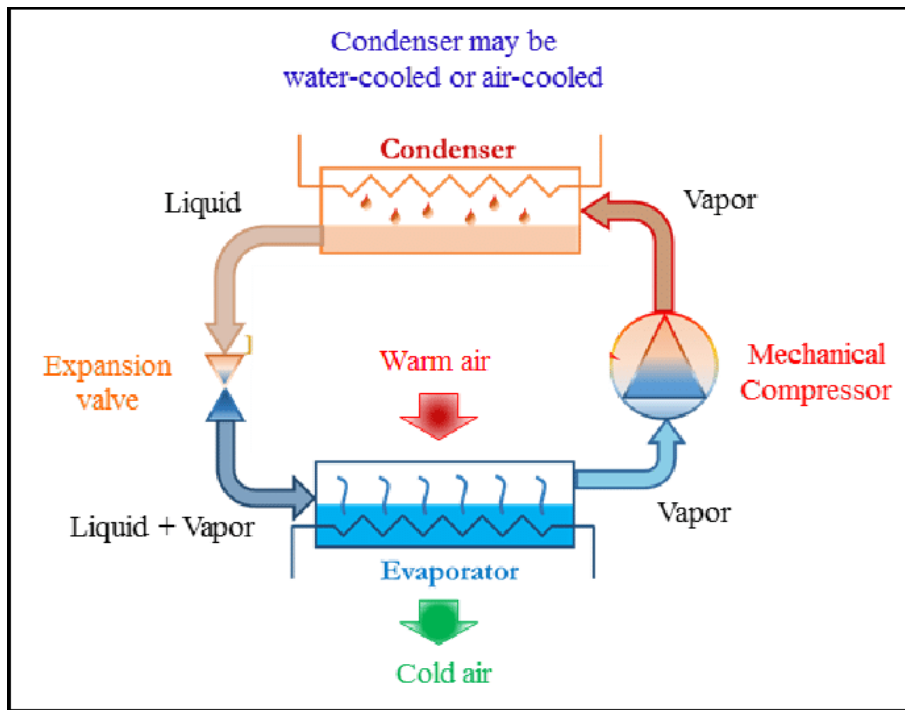


Figure 2: Vapor compression cycle [10]

Figure 3 below shows the difference between a Carnot cycle and an ideal vapor compression cycle.

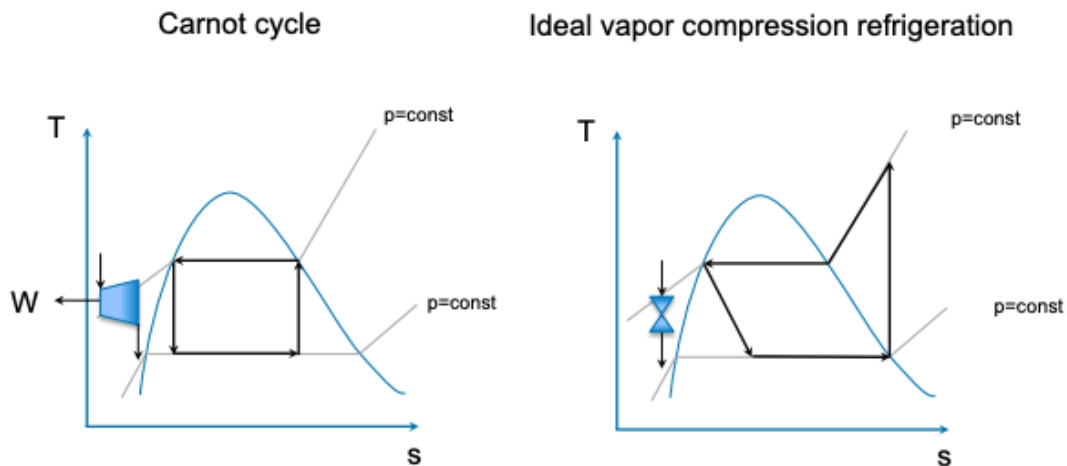


Figure 3: Carnot cycle vs ideal vapor compression cycle in a temperature-entropy diagram [11]

The expansion device used in a vapor compression cycle can be a Joule-Thomson valve or a gas-expander which leads to an isenthalpic expansion or isentropic expansion, respectively as shown in Figure 4. Isentropic expansion can lead to more cooling gas production and work production that can be used somewhere else in the process. This is because an isentropic expansion follows a constant entropy line while an isenthalpic expansion follows a constant enthalpy line [12]. Therefore, a gas expander will lead to larger liquid fraction production to be used in the evaporator which leads to larger refrigeration capacity compared to a process using Joule-Thomson valve. Figure 4 below shows the difference between isenthalpic expansion and isentropic expansion on a

temperature entropy diagram [13].

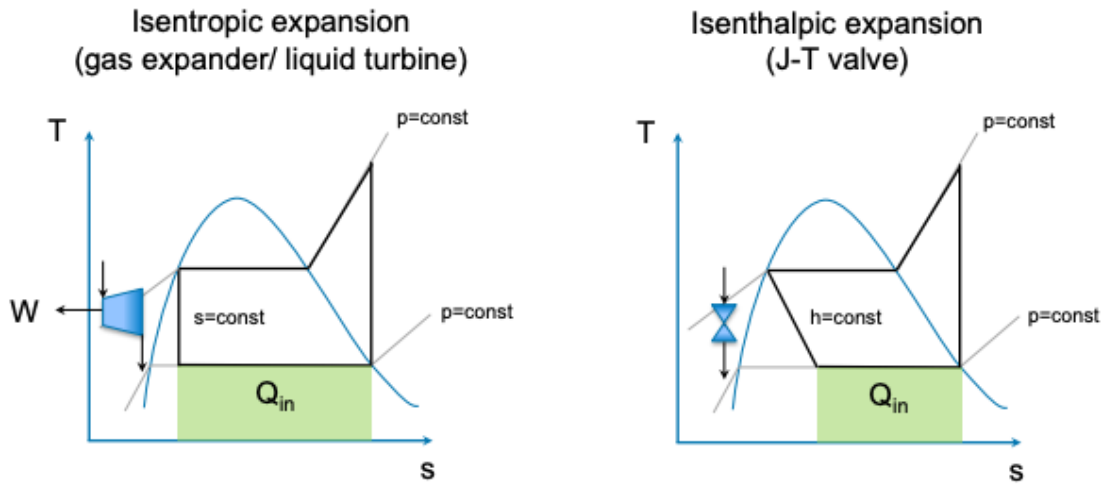


Figure 4: Isentropic expansion vs isenthalpic expansion in a temperature-entropy diagram [11]

### 2.1.1 History of Refrigerant

The first vapor compression system was invented by Jacob Perkins in 1834. Perkin used ether as a working fluid. Later, natural working fluids such as  $\text{CO}_2$ , ammonia, sulfur dioxide and hydrocarbon were used. Since 1930, ChlorideFluorideCarbone(CFC) which are also called freons started to be more used as they performed better and were more safe for human use. The depletion of the stratospheric ozone led to phasing them out after the international agreement Montreal Protocol in 1987. Hydrochlorofluorocarbon (HCFC) were not phased out as they have very low ozone depletion potential, also Hydrofluorocarbons (HFCs) were a good substitute for CFC that many industries adopted as they could switch the working fluid in their systems with minor changes. Due to rising concerns regarding global warming, during UNFCCC (United Nations Framework Convention on Climate Change) in 1992 and Kyoto Protocol in 1997 HFCs working fluids were limited due to their high global warming potential. Natural working refrigerant such as  $\text{CO}_2$  and ammonia are the real solutions to refrigeration industry as are available and are becoming more efficient as refrigeration technologies are improving [14].

### 2.1.2 $\text{CO}_2$ as a Refrigerant

$\text{CO}_2$  has gained a lot of interest as a refrigerant due to its thermal properties compared to hydrofluorocarbons which are strong greenhouse gases that are manufactured for the use in refrigeration cycles [15]. Table 1 below shows the values of GWP and ODP for some HFCs such as R134a, R410a, and R404a, followed by propane R290, ammonia R717, and  $\text{CO}_2$  R744.

Refrigerant type	ODP	GWP
R134a	0	1430
R410a	0	2088
R404a	0	3922
R290	0	3
R717	0	0
R744	0	1

Table 1: GWP and ODP for different refrigerants [16]



CO<sub>2</sub> compared to hydrofluorocarbons has lower viscosity, higher latent heat, higher thermal conductivity, higher density, higher volumetric cooling capacity, and higher specific heat. Furthermore, CO<sub>2</sub> non flammability, non-toxicity, availability, price, and negligible global warming potential made it more appealing for the industry [17, 18]. CO<sub>2</sub> as a refrigerant has been used in commercial refrigeration systems that provide refrigeration capacities at various temperature levels, air conditioning (AC), dehumidification, heating and even domestic hot water production at adequate temperature levels [18] [19]. Figure 5 below shows the pressure-enthalpy diagram of CO<sub>2</sub> with its liquid, two-phase, vapour, and supercritical region.

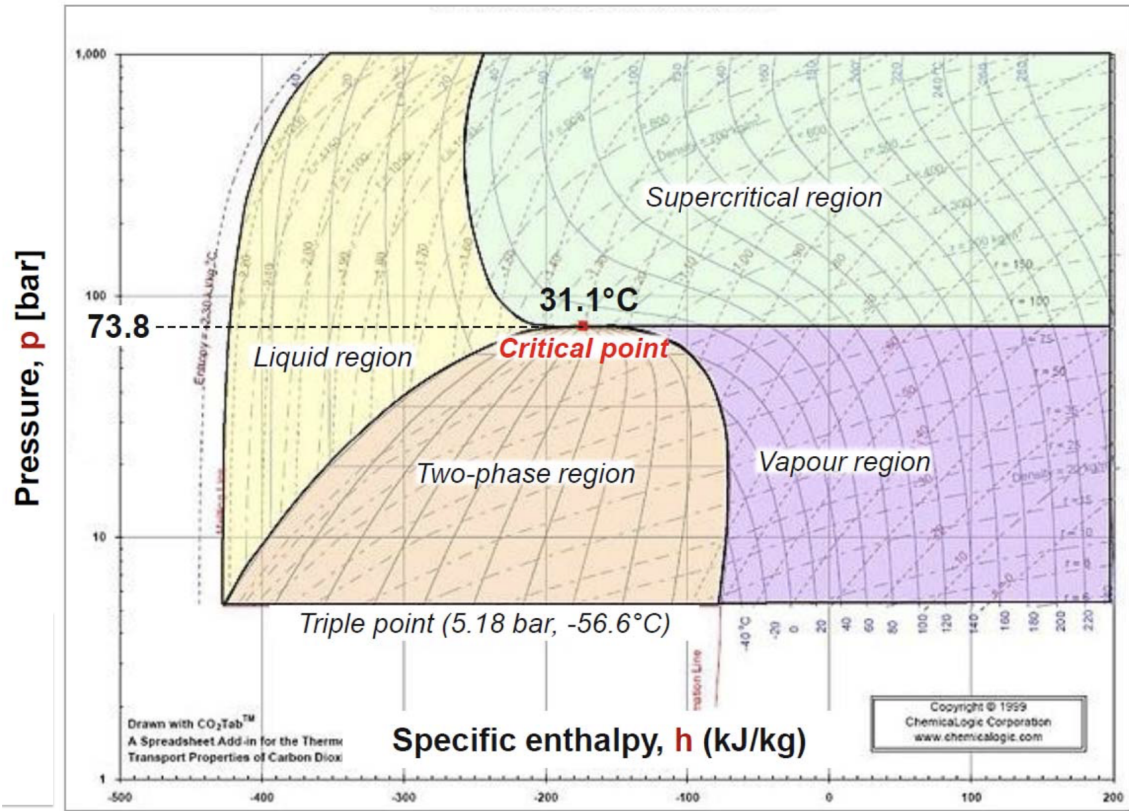


Figure 5: CO<sub>2</sub> pressure enthalpy diagram [20]

### 2.1.3 CO<sub>2</sub> Transcritical Cycle

A transcritical cycle is a cycle that operates with a maximum pressure that is higher than the critical pressure of the refrigerant, while the low side pressure of the cycle is below the critical pressure [21]. In a conventional vapor compression cycle the heat rejection happens at saturated conditions by condensing the high pressure refrigerant while heat absorption happens by evaporating the refrigerant. In a transcritical cycle the heat absorption part stays the same, however the heat rejection happens above the critical pressure and therefore no condensation of the CO<sub>2</sub> happens. The heat rejection happens throughout changing the sensible heat of the CO<sub>2</sub> dense phase which happens at gliding temperatures [22]. Transcritical CO<sub>2</sub> cycles have some potentials due to CO<sub>2</sub> properties in the super critical region. The viscosity of CO<sub>2</sub> in the supercritical region shown in Figure 5 is low and this helps with producing turbulent flow even at reduced flow rates which can result in better heat transform performance [23]. This makes the transcritical cycle efficient for applications with heating function that have high temperature range such as domestic hot water, which can vary from 10 °C to 90 °C. Figure 6 below shows the transcritical cycle on the right and subcritical cycle on the left on pressure enthalpy diagram.

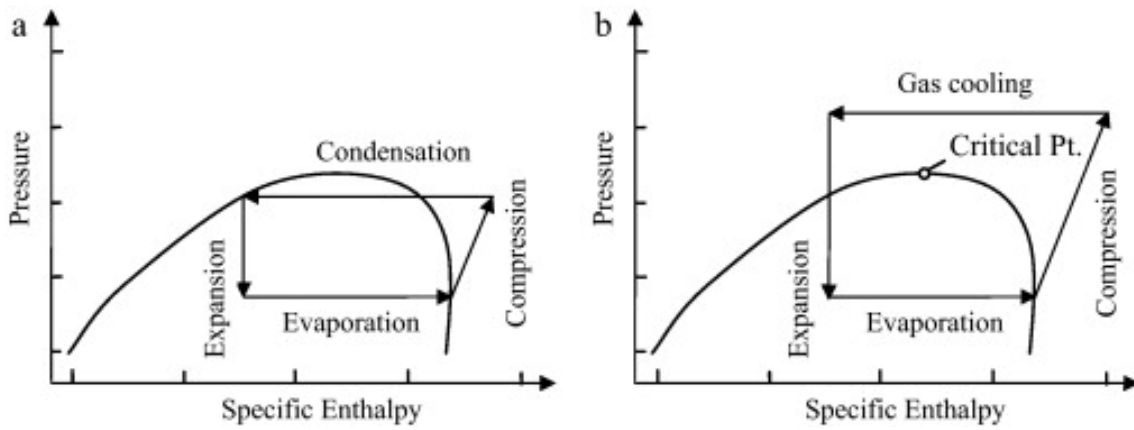


Figure 6: CO<sub>2</sub> transcritical cycle shown in figure a and subcritical cycle shown in figure b [22]

## 2.2 Thermal Energy Storage

Thermal energy storage is the storing of heat to be used at a later time. There are different methods for storing thermal energy storage such as sensible heat, latent heat, or chemical storage. These different storage types can be used alone or combined together. Thermal energy storage consists of three main stages which is charging, storing, and discharging. Figure 7 below shows different classification of thermal energy storage.

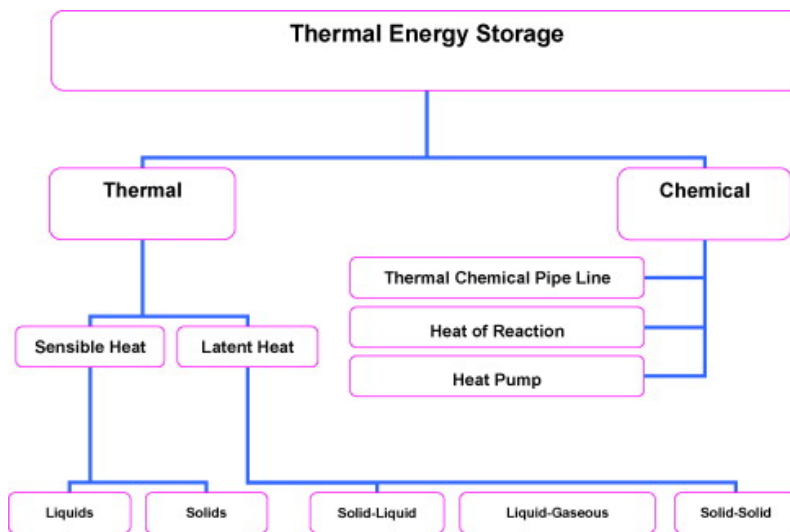


Figure 7: Types of thermal energy storage [24]

### 2.2.1 Sensible Heat Storage

The storage of heat by causing the storage medium to rise or lower in temperature. The specific heat capacity of the storage medium together with the temperature change is what determine the energy storage density in sensible heat storage. The energy stored can be calculated using the formula

$$Q(t) = \int_{T_f}^{T_i} mC_p(T)dT \quad (1)$$

---

Assuming a constant specific heat capacity in the considered range of temperature the equation can be simplified into the following equation

$$Q(t) = mC_p(T_f - T_i) \quad (2)$$

$Q(t)$ = Sensible heat stored [W]

$T_i$ = Initial temperature [K]

$T_f$ = Final temperature [K]

$m$ = Mass flow rate [kg/s]

$C_p$ = Specific heat [J/kg.k]

Water is considered to have high specific heat and therefor a good sensible heat medium for temperatures lower than 100 °C [25].

### 2.2.2 Latent Heat Storage

Latent heat is the amount of heat a material absorbs or releases during its phase change. For example from gas to liquid to solid and vice versa [26] . Latent heat is among the most efficient ways of storing thermal energy as it provides high storage density with little temperature difference between storage and releasing heat. The stored latent heat in a phase change material can be calculated from the following equation:

$$Q(t) = ma_m\Delta h_m \quad (3)$$

$Q(t)$ = Latent heat stored in the material [W]

$m$ = Mass flow rate [kg/s]

$a_m$ = Fraction melted

$\Delta h_m$ = heat of fusion per unit mass [J/kg]

In a process where a PCM goes through phase change, first, the material gains sensible heat to reach the temperature of phase change. Second, the phase change happens and the material stores the latent heat. Third, the material keeps gaining sensible heat according to the specific heat capacity of the new phase. The total energy stored by this process is found using the following equation:

$$Q(t) = \int_{T_m}^{T_i} mC_p(T)dT + ma_m\Delta h_m + \int_{T_f}^{T_m} mC_p(T)dT \quad (4)$$

The expressions can be further simplified assuming that heat capacity does not change in the given temperature range

$$Q(t) = m[C_p(T_m - T_i) + a_m\Delta h_m + C_p(T_f - T_m)] \quad (5)$$

$T_m$ =Melting temperature [K]

Latent heat storage is higher than sensible heat storage for a given volume. Latent heat has a high energy storage density making it preferred over sensible energy storage. Figure 8 below shows how the phase change material stores energy before changing phase by sensible heat, while changing phase by latent heat, and after changing phase by sensible heat. The figure below also shows how a

material that only stores heat through sensible heat would store much less heat than the material which goes through phase change for the same amount of temperature increase.

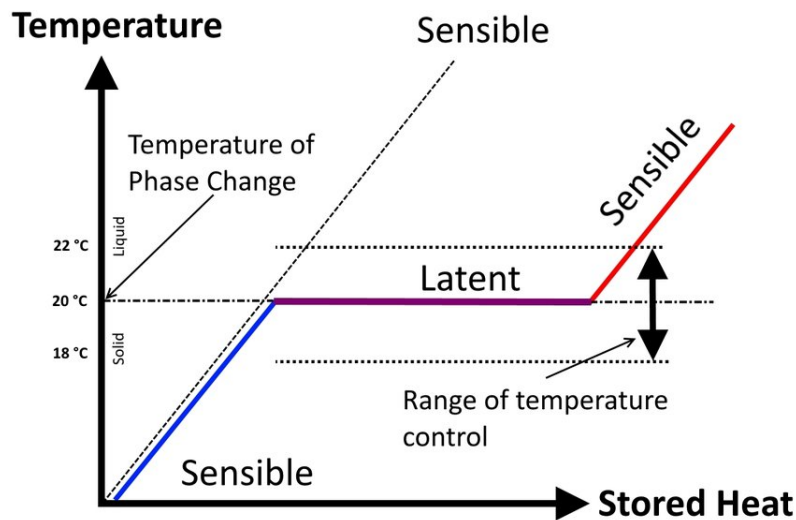


Figure 8: Sensible heat vs latent heat temperature change [27]

### 2.2.3 Advantages of TES

Thermal energy systems play an important role in energy saving programs across the different sectors including residential, commercial, and industrial sectors. TES can be utilized to reduce energy consumption or to transfer the load from one period to another [28].

- Utilization of waste heat
 

This is done simply by storing the heat produced by different equipment that would normally be released to the atmosphere such as hot or cold gases or surplus energy as solar energy during the day. Later this heat can be used where it is needed in the process leading to reduced energy consumption.
- Reduction of demand charges
 

This concerns electrically produced thermal energy as it can be purchased and stored during off peak times to be later used during high-peak times leading to savings in the purchased energy. For example; storing cold thermal energy using a chiller during the night to reduce the demand on the chiller during high-rate electricity periods.
- Deferring equipment purchases
 

The equipment are designed in order to meet the demand at the average and extreme conditions that occur few times a year. This lead to the need of purchasing bigger equipment even though it will be used for short periods. This can be avoided by storing the thermal energy when the demand is low, and then use this stored thermal energy to meet the demand when thermal loads exceed the capacity of the chillers.

### 2.2.4 Sizing Strategies

There are different sizing strategies for the TES system that result in different system responses to cover the cooling loads during peak time hours. These are full, near full, and partial storage. Figure 9 below shows the different sizing strategies of the TES system and how the cooling load will be satisfied for each one of them, i.e. full storage which is designed to cover the entire load during peak hours, partial storage which is designed to cover the cooling load together with the

chillers during peak hours, and near full storage which comes in between the full storage and partial storage and is designed to cover the cooling load with reduced chiller capacity during peak time hours [28].

- A - Chilling is provided from CTES
- B – Chilling is provided using the chiller
- C – Charging the CTES by the chiller

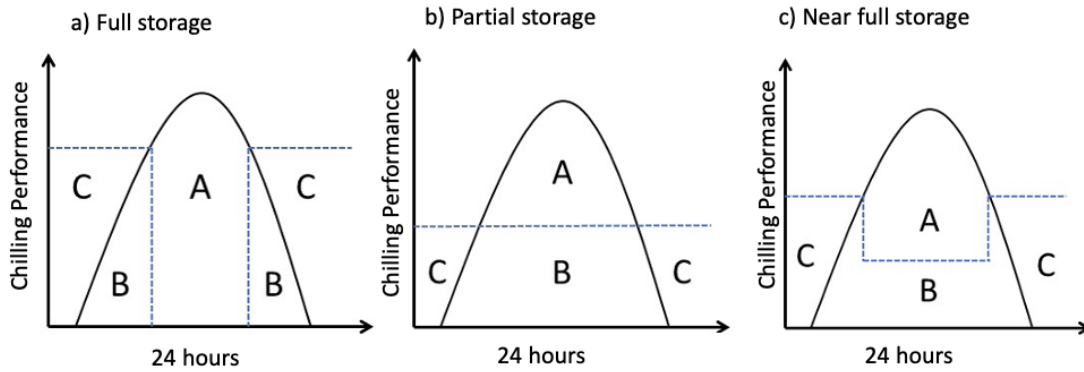


Figure 9: Outcome of different integrating possibilities [29]

## 2.3 Phase Change Material

Phase change materials are latent heat storage materials that have a lot of use in TES applications. There are selection criterias for the PCM based on its thermophysical, kinetics and chemical properties which are as follow:

- Thermal properties

The most important thermal properties for the PCM to have is a suitable phase-transition temperature as it should be matched to the operating temperature of cooling or heating, a high latent heat of fusion, and good thermal conductivity to assist with the charging and discharging of the unit [30].

- Physical properties

Phase stability during phase change, high density, small volume change, and low vapor pressure are important physical properties to be considered when selecting a PCM. The high density is desired to have a low size container for the storage medium. The small volume change among the low vapor pressure are desired to minimise any containment issues [30].

- Kinetic properties

No supercooling and adequate rate of crystallization are important properties when choosing PCMs. Supercooling is when the material goes down in temperature below its freezing point without freezing, and it is avoided because it makes it hard to extract the latent heat from the PCM [31].

- Chemical properties

Long term chemical stability, compatibility with materials of construction, non toxic, and non flammability are considered when choosing a PCM. These properties are important as the PCM can degrade due to hydration and chemical decomposition. Non toxicity and non flammability are important for safety purposes.

- Economic

The PCM should be abundant, available, and cost effective.

PCMs are considered to have high thermal energy storage compared with sensible thermal energy storage as thermal energy is stored in the form of latent heat [32]. The transfer of energy happens when the material shifts from one phase to another. The following are the categories of PCMs; solid-solid, solid-liquid, solid-gas and liquid-gas PCMs [28]. Solid-solid store latent heat by the change of their internal molecular arrangement from crystalline structure to a disordered amorphous structure [32]. The disadvantages with the solid-solid is the low heat storage density and availability [33]. The disadvantage with the liquid-gas and solid-gas is the high variations in volume and pressure when shifting to the gas phase [34]. The solid-liquid phase change materials absorb latent heat at almost constant temperature when going from solid to liquid and they release it when melting at almost constant temperature as well with moderate volume change when shifting between these two phases. Different phase change materials are categorised based on factors such as temperature, phase transition, and the compounds making up the phase change material. Figure 10 below shows the different classifications of phase change materials.

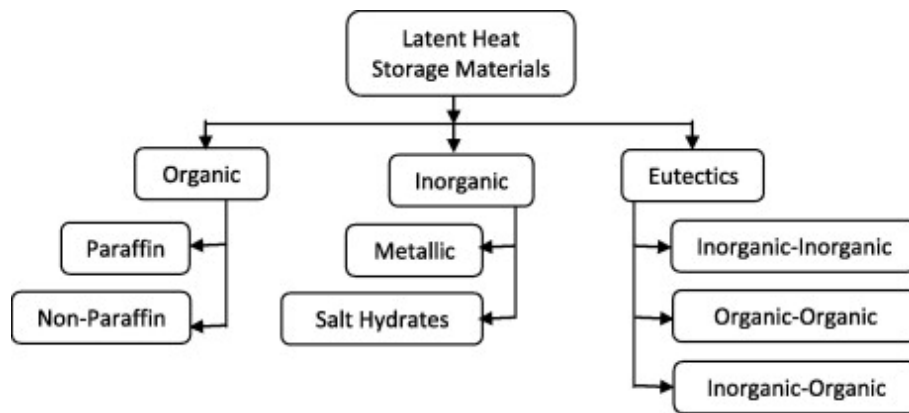


Figure 10: Latent heat storage classification [35]

### 2.3.1 Organic PCM

Organic PCMs are carbon based compounds that can be classified into paraffin or non paraffin. An increase in the molecular weight of the organic compound or the number of carbon atoms results in an increase in the latent heat of fusion [36]. There are several advantages for organic PCMs in energy storage such as:

- availability in a large temperature range
- phase transition over a narrow temperature range
- high energy storage density
- No super cooling
- chemically stable and recyclable
- good compatibility with other materials
- non-corrosive, reusable, and low initial cost

There are some disadvantages to organic PCMs such as:

- Low thermal conductivity (around 0,2 W/m.K) [37]

Adding high thermal conductive fillers to the organic PCMs can result in higher thermal conductivity as they can accelerate storing and releasing of heat [34].

- Large volume change when shifting from one phase to another
- Flammability

Paraffin and fatty acids are among the most used organic PCMs as they have high latent heat [38]. Organic PCMs can also be into different categories such as polyalcohol and polyethylene. These two can experience solid-solid phase transformation and have been considered as a favourable PCMs [39].

### Paraffin Waxes

Paraffin waxes consist of a mixture of mostly straight-chain n-alkanes  $\text{CH}_3\text{-(CH}_2)_n\text{-CH}_3$ . Paraffin waxes have high latent heat storage capacities between 200 kJ/kg and 250 kJ/kg, they have different phase change temperatures, and they are thermally stable up until 250 °C [40]. Latent heat is released in paraffin waxes by the crystallization of the (CH<sub>3</sub>)- chain. The latent heat storage capacity of paraffin wax is dependent on the chain length as the increase of the length of the chain causes the increase in latent heat capacity. Furthermore, the melting temperature and the melting enthalpy of n-alkanes are related to the number of (C) atoms [41]. This can be due to the induced attractions between n-alkane chains.

Paraffin waxes are also reliable, non-corrosive, they have small volume change when melting, and low volume pressure [24]. Further, paraffin waxes are considered to be chemically inert, odorless, available, ecologically harmless, and non-toxic [42]. The low thermal conductivity, moderate flammability, and incompatibility with plastic containers are the main disadvantages of paraffin waxes [43]. Table 2 below shows the melting point and latent heat of fusion of some paraffin waxes with different number of carbon atoms.

No. of carbon atoms	Melting point (°C)	Latent heat of fusion (kJ/kg)
14	5.5	228
16	16.7	237.1
18	28.0	244
20	36.7	246
28	61.6	253
33	73.9	268

Table 2: Properties of different paraffin waxes [24, 44]

### Non-Paraffin

The non-paraffin have highly varied properties and are hard to give generalised properties such paraffin's PCMs. Non-paraffins have the largest category of materials that are suitable for phase change storage. They are further subgrouped into fatty acids and other non-paraffin organic. Fatty acids are purified and separated mixtures that are first produced by hydrolyzing animal and plant based fats and oils [45]. Fatty acids have properties that can be compared with the paraffin waxes properties. They have the chemical formula  $\text{CH}_3\text{-(CH}_2)_n\text{-COOH}$ . They have low temperature melting points, and high latent heat of transition per unit mass. They show no super-cooling when freezing, and they show small volume change when shifting phase [46]. Fatty acids have some bad properties such as bad odor, corrosivity, and high sublimation rate [41]. they are also more expensive than paraffin waxes [47].

Non-paraffins are generally flammable and should not be subjected to high temperatures or flames [48]. Glyolic acid, alpha naphthol, benzoic acid, and formic acid are some of the non-paraffin that are used as PCMs [24]. Table 3 shows some non paraffin properties

---

Compound	Melting point (°C)	Heat of fusion (kJ/kg)
Butyl stearate	19	140
Dimethyl sabacate	21	120
1-Dodecanol	26	200
Vinyl stearate	27–29	122
Glycolic acid	63	109
Acetanilide	118.9	222

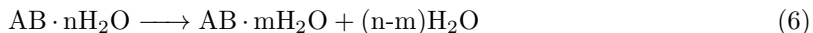
Table 3: Properties of different Non-paraffin  
[24, 49]

### 2.3.2 Inorganic PCMs

Inorganic PCMs are generally metallic and hydrated salts. They can be used in applications with up to 1500 °C. Inorganic compounds have low cost compared to organic compounds, a high thermal conductivity, high latent heat per unit mass, and are non-flammable [50]. Inorganic compounds have corrosive nature with the construction materials, they show super-cooling, and weak cycling stability [35]. However, metals and metallic alloys are excluded from these disadvantages which makes them potential PCMs for applications with high temperature requirement [51].

#### Salt Hydrates

Salt hydrates are alloys of inorganic salts and water which can be described by the formula of  $AB \cdot nH_2O$  where  $n$  represents the number of water molecules and  $AB$  represents metal carbonate, sulfite, phosphate, nitrite, acetate, or chloride. Salt hydrates have ion-dipole bonds which is made of an ion and a polar molecule [50]. The latent heat is absorbed or released by the dehydration and hydration of the salts. This can be described as melting and freezing from thermodynamic point of view. The outcome of the dehydration process is salt hydrates with less water molecules or anhydrous salt and water as shown in the two equations below:



Salt hydrates are commonly used PCM for thermal energy storage as they have high latent heat capacity, relatively high thermal conductivity compared with paraffin, and small volume variations when shifting phases. At the same time salt hydrates can undergo supercooling and phase segregation which are considered as disadvantages for salt hydrates. Supercooling prevents the release of latent heat stored in it at the phase change temperature [52][53]. Supercooling can be avoided by mixing nucleation seeds or by using an external device that is kept at a temperature below supercooling temperature called the cold finger leading to forming crystals faster and starting the nucleation process [54][55]. Examples of the nucleating agents which can be used to reduce supercooling of salt hydrates are sodium tetra borate, aluminum nitride, and silver nanoparticles [56][57][58]. Furthermore, increasing the roughness of the surrounding surfaces can reduce supercooling of salt hydrates [59]. Salt hydrates can be categorized into three melting behaviours which are [53]:

- Congruent melting which occurs when the anhydrous salt is completely soluble at the melting temperature in the water of hydration.
- Incongruent melting which occurs when the salt is not entirely soluble at the melting temperature in its water of hydration.
- Semi-congruent melting which occurs when the liquid and solid phases have different melting composition due to production of less-hydrated material through the loss of water.



Phase segregation in salt hydrates happen when incongruent melting takes place. This is because the number of water molecules of hydration available is not sufficient to dissolve one mole of salt which results in a supersaturated solution at the melting temperature. The solid salts having higher density ends up settling down in the PCM container making it unavailable for the reverse process of freezing. This is an irreversible process that happen with every charging and discharging cycle of the PCM lowering down its latent heat capacity. There are several ways to avoid this problem such as

- Mechanical stirring [60]
- Encapsulating the PCM [61]
- Increase the ratio of water in the solution to avoid supersaturated solution [62]

Table 4 below shows some examples of salt hydrates PCMs

PCMs	Melting temperature (°C)	Heat of fusion (kJ/kg)
KF4H2O	18.5	231
Mn (NO3)6H2O	25.8	125.9
Cacl26H2O	29.7	171

Table 4: Properties of different salt hydrates [63–66]

## Metallic

Low melting metals and metal eutectics constitute the category of metallic. Metallic phase change materials have high thermal conductivity, relatively high volumetric heat of fusion, low specific heat and vapor pressure, good thermal stability, good cyclic loading and can operate in temperatures above 560 °C and therefore they are presented as compact, and fast thermal solution [67]. The performance results of metallic PCMs based on models of heat transfer showed better figures compared with the performance results of organic PCMs [68]. The low heat of fusion of metallic per unit rate is what considered its main disadvantage. The metallic PCMs are an attractive option in systems where weight is not of a concern and high heat transfer rates are what is needed [68]. Table 5 below shows some potential metallic PCMs with high melting temperatures.

Compound	Melting temperature (°C)	Heat of fusion (kJ/kg)
Pb	328	23
Al	660	397
Cu	1083	193.4
Cu–Zn–Si (74/19/7 wt%)	765	125
Mg–Ca (84/16 wt%)	790	272
Mg–Si–Zn (47/38/15 wt%)	800	314

Table 5: Potential metallic for use as PCMs [69]

Metallic can also be used for low temperature thermal energy storage applications. Low melting temperature liquid metals have the same properties as high temperature melting metallic alloys mentioned earlier. Table 6 shows some examples for low melting temperature metals.

Liquid metals	Melting point (°C)	Evaporation point (°C)
Mercury	38.87	356.65
Cesium	28.65	2023.84
Gallium	29.8	2204.8

Table 6: Low melting point metals [70]

### 2.3.3 Eutectic PCMs

Eutectic PCM is a mixture of different PCMs with varying contents that are adjusted to achieve the required melting point [36]. Eutectic PCMs have good cyclic stability when freezing and melting as they don't segregate due to the formation of compatible blend of crystals [50]. There are inorganic and organic eutectic PCMs which can be used for high or low temperature cooling systems [71]. Eutectic PCMs have sharp melting temperature, and high volumetric thermal storage density. Tables 7 and 8 below show some organic and inorganic eutectic materials that are potential PCMs.

Material composition	Melting point (°C)	Heat of fusion (kJ/kg)
91.67% tetradecane+8.33% hexadecane	1.7	156.2
Hexadecane+tetradecane (2:3-0:1 by volume)	1.7–5.3	148.1–211.5
Capric acid+stearic acid	26.8	152
50% CH <sub>3</sub> CONH <sub>2</sub> +50% NH <sub>2</sub> CONH <sub>2</sub>	27	163

Table 7: Organic eutectic materials  
[72–75]

Material composition	Melting point (°C)	Heat of fusion (kJ/kg)
31% Na <sub>2</sub> SO <sub>4</sub> +13% NaCl+KCl 16%+40% H <sub>2</sub> O	4	234
40% tetra n-butyl ammonium bromide+2% borax	9	187
47% Ca(NO <sub>3</sub> ) <sub>2</sub> .4H <sub>2</sub> O+53% Mg(NO <sub>3</sub> ) <sub>2</sub> .6H <sub>2</sub> O	30	136
60% Na(CH <sub>3</sub> COO).3H <sub>2</sub> O+40% CO(NH <sub>2</sub> ) <sub>2</sub>	30	200.5

Table 8: inorganic eutectic materials  
[64, 73, 76, 77]

### 2.3.4 Measurement of Thermal Properties of PCMs

Thermal properties such as melting temperature, thermal conductivity, and heat of fusion are very important aspects of deciding whether the PCM is a good fit for the system. Therefore, there are multiple methods to measure these properties such as conventional calorimetry, differential scanning calorimetry (DSC), differential thermal analysis (DTA) and T-history method [65, 71, 78]

- Differential scanning calorimetry (DSC):

DSC is a thermal analysis method which is based on measuring the heat input difference into the sample and the reference material when both are being subjected to the same temperature program. This is done by heating the sample and the reference material using two different heaters and simultaneously measure the energy required to get to zero temperature difference between the two materials. This makes it possible to obtain many thermal properties such as heat of fusion, heat capacity, and phase change temperature. An approximate sample size for this application can be between 1-30 mg [37, 65].

- Differential thermal analysis (DTA):

DTA is a thermal analysis method which is based on measuring the temperature difference between the sample and the reference while subjecting both to the same amount of heat. The thermal properties are then found based on the measured temperature difference.

There are common disadvantages in both DSC and DTA methods such as the small size of the samples that go through the testing (1-10) mg. This can cause a problem due to the difference in thermal properties for some PCM materials when they are in big quantities as they are used for real life applications and small quantities. For example: super-cooling is increased in salt hydrates while segregation is decreased when the PCM is tested in small containers [64]. Furthermore, DSC and DTA experimental unit are complicated and expensive and can only take one sample at a time [65].

- 
- T-history method

The T-history method was found by analysing each of the conventional calorimetry, differential scanning calorimetry (DSC), differential thermal analysis (DTA) methods among their limitations [79]. This method is characterised by simple experiment unit, ability to measure thermal properties for multiple PCMs simultaneously, and allows to observe the phase change of the different PCMs used in the experiment unit [79]. These advantages make this unit useful when the rapid measurement of different PCMs is needed for engineering applications.

### 2.3.5 Physical and Thermal Properties Enhancement

#### Thermal Conductivity Enhancement

Low thermal conductivity is a problem that many high density storage PCMs and low temperature melting PCMs have [80, 81]. The low thermal conductivity will lead to some problems such as incomplete storing and extraction of thermal energy during the melting or freezing processes [36]. Melting the PCM goes faster than freezing it due to buoyancy effect which contributes to faster heat transfer in the system [82]. There are multiple methods to improve thermal conductivity such as the inclusion of nano-structures in the PCM, encapsulation of the PCM, metallic fillers, metal matrices, and filling high-conductivity particles into PCMs structure [83, 84]. The thermal conductivity of a paraffin PCM was improved 3,93 from 0,305 W/m.K to 1,2 W/m.K times by adding nickel foam as a metal additive [85]. Further, encapsulating paraffin n-octadecane using silica shells improved its thermal conductivity 4,13 times from 0,1505 to 0,6213 [86].

- **Inclusion of nano-structures**

Thermal conductivity can be improved by dispersion of nano-particles into the pure PCM material. These nano-particles are considered to be high conductive fillers such as metal, metal oxide, and carbon fiber. They are used in paraffin and fatty acids in order to improve their thermal conductivity [87]. These fillers cause the increase in thermal conductivity of the PCM due to the micro convection effect between the fillers and the PCM material [36]. PCMs show better improvement of thermal properties when carbon-based nano-structures are added compared with other material based nano-structures [7]. This can be attributed to the geometrical ratio of carbon nano-structures that creates very conductive paths within the PCM [88]. The geometrical shape of the nano-particles, chemical properties, and physical properties can affect thermal conductivity, latent heat capacity, viscosity, and super-cooling of the pure PCM material [87]. Carbon nanotubes were used with mass fraction of 0,5% as an additive with multiple composites of PCMs resulting in a 69% improvement in thermal conductivity compared with pure composites PCMs [85].

- **Encapsulation of PCM**

Encapsulating the PCM is covering the PCM with the proper coating or shell material in order to keep the liquid or solid phase of the PCM isolated from the surrounding [89]. Encapsulation can have multiple advantages such as reducing the reaction and mixing of the PCM with the surroundings which maintains the right composition of the PCM, increased thermal conductivity and increased thermal and mechanical stability [90]. There are different type of encapsulation such as macro-encapsulation, micro-encapsulation and nano-encapsulation. Macro-encapsulation means that the PCM is filled in capsules that can have different shapes in macro scale, and different materials such a metallic or polymeric film [36]. Micro-encapsulation and nano-encapsulation means that the PCM is filled in capsules that are in micro scale and nano scale, respectively [91]. Paraffin n-octadecane thermal conductivity was improved by encapsulating the PCM with calcium carbonated shell  $CaCO_3$  by 8,26 times from 0,153 W/m.K to 1.264 W/m.K [85].

#### Phase Segregation and Supercooling

Salt hydrates have high thermal energy storage, however this high energy storage decreases with time due to phase segregation. This is because of the congruent melting and the formation of

lower hydrate salt making an irreversible process and continuously decreasing the thermal energy storage capacity of the PCM [81][73]. There are different methods that are used to avoid phase segregation such as gelling or adding thickening agents. Adding different materials to salt hydrates is one way to stop the heavier phases to sink to the bottom of the container. Gelling means adding a cross linked material such as cellulose derivatives or polymers to the salt hydrates which creates a three dimensional network that prevents the segregation of salt hydrates and holds it together [73][7]. Thickening agents are added in order to increase the viscosity of the solution and therefore prevents the segregation of the salt hydrates [92]. Adding thickening agents can reduce the latent heat capacity of salt hydrates with a range that is between 4% up to 35% depending on how much thickening agent is added [93] [56]. However, adding thickening agents between 0,5% and 4% can result in reduced segregation and super-cooling while maintaining the latent heat capacity of the PCM [94] [95]. Some other methods to prevent segregation can be mechanical stirring and encapsulating the PCM.

Supercooling happens when the PCM starts to solidify at temperatures below its freezing temperature. The slow rate of nucleation, and the slow rate of growth of the nuclei can both be reasons for supercooling [96]. It is a problem associated with salt hydrates [65]. There has been a lot of research in order to reduce and eliminate super-cooling. There are many methods to do so such as adding nucleating agents which is considered to be the most efficient method in the reduction of super-cooling as 1% addition of it can reduce super-cooling more than 90% [97]. The added nucleating agents and the PCM have a similar crystal structure. The nucleating agents support the crystal growth within the PCM as it reaches its freezing temperature and hence reduces super-cooling [7]. The other methods are active methods that try to externally trigger the crystallization of the PCM such as mechanical stirring or ultrasonic waves [97]. Figure 11 below shows the effect of supercooling on latent heat capacity.

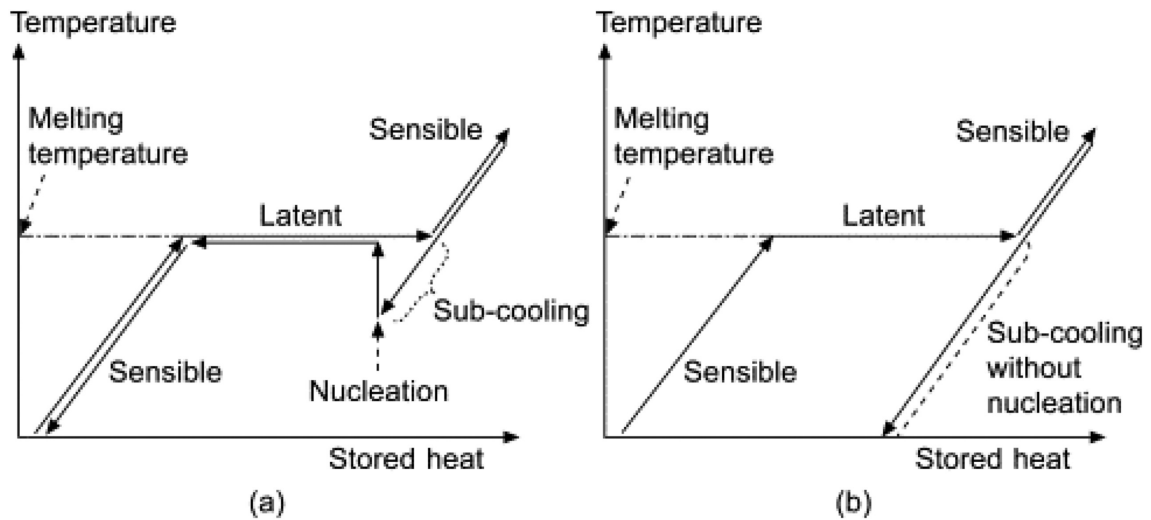


Figure 11: Effect of supercooling on heat storage [96]

## 2.4 Applications of Cold Thermal Energy Storage

Cold thermal energy storage has gained interest due to its energy efficiency and cost saving potentials in operation, maintenance, and capital costs [98]. CTES can be used across different applications such as air conditioning, free cooling, refrigeration, medical, and food storage. The research on PCM applications for the last decade was mainly focused on building applications and domestic refrigeration [99][100].

### 2.4.1 Air Conditioning(AC)

Air conditioning systems provide thermal comfort for the people, and it has become an essential part in many parts of the world. However, air conditioning systems consume a lot of energy. Air conditioning systems used in buildings and vehicles consumes around 20% of the total auxiliary energy[101]. Furthermore, in commercial vehicles air conditioning systems consume up to 17% of the available engine power which lead to shorter driving distance [96, 102]. Therefore the reduction of this high energy consumption is important. Integrating CTES systems have the potential to reduce this power consumption, equipment size reduction, and emission and noise pollution reduction [103]. This is due to its large latent heat storage capacity which can solve the fluctuation problems faced by air conditioning systems now and maintain the desired output temperature. Furthermore, promising results such as significant cost and energy savings and improved thermal comfort were shown for studies that integrate CTES with HVAC systems in buildings [96].

There are different TES integrated air conditioning systems which was proven to show promising results in terms of operating cost and maintaining thermal comfort. A PCM-based air distribution system was tested for peak shaving goals. The PCM used was mixture of paraffin waxes with heat of fusion of around 90 kJ/kg. A simulation was conducted to evaluate the system performance. the CTES unit was charged during off peak hours, and the cooling was provided using the CTES system during peak hours. It was found that using 400 kg of the PCM can be sufficient to maintain comfortable indoor temperature in a room with an area of 73,8 m<sup>2</sup> without using external chiller capacity [104]. Furthermore, it was concluded that the system could help with peak shaving for buildings. Figure 12 below shows a schematic for the proposed HVAC system.

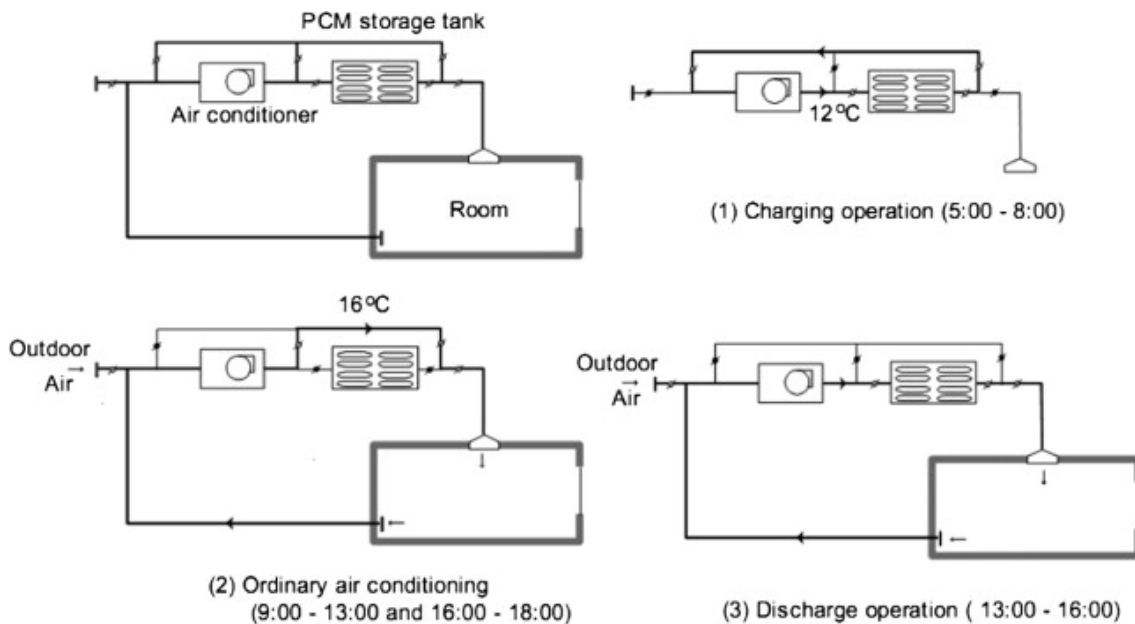


Figure 12: CTES system proposed for an HVAC system [3]

A PCM-based air conditioning system for a telecommunication station in china was tested to be compared with the conventional system. This system was made to support the already existing AC system and not as a replacement. The system used an organic PCM with a range of transition temperature between 18-20 °C [105]. The system was charged using outdoor air, and discharged using indoor air. Water was used as the medium to transfer heat between the PCM and the surrounding. The PCM-based system showed potential for improving the energy efficiency up to 4 times more than the conventional non-PCM system. Furthermore, the the system showed around 50% energy saving. Figure 13 shows the charging and discharging mode of this system.

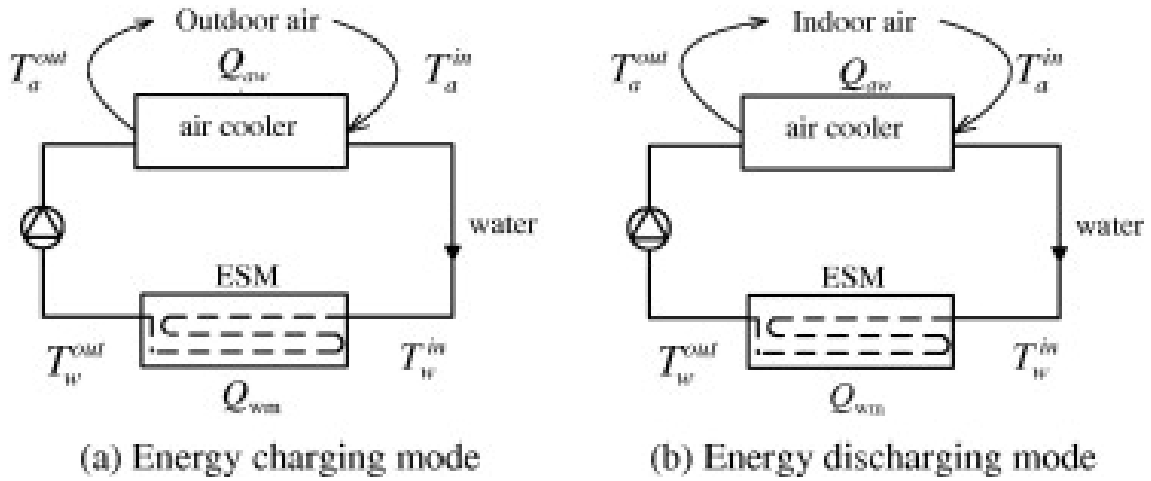


Figure 13: Charging and discharging modes [105]

A prototype of a thermoelectric system was integrated with TES using PCM for the purpose of space cooling. The PCM used was RT22 which belongs to the organic group PCMs with a melting temperature between 19-23 °C [106]. The system uses the outdoor air temperature to charge the PCM using water as a medium to transfer heat. The heat generated by the thermoelectric unit can be dissipated in the PCM leading to melting it, hence discharging mode. The system was tested in a reduced scaled facility, and the results showed an average coefficient of performance of 0,87 reaching to 1,22. Furthermore, electricity usage was reduced with 35,3% compared with a system not using the PCM storage. Figure 14 shows the schematic of the experimental setup of the system.

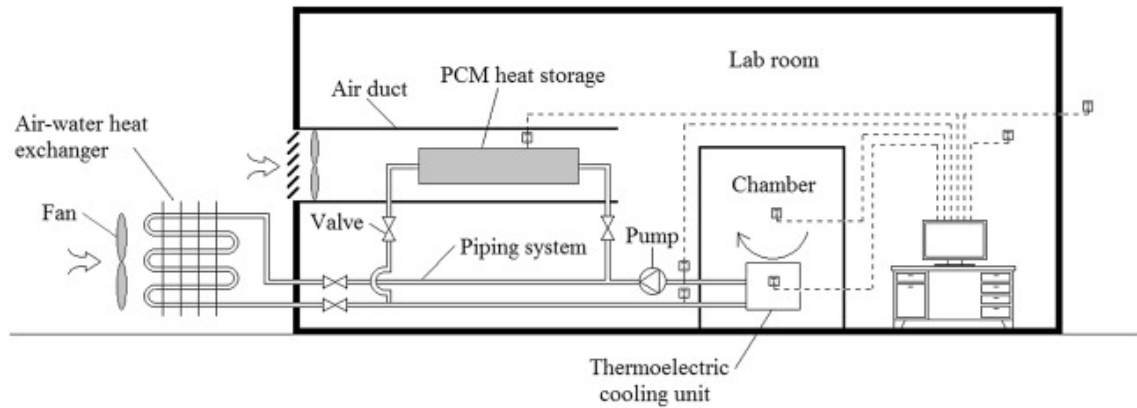


Figure 14: A prototype of thermoelectric system using PCM as TES for space cooling [106]

A study was conducted on a system that integrates TES using PCM with a conventional AC system. The PCM-AC system and the AC system were both compared in terms of different aspects such as temperature fluctuation, coefficient of performance(COP), and energy savings[101]. The PCM used was RT18HC with latent heat capacity of 220 kJ/kg, and phase change temperature range between 17-19 °C. The experiment consisted mainly of a conventional AC system, a PCM based TES unit, and an insulated temperature controlled room. The heat load was generated inside the room using electric heater, the cold air coming form the AC was used to charge the TES first before it starts cooling the room. When the TES is fully charged, heat is dissipated into the TES unit, hence discharging mode. The system was first simulated, and then the experiment was done. The experimental and simulation results were very similar. The results show that the temperature fluctuation decreased to 2,56 °C when using the TES from 4,31 °C without the TES system. Furthermore, the system COP was increased with 19,05 %, and the compressor on-off

frequency was reduced by 27%. Figure 15 below shows a schematic for the AC-PCM system used.

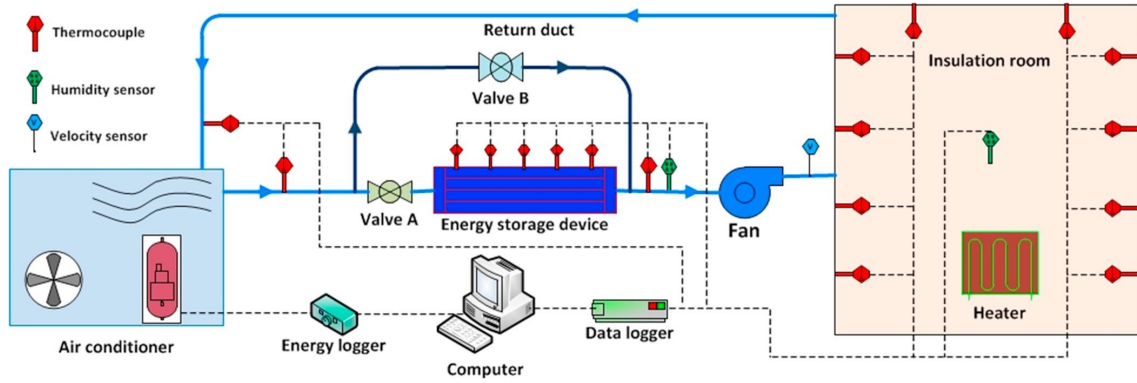


Figure 15: A schematic diagram of the PCM-AC system [101]

A PCM based TES system was made to support air-conditioning system. The TES system was designed to be integrated with the vapor compression cycle of the refrigeration system. The PCM used was paraffin wax (n-Tetradecane) with latent heat storage of 180 kJ/kg and melting range of 4 °C to 6 °C. The PCM is charged using the air cooled in the evaporator at night when temperatures are low. Discharging happens during peak hours where a part of the incoming hot air goes through the PCM and dissipate its heat there. The simulation results showed potential to reducing the compressor size by 50%, lower the electricity consumption by 30%, and lowering down CO<sub>2</sub> emissions by 30% [107]. Lab results showed agreement with the simulation results, however, the study was lacking some important aspects such as integration inefficiencies, energy losses, and complexities related to real life situations. Figure 16 shows the schematic of the TES-AC proposed system in the discharge mode.

**Overall Conceptual Block Flow Diagram  
Charging and discharging modes of operation**

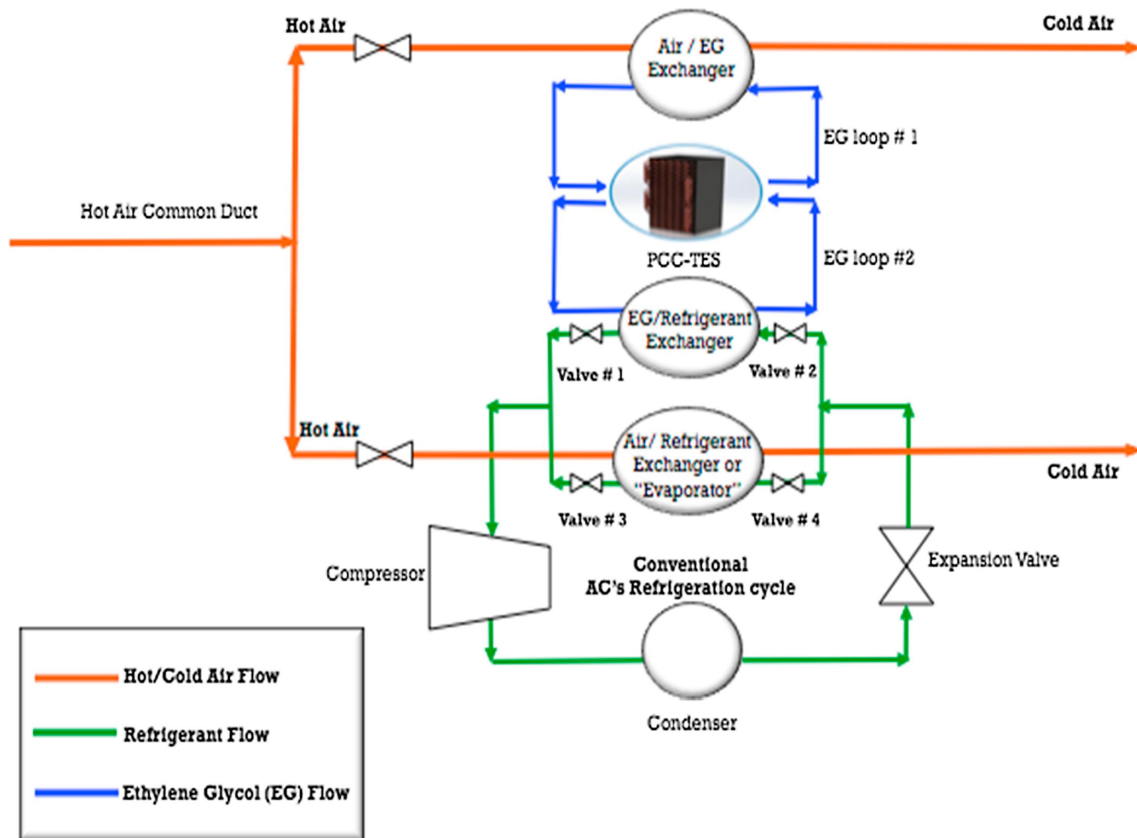


Figure 16: A schematic diagram of the PCM-AC system [107]

**2.4.2 Free Cooling**

Free cooling is the use of low air temperature degrees to assist in air conditioning systems and chilling water systems. PCMs can be used to store the sensible night time free cooling and use it again when it is needed reducing the load on the chillers [36]. A study was conducted on a mechanical ventilation system that uses latent heat thermal energy storage that used paraffin as a PCM. The study showed that the system lead to an improved thermal comfort in the building by utilising the paraffin with a melting point of 22 °C [36]. Figure 17 below shows the schematic of the used system for free cooling.



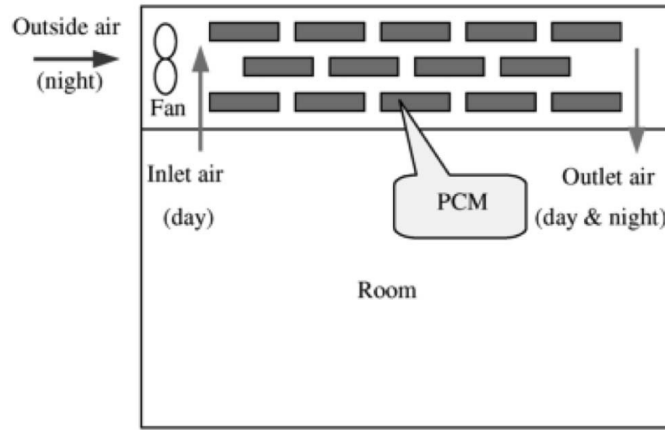


Figure 17: Schematic of the integrated free cooling system [3]

A mechanical ventilation system including an integrated PCM system and a control unit in order to utilize low night temperatures for cooling the building. The PCM used was organic PCM with latent heat capacity of 142 kJ/kg. The system was charged when the inlet temperature to the PCM unit  $T_a$  was lower than the outlet temperature  $T_o$  which is usually during the night. The system was discharged when the inlet air temperature to the PCM unit was higher than the outlet air temperature from the PCM unit which is usually during day. It was found out that 1 to 1,5 kg of PCM per  $m^3/h$  of fresh ventilation air is the optimal amount of PCM to be used [108]. Furthermore, the optimum temperature of phase change is to be equal to the average ambient air temperature in the hottest month. Figure 18 below shows the air flow during charging and discharging cycles.

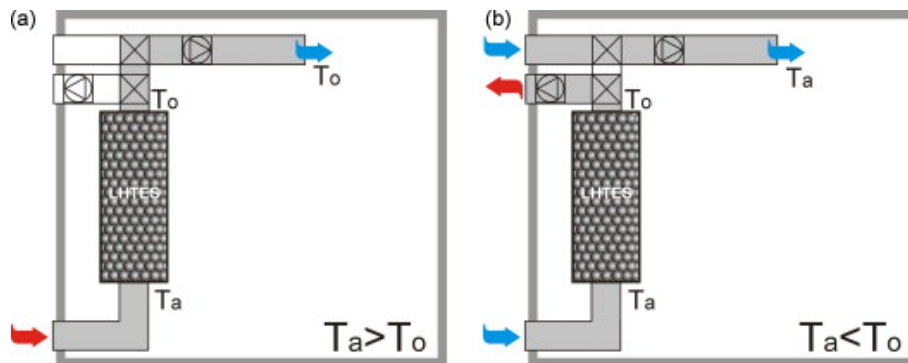


Figure 18: System showing airflow during discharging in part a and during charging in part b [108]

A study on the utilisation of free cooling in a low energy building using an integrated latent heat thermal energy storage device into a mechanical ventilation system [109]. The PCM used was encapsulated RT20 paraffin which was placed in a cylindrical latent heat thermal energy storage device. The study found that the optimum phase change temperature for a continental climate was between 20 °C and 22 °C. Furthermore, the study found that thermal comfort can be achieved with the use of 6,4 kg of PCM per square meter of floor area [109].

A study was conducted to evaluate the potential use of free cooling in assisting and reducing cooling loads of a building in the summer period in the continental Mediterranean climate [110]. The PCM used inside the air channel was contained in macro-encapsulated panels being salt hydrate SP-22 with heat storage capacity of 160 kJ/kg and a melting and solidification temperature of 22 °C and 18 °C, respectively. The system is a type of ventilated facade with an integrated PCM-based TES in the facade air cavities. There were a total of 112 panels which were distributed in the facade over

---

14 airflow channels. The PCM was charged during the night leading to its solidification. During the day when cooling was needed, mechanical ventilation was used to release the coldness stored inside the PCM leading to discharging the PCM and melting it. A maximum capacity of 42,8 MJ per day was achieved in this study [110].

A study investigated the potential use of PCM-infused gypsum boards combined with night ventilation for cooling purposes. The PCM used was PT20 which is organic PCM with heat storage capacity of 180 J/g and melting temperature of 20 °C [111]. The study compares electricity consumption between two different huts built at Tamaki Campus, University of Auckland shown below in Figure 19. One hut is built with the PCM-infused gypsum board, and the other is built with normal gypsum board. An AC system is built in each room. The system was tested first without using night ventilation. The PCM was charged using the cold air coming from the AC during low peak period, and then the PCM was discharged during peak periods leading to very little savings in energy consumption. However, when free cooling was used to charge the PCM, weekly electricity consumption decreased by 73 % [111].



Figure 19: Test huts at the University of Auckland campus [111]

### 2.4.3 Refrigeration

Mechanical vapor compression based refrigeration cycles generally dominate the industry and is responsible for a large energy consumption and green house gas emissions. CTES systems used for refrigeration can significantly reduce the energy consumption and green house gas emissions. In a comparison between conventional refrigeration systems and PCM based systems, PCM-based consumed less energy and generated significantly lower emissions [96]. PCM-CTES can be integrated into the primary refrigeration circuit based on a PCM/two-phase fluid heat exchange design , and into the secondary refrigeration circuit based on a single phase fluid heat exchange design [7]. These two methods of integrating PCM are shown in Figure 20 where part a is a PCM unit directly integrated into the primary refrigeration circuit, and part b is the PCM unit integrated into the secondary refrigeration circuit.

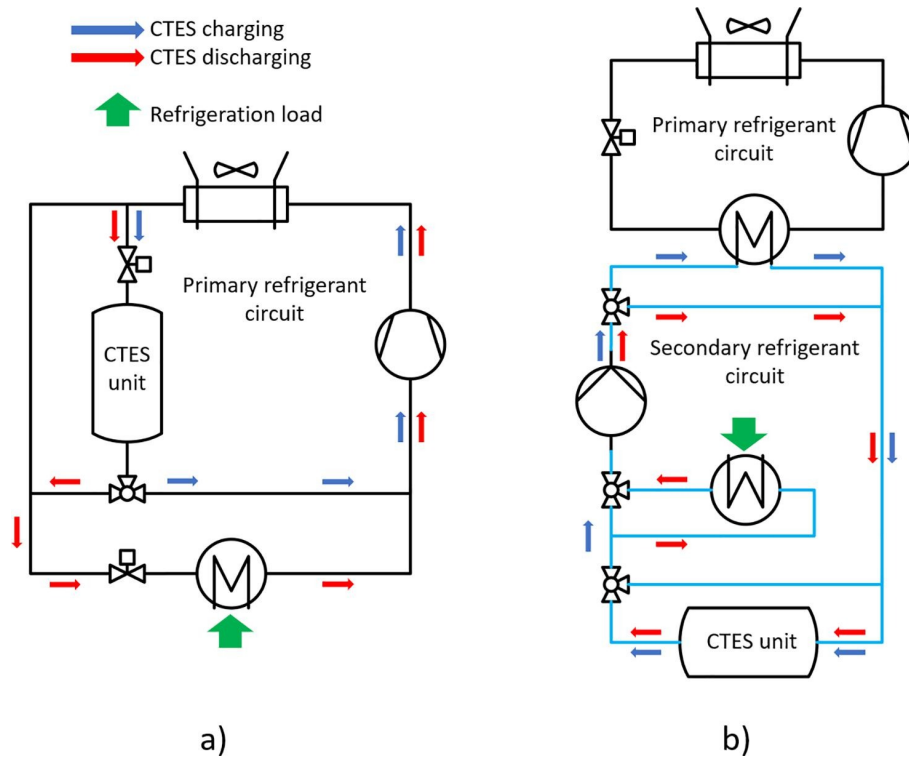


Figure 20: PCM-CTES integration methods [7]

A PCM based TES refrigeration system was designed to maintain a refrigeration truck at  $-18\text{ }^{\circ}\text{C}$ . The system used inorganic salt water solution PCM with a melting temperature of  $-26.7\text{ }^{\circ}\text{C}$  and  $154,4\text{ kJ/kg}$  latent heat capacity. Thin flat containers were used to encapsulate the PCM. The flat containers were also contained in a well insulated case referred to as PCTSU (phase change thermal storage unit). The system was charged when the truck was stationary in a warehouse using the refrigerating system powered by electricity instead of internal combustion engine. The system was discharged when the vehicle was moving. Figure 21 below shows the configuration of the system. Each of valves 1 and 2 are open during the charging mode while valves 3 and 4 are closed and vice versa in the discharging mode. The temperature was controlled using a thermostatic on-off controller. The built system in this experiment operated with less than half of the energy cost of a conventional system, produced much lower green house gas emissions, had improved temperature control, and reduced noise level [112].

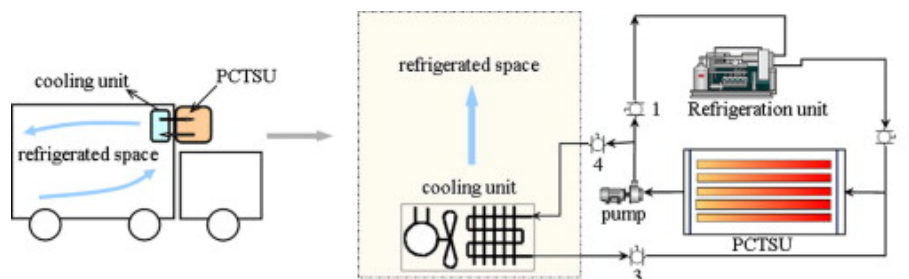


Figure 21: The built refrigeration system [112]

The effect of integrating a PCM slab as a cold thermal energy storage on the exterior side of a refrigerator's evaporator was simulated and verified experimentally [113]. The PCM used was eutectic aqueous solution with a phase change temperature of  $-3\text{ }^{\circ}\text{C}$ . Numerical solutions were conducted to study the integration effect on the energy efficiency of the refrigerator according to

different operating conditions. Figure 22 below shows the proposed integrating method of the PCM unit with the evaporator. The model results predicted a 5-15 % increase in the COP, a decrease in the frequency of on-off switching in the compressor, a decrease in the temperature fluctuation inside the fridge, and possibility to maintain the area refrigerated without extra power for up to 8 hours [113].

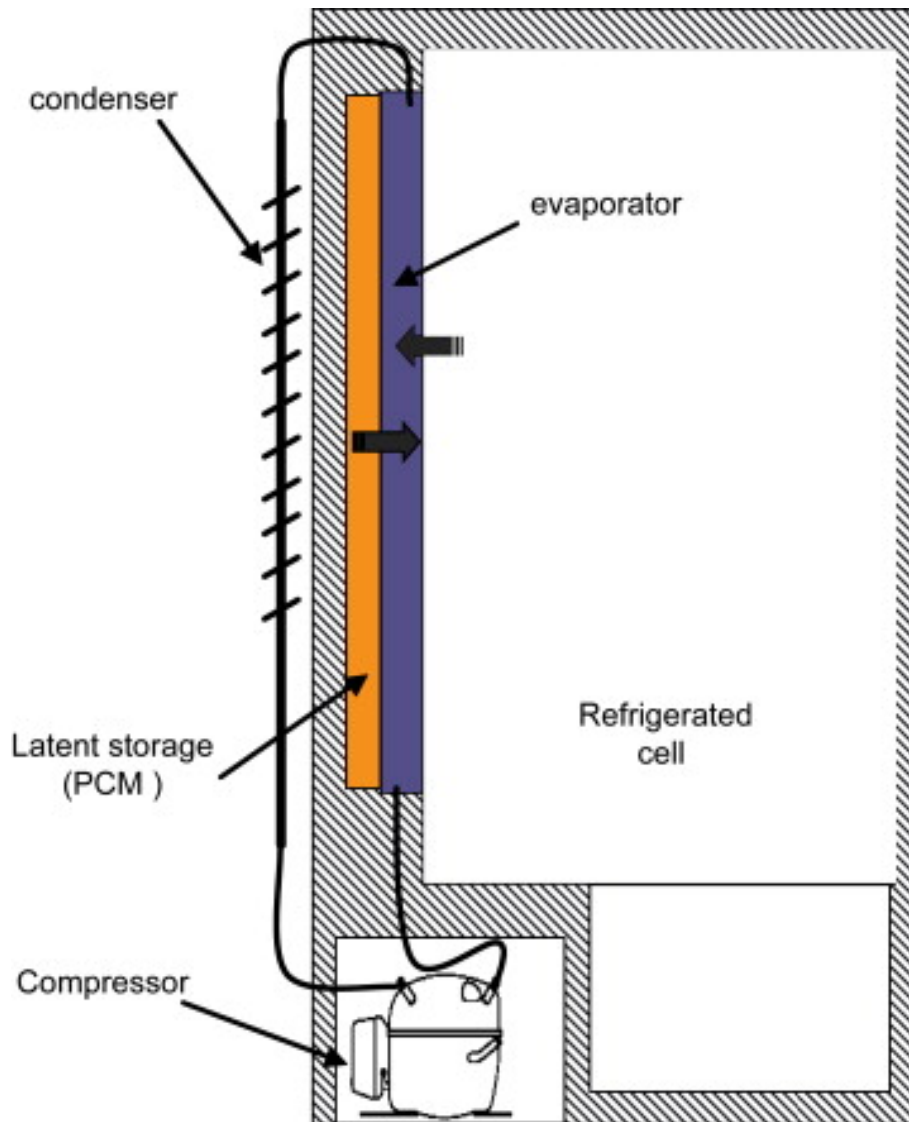


Figure 22: PCM integration with the evaporator [113]

A study was done to evaluate the effect of adding a PCM to a cold storage room that is supposed to be maintained at  $-18\text{ }^{\circ}\text{C}$ . The PCM used was commercial eutectic mixture with a melting onset and peak temperature of  $-14,7/-10,7\text{ }^{\circ}\text{C}$  [114]. The PCM integrated system was designed to solve the problem of an operational failure or electricity shortage. The results showed the PCM load covering 10% of the total heat transfer surface area can result in maintaining the required temperature under all ambient conditions and extend the time to break the cold chain [114].

A household refrigeration system with an integrated novel PCM heat exchanger was investigated in order to study the potentials of improving the refrigeration system energy efficiency and temperature stabilization. The PCM had a melting temperature of  $4\text{ }^{\circ}\text{C}$  and a latent heat of fusion of  $200\text{ kJ/kg}$ . The refrigerator had a vapor compression cycle, and the heat exchanger PCM was placed on the evaporator as shown in Figure 23 b) below. The results showed reduced power consumption by 12 % and an increased COP by 8% compared with the same refrigerator without the PCM.

Figure 23 a) below shows the household refrigerator model, and b) shows the design of the PCM heat exchanger.

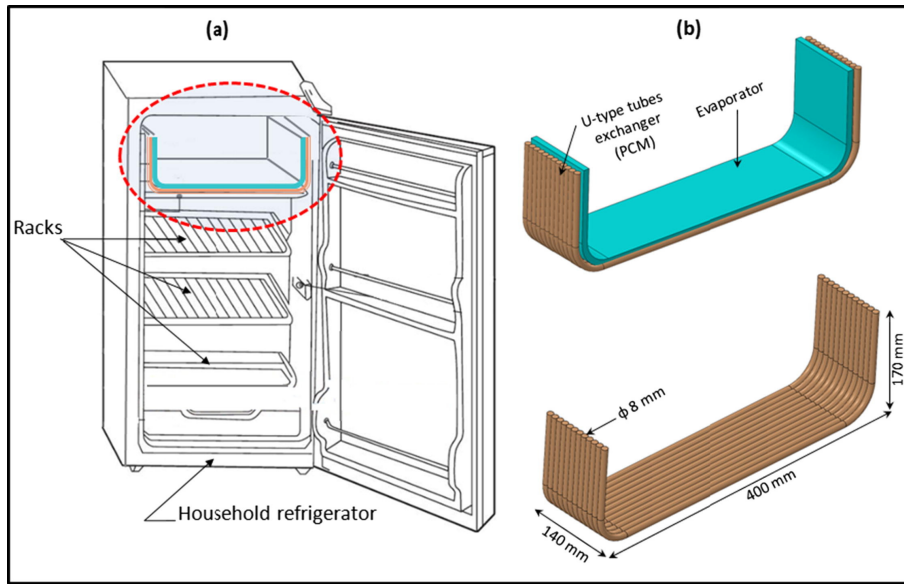


Figure 23: a) Refrigeration model b) the design of the novel PCM heat exchanger [115]

Integrating PCMs with refrigeration systems can lead to huge savings in energy consumption and increase in efficiency which can lead to significant reduction in pollution caused from the vapor compression cycle. Furthermore, it can lead to an extended operational life of the refrigeration system which means lower cost and better utilisation of the equipment.

#### 2.4.4 Food Storage and Transport

PCMs have a lot of use in food industry when it comes to transporting the food and saving the food [6]. Maintaining the quality of the food while transporting it lies in maintaining the required thermal conditions to do so. Therefore, it is very important to improve the refrigerating systems transporting food to ensure high food quality. Studies show that using PCM as TES in refrigerated transport vehicles is one strategy that lead to lower peak demands and reduced heat transfer into the containers. Transporting food requiring refrigeration happens in temperatures that range between  $-25^{\circ}\text{C}$  and  $15^{\circ}\text{C}$  depending on the type of food being transported [116].

A study modified the conventional method of insulation of the refrigeration truck using PCMs [117]. This was done by implementing the PCM in the truck walls to reduce the heat transfer. The PCM used was paraffin based with a melting point of  $7^{\circ}\text{C}$  and a heat storage capacity  $156\text{ kJ/kg}$ . Peak heat transfer rate was reduced by  $29,1\%$  when all the Walls were covered with the PCM. The overall daily heat transfer into the refrigerated trailer was reduced by  $16,3\%$  compared with the conventional system and temperature fluctuation inside the refrigerated container was decreased. This heat flow reduction into the refrigerated space can result in energy savings, more energy friendly refrigeration as the system will have less green house gas emissions, and prolonged refrigeration system life span as the the pressure on it will be reduced. Figure 24 below shows a schematic diagram of the cooling system among the two refrigeration trailers that were compared for the purpose of this experiment.

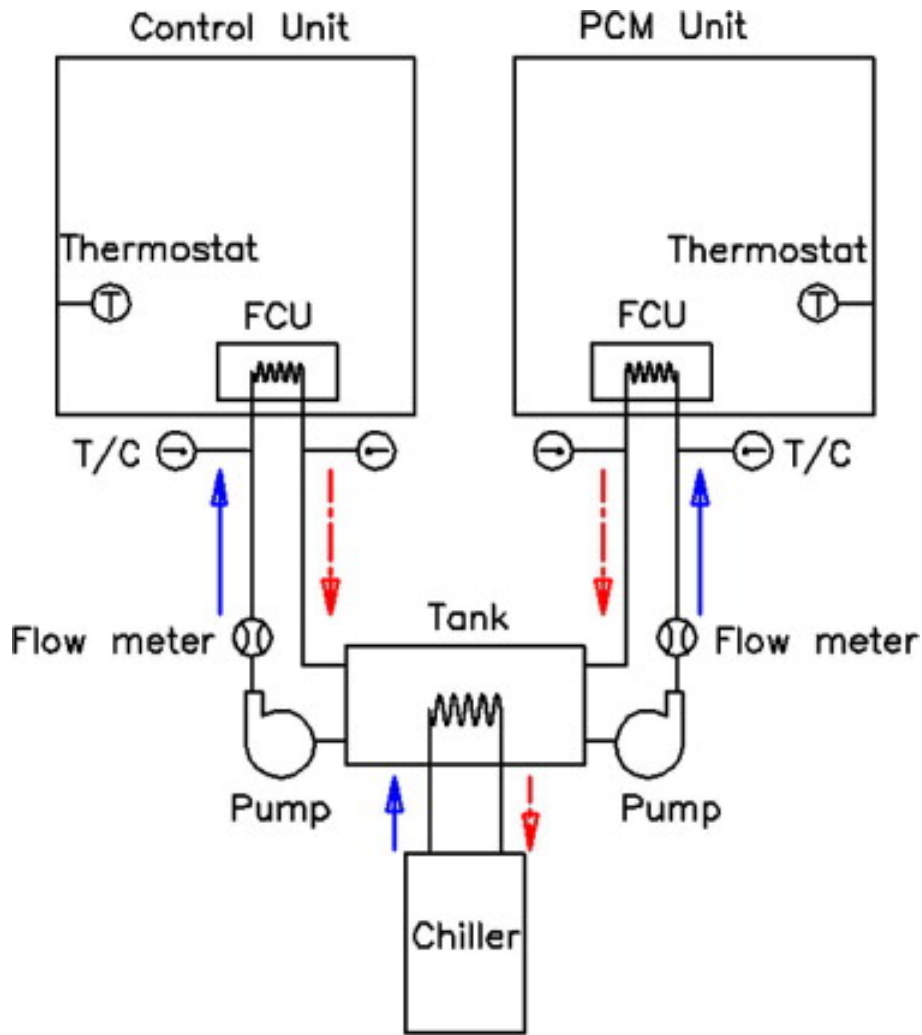


Figure 24: Experiment design comparing PCM-based truck and conventional truck [117]

A study was done in order to evaluate the theoretical energy benefits resulting from integrating different PCMs into the walls of a standard refrigeration container under different weather conditions in Italy[118]. The PCMs used were paraffin RT27, RT31, RT34, RT35HC, RT44HC, RT47, and salt hydrate C48. The fitted walls with PCM gained thermal inertia leading to a reduction and shift in the heat load compared with the traditional container without PCM. RT35HC was the PCM showing the optimal results with a melting temperature of 35 °C and latent heat capacity of 105 kJ/kg. The reduction in peak heat load was between 20,01 % and 20,87 %, whereas the reduction in energy consumption was between 4,55-4,74 % [118]. The results were later experimentally verified and it was found that the experimental results match the simulation results[118].

There are also simple applications of the use of PCM in storing food such as:

- Simple containers for temperature sensitive food that are put in the refrigerator to freeze the PCM in it before they are used to keep the food cold. Some of these containers are shown in Figure 25 below:



Figure 25: Gel containers for food storage  
[119]

- Isothermal water bottles which are double wall bottles with a PCM as active part.
- PCM containers for catering products to be transported while maintaining its heat. The container has the PCM around its inner walls keeping the inner temperature of the container as desired. Figure 26 below shows some of these containers.



Figure 26: PCM containers  
[120]

#### 2.4.5 Building Applications

There has been a lot of studies on integrating PCM based TES in building materials. These technologies have the potential to improve buildings thermal indoor conditions while at the same time decreasing the energy consumption [121]. PCMs can be integrated with windows, walls, ceilings, and floors leading to stabilizing the building indoor climate and saving energy. It can also be used to improve the thermal performance of the building in regards to the application related to water heaters and coolers [122]. studies were conducted on integrating PCMs into gypsum and wallboards, concrete, bricks, composites and other materials [123].

Gypsum board is a light weight construction material that can gain thermal mass by and integrating PCM with it. Consequently, temperature fluctuations will decrease in buildings using such technologies [123].

The effect of using a modified gypsum board in a special light weight chambers was studied in order to see the improvements in the thermal conditions of that room [124]. The modified gypsum boards were built in with an integrated PCM materials, mineral aggregates, and some admixtures. The PCM used was micro-encapsulated paraffin with a melting temperature range between 25 and 28 °C. The results showed a reduction in peak temperature of up to 4 K compared with the room not using the modified gypsum board.

A study was done to investigate the effect of adding a PCM copolymer composite wallboard into a room [125]. The wallboard consists of 60 % microencapsulated paraffin within a copolymer.

---

The PCM has a melting and a freezing temperatures of 13,6 °C and 23,5 °C, respectively. The experiment tested the effect of using the new gypsum board under winter, summer, and spring like conditions. The results showed that the PCM composite is good for enhancing thermal comfort conditions for the following reasons :

- The over heating effect was reduced due to the use of PCM based wallboard
- The temperature peaks of the wall surfaces were lower
- The stratification was avoided due to improved natural convection mixing of the air

PCMs can further be integrated into concrete materials in order to increase its heat storage capacity which can translate into energy savings for cooling and heating applications [123].

A study was done to study the effect of integrating PCM materials with conventional and alveolar brick materials for buildings in Spain [126]. The PCM used was macroencapsulated RT-27 and SP-25 A8 with melting temperature of 28 °C and 26 °C, respectively. Multiple cubicles using the PCM based bricks, and one reference cubicle using normal bricks were constructed in order to study the thermal effect of using the PCM based bricks. The cubicles had a cooling system and energy consumption was recorded for the different cubicles. It was concluded that the PCM based bricks reduced peak temperature up to 1 °C and the temperature fluctuations throughout the day were reduced. Furthermore, The maximum energy consumption savings achieved in a summer day was about 15 %.

#### **2.4.6 Sub-zero Applications**

There are a lot of subzero applications that CTES systems can be integrated with such as building applications or food storage and transportation applications. Eutectic water salt solutions are what is most used for subzero thermal energy storage due to their advantages of higher thermal conductivity, fusion heat and density, and lower flammability than non-eutectic water salt PCMs [127]. An experimental investigation was done on adding a PCM to the evaporator in a household refrigeration system. The PCM used was an eutectic water-salt solution with a phase change temperature of -3 °C. The results showed improved performance compared to the conventional system and allowed for operating the system without the use of power for several hours [127].

#### **2.4.7 Other Applications**

- Vest cooling

Integrating PCM into vest-cooling technology can provide thermal comfort for the users during physical activities. This is because the PCM will absorb the excess heat from the body and hence cool it down [128]. A study was done on a personal cooling vest that incorporates ventilation fans and PCM material as shown in Figure 27 below [128]. The PCM used was salt mixtures including sodium sulfate, water, and additives with a melting temperature of 21 °C. The vest was tested on a sweating human manikin in high humidity and high temperature weather conditions 34 °C and 75% relative humidity. The results showed that the cooling vest can effectively remove the heat from the body and provide evaporative cooling .



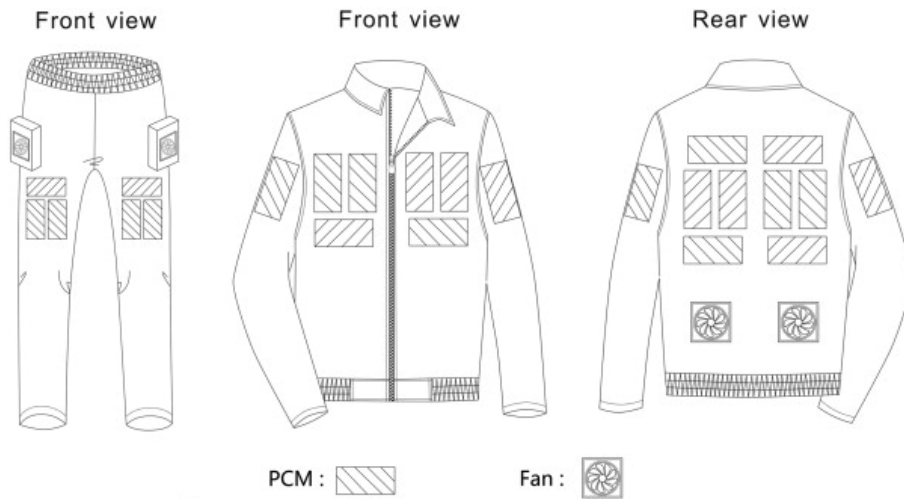


Figure 27: Cooling vest with integrated fans and PCM material [128]

- Cooling of photo-voltaic(PV) panels

Keeping PV panels cold is important to maintain high efficiency [129]. Using PCM based TES to keep the PV cold can have a big impact on the PV technology. A study was done on the effect of integrating PCM on the back side of the PV panels to investigate thermal regulation and efficiency enhancement [130]. The PCM used was paraffin wax RT55 with a melting range of 51-57 °C and heat storage capacity of 170 kJ/kg. The results showed the the modulus increased in efficiency by 13,2 % and dropped in temperature by 10,6 °C.

- Hybrid heat sink

A study was done on a hybrid heat sink that is made of a plate fin heat sink with the tip immersed in PCM [131]. This approach combines passive and active cooling. Heat dissipation will happen through the exposed area of the fins throughout high convective cooling when its possible. Otherwise, heat will be absorbed by the PCM. the results showed improved thermal performance of the hybrid heat sink compared with the normal heat sinks.

### 3 Experimental Setup

The following experimental set up is a prototype of a CTES system that is planned to be used on an industrial scale. The system consists of the CTES unit which is an insulated welded box of stainless steel filled with liquid PCM. First, water was used as the phase change material in order to study the general performance of the system, then it was replaced with RT-9HC which is an organic PCM. The latent heat is stored by freezing the PCM and released by melting it depending on whether the system is charging or discharging. Figure 28 below shows the path the  $CO_2$  follows during charging and discharging modes. During the charging mode, the valves V4, and V6 are closed while V7 and V5 are kept open. During the discharging mode, the valves V5 and V7 are kept closed while V4 and V6 are kept open. The closing and opening of the valves is done manually before starting charging or discharging of the CTES unit.

The CTES unit is connected to the main  $CO_2$  circuit, which is pump-circulated. Furthermore, the system has an evaporator which is connected to a glycol circuit acting as the heat source. The set up is also connected to a condenser which is connected to a separate centralized  $CO_2$  refrigeration cycle acting as the the heat sink to the CTES system. The set up is also connected to a liquid receiver to store the refrigerant circulating in the CTES system being also  $CO_2$ . The liquid receiver is cooled by the centralized  $CO_2$  system to keep the refrigerant temperature and pressure low all the time. In addition, the system is connected to a pump which controls the flow rate of the  $CO_2$  inside the CTES system by changing its frequency between 35 Hz and 50 Hz. The pump pumps

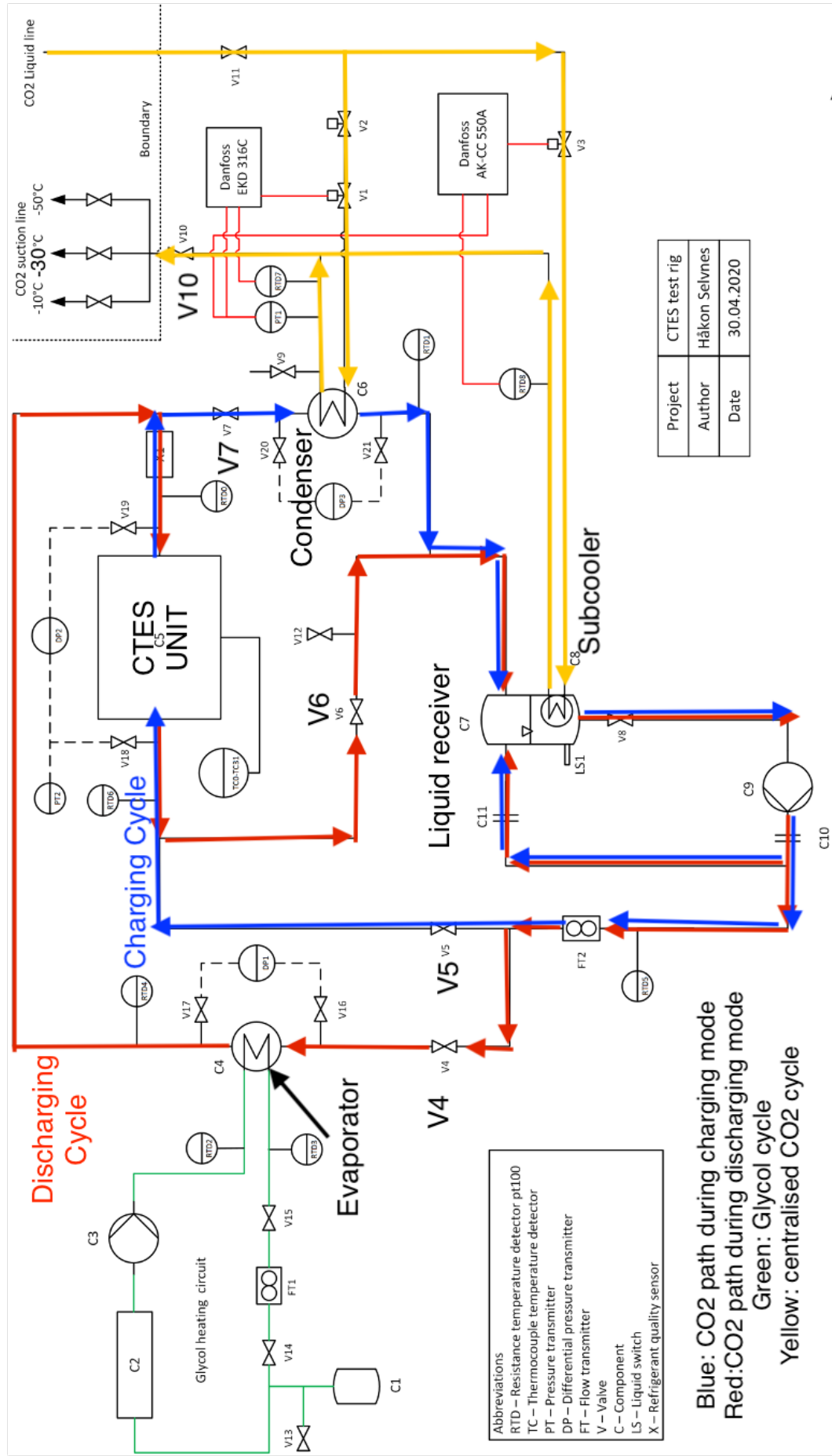


Figure 28: Diagram of the experimental setup

---

the flow towards the CTES unit or the evaporator depending on the valves arrangement that are set based on the system operating mode. The exchange of heat between the the PCM in the CTES unit and the rest of the system happens through a set of ten pillow plates heat exchangers that are immersed in the PCM and distributed vertically above each other with equal distance between the plates. The plates are connected together using a manifold at the inlet and the outlet. This causes the refrigerant to flow into the manifold and then gets distributed throughout all the ten pillow plates heat exchangers. These plates connect the CTES unit with the rest of the equipment in the system such as the evaporator and the condenser. The system contains temperature, pressure, flow, and phase sensors that are distributed along the system to allow for the control and analyse of the system. Figures 29, 30, and 31 below show the system with its different components.

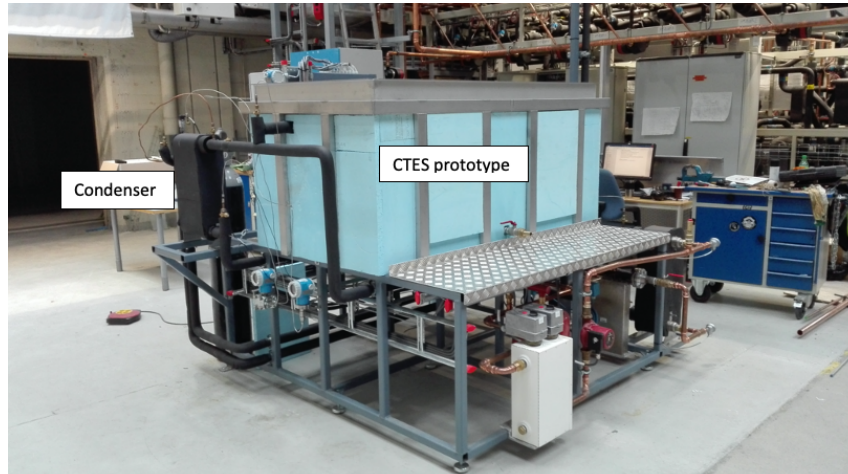


Figure 29: CTES system with the condenser.

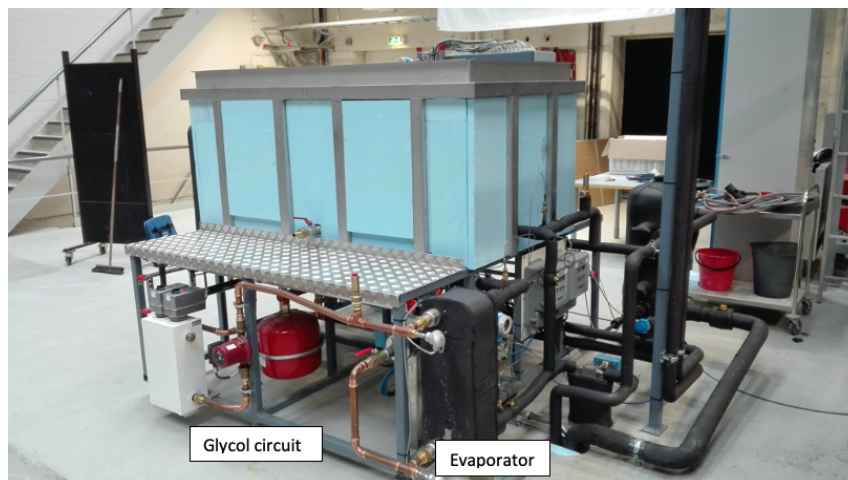


Figure 30: CTES system with the evaporator and glycol circuit

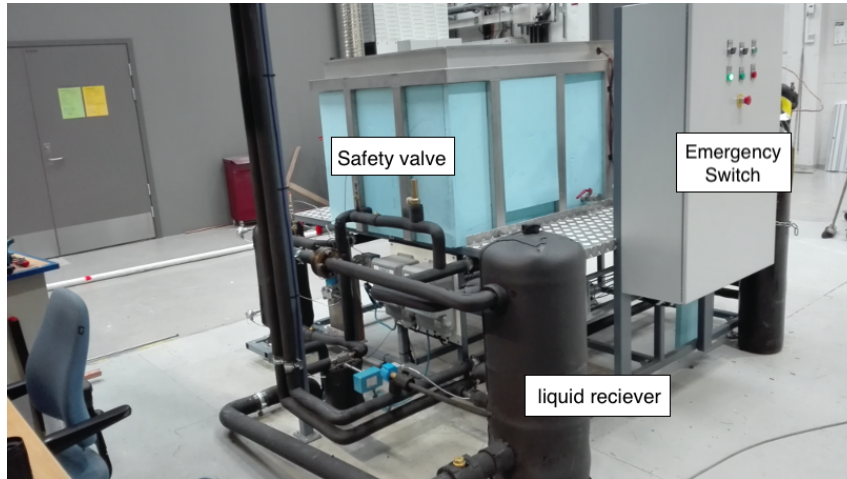


Figure 31: CTES system with the liquid receiver

The system is designed to work in two modes which are charging and discharging. During charging mode, the latent heat is stored by freezing the PCM inside the CTES. This entails that the  $\text{CO}_2$  will flow inside the plate heat exchangers as a liquid and flow out mainly as a gas. This mode utilises the pillow plate heat exchangers as evaporators for the internal  $\text{CO}_2$  system. After the  $\text{CO}_2$  has evaporated, it leaves the pillow plate heat exchangers and goes into the condenser where it condenses back to liquid. The condensed  $\text{CO}_2$  flows into the liquid receiver, which then goes out of the liquid receiver to the pump located one floor below the test unit. The pump pumps the cold  $\text{CO}_2$  up towards the test unit and the cycle starts again. The heat flows from the PCM into the  $\text{CO}_2$  during this mode.

During discharging mode the inlet and outlet of the pillow plate heat exchangers are switched, and the PCM is melted to extract the stored latent heat from it. This entails that the  $\text{CO}_2$  will flow inside the pillow plate exchangers as a gas and flow out as a liquid. This mode utilises the pillow plate heat exchangers as a condenser for the internal  $\text{CO}_2$  system. After the  $\text{CO}_2$  has exchanged heat with the solid PCM and has condensed, it flows out of the pillow plate heat exchangers and it goes into the liquid receiver. The  $\text{CO}_2$  flows out of the liquid receiver and goes down into the pump where it is pumped up to go inside the evaporator as a liquid. In the evaporator, the liquid  $\text{CO}_2$  exchanges heat with the glycol circuit leaving it in gas phase at approximately the same temperature as the inlet temperature. The  $\text{CO}_2$  then flows inside the pillow plate heat exchangers as a heat resource to extract the heat from the solid PCM. The cycle continues and it repeats itself again. The heat flows from the centralised  $\text{CO}_2$  into the PCM during this mode.

### 3.1 Components

The various components of the experimental setup will be further explained below:

#### 3.1.1 Pillow Plates Heat Exchangers

Pillow plates heat exchangers have a wavy fully welded structure. They provide a fully sealed construction and high structural stability which is important for the applications that require high pressure [132]. These exchangers are made by spot welding two metal sheets by laser or resistance welding, and then sealing the two metal plates at the edges by roll steam, laser, or resistance welding except for the inlet and outlet. Finally, the two sheets are inflated by hydroforming which gives the plates its wavy structure [133]. The wavy surface of the plates heat exchangers together with the welding spots lead to an improved mixing in the fluid boundary layers which lead to turbulent flow inside the pillow plates leading to good thermo-hydraulic performance [134]. The design of the plate heat exchangers is very important and is dependent on the refrigerant and type

---

of the application which they will be used for. The thermo-hydraulic performance among some other factors such as the pressure drop through the heat exchanger, and the heat transfer are very dependent on the arrangements of the welding spots between the two metal sheets [135]. There are ten pillow plates heat exchangers inside the CTES system stacked above each others with distance that can be varied. This report will discuss the results of the experiment run with a distance of 15 mm and 30 mm between the plates. These pillow plates exchangers work as an evaporators of the internal  $\text{CO}_2$  during charging mode and condensers during discharging mode. Figure 32 below shows the stack of plates above each others inside the CTES unit.

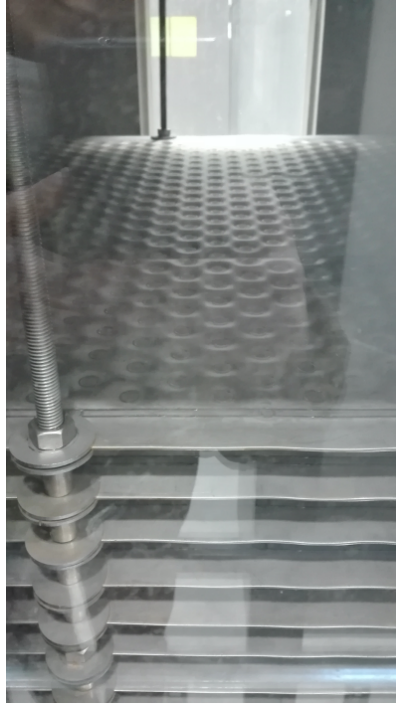


Figure 32: Stack of pillow plates

### 3.1.2 Liquid Receiver

The liquid receiver contains the  $\text{CO}_2$  that runs through the CTES system. The liquid receiver is sub-cooled by the centralized  $\text{CO}_2$  system to keep the pressure and temperature of the  $\text{CO}_2$  low all the time and especially when the experiment is not running. The liquid receiver contains  $\text{CO}_2$  in liquid and gas form in the same container. Therefore, we know that the liquid and the gas are at saturation conditions all the time. Figure 33 shows the inlet, outlet, and re-circulation connections of the CTES unit.



Figure 33: Liquid receiver

### 3.1.3 Evaporator and Condenser

The evaporator and the condenser are both brazed plate heat exchangers that are responsible on acting as the heat source and heat sink in this system. They are connected to the glycol circuit and the centralized CO<sub>2</sub> system, respectively. Figures 34 and 35 below show the condenser and the evaporator respectively.

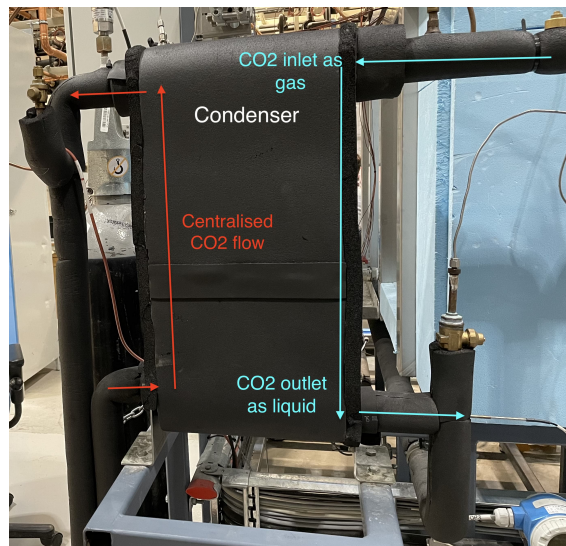


Figure 34: Condenser



Figure 35: Liquid receiver

### 3.1.4 Glycol Circuit

The glycol circuit consists of two heaters which can each provide 9 kW of heat with thermostatic control from 0 °C until 50 °C. Furthermore, the system contains a pump to maintain the flow, and an expansion vessel to keep the pressure constant when the glycol temperature increases. The glycol circuit provides heat to the system throughout the brazed plate heat exchanger which is the evaporator in the CTES system. The glycol system is controlled by setting the temperature of the CO<sub>2</sub> outlet of the evaporator. When the temperature of the CO<sub>2</sub> crosses a certain limit, there is a pulse width modulation device which controls one of the heaters by turning it on and off. If the PWM control shuts down the heater completely, and the CO<sub>2</sub> temperature is still above the required limit, the second heater is manually turned off through LabVIEW, which turns on the

---

controlled heater by the PWM again. This way the total heat input is controlled from 18 kW until 0 kW. Figure 36 below shows the glycol circuit.

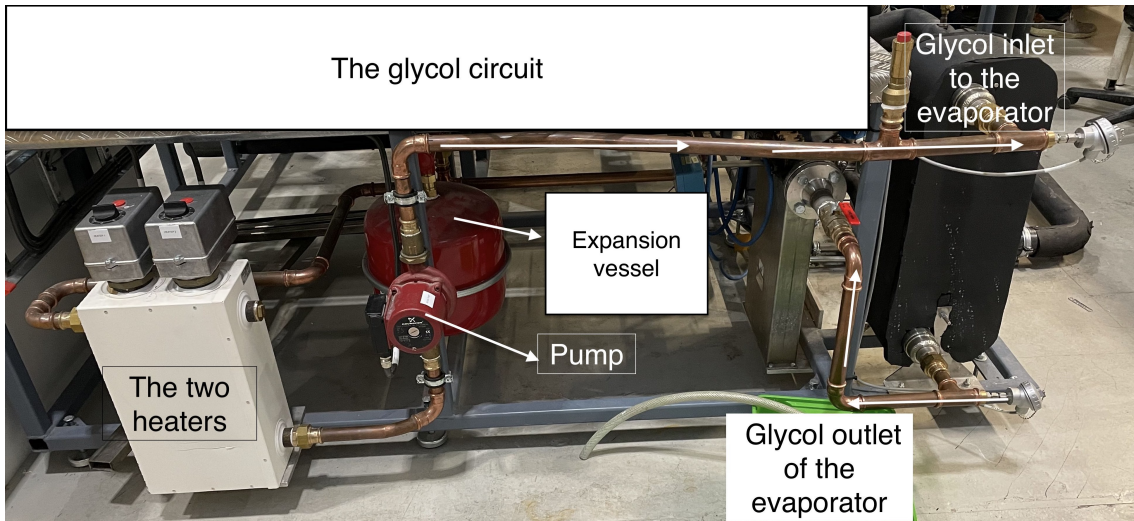


Figure 36: Glycol circuit

### 3.1.5 Centralised CO<sub>2</sub> System

The centralised CO<sub>2</sub> system provides the heat sink for The CTES system. There are three different suction lines temperatures' that can be provided by the centralised CO<sub>2</sub> system which are -10 °C, -30 °C, and -50 °C. The suction line which was first connected to the CTES system using water as PCM was the one providing CO<sub>2</sub> with a temperature of -30 °C. When the PCM was switched to RT-9HC, the system was connected to the -50 °C suction line so steady state can be achieved faster. During the charging mode, the CO<sub>2</sub> evaporates after it had exchanged heat with the PCM. The CO<sub>2</sub> flows then into the condenser and condenses to liquid again and continues its flow into the liquid receiver. The centralised CO<sub>2</sub> system provides low temperature CO<sub>2</sub> to the condenser where it evaporates and is then sucked to the centralised system which operates in a vapor compression cycle. Furthermore, the centralised CO<sub>2</sub> system is used to subcool the CO<sub>2</sub> in the liquid receiver. This is done by a pipe that goes around the liquid receiver container which lead to exchanging heat with it as shown in figure 33. The centralised CO<sub>2</sub> system is controlled during the charging mode by controlling the valve 10 shown in figure 28 which lets the centralized CO<sub>2</sub> flows back to its system. This increases the pressure upstream the valve of the centralised CO<sub>2</sub> system which increases the temperature of the CO<sub>2</sub>. This affects the driving forces in the condenser causing less cooling for the CTES CO<sub>2</sub> system.

### 3.1.6 Electrical Cabinet

The electrical cabinet collects all the data from the sensors and sends it to the computer. Furthermore, the equipment can be shut on and off from the electrical cabinet.

### 3.1.7 Sensors

The test unit is connected with different sensors in order to be able to analyze and control the system. The main measuring parameters are the temperature, the pressure, and the flow rate across the system. The data from these sensors are collected by hardware from National Instruments and logged using the software LabVIEW.

- Temperature sensors



---

There are two types of temperature sensors used in this experiment which are resistance temperature detectors (RTD) with an accuracy of 0.12 % and thermocouple sensors with an accuracy of 0.75 %. There are 27 thermocouple sensors distributed evenly on the surface of the bottom, middle, and top plates inside the CTES unit with 9 sensors on the top of each one of these plates. There are total of 7 RTD sensors distributed over the glycol circuit and the CTES system. The glycol circuit has two sensors installed in the inlet and outlet of the evaporator from the glycol circuit side. Furthermore, there are 5 sensors distributed in the CTES circuit at the condenser outlet, the evaporator inlet, liquid receiver outlet, and inlet and outlet of the CTES unit.

- Mass flow rate sensor

There are two Coriolis mass flow meters installed, namely at the glycol circuit and the inlet of the CTES unit with respect to the charging mode. The mass flow rate sensors have an accuracy of 0,2 %.

- Pressure sensors

The system is equipped with two types of pressure sensors, which are three differential pressure sensors with an accuracy of 0.05 % and one absolute pressure sensor with an accuracy of 0.075 %. The CTES system or the refrigeration cycle is installed with differential pressure sensors to measure the drop in pressure across the evaporator, the condenser, and across the CTES unit. The absolute pressure sensor is installed at the outlet of the CTES unit with respect to the charging mode.

- Vapor fraction sensor

This sensor is installed to analyse the vapor and liquid fraction of the CO<sub>2</sub> coming out of the CTES unit.

---

## 4 Methods

### 4.1 PCM Used in Experimental Facility

The experiment used two different PCMs which are water and the organic RT-9HC. First water was used, and then it was replaced with RT-9HC. Water was chosen to be the first PCM of this experiment due its characteristics and to better understand the newly built system performance using an easily accessible PCM. Water exhibits unique behaviour among other liquids which is that it decreases in density between 0 °C and 4 °C causing stratification while running charging modes which help make the heat exchange faster as the cold water will go up and the warmer water will go down closer to the heat exchangers. Furthermore, ice has good thermal conductivity which is important for the application of CTES systems. Table 9 below shows the different properties of water in both liquid and solid states.

<b>Property</b>	<b>water</b>	<b>Ice</b>
Density at 0 °C [g/cm <sup>3</sup> ]	1	0,916
Thermal conductivity [W/m.K]	0,56	2,22
specific heat [kJ/kg.K]	4.217	2,050
Specific latent heat of fusion [kJ/kg]	334	334

Table 9: Properties of water and ice  
[136]

The CTES unit is to be integrated in a secondary fluid refrigeration circuit using CO<sub>2</sub> as a refrigerant with a -5 °C temperature level. This integration is done to shift the peak load of the compressor power by utilizing the CTES to condense the CO<sub>2</sub> at -5 °C. 5 K temperature difference between the solid PCM and the refrigerant is a reasonable choice to generate enough driving forces for heat exchange to happen. Therefore, the needed phase change temperature for this application needs to be around -10 °C. Based on this, the potential PCMs for this should be paraffin or salt-hydrate/water mixture. Salt-hydrates disadvantages such as super-cooling and phase segregation was a big reason for phasing it out. Therefore, organic materials were preferred over salt-hydrates due to their properties. The organic RT line has a very interesting properties such as high thermal energy storage capacity, constant phase change temperature, no super-cooling, long life, stable performance, and the desired melting range for this application and therefore it was chosen to pick the needed PCM from [137]. RT-9HC was chosen as it approximately matches the required melting temperature of -10 °C and its the PCM with the lowest melting temperature that is available in the RT line. Table 10 below shows the properties of the organic RT-9HC.

<b>Property</b>	<b>solid</b>	<b>liquid</b>
Density at -15 °C [kg/l]	0,88	0,77
Thermal conductivity [W/m.K]	0,2	0,2
specific heat [kJ/kg.K]	2	2
Specific latent heat of fusion [kJ/kg]	208	208
phase change temperature °C	-9,7	-9,7

Table 10: Properties of RT-9HC solid and liquid phases  
[138]

### 4.2 CTES Test Rig

The CTES unit is built to be flexible and modified to experiment with the outcome of different input parameters. The distance between the plates heat exchangers, the CO<sub>2</sub> mass flow rate, and the CO<sub>2</sub> inlet temperature to the test unit were all varied throughout the experiment. These changes were done one at a time to analyse the effect of changing that particular parameter on the system. This allows the results of this experiment to map out different strategies for charging and

discharging this CTES unit. There are two main cycles in this experiment; one is charging cycle or charging mode and that is when the latent heat is stored by freezing the PCM. The other main cycle is the discharging which is when the latent heat is extracted from the PCM by melting it. The different input parameters for these two modes will be further discussed below.

### 4.3 Charging Mode

The charging mode requires both valves 4 and 6 to be closed while valves 7 and valves 5 are kept open as shown in figure 28. This allows the CO<sub>2</sub> to follow the charging cycle mentioned in the section Experimental Setup. The closing and opening of the valves is done manually each time before starting the mode. In this work, the charging mode was run with 15 mm and 30 mm distances between the plates for both PCMs. Starting with the water, there were 11 charging cycles for each geometrical configuration. Table 11 below shows the different input parameters used with the two different geometric configurations.

Charging mode ID	Inlet CO <sub>2</sub> temperature [°C]	CO <sub>2</sub> mass flow rate [kg min <sup>-1</sup> ]
C1	-2.5	4
C2	-2.5	7
C3	-2.5	10
C4	-5	4
C5	-5	7
C6	-5	10
C7	-10	4
C8	-10	7
C9	-10	10
C10	-15	4
C11	-15	7

Table 11: Charging mode running parameters with 15 mm and 30 mm distance between the plates for water

The different CO<sub>2</sub> mass flow rates were adjusted by changing the frequency of the pump from 35 Hz to 50 Hz. Lowering down the frequency to 35 Hz was not enough to get to 4 kg min<sup>-1</sup> flow rate, therefore valve 7 shown in figure 28 was partially closed to get to the desired mass flow rate of CO<sub>2</sub>. It was not possible to get to a temperature of -15 °C with a flow rate of 10 kg min<sup>-1</sup> due to operating limitation hence it was not performed. The CO<sub>2</sub> inlet temperature was controlled by controlling the valve upstream the centralised CO<sub>2</sub> system after it flows out of the condenser. This would increase the evaporation pressure of the CO<sub>2</sub> from the centralized CO<sub>2</sub> system. Consequently, the temperature increases which leads to less heat exchange in the condenser due to less driving forces between the centralized and the internal CO<sub>2</sub> systems.

The charging mode is started using LabVIEW by turning on the CO<sub>2</sub> pump and the magnetic valve of the centralised CO<sub>2</sub> system so it can start flowing inside the condenser. After the system is turned on, the liquid CO<sub>2</sub> goes inside the pillow plate heat exchangers through the manifold connecting all 10 pillow plates heat exchangers. The CO<sub>2</sub> completely evaporates when leaving the pillow plate heat exchangers and is collected again through the manifold connecting the 10 pillow plates heat exchangers outlet. The evaporation happens due to exchanging heat with the PCM which is PCM in this case. The outlet temperature of the CO<sub>2</sub> is approximately the same as its inlet temperature as only latent heat of evaporation is used to cool down the PCM. At the start of the charging, if the PCM was at room temperature, the CO<sub>2</sub> outlet can be superheated inside the pillow plate heat exchangers leaving it at a higher temperature than its inlet temperature. The gaseous CO<sub>2</sub> continues the cycle into the condenser where it is liquefied again. The condensation happens because it exchanges heat with the centralised CO<sub>2</sub> system inside the condenser. The pressure of the CO<sub>2</sub> is constant throughout the condenser. However, the CO<sub>2</sub> can be subcooled due to the low temperature of the suction line of the centralised CO<sub>2</sub> reaching -30 °C especially

when running low flow rates such as  $4 \text{ kg min}^{-1}$ .

The condensed  $\text{CO}_2$  continues the cycle towards the liquid receiver where it is collected and kept under saturation conditions. The liquid  $\text{CO}_2$  flows out of the liquid receiver into the pump installed a floor below the CTES unit and is pumped up again to go into the pillow plate heat exchangers with a part of the flow going into the liquid receiver for re-circulation purposes. Solid PCM starts forming on both surfaces of the pillow plate and keeps growing until it meets the solid PCM growing on the surfaces of the upper or below next pillow plate. That is when the charging is considered to be completed. Therefore, all the charging cycles for the same configuration and PCM are assumed to have the same amount of latent heat capacity.

The RT-9HC has a melting temperature of  $-9,7 \text{ }^\circ\text{C}$ , therefore the charging cycles were planned differently than the water charging cycles. The  $\text{CO}_2$  suction line which the experiment was connected to was changed to the one providing  $\text{CO}_2$  at  $-50 \text{ }^\circ\text{C}$  in order to reach the desired low temperature faster. Starting with the 15 mm distance between the plates, the tests were run using a fixed inlet  $\text{CO}_2$  temperature of  $-16 \text{ }^\circ\text{C}$ , while the mass flow rate was varied between  $4 \text{ kg min}^{-1}$  and  $10 \text{ kg min}^{-1}$ . Based on the results, the experiment was further run with a fixed mass flow rate of  $8 \text{ kg min}^{-1}$ , while varying the inlet  $\text{CO}_2$  temperature between  $-12 \text{ }^\circ\text{C}$  and  $-26 \text{ }^\circ\text{C}$ . Table 12 and 13 show the charging cycles which were performed for the 15 mm distance between the plates.

Charging mode ID	Inlet $\text{CO}_2$ temperature [ $^\circ\text{C}$ ]	$\text{CO}_2$ mass flow rate [ $\text{kg min}^{-1}$ ]
C-MF1	-16	4
C-MF2	-16	5
C-MF3	-16	6
C-MF4	-16	7
C-MF5	-16	8
C-MF6	-16	9
C-MF7	-16	10

Table 12: 15 mm configuration first set of experiment with RT-9HC

Charging mode ID	Inlet $\text{CO}_2$ temperature [ $^\circ\text{C}$ ]	$\text{CO}_2$ mass flow rate [ $\text{kg min}^{-1}$ ]
C1	-12	8
C1.5	-13	8
C2	-14	8
C2.5	-15	8
C3	-16	8
C4	-18	8
C5	-20	8
C6	-22	8
C7	-24	8
C8	-26	8

Table 13: Set of charging cycles with fixed inlet  $\text{CO}_2$  temperature while varying the mass flow rate for the 15mm distance with RT-9HC

A similar approach was followed when the distance between the plates changed to 30 mm. The inlet  $\text{CO}_2$  temperature was fixed to  $-18 \text{ }^\circ\text{C}$ , while the mass flow rate was varied between  $7 \text{ kg min}^{-1}$  and  $10 \text{ kg min}^{-1}$ . Based on the results, the experiment was further run with a fixed mass flow rate of  $8 \text{ kg min}^{-1}$  and varied inlet  $\text{CO}_2$  temperature between  $-13 \text{ }^\circ\text{C}$  and  $-24 \text{ }^\circ\text{C}$ . Table 14 and 15 show the charging cycles which were performed for the 30 mm distance between the plates.

---

Charging mode ID	Inlet CO <sub>2</sub> temperature [°C]	CO <sub>2</sub> mass flow rate [kg min <sup>-1</sup> ]
C-MF4	-18	7
C-MF5	-18	8
C-MF6	-18	9
C-MF7	-18	10

Table 14: 30 mm configuration first set of experiment with RT-9HC

Charging mode ID	Inlet CO <sub>2</sub> temperature [°C]	CO <sub>2</sub> mass flow rate [kg min <sup>-1</sup> ]
C2	-13	8
C3	-14	8
C3.5	-15	8
C4	-16	8
C4.5	-17	8
C5	-18	8
C5.5	-19	8
C6	-20	8
C7	-22	8
C8	-24	8

Table 15: Set of charging cycles with fixed inlet CO<sub>2</sub> temperature while varying the mass flow rate for 30 mm configuration with RT-9HC

The latent heat stored in both of these configurations was theoretically calculated for both PCMs. This is done by calculating the latent heat stored in the theoretical amount of solid PCM that is supposed to be formed after every charging cycle for these two different configurations. The theoretical amount of solid PCM was found by calculating the volume between two pillow plates and consequently multiplying it by 10 considering that the test unit has 10 equivalent volumes. The following two equations were used to calculate this:

$$Q = ML \quad (8)$$

$M$ = Mass of ice which will be formed [kg]

$L$ = Specific latent heat of fusion of ice 344 [kJ/kg]

$Q$ = Latent heat stored in the ice [kJ]

$$M = V\rho \quad (9)$$

$V$ = Volume of ice [m<sup>3</sup>]

$\rho$ =Density of ice 917 [kg/m<sup>3</sup>]

Table 16 and 17 below show the total heat stored after a full charging cycle for water and RT-9HC and both configurations.

Configuration	Total volume $m^3$	Heat of fusion J/g	Total heat stored kJ	Total heat stored kW
15 mm	0,143	334	43783,59	12,16
30 mm	0,286	334	87567,18	24,32

Table 16: Latent heat stored in ice for the two different configurations

---

Configuration	Total volume $m^3$	Heat of fusion J/g	Total heat stored kJ	Total heat stored kW
15 mm	0,143	208	26166,25	7,27
30 mm	0,286	208	52332,51	14,54

Table 17: Latent heat stored in the solid RT-9HC for both configurations

#### 4.4 Discharging Mode

The discharging mode requires each of valves 4 and 6 to be open while valves 7 and 5 are closed so the CO<sub>2</sub> can follow the discharging cycle mentioned in the section experimental setup and shown in figure 28. This is done manually before starting the discharging cycle. The discharging cycles are run after the charging cycles as the solid PCM is fully formed. In this work, the discharging mode was run with 15 mm and 30 mm distances between the plates. Starting with the water, there were 9 discharging cycles done for the 15 mm distance and the 30 mm distance which makes a total of 18 discharging cycles. Table 18 below shows the different input parameters used with the two different geometric configurations.

Discharging mode ID	inlet CO <sub>2</sub> [°C]	CO <sub>2</sub> mass
		flow rate [kg min <sup>-1</sup> ]
D4	5	4
D5	5	7
D6	5	10
D7	7.5	4
D8	7.5	7
D9	7.5	10
D10	10	4
D11	10	7
D12	10	10

Table 18: Discharging mode running parameters with 15 mm and 30 mm distances between the plates for the water

The different CO<sub>2</sub> mass flow rates were achieved by the same procedure as in the charging mode, tho for the 4 kg min<sup>-1</sup> flow rate, valve 4 shown in figure 28 was partially closed to get to the required mass flow rate. The temperature of the evaporator outlet can be controlled from LabVIEW which in turn controls the heating capacity of the glycol circuit using the PWM. The discharging mode is started using LabVIEW by turning both of the glycol heaters on, the glycol pump on, and the CO<sub>2</sub> pump on.

The discharging cycle always starts with a full block of solid PCM surrounding the pillow plate heat exchangers. The gaseous CO<sub>2</sub> goes inside the CTES unit through the manifold connecting all the plates and gets distributed over the 10 plates. The gaseous CO<sub>2</sub> condenses and leaves the plates in liquid state at approximately equal temperature of the inlet CO<sub>2</sub> to the test unit and is collected again in the manifold leaving the CTES unit. The liquid CO<sub>2</sub> flows into the liquid receiver and then continues to flow towards the CO<sub>2</sub> pump and is then pumped up to go into the evaporator. The liquid CO<sub>2</sub> goes into the evaporator as liquid and leaves as gas at approximately the same temperature as only latent heat is gained. However, with low flow rates the gas can be superheated as it can gain some sensible heat besides the latent heat. The solid PCM starts to melt and the heater capacity is constantly reduced to keep the CO<sub>2</sub> inlet temperature constant. When the heater controlled by the PWM reaches 0% the other heater is turned off so the PWM controlled heater can go back to 100% and is then reduced gradually again with further melting of the solid PCM. The discharging mode is considered to be finished when all the solid PCM has melted or when no more heat can be rejected to the PCM from the refrigerant without increasing the refrigerant pressure resulting in 0% output for both of the heaters of the glycol circuit.

The RT-9HC discharging cycles were also planned differently. The experiment was run with a

fixed inlet CO<sub>2</sub> temperature of 0 °C and varying CO<sub>2</sub> mass flow rate between 4 kg min<sup>-1</sup> and 10 kg min<sup>-1</sup> as shown in Table 19 below. Based on the results, the experiment was further run with a fixed mass flow rate of 5 kg min<sup>-1</sup> and varying inlet CO<sub>2</sub> temperatures between -6 °C and 6 °C as shown in table 20.

Discharging mode ID	inlet CO <sub>2</sub> [°C]	CO <sub>2</sub> mass flow rate [kg min <sup>-1</sup> ]
D-MF1	0	4
D-MF2	0	5
D-MF3	0	6
D-MF4	0	7
D-MF5	0	8
D-MF6	0	9
D-MF7	0	10

Table 19: 15 mm configuration first set of discharging tests with the RT-9HC

Discharging mode ID	inlet CO <sub>2</sub> [°C]	CO <sub>2</sub> mass flow rate [kg min <sup>-1</sup> ]
D1	-6	5
D2	-4	5
D3	-2	5
D4	0	5
D5	2	5
D6	4	5
D7	6	5

Table 20: Set of discharging cycles with fixed inlet CO<sub>2</sub> temperature while varying the mass flow rate for the 15mm distance with the RT-9HC

The configuration was changed to 30 mm distance between the plates, and the same set of experiments shown in table 19 were repeated. Based on the results, the experiment was further run with a fixed CO<sub>2</sub> mass flow rate of 7 kg min<sup>-1</sup> and varying inlet CO<sub>2</sub> temperature range between -6 °C and 6 °C as shown in Table 21 below.

Discharging mode ID	inlet CO <sub>2</sub> [°C]	CO <sub>2</sub> mass flow rate [kg min <sup>-1</sup> ]
D1	-6	7
D2	-4	7
D3	-2	7
D4	0	7
D5	2	7
D6	4	7
D7	6	7

Table 21: Set of discharging cycles with fixed inlet CO<sub>2</sub> temperature while varying the mass flow rate for the 30mm distance with the RT-9HC

The heat input from the CO<sub>2</sub> into the PCM was calculated throughout calculating the heat input from the glycol circuit using Equation 2 since the two equal each others. This is because the heat is first transferred from the glycol circuit to the CO<sub>2</sub> in the evaporator, and afterwards, the heat is transferred from the CO<sub>2</sub> into the PCM in the pillow plate heat exchangers.

$$Q_{Glycol}(t) = mC_{p, glycol}(T_f - T_i)_{glycol} = Q_{CO_2}(t) \quad (10)$$

Q= Heat input [kW]

---

$m$ = Mass flow rate kg/s

$C_p$ = Specific heat capacity [J/kg.K]

$T_i$ = Inlet temperature to the evaporator [K]

$T_f$ = Outlet temperature of the evaporator [K]

The mass flow rate of the glycol among the inlet and outlet temperatures of the glycol in the evaporator were measured using the sensors installed in the system.



---

## 5 Results

Starting with the water results the experiment was performed with the different parameters mentioned in Tables 11 and 18. As for RT-9HC the experiment was run with different parameters shown in Tables 12-15 for the charging mode, and Tables 19-21 for the discharging mode. The following sections will show the performance of the system and the outcome of these experiments:

### 5.1 Charging Mode

#### 5.1.1 Water as PCM

The charging mode was run according to the different parameters shown in table 11. The actual parameters which were achieved by the experiment are shown in tables 22 and 23 below which show the results for the 15 mm configuration and 30 mm configuration respectively. All the results in the charging mode are plotted and measured as soon as the average PCM temperature equals 0,1 °C. This was done so all cycles can be compared to each other, having the same starting conditions.

	Time to freeze [min]	Average inlet CO <sub>2</sub> temperature [°C]	Flow rate [kg min <sup>-1</sup> ]
C1	68,3	-2,85	4,18
C2	71,0	-2,68	7,29
C3	70,0	-2,60	10,03
C4	57,7	-5,20	4,08
C5	40,0	-5,15	7,15
C6	41,7	-4,69	10,05
C7	53,2	-9,59	4,14
C8	35,3	-9,67	7,14
C9	32,0	-6,13	9,65
C10	35,5	-13,80	4,18
C11	27,6	-11,38	6,78

Table 22: Charging test results for the 15 mm configuration for water

	Time to freeze [min]	Average inlet CO <sub>2</sub> temperature [°C]	Flow rate [kg min <sup>-1</sup> ]
C1	112,50	-2,64	4,07
C2	89,12	-2,65	7,07
C3	87,83	-2,60	10,05
C4	58,83	-4,72	4,21
C5	68,00	-4,96	6,82
C6	52,50	-4,38	9,32
C7	40,17	-9,93	4,24
C8	28,50	-8,71	6,11
C9	30,50	-7,70	7,87
C10	36,83	-10,85	4,19
C11	33,43	-8,78	5,55

Table 23: Charging test results for the 30 mm configuration for water

Figures 37 and 38 show the time to finish the charging cycles for the 15 mm configuration and the 30 mm configuration, respectively. The time to freeze is shown from the moment the average PCM temperature in the CTES unit equals 0,1 °C. Both figures show the same trend which is shorter charging times with lower inlet CO<sub>2</sub> temperatures. Furthermore, both figures are showing that mass flow rate has less effect on charging time, and it is the inlet CO<sub>2</sub> temperature that influences the charging time the most. Figure 37 shows that the fastest charging cycle being 27,6 minutes was recorded for C11 with an average inlet CO<sub>2</sub> temperature of -11,38 °C.

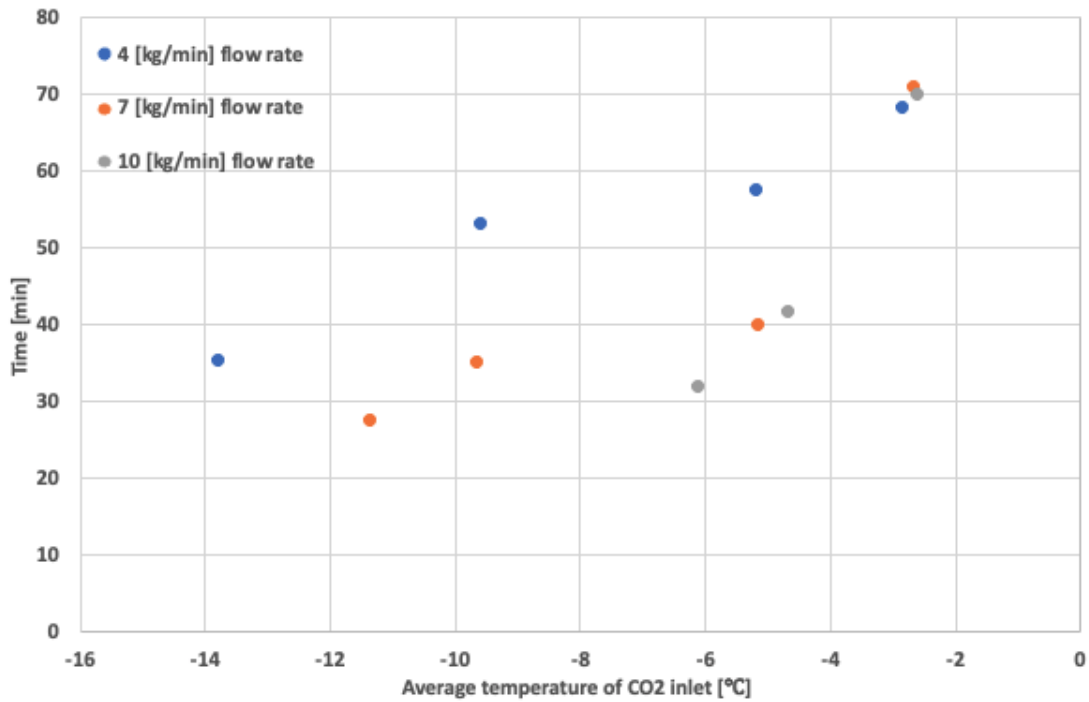


Figure 37: Time to complete the charging process for different average inlet CO<sub>2</sub> temperatures with respect to their flow rate for the 15 mm configuration for water

Figure 38 below shows that the fastest charging cycle being 28,5 minutes was recorded for C8 with an average inlet temperature of -8,71 °C.

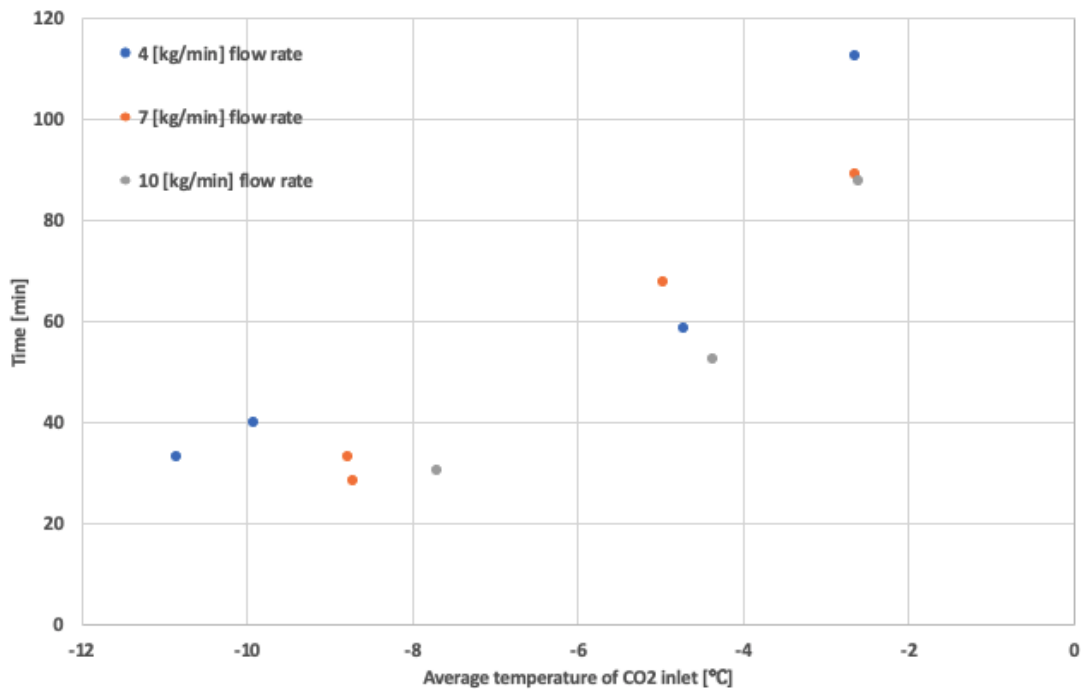


Figure 38: Time to complete the charging process for different average inlet CO<sub>2</sub> temperatures with respect to their flow rate for the 30 mm configuration for water

Figures 39 and 40 show the pressure drop across the CTES unit vs the inlet temperatures of the CO<sub>2</sub> grouped according to their respective mass flow rates. Both figures show similar trends which

is a higher pressure drop with increasing mass flow rate and lower inlet CO<sub>2</sub> temperature.

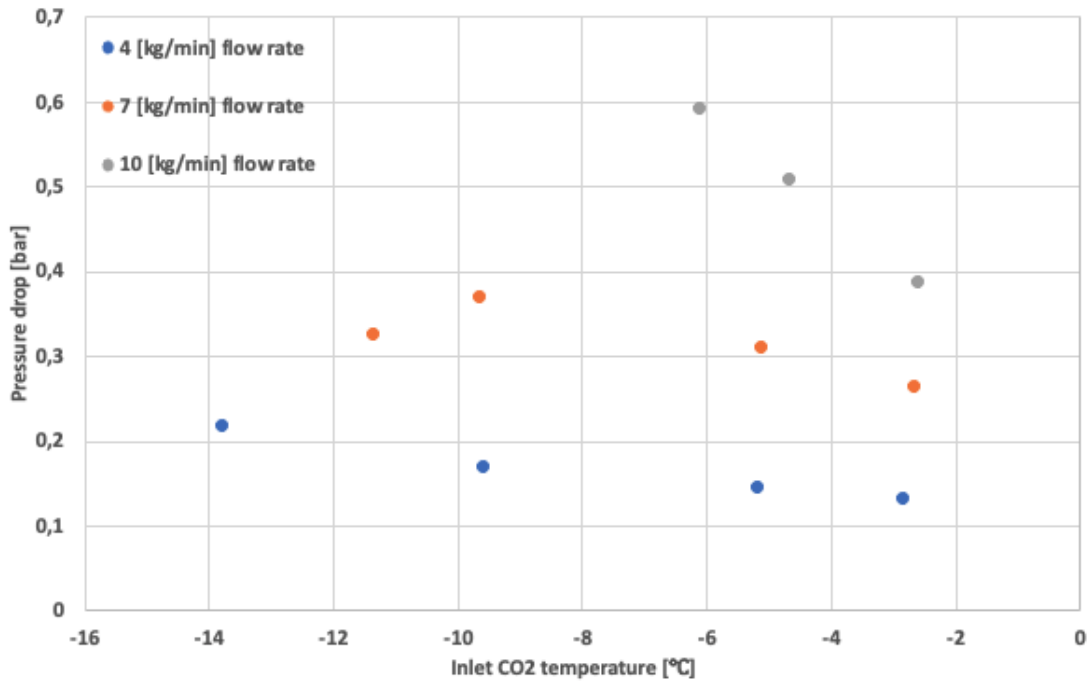


Figure 39: Pressure drop for different CO<sub>2</sub> inlet temperatures grouped in their respective flow rates for the 15 mm configuration for water

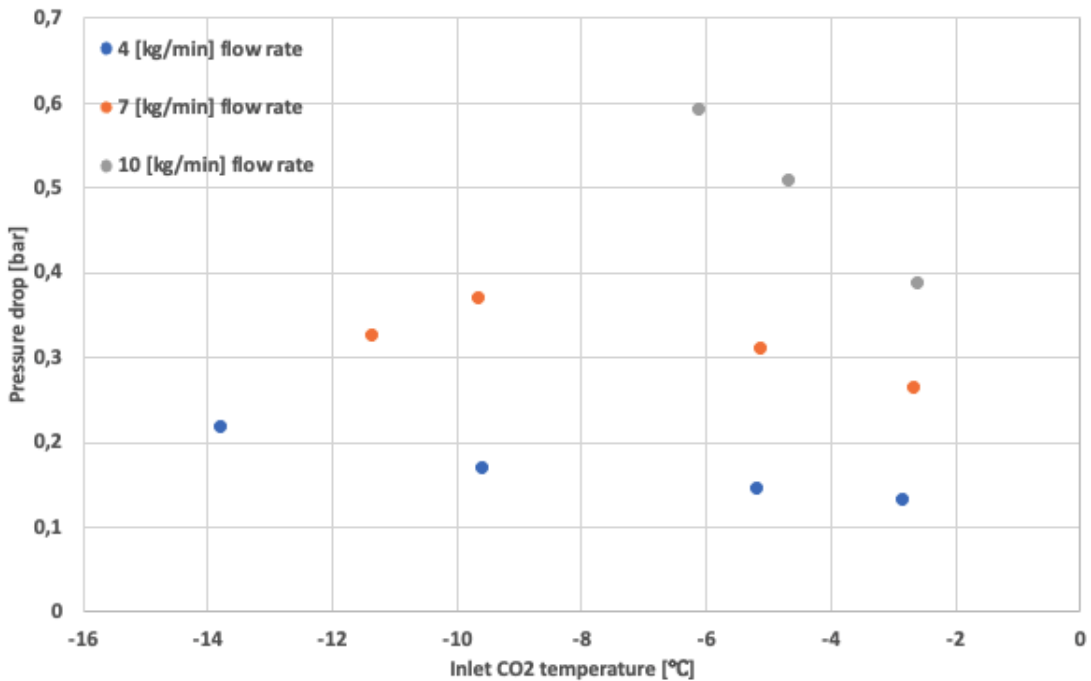


Figure 40: Pressure drop for different CO<sub>2</sub> inlet temperatures grouped in their respective flow rates for the 30 mm configuration for water

Figures 41 and 42 below show the temperature difference between the inlet CO<sub>2</sub> temperature and the average PCM temperature plotted as a function of time for the 15 mm configuration and 30 mm configuration. Figure 41 below showing C10 in maroon, C7 in dark blue, and C8 in light

brown having the highest, second highest, and third highest temperature difference between the inlet CO<sub>2</sub> and average PCM temperature, respectively. The difference in temperature between the inlet CO<sub>2</sub> and the average PCM temperature for C10 starts with 8,4 °C. This is followed by an increase in the temperature difference up until 10,1 °C over 6 minutes, and consequently followed by a drop in temperature difference up until it approximately reaches 1,1 °C temperature difference over 30 minutes. C1 on the other hand starts with the lowest temperature difference of 2,5 °C which is close to the inlet CO<sub>2</sub> temperature, and approaches zero over 65 minutes. The difference in temperature for other cycles starts with values between 8,4 and 2,5 °C and gradually drops to approximately 0 °C over the experiment time. This means that the average PCM temperature approaches the inlet CO<sub>2</sub> temperature over the experiment time.

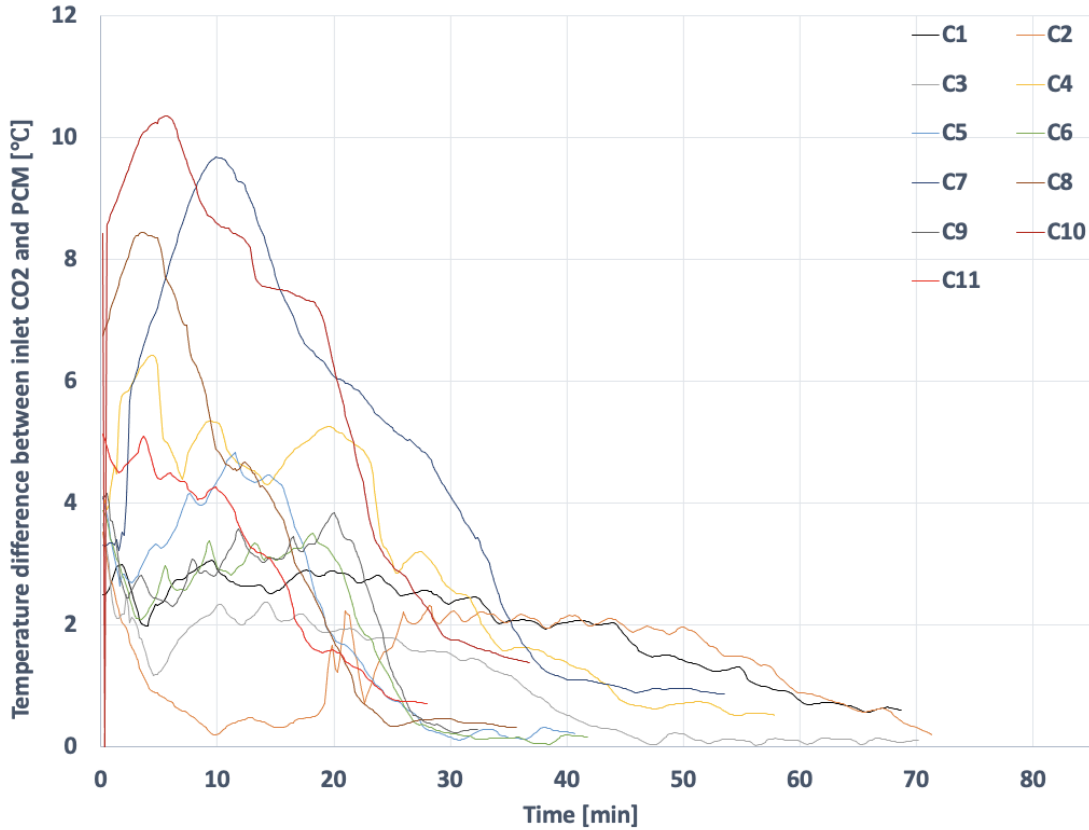


Figure 41: Temperature difference between the inlet CO<sub>2</sub> temperature and the average PCM temperature for the 15 mm configuration for water

Figure 42 below shows a trend with dropping difference in temperature between the inlet CO<sub>2</sub> and the mean temperature of the PCM. The highest difference starts at 12,1 °C for C11 and drops gradually to 2 °C over 34 minutes. The lowest temperature difference starts at 2,9 °C and drops gradually to 0,8 °C over 79 minutes. The rest of the cycles start with a temperature difference between 12,1 °C and 2,9 °C and drop gradually to below 1 °C over the experiment time. This means that the PCM approaches the inlet CO<sub>2</sub> temperature over the experiment time for all cycles.

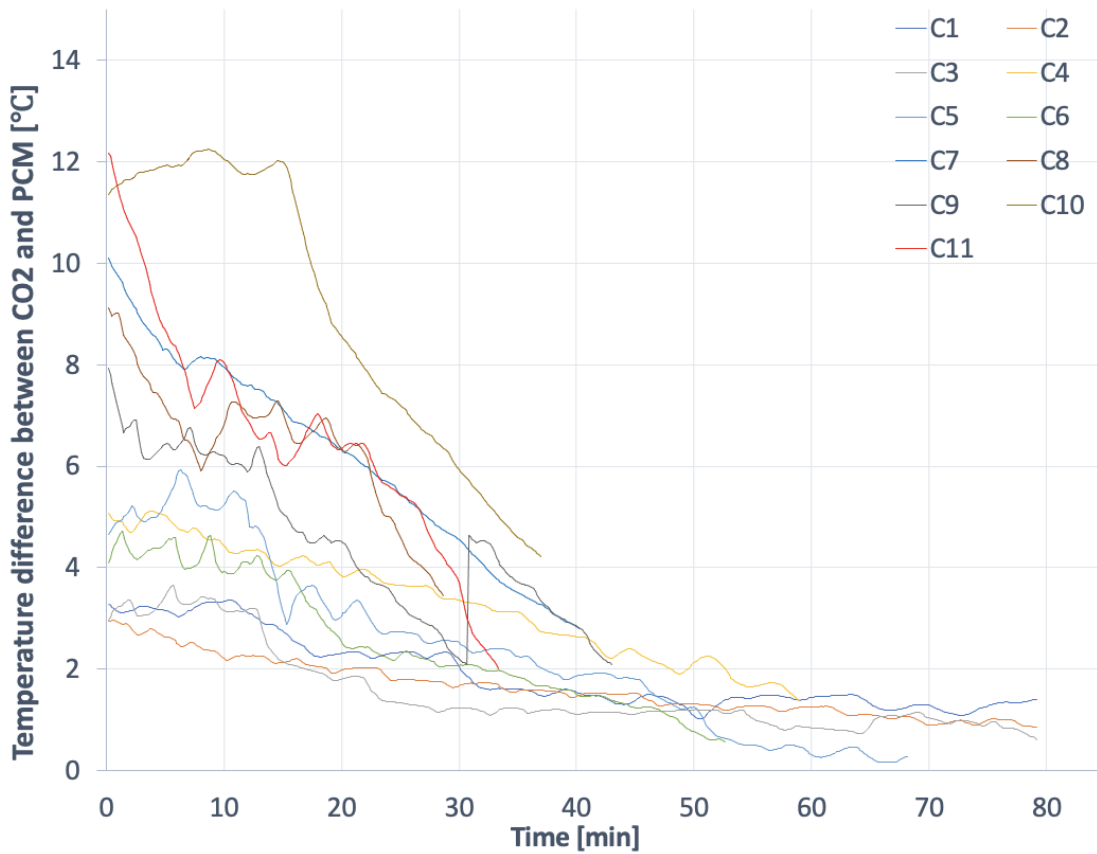


Figure 42: Temperature difference between the inlet CO<sub>2</sub> temperature and the average PCM temperature for the 30 mm configuration for water

The experiment is designed so the CO<sub>2</sub> stays in saturated conditions the entire cycle. Hence, the goal is that the CO<sub>2</sub> exits the CTES unit as a mixture of vapour/liquid within the two-phase region. However, when the experiment was performed, it was noticed that during the start of the experiment the CO<sub>2</sub> leaves the CTES unit super heated as it absorbs more heat from the PCM causing a temperature difference between the inlet CO<sub>2</sub> and outlet CO<sub>2</sub>. Figures 43 and 45 below are showing the difference between the inlet and outlet CO<sub>2</sub> temperatures with respect to time for the 15 mm configuration and 30 mm configuration. Towards the end of the experiment this temperature difference tends to be 0 °C, which means that the CO<sub>2</sub> is operating in saturated conditions. This means that the CO<sub>2</sub> leaves the CTES unit in a mixture of gas and liquid phase. Figure 43 below shows that the highest differences between the inlet CO<sub>2</sub> temperature and its outlet were recorded for C10, C7, and C8 in that order. The increase in temperature difference followed by a decrease is caused by a dropping inlet CO<sub>2</sub> temperature as it takes time to reach the steady state conditions while simultaneously the outlet CO<sub>2</sub> temperature is super heated causing this increase in temperature difference.

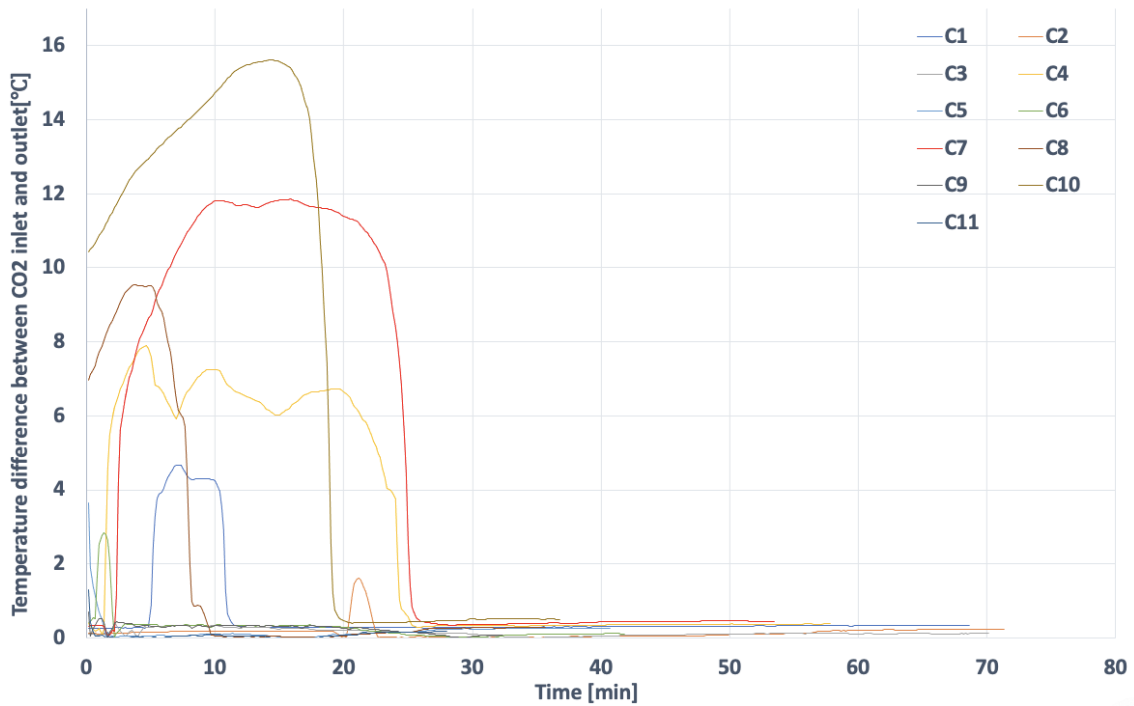


Figure 43: Temperature difference between the inlet CO<sub>2</sub> temperature and outlet CO<sub>2</sub> temperature for the 15 mm configuration for water

Figure 44 below shows how the inlet CO<sub>2</sub> temperature drops with time for C10, C7, and C8. C10 has the lowest inlet CO<sub>2</sub> temperature and the lowest flow rate in this set of experiment followed by C8 and C7 with approximately equal inlet CO<sub>2</sub> temperatures and flow rates of 7,14 and 4,14 kg min<sup>-1</sup>, respectively. The lower mass flow rate leads to early evaporation of the CO<sub>2</sub> and consequently superheating it. This leads to a higher difference in temperature between the inlet CO<sub>2</sub> and outlet CO<sub>2</sub> temperature.

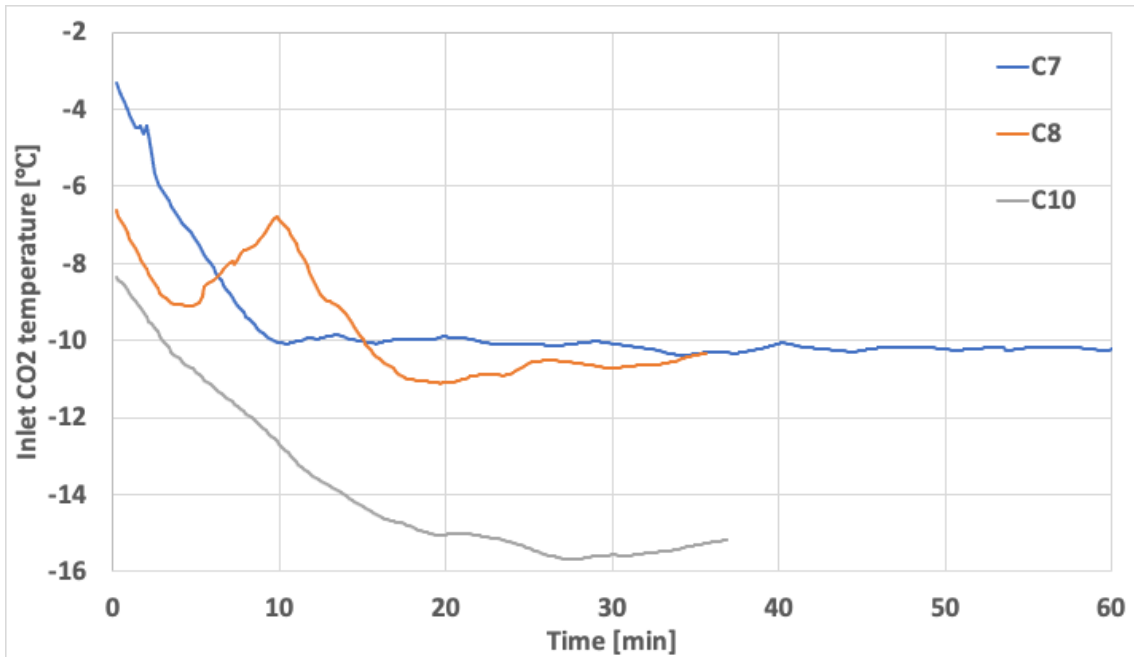


Figure 44: Inlet CO<sub>2</sub> temperature during the charging cycle for the 15 mm configuration for water

Figure 45 below shows a dropping trend in temperature difference between the inlet and outlet CO<sub>2</sub> temperatures. The increasing trend showing in figure 43 is not showing here because the results were recorded when the average PCM temperature equals 0,1 °C which took longer time during the experiments run with the 30 mm configuration giving the inlet CO<sub>2</sub> temperature enough time to reach its chosen value before the PCM average temperature reaches 0,1 °C. C10, C7, C8, and C11 recorded the highest temperature differences respectively. C10 had the lowest average inlet CO<sub>2</sub> temperature combined with the lowest flow rate, hence it had the highest temperature difference between inlet and outlet CO<sub>2</sub> temperatures.

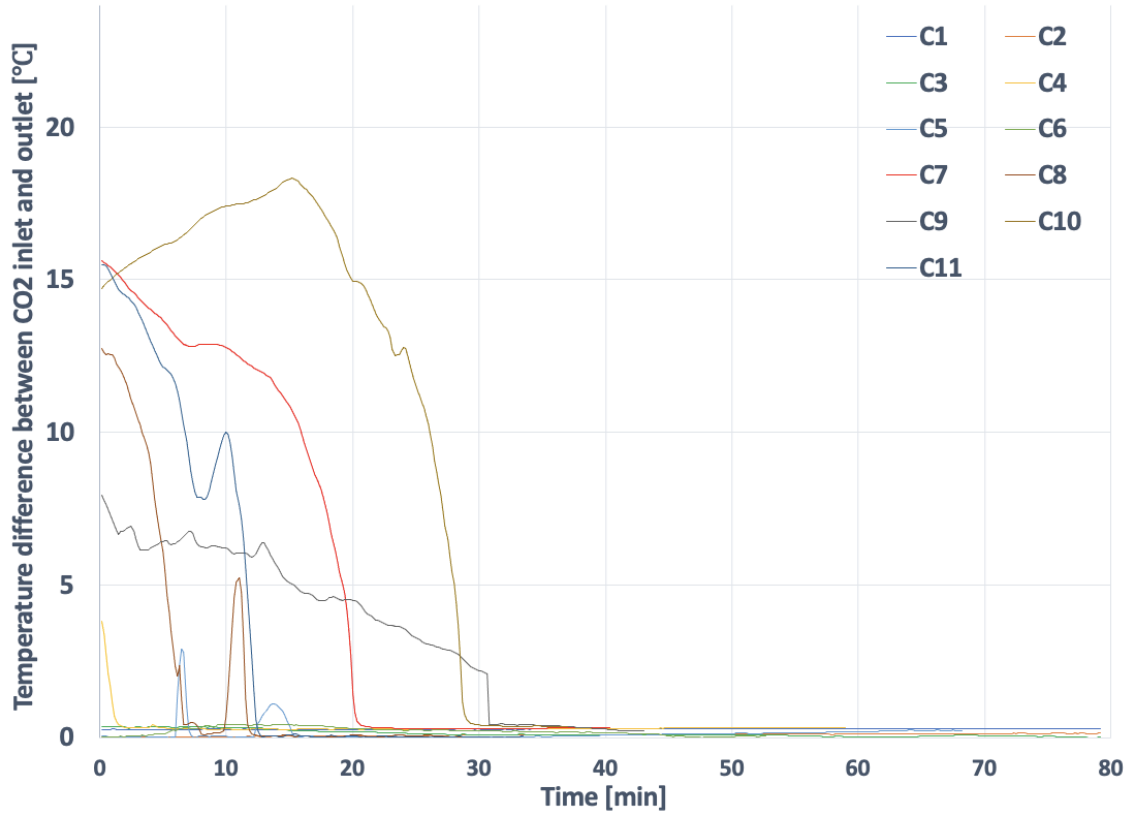


Figure 45: Temperature difference between the inlet CO<sub>2</sub> temperature and outlet CO<sub>2</sub> temperature for the 30 mm configuration for water

### 5.1.2 RT-9HC as PCM

The charging mode was started for both configurations by running the experiment with a fixed inlet CO<sub>2</sub> temperature while varying the mass flow rate as shown in tables 19 and 21 to determine the optimum mass flow rate based on the charging time and pressure drop across the system. Figures 46 and 47 below show the results for the 15 mm and 30 mm configurations

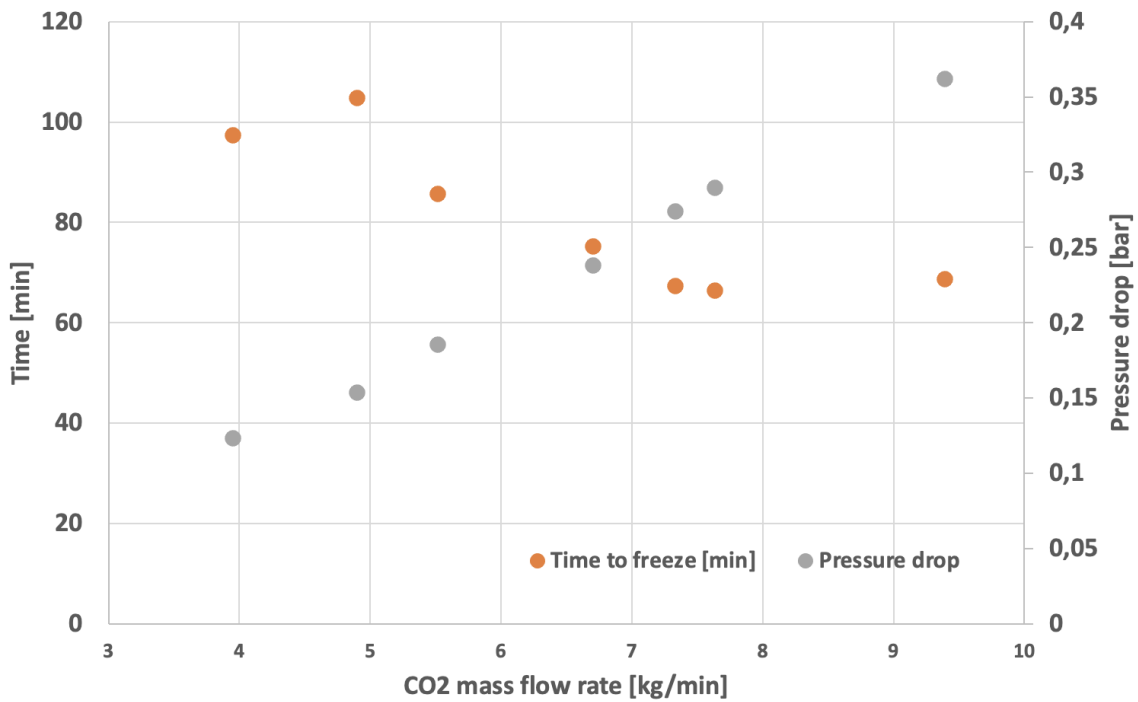


Figure 46: Charging time and pressure drop across the CTES for the different mass flow rates with a fixed inlet CO<sub>2</sub> temperature for the 15 mm configuration for RT-9HC

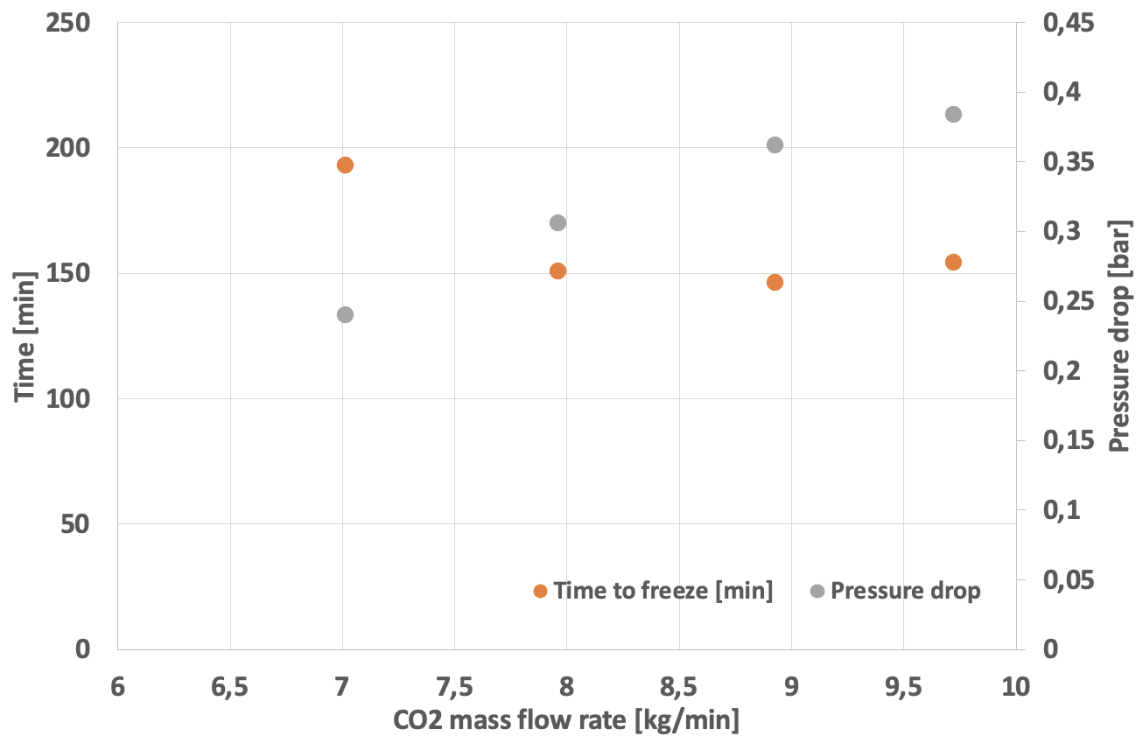


Figure 47: Charging time and pressure drop across the CTES for the different mass flow rates with a fixed inlet CO<sub>2</sub> temperature for the 30 mm configuration for RT-9HC

Figure 46 shows the lowest pressure drop and the longest time to charge at 4 kg min<sup>-1</sup> CO<sub>2</sub> mass flow rate with values of 0,12 bar and 97,33 minutes. The shortest time to charge was recorded to be 66,33 minutes for the 7,6 kg min<sup>-1</sup> CO<sub>2</sub> mass flow rate with 0,29 bar pressure drop. Figure



---

47 shows that at  $8 \text{ kg min}^{-1}$   $\text{CO}_2$  inlet mass flow rate, the charging time was 151 minutes, and the recorded pressure drop was 0,31 bar. The pressure drop in both figures 46 and 47 shows a linear relation with the mass flow rate, which means that the higher the  $\text{CO}_2$  mass flow rate, the higher the pressure drop across the CTES system. As for the charging time, it shows a dropping trend with higher mass flow rate up until  $7,6 \text{ kg min}^{-1}$ , and then it starts to be approximately constant at higher mass flow rates. Therefore an  $8 \text{ kg min}^{-1}$  mass flow rate was chosen to continue the experiment with as it approximately has the shortest charging time combined with the lowest pressure drop compared with the experiments that have approximately the same charging time.

The experiments were run following the parameters shown in tables 13 and 15. Figures 48 and 49 below show the charging time for the different average inlet  $\text{CO}_2$  temperature for the 15 mm and 30 mm configurations, respectively. Both figures show an exponential decrease of the charging time with a dropping inlet  $\text{CO}_2$  temperature. Figure 48 shows the shortest charging time to be 35,8 min with an average inlet  $\text{CO}_2$  temperature of  $-21,76 \text{ }^\circ\text{C}$ . Figure 49 shows the shortest charging time to be 97,2 min with an average inlet  $\text{CO}_2$  temperature of  $-22,76 \text{ }^\circ\text{C}$ .

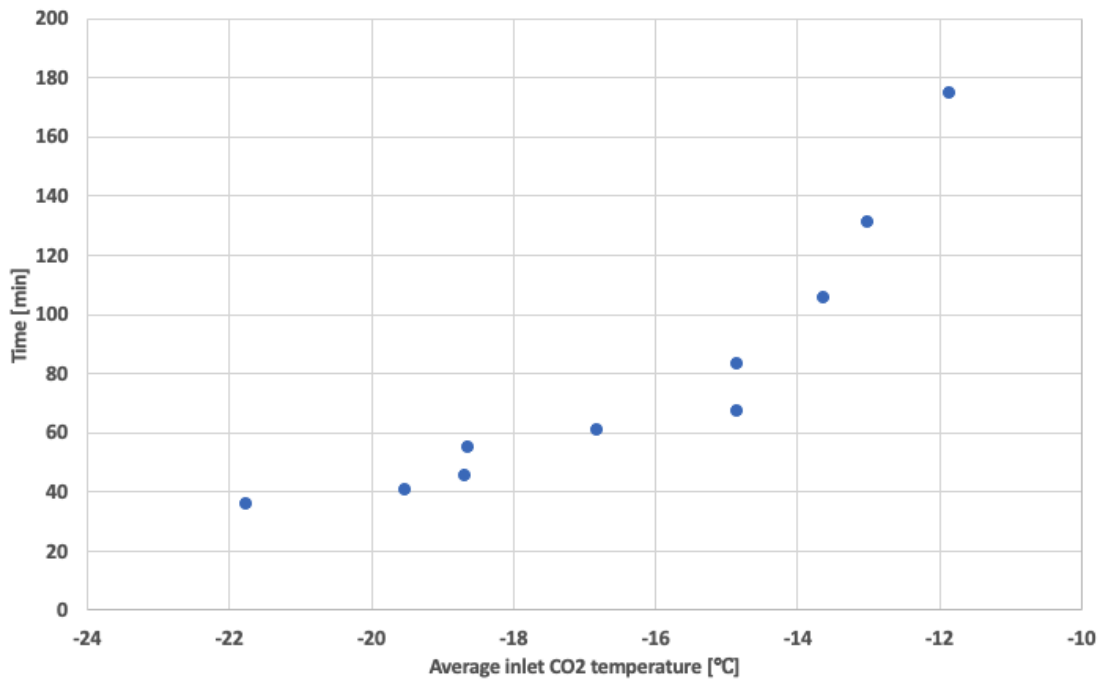


Figure 48: Charging time vs average inlet  $\text{CO}_2$  temperature for the 15 mm configuration for RT-9HC

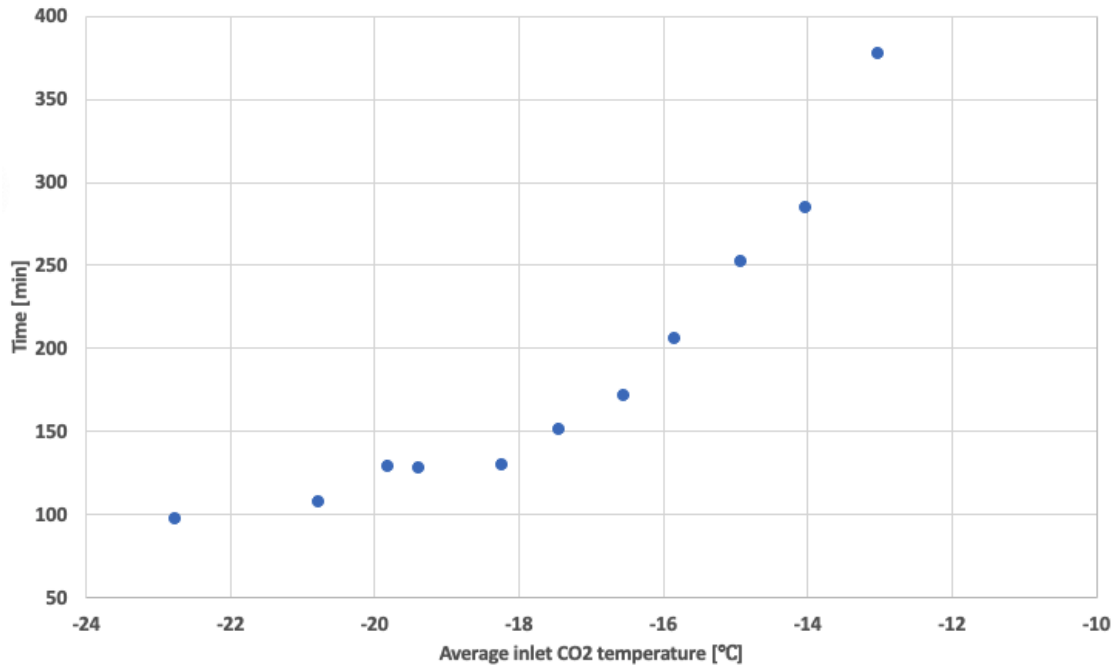


Figure 49: Charging time vs average inlet CO<sub>2</sub> temperature for the 30 mm configuration for RT-9HC

The pressure drop across the CTES was recorded for the different charging runs. Figures 50 and 51 show pressure drop across the CTES for the different average inlet CO<sub>2</sub> temperatures. Both figures 50 and 51 show higher pressure drop with a dropping inlet CO<sub>2</sub> temperature with an approximate linear trend. The pressure drop values vary between 0,21 bar and 0,54 bar. The lowest pressure drop value was 0,21 bar which was recorded for for the -12 °C charging test in the 15 mm configuration and -13 °C charging test in the 30 mm configuration. The highest pressure drop value of 0,54 bar was recorded for the inlet CO<sub>2</sub> temperature of -22 °C for the 15 mm configuration.

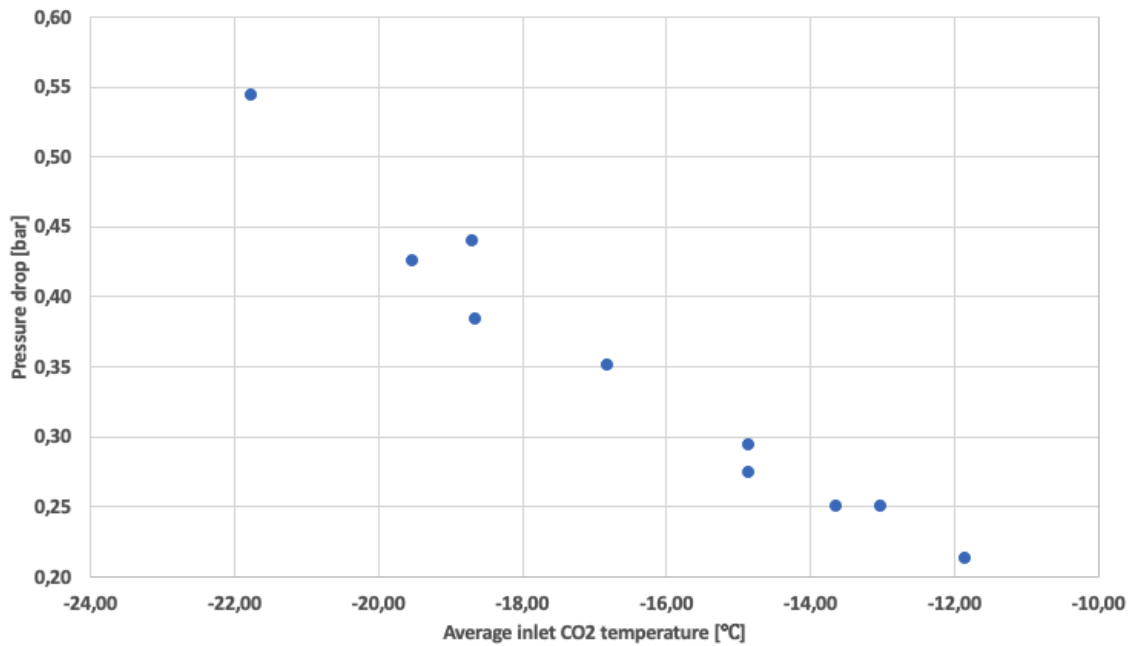


Figure 50: Pressure drop vs average inlet CO<sub>2</sub> temperature for the 15 mm configurations for RT-9HC

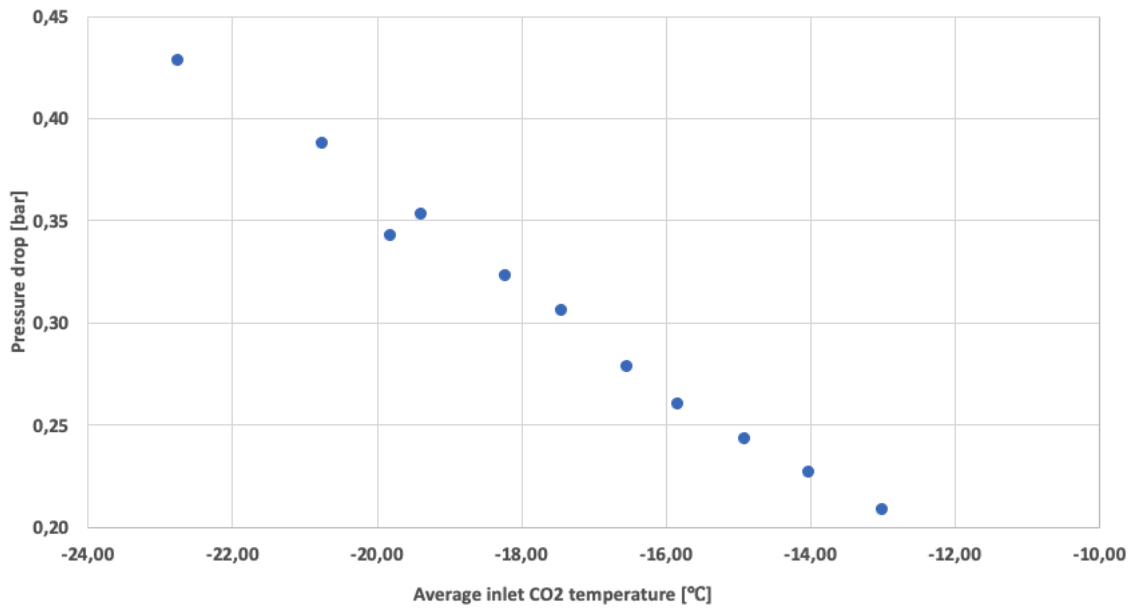


Figure 51: Pressure drop vs average inlet CO<sub>2</sub> temperature for the 15 mm configuration for RT-9HC

The temperature difference between the inlet CO<sub>2</sub> temperature and the average PCM temperature was studied throughout the experiment. However, the inlet CO<sub>2</sub> temperature used was calculated using the absolute pressure value of the inlet CO<sub>2</sub>. Figure 52 below shows the temperature difference between the inlet CO<sub>2</sub> temperature and the average PCM temperature, followed by figure 53 showing the development in the inlet CO<sub>2</sub> temperature calculated based on the pressure values for the 15 mm configurations. Figure 52 shows a trend with a dropping difference in the first five minutes as the PCM starts with relatively high temperature that can reach 15 °C and drops very quickly, therefore it will be disregarded when evaluating the test with highest temperature difference. The fast dropping in temperature difference is followed by an increase due to dropping inlet CO<sub>2</sub> temperature much faster than dropping average PCM temperature. Figure 52 shows that the highest temperature difference between the inlet CO<sub>2</sub> and average temperature was recorded for C8 at 18,6 minute with 12,4 °C and C7 at 20,6 minute with 12,4 °C. C8 and C7 have the lowest two inlet CO<sub>2</sub> temperatures of -22 °C and -20 °C, respectively. Figure 53 below shows how each of C8 and C7 took longest to reach their desired values of inlet CO<sub>2</sub> temperature.

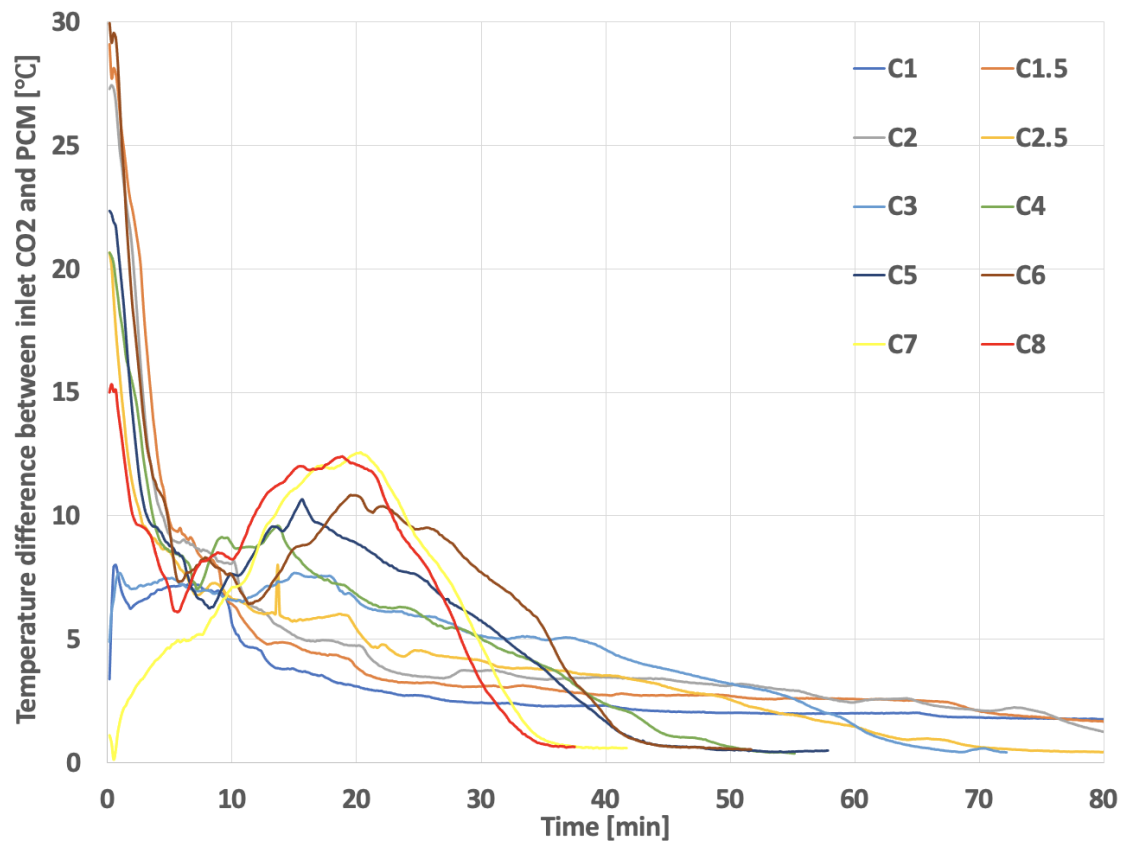


Figure 52: Temperature difference between inlet CO<sub>2</sub> temperature and PCM for the 15 mm configuration for RT-9HC

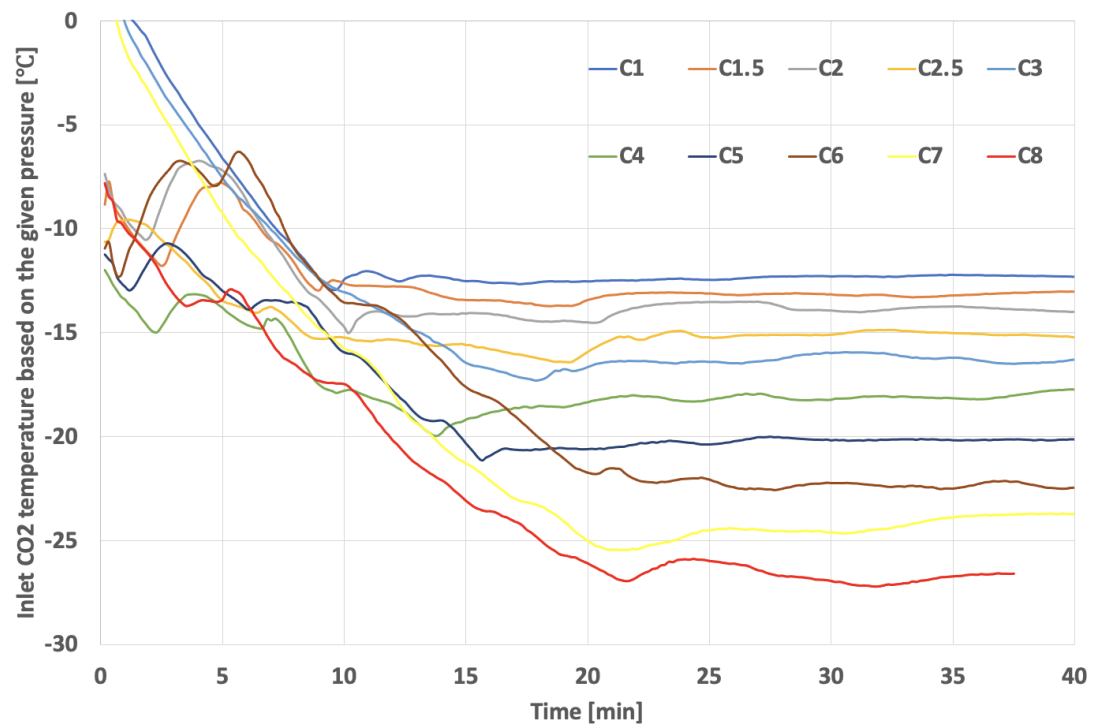


Figure 53: Inlet CO<sub>2</sub> temperature calculated based on the pressure for the 15 mm configuration for RT-9HC

Figure 54 below shows the temperature difference between the inlet CO<sub>2</sub> temperature and the average PCM temperature, followed by figure 55 showing the development in the inlet CO<sub>2</sub> temperature calculated based on the pressure values for the 30 mm configurations. The same trend of increasing temperature difference followed by a decrease is due to faster dropping in temperature for the inlet CO<sub>2</sub> temperature compared with the average PCM temperature. Figure 54 shows C8 at minute 19,6 and C7 at minute 18,5 having the highest temperature difference between the PCM and the inlet CO<sub>2</sub> temperature with values of 11,7 °C and 10,9 °C, respectively.

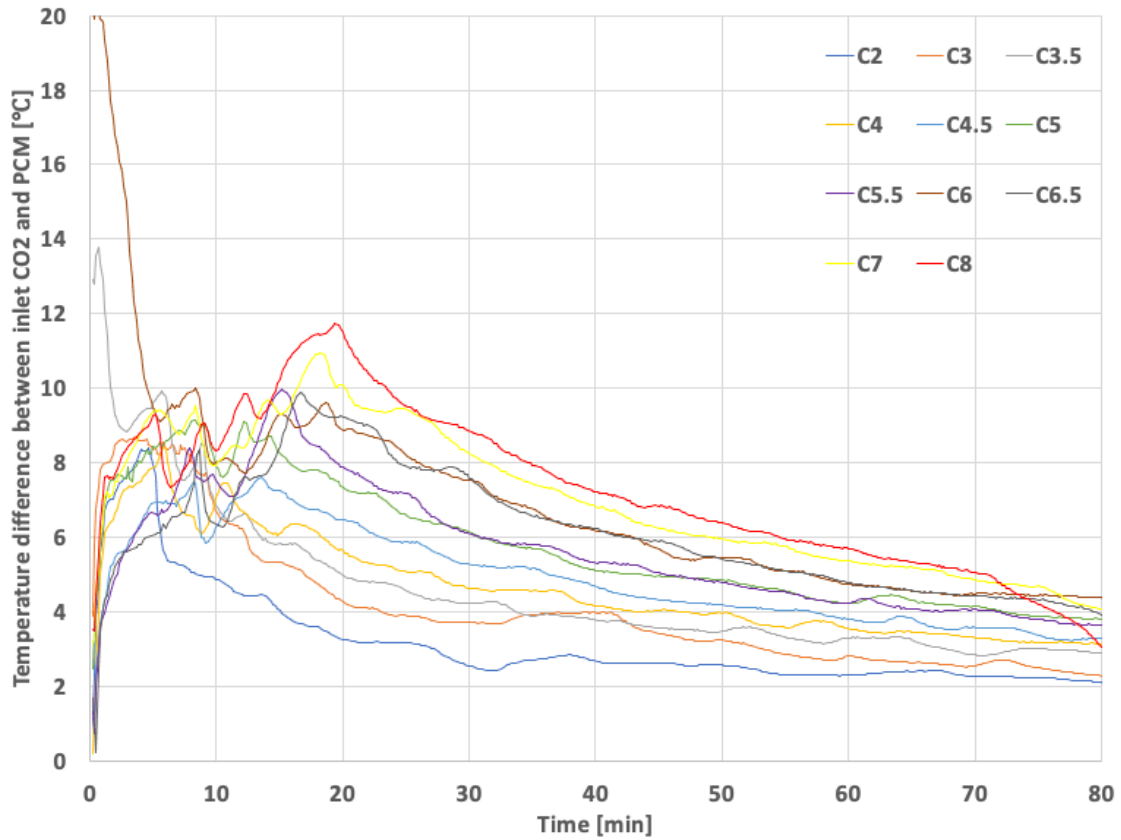


Figure 54: Temperature difference between inlet CO<sub>2</sub> temperature and PCM for the 30 mm configuration for RT-9HC

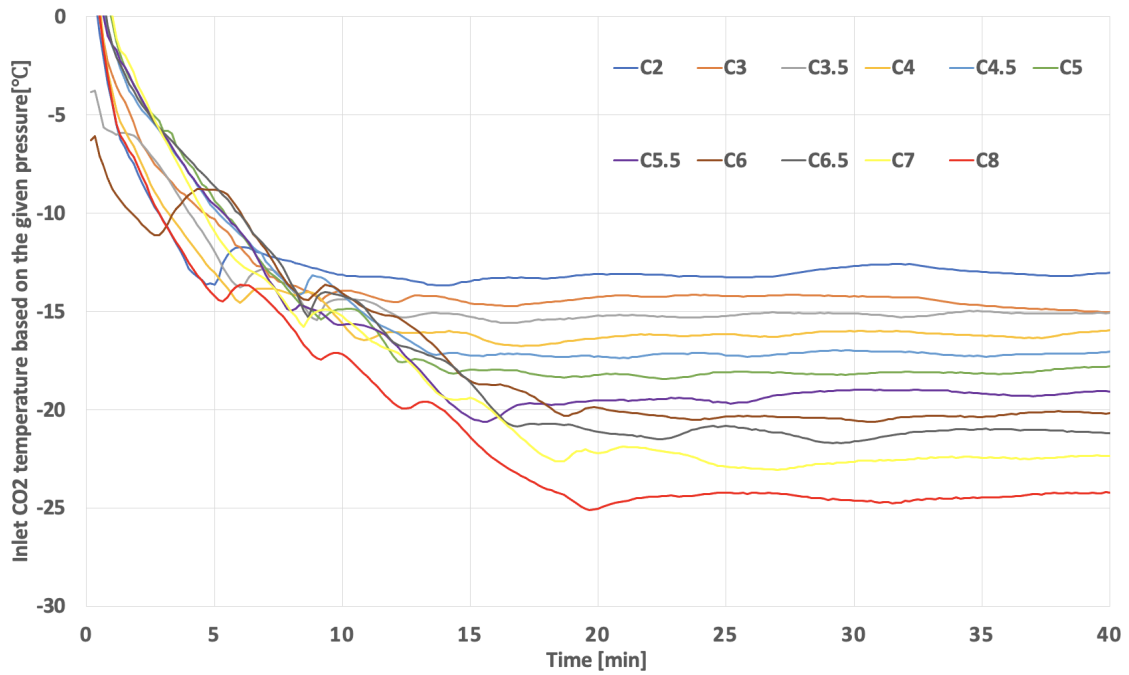


Figure 55: Inlet CO<sub>2</sub> temperature calculated based on the pressure for the 30 mm configuration for RT-9HC

Figures 56 and 57 show the average temperature of the nine sensors placed on the top, middle, and bottom plate for the 15 mm and 30 mm configurations, respectively. Both figures show very similar trend where the temperature of the PCM drops at the same rate in the three locations in the beginning of the charging test. However, after sometime the temperature drops faster on the top plate, followed by the middle, and then at last the bottom plate before they all reach the same temperature towards the end of the experiment. The same trend was noticed for all the charging tests, the difference in the three locations increased with lower inlet CO<sub>2</sub> temperatures and increased with higher inlet CO<sub>2</sub> temperature.

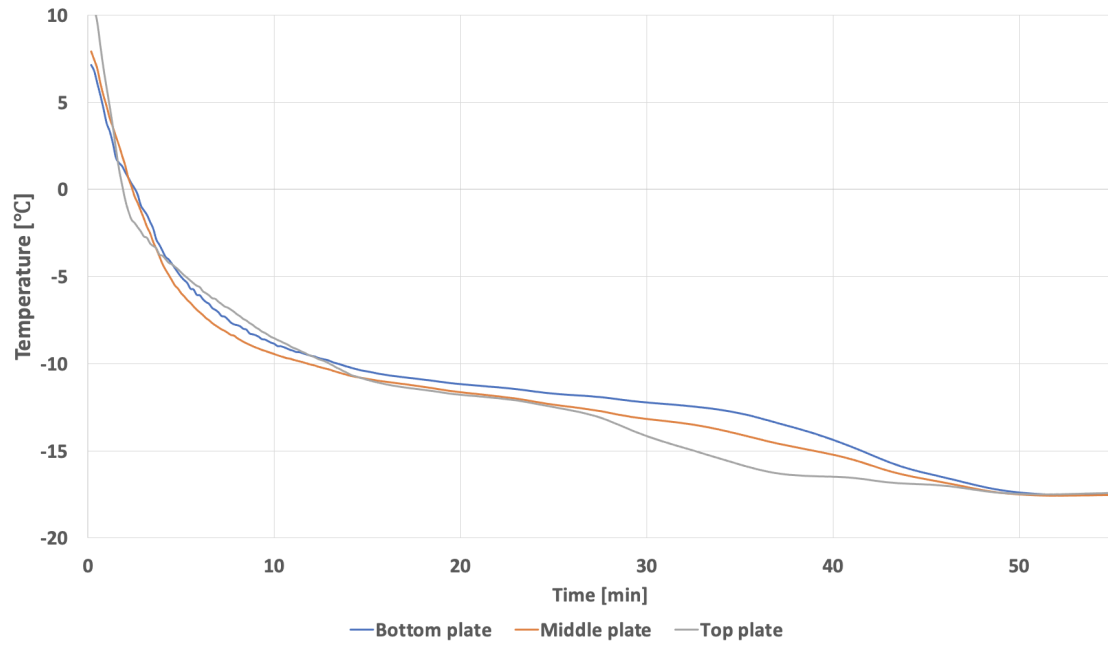


Figure 56: The average temperature above the bottom, middle, and top plate during C4 charging test for the 15 mm configuration for RT-9HC

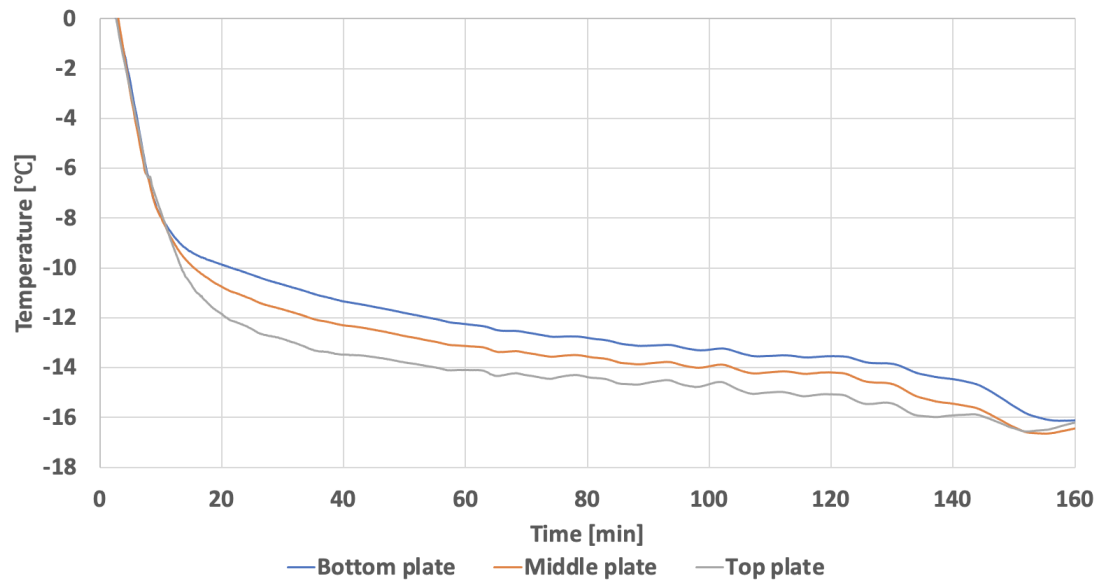


Figure 57: The average PCM temperature above the bottom, middle, and top plate during C4.5 for the 30 mm configuration for RT-9HC

## 5.2 Discharging Mode

### 5.2.1 Water

While running the experiment it was noticed that each of D1, D2, and D3 doesn't generate enough driving force for the ice to melt and hence the results were not considered. Figures 58 and 59 show the pressure drop across the CTES unit for the two different configurations of 15 mm and 30 mm. The pressure drop across the CTES unit was measured for the different discharging cycles

and it was noticed that the higher the flow rate was the higher the pressure drop is. Increasing the inlet CO<sub>2</sub> temperature had an insignificant effect on the pressure drop compared to increasing the mass flow rate. The pressure drop was almost insignificant for all cases, however this can be important if the system is to be largely scaled to have a better idea of the energy consumption of the system as the compressor will have to compress the extra difference represented in this pressure drop causing more energy consumption for the refrigeration system. Figure 58 below shows the highest pressure drop for D12 with the highest average flow rate of 9,5 kg min<sup>-1</sup> and the highest inlet CO<sub>2</sub> temperature of 8,6 °C. The lowest pressure drop was recorded for D4 with the lowest inlet CO<sub>2</sub> temperature of 4,6 °C and lowest mass for rate of 4 kg min<sup>-1</sup>.

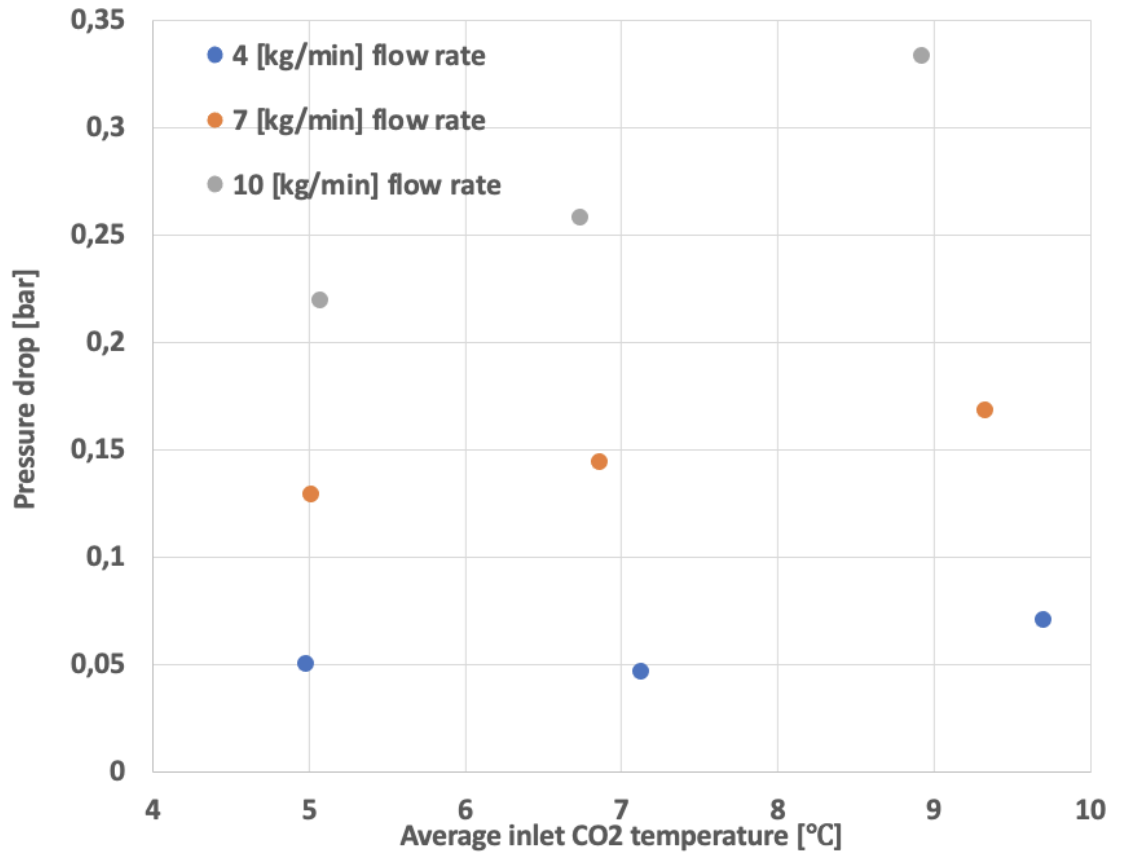


Figure 58: Pressure drop for different average inlet CO<sub>2</sub> temperatures grouped in their respective flow rates for the 15 mm configuration for water

Figure 59 below shows the same trend of increasing pressure drop with increasing mass flow rate. However increasing the inlet CO<sub>2</sub> temperature with the highest flow rate of 10 kg min<sup>-1</sup> had a more significant effect on increasing the pressure drop compared to increasing the inlet CO<sub>2</sub> temperature with the other flow rates. The highest pressure drop recorded to be 0,33 bar was for D12 with 8,93 °C average inlet CO<sub>2</sub> temperature and 9,29 kg min<sup>-1</sup> mass flow rate which was 27% higher than the pressure drop recorded for D9 of 0,26 bar with 6,74 °C average inlet CO<sub>2</sub> temperature and 9,69 kg min<sup>-1</sup> mass flow rate.



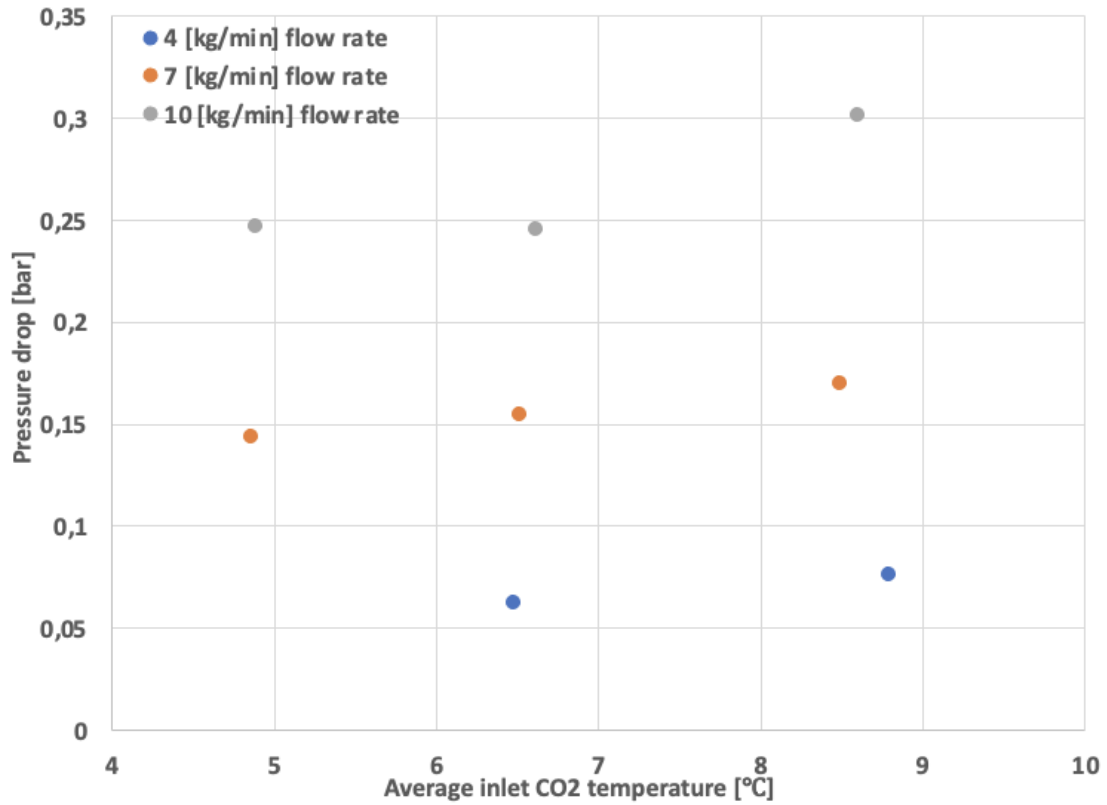


Figure 59: Pressure drop for different average inlet CO<sub>2</sub> temperatures grouped in their respective flow rates for the 30 mm configuration for water

The heat input into the CTES unit was calculated following Equation 10 shown in the method section. Tables 24 and 25 show the values calculated for the heat extracted from the system due to the heat input from the glycol cycle. The specific heat of the glycol/water mixture of 30 % concentration is 3,85 kJ/kg.K.

	Time to discharge min	CO <sub>2</sub> inlet temperature °C	Mass flow rate of CO <sub>2</sub> kg min <sup>-1</sup>	Mean discharge duty kW	Heat extracted kWh
D4	44,33	4,60	4,04	7,18	5,31
D5	89,17	4,86	7,05	5,31	7,89
D6	69,83	4,88	9,90	4,76	5,54
D7	89,67	6,47	4,03	6,32	9,45
D8	94,17	6,51	7,08	6,30	9,88
D9	64,50	6,62	9,76	7,91	8,50
D10	82,33	8,79	4,06	8,42	11,56
D11	97,33	8,49	7,04	7,68	12,46
D12	72,05	8,60	9,52	9,02	10,84

Table 24: Results of the discharging tests for the 15 mm configurations for water

	Time to discharge min	CO <sub>2</sub> inlet temperature °C	Mass flow rate of CO <sub>2</sub> kg min <sup>-1</sup>	Mean discharge duty kW	Heat extracted kWh
D4	89,83	4,99	4,30	3,80	5,68
D5	189,67	5,02	7,05	4,09	12,92
D6	157,00	5,08	9,98	2,94	7,69
D7	179,50	7,13	4,04	4,16	12,44
D8	178,33	6,87	7,11	5,37	15,95
D9	135,17	6,74	9,69	5,93	13,35
D10	131,67	9,71	3,92	8,00	17,55
D11	120,50	9,33	6,56	9,56	19,20
D12	93,17	8,93	9,29	10,67	16,57

Table 25: Results of the discharging tests for the 30 mm configurations for water

Figures 60 and 61 show the mean discharge duty plotted as a function of the mean CO<sub>2</sub> inlet temperature grouped in their relative flow rates for the 15 mm configuration and 30 mm configuration respectively. Figure 60 below shows the highest mean discharge duty calculated to be 9,02 kW for the D12 discharging cycle with high mass flow rate and high mean inlet CO<sub>2</sub> temperature. Comparing this mean discharge duty with the mean discharging duty of the discharging cycles with the same mass flow rate shows that it is 14,1% higher than D9 mean discharge duty of 7,91 kW with inlet CO<sub>2</sub> temperature of 6,6 °C, and 89,5% higher than D6 mean discharge duty of 4,76 kW with inlet CO<sub>2</sub> temperature of 4,9 °C. This shows how increasing the inlet CO<sub>2</sub> temperature increased the mean discharge duty.

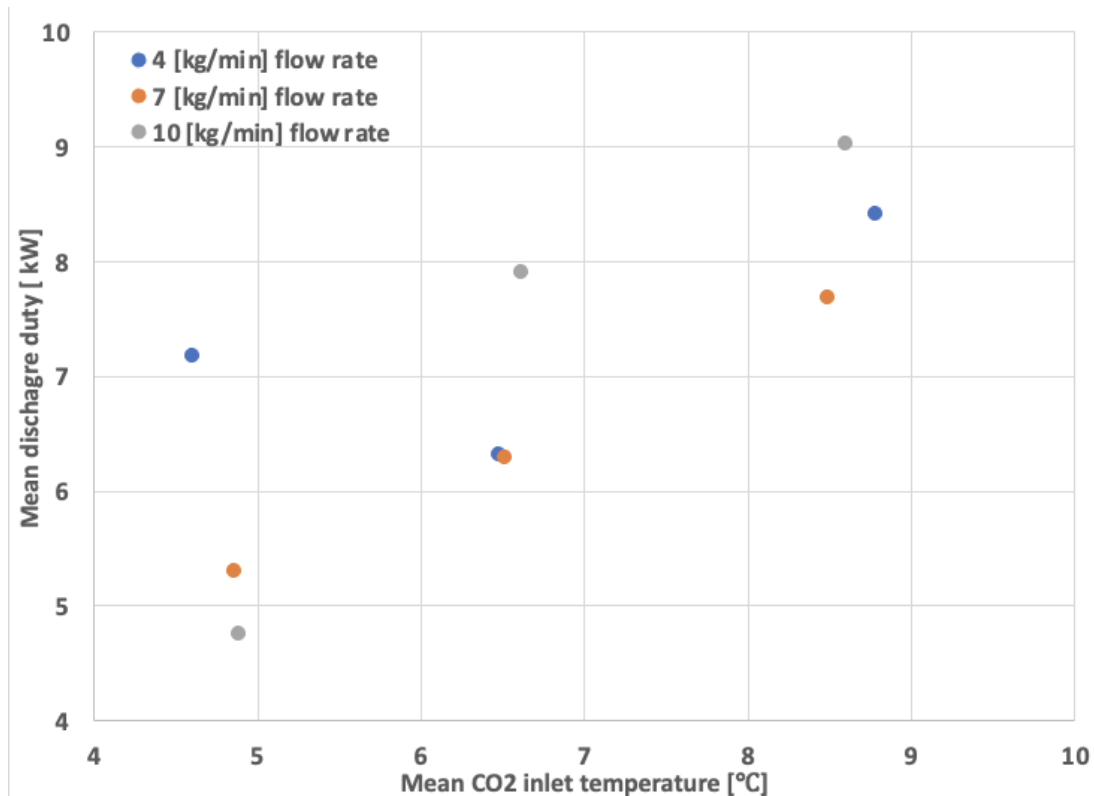


Figure 60: Mean discharge duty of the different mean inlet CO<sub>2</sub> temperatures grouped according to their respective flow rate for the 15 mm configuration for water

Figure 61 below shows the highest mean discharge duty for D12 as well to be 10,67 kW. Comparing this mean discharge duty with the mean discharging duty of the discharging cycles with the same mass flow rate shows that it is 80,1% higher than D9 mean discharge duty of 5,93 kW with inlet CO<sub>2</sub> temperature of 6,74 °C, and 262,9% higher than D6 mean discharge duty of 2,94 kW and

inlet CO<sub>2</sub> temperature of 5,08 °C.

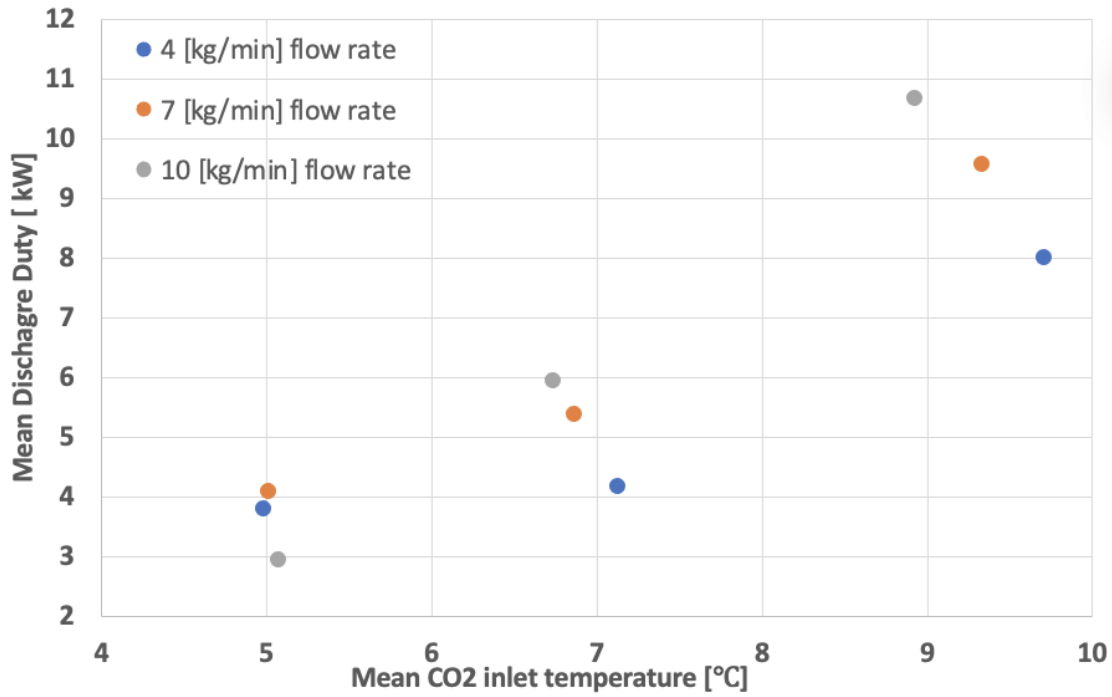


Figure 61: Mean discharge duty of the different mean inlet CO<sub>2</sub> temperatures grouped according to their respective flow rate for the 30 mm configuration for water

Figures 62 and 63 below show the heat flow as a function of time for the 15 mm configuration and 30 mm configuration respectively. Figure 62 below shows that each of D10, D11, and D12 keeps the highest heat flow for the longest time before the decay starts to happen followed by D7, D8 and D9 and finally D4, D6, and D7.

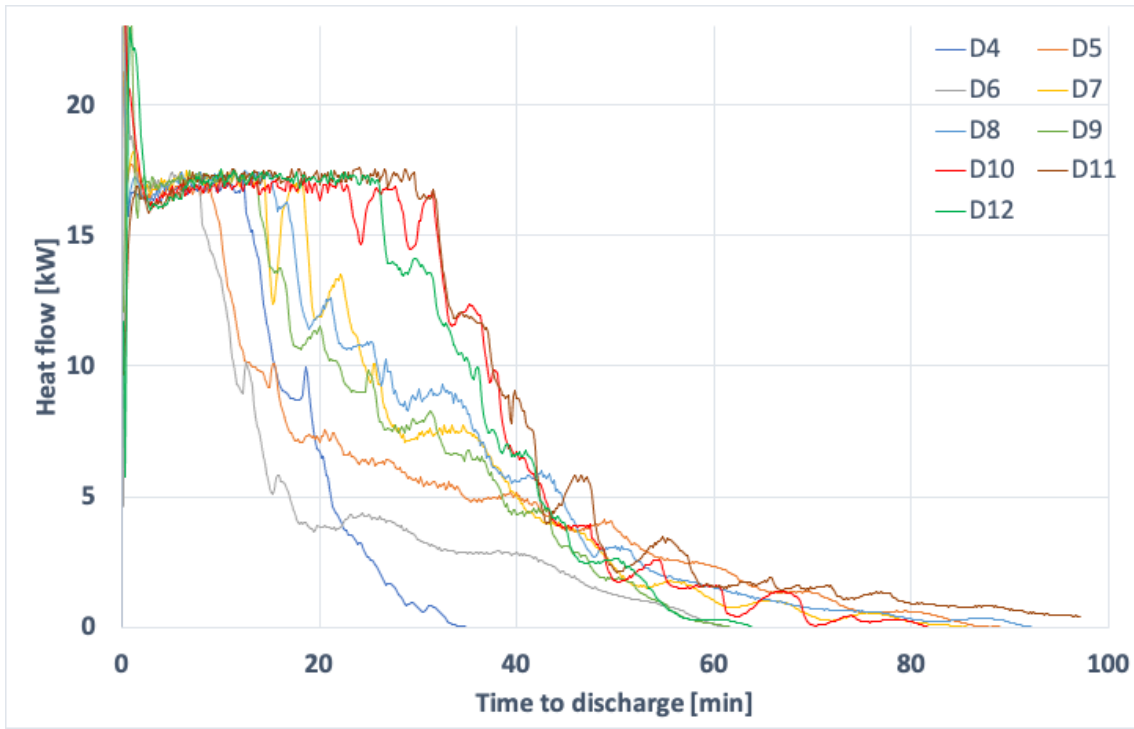


Figure 62: Heat flow vs time to discharge for the different operating conditions for the 15 mm configuration for water

Figure 63 below shows a similar trend to the 15 mm configuration. The heat flow starts at its highest for all discharging cycles at an approximate average of 17 kW followed by a decay until it reaches 0 kW. Furthermore, each of D10, D11, and D12 keeps the highest heat flow for the longest time before the decay starts to happen followed by D7, D8 and D9 and finally D4, D6, and D7. The 17 kW limit is limited due to the upper limit of the heaters in the glycol cycle of 18 kW, and the efficiency of heat transfer within the glycol circuit.

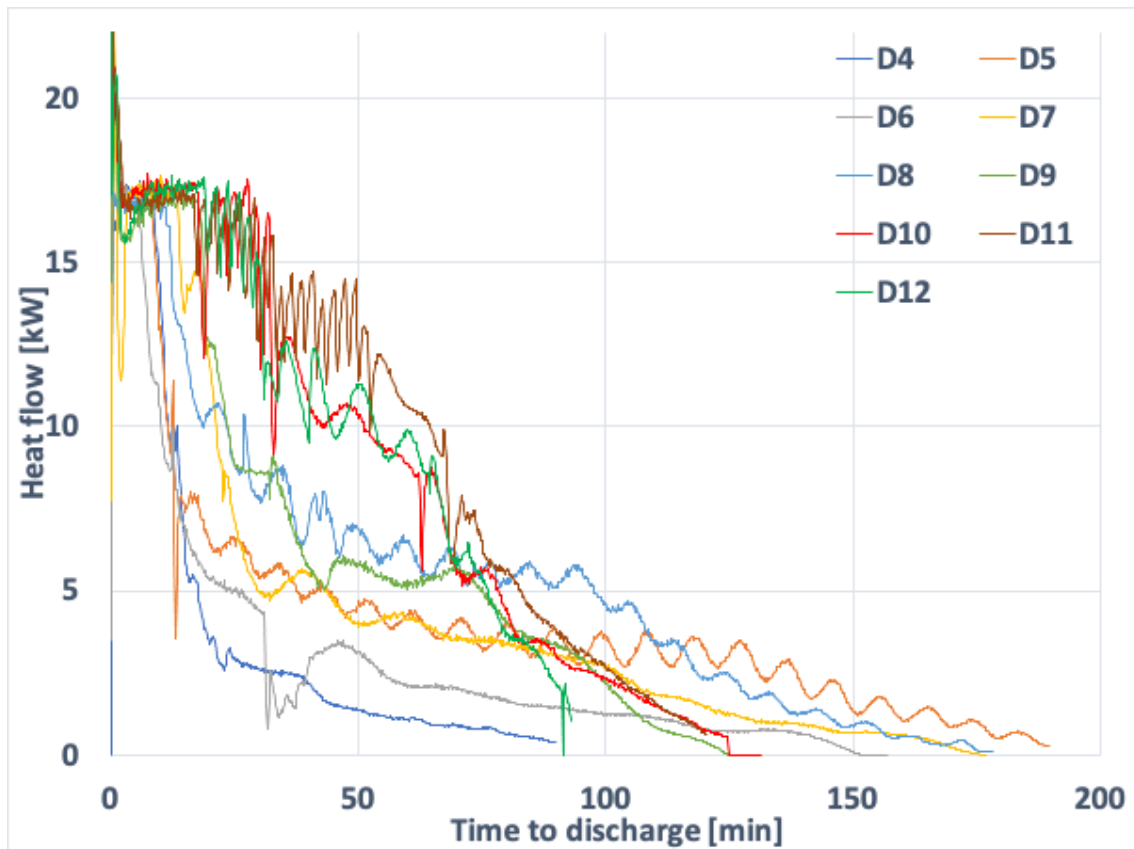


Figure 63: Heat flow vs time to discharge for the different operating conditions for the 30 mm configuration for water

Figures 64 and 65 show the cumulative energy discharged with respect to time for both configurations of 15 mm and 30 mm. The highest amounts of cumulative discharged energy in both figures are D10, D11, and D12, which have a CO<sub>2</sub> steady state condition of 10 °C. This is followed by D8, D7, and D9, which have 7,5 °C inlet CO<sub>2</sub> steady state conditions. The lowest amounts of cumulative discharged energy are observed for D5, D6 and D4 which have 5 °C steady state inlet CO<sub>2</sub> conditions. This trend shows that the higher the CO<sub>2</sub> inlet temperature is, the higher the cumulative energy discharged is.

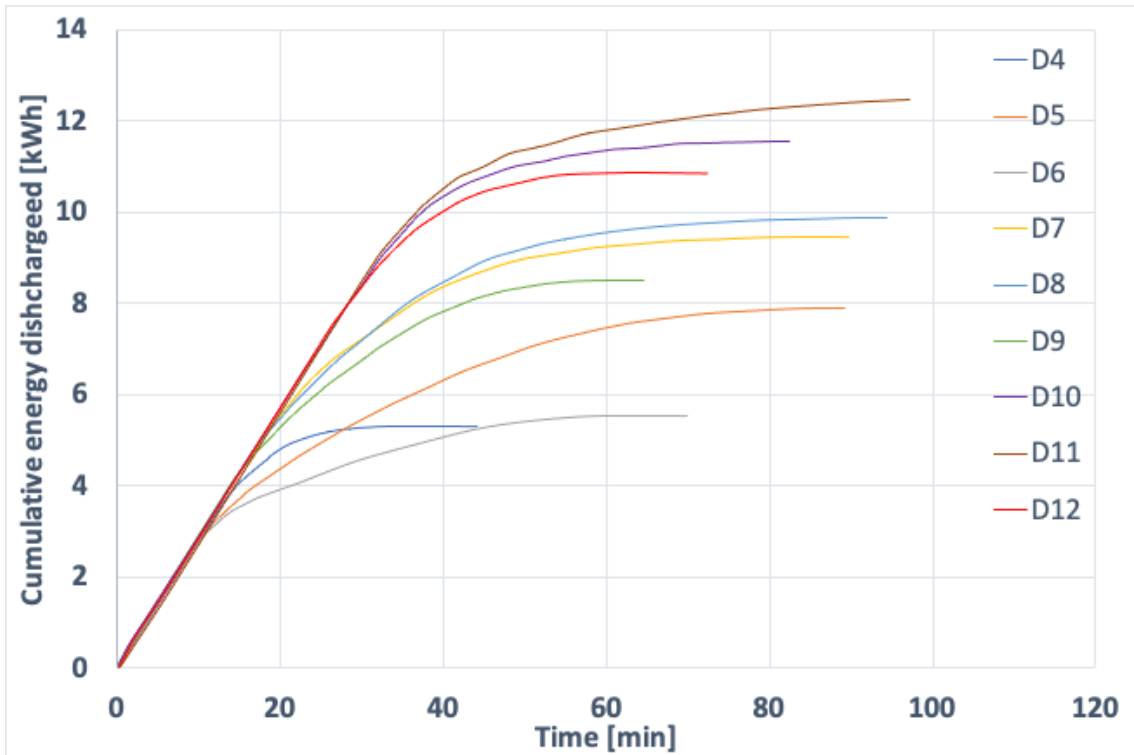


Figure 64: Cumulative energy discharged throughout the cycle time for the 15 mm configuration for water

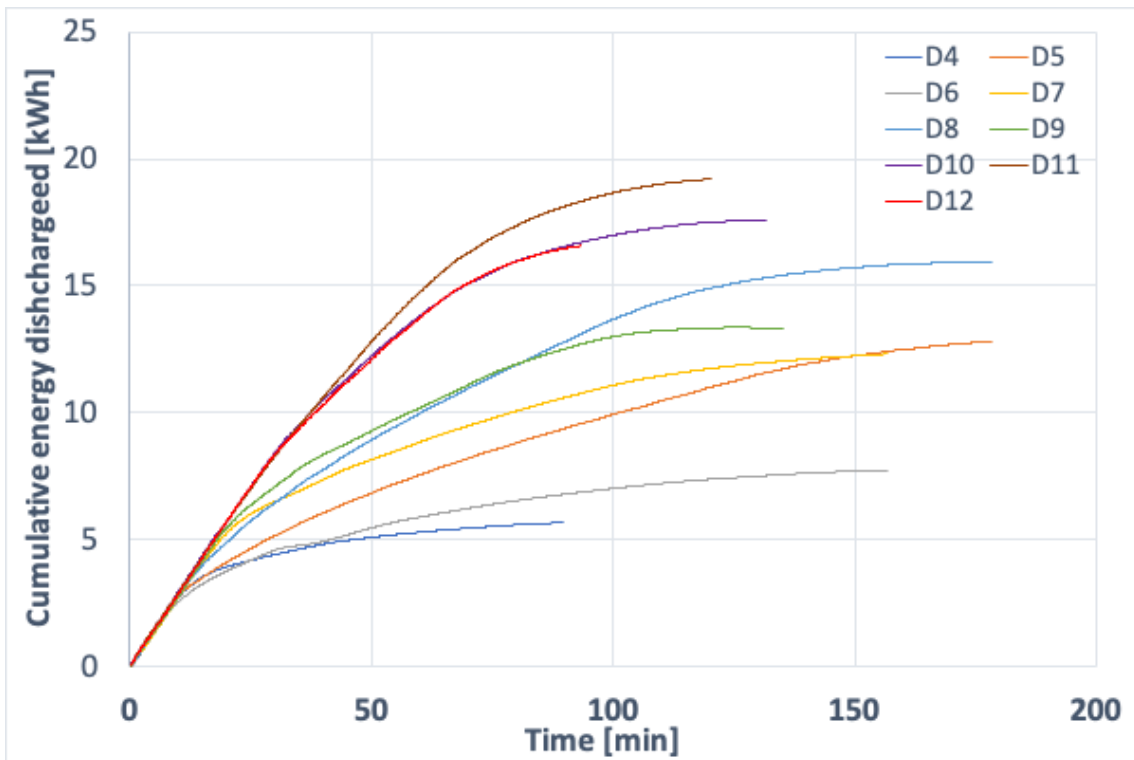


Figure 65: Cumulative energy discharged throughout the cycle time for the 30 mm configuration for water

Figures 66 and 67 show the difference in temperature between the inlet CO<sub>2</sub> and outlet CO<sub>2</sub> along

the experiment time. The CO<sub>2</sub> flows inside the pillow plate heat exchangers in a gas phase in saturated conditions. Then, the CO<sub>2</sub> condenses due to exchanging heat with the ice. When the CO<sub>2</sub> condenses before reaching the end of the pillow plate heat exchangers, it is further cooled down by exchanging sensible heat with the ice causing what is called subcooling of the CO<sub>2</sub>.

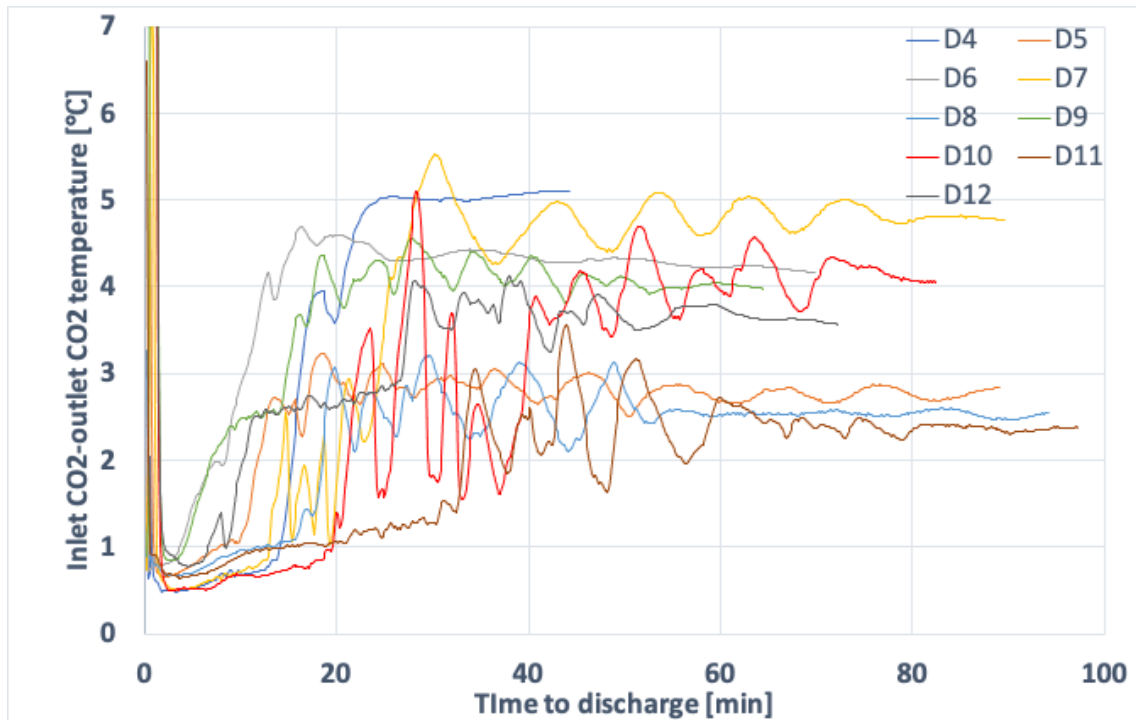


Figure 66: Difference between inlet CO<sub>2</sub> and outlet CO<sub>2</sub> temperature for the 15 mm configuration for water

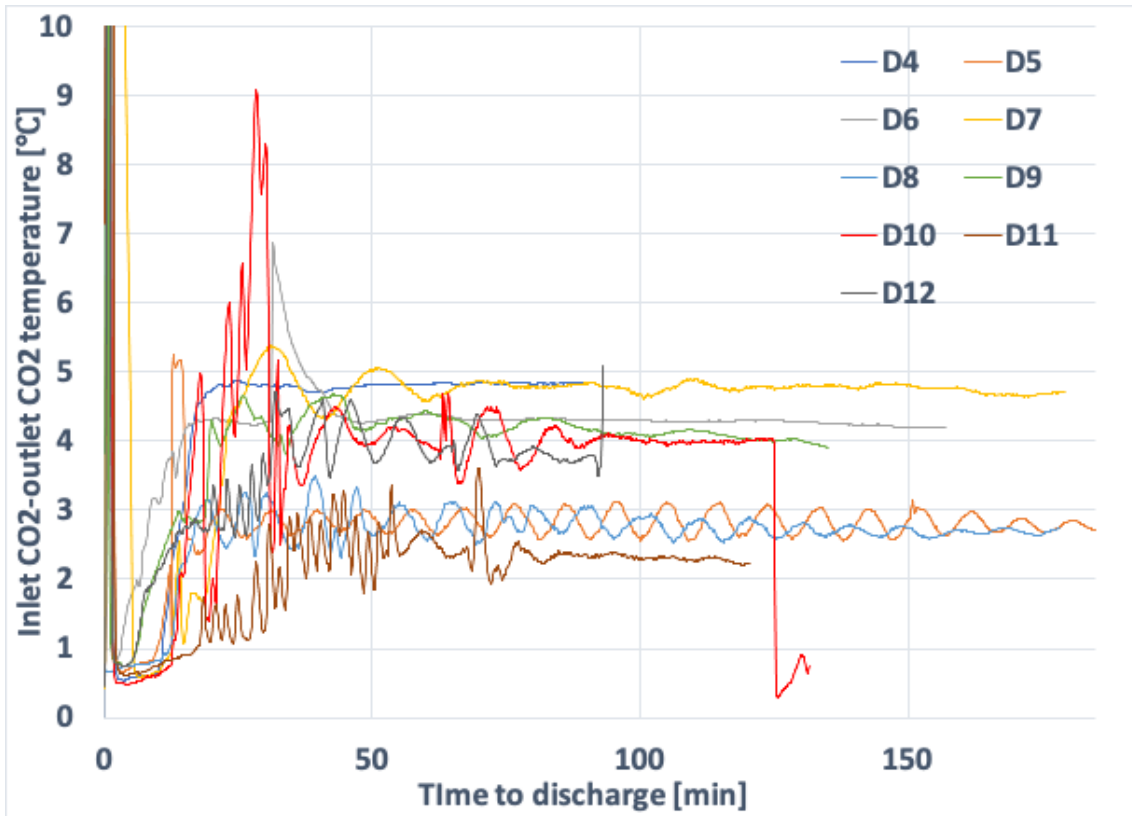


Figure 67: Difference between inlet CO<sub>2</sub> and outlet CO<sub>2</sub> temperature for the 30 mm configuration for water

The subcooling shown above in Figure 66 and 67 represents extra heat extracted from the system and not accounted for by calculating the heat input from the glycol cycle. This is because the pressure of the system is constant, and the inlet CO<sub>2</sub> into the evaporator is at saturation conditions while the CTES outlet is subcooled. The sensible heat extracted from the CO<sub>2</sub> was calculated by using equation 2 and using the specific heat of CO<sub>2</sub> at saturation conditions and 5 °C to be 2,8 [kJ/kgK]. Table 26 shows the total heat extracted from the system which is found by adding the sensible heat flow due to subcooling of the CO<sub>2</sub> to the heat input from the glycol circuit.

	15 mm configuration		30 mm configuration	
	Total discharged energy kWh	Total heat extracted %	Total discharged energy kWh	Total heat extracted %
D4	5,8	47%	6,6	27%
D5	9,2	75%	13,8	57%
D6	7,5	62%	9,7	40%
D7	10,5	87%	13,3	55%
D8	11,1	91%	16,8	69%
D9	10,4	85%	15,1	62%
D10	12,4	102%	18,3	75%
D11	13,5	111%	19,9	82%
D12	12,5	103%	18,1	74%

Table 26: Total system performance for water

### 5.2.2 RT-9HC

The discharging mode was initially performed by running the experiment with a fixed inlet CO<sub>2</sub> temperature of 0 °C, while varying the mass flow rate between 4 and 10 kg min<sup>-1</sup> in order to



determine the optimum mass flow rate. The optimum mass flow rate was determined based on the discharging mode with the highest heat extraction percentage. The amount of heat extracted was calculated using the same method that was used with the water results using equation 10. The initial tests for the 15 mm configuration were run using the same glycol mixture used for the water experiment with a specific heat of 3,85 kJ/kg.K. However, all the other experiments were carried using a glycol/water mixture of 47% concentration with a specific heat of 3,25 kJ/kg.K. Tables 27 and 28 show the outcome of these results. The highest extraction rate was recorded for D-MF2 for the 15 mm configuration, and D-MF4 for the 30 mm configuration with values of 99,51% and 84,19%, respectively. Therefore, the 15 mm configuration was carried with a mass flow rate of 5 kg min<sup>-1</sup>, while the 30 mm configuration was carried with mass flow rate of 7 kg min<sup>-1</sup>.

	Time to discharge min	Mass flow rate of CO <sub>2</sub> kg min <sup>-1</sup>	Mean discharge duty kW	Heat extracted kWh	Total heat extracted %
D-MF1	61,50	4,1	6,9	7,0	96,5%
D-MF2	69,50	5,1	6,2	7,2	99,5%
D-MF3	68,33	6,1	6,3	7,1	97,9%
D-MF4	54,33	7,1	7,0	6,3	87,3%
D-MF5	48,00	8,0	7,6	6,1	84,0%
D-MF6	45,67	9,0	7,8	5,9	81,7%
D-MF7	43,50	9,9	7,7	5,6	76,6%

Table 27: Results for the initial tests with fixed inlet CO<sub>2</sub> temperature for the 15 mm configuration for RT-9HC

	Time to discharge min	Mass flow rate of CO <sub>2</sub> kg min <sup>-1</sup>	Mean discharge duty kW	Heat extracted kWh	Total heat extracted %
D-MF1	144,17	4,03	4,18	10,05	69,1%
D-MF2	131,83	5,03	5,01	11,02	75,8%
D-MF3	133,67	6,05	5,09	11,33	78,0%
D-MF4	134,50	7,03	5,46	12,24	84,2%
D-MF5	113,67	8,06	5,84	11,07	76,1%
D-MF6	98,67	8,98	5,94	9,76	67,2%
D-MF7	92,00	9,97	6,19	9,50	65,3%

Table 28: Results for the initial tests with fixed inlet CO<sub>2</sub> temperature for the 30 mm configuration for RT-9HC

The experiment was further carried based on the parameters showed in tables 20 and 21. Tables 29 and 30 show the results obtained following these discharging cycles.

	Time to discharge min	CO <sub>2</sub> inlet temperature °C	Mean discharge duty kW	Heat extracted kWh	Total heat extracted %
D1	25,17	-7,3	5,80	2,43	33,4%
D1.5	43,83	-4,1	3,43	2,50	34,4%
D2	72,83	-3,8	3,57	4,33	59,5%
D3	61,83	-2,6	5,54	5,71	78,5%
D4	54,17	-0,9	7,59	6,85	94,3%
D5	52,50	1,3	8,72	7,63	105,0%
D6	59,00	1,5	9,05	8,90	122,5%
D7	56,83	4,0	8,91	8,44	116,1%

Table 29: Results obtained from performing the discharging cycles for the 15 mm configurations for RT-9HC

	Time to discharge min	CO <sub>2</sub> inlet temperature °C	Mean discharge duty kW	Heat extracted kWh	Total heat extracted %
D1	118,00	-5,80	1,60	3,14	21,6%
D2	164,83	-3,94	2,78	7,64	52,6%
D3	138,67	-2,05	3,99	9,22	63,4%
D4	134,50	-0,13	5,46	12,24	84,2%
D5	116,50	1,53	6,98	13,56	93,3%
D6	102,33	3,43	8,40	14,32	98,5%
D7	104,67	4,36	9,24	16,13	110,9%

Table 30: Results obtained from performing the discharging cycles for the 30 mm configurations for RT-9HC

Figure 68 and 69 show how changing the inlet CO<sub>2</sub> temperature affects the total discharging time. Figure 68 shows two discharging cycles with inlet CO<sub>2</sub> temperature of -7,3 °C and -4,1 °C having faster discharging times compared with discharging cycles with higher inlet CO<sub>2</sub> temperature because these experiments weren't finished as it wasn't possible to melt down all the solid PCM. Figure 69 is showing the same with the discharging cycle having the inlet CO<sub>2</sub> temperature of -5,8 °C. When disregarding these exceptions, both graphs show a dropping trend of the discharging time with the a higher inlet CO<sub>2</sub> temperature. Comparing D4 in both configurations which have a an approximate inlet CO<sub>2</sub> temperature of 0 °C, it took 54,17 minutes to discharge the 15 mm configuration, and 134,5 minutes to discharge the 30 mm configuration which is 248% increase in discharge time.

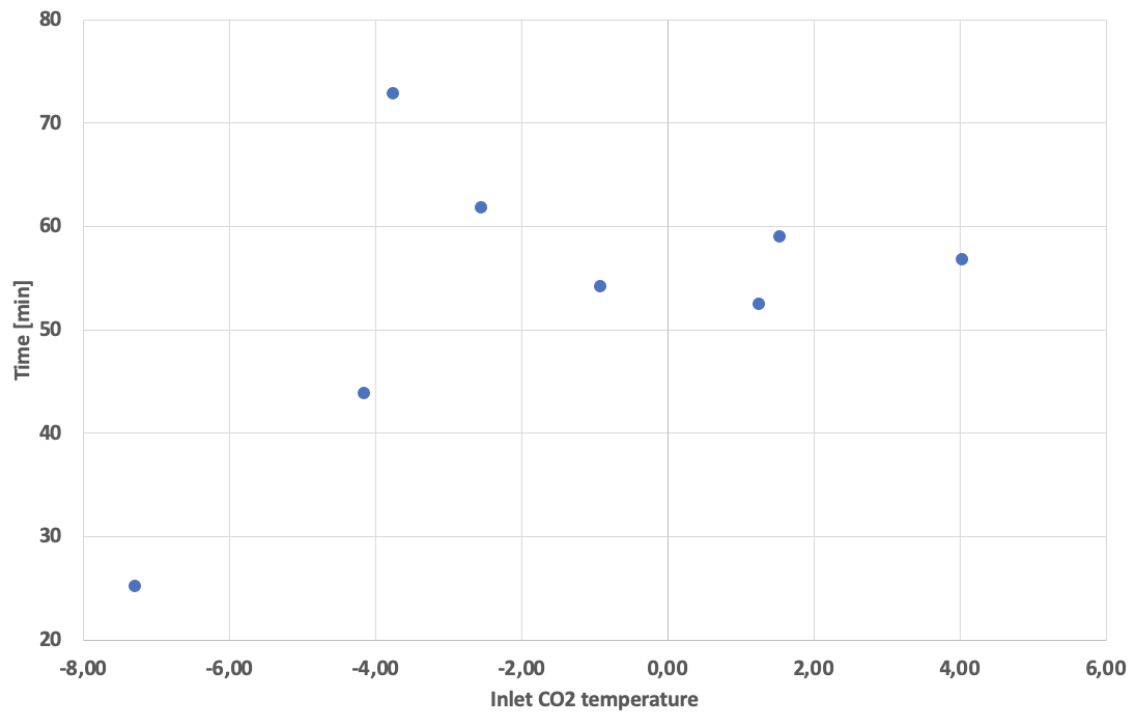


Figure 68: Discharging time for the different inlet CO<sub>2</sub> temperature for the 15 mm configurations for RT-9HC

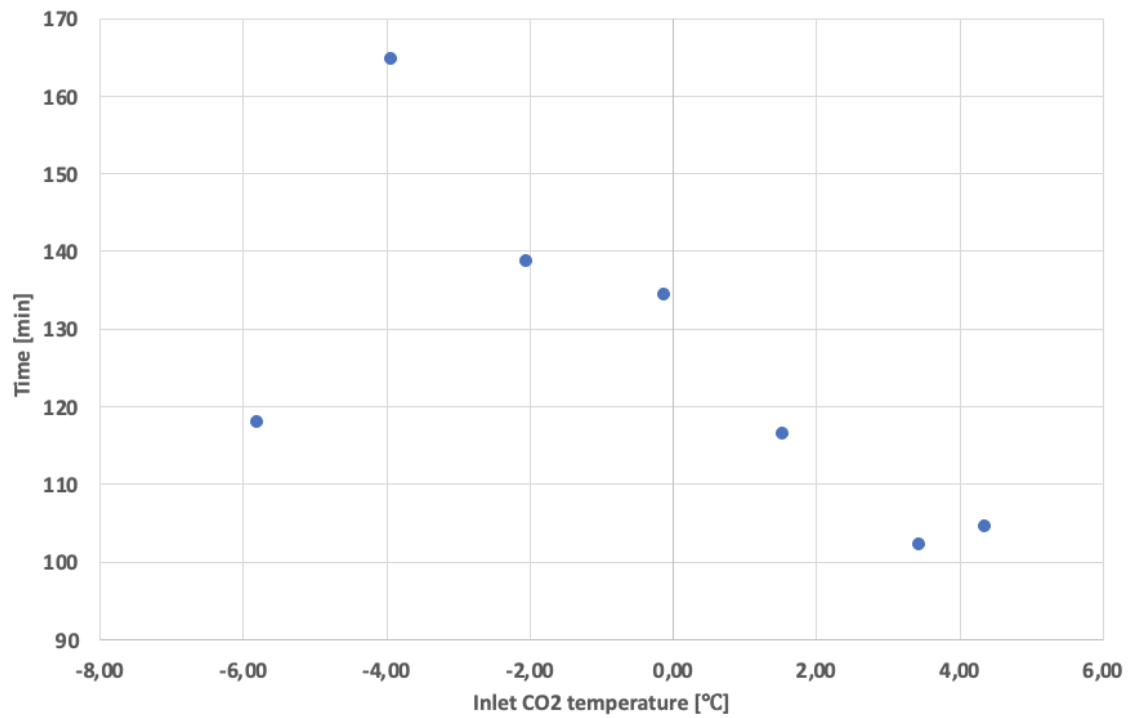


Figure 69: Discharging time for the different inlet CO<sub>2</sub> temperature for the 30 mm configurations for RT-9HC

Figures 70 and 71 show how the mean discharge duty increases with an increasing inlet CO<sub>2</sub> temperature. The highest recorded mean discharge duty for the 15 mm configuration was 9,05 kW for D6. Furthermore, for the 15 mm configuration, the increase in the mean discharge duty starts to flatten out starting with D5, and followed by D6, and D7. The highest recorded mean discharged duty for the 30 mm configuration was 9,24 kW for D7. Figure 71 shows a clearer linear trend of increasing mean discharge duty with the increase of inlet CO<sub>2</sub> temperature.

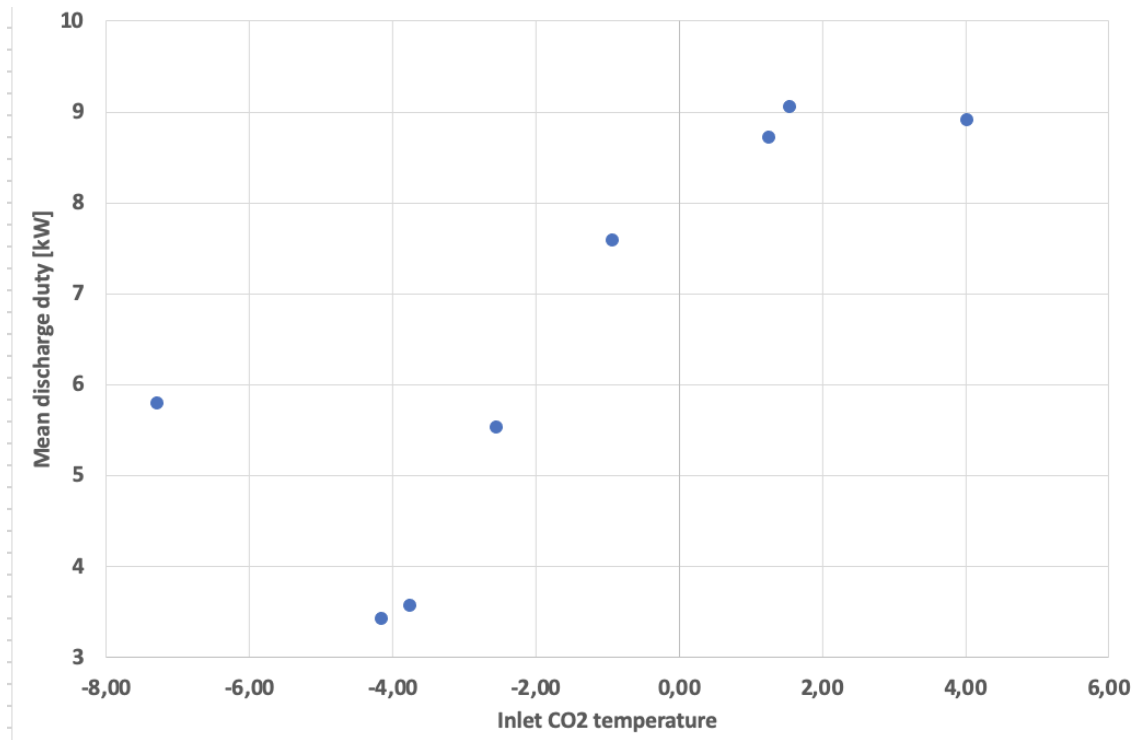


Figure 70: Mean discharge duty for the different inlet CO<sub>2</sub> temperature for the 15 mm configurations for RT-9HC

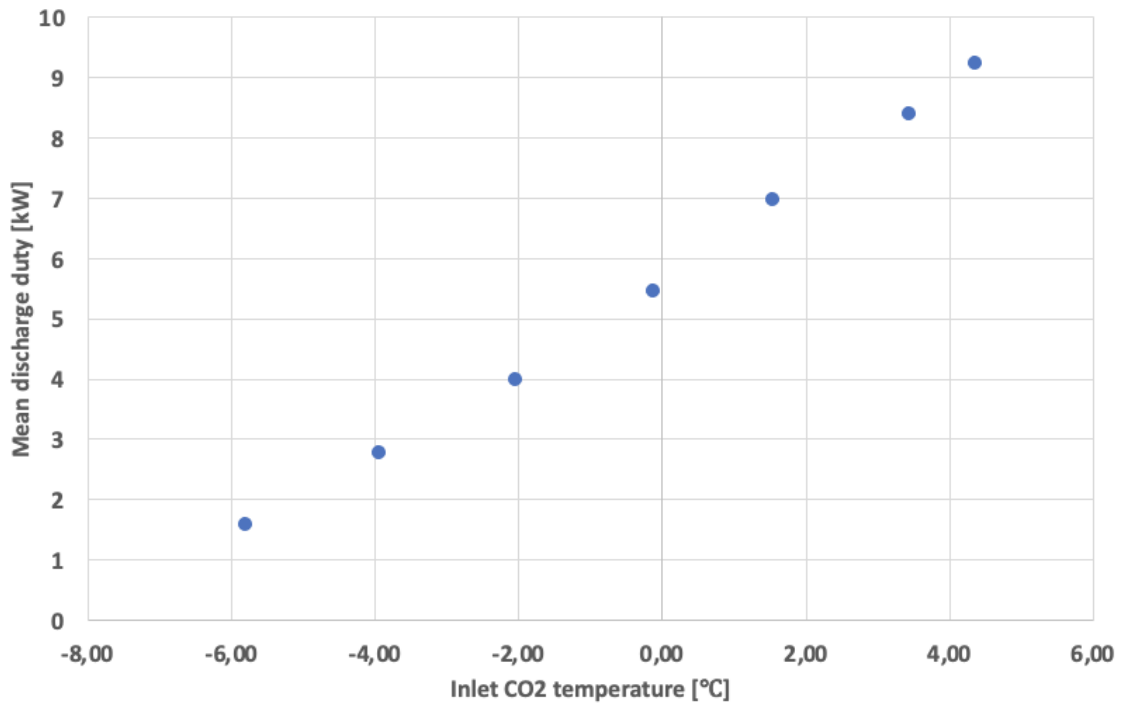


Figure 71: Mean discharge duty for the different inlet CO<sub>2</sub> temperature for the 30 mm configurations for RT-9HC

Figure 72 and 73 below show the development of heat flow into the CTES unit during the discharging cycle. All the discharging cycles starts with a heat flow of approximately 17 kW and then drops to 0 kW towards the end of the experiment. Furthermore, both figures show that the higher

the inlet CO<sub>2</sub> temperature is, the longer the high value of heat flow is kept for, and the longer it takes it to drop to 0 kw. Figure 72 shows how D7 in red, and D6 in green hold the high heat flow for the longest time, around 25 minutes. Figure 72 shows that D7 with red holds the high heat flow for the longest, around 44 minutes, followed by D6 in green which holds it for around 22 minutes.

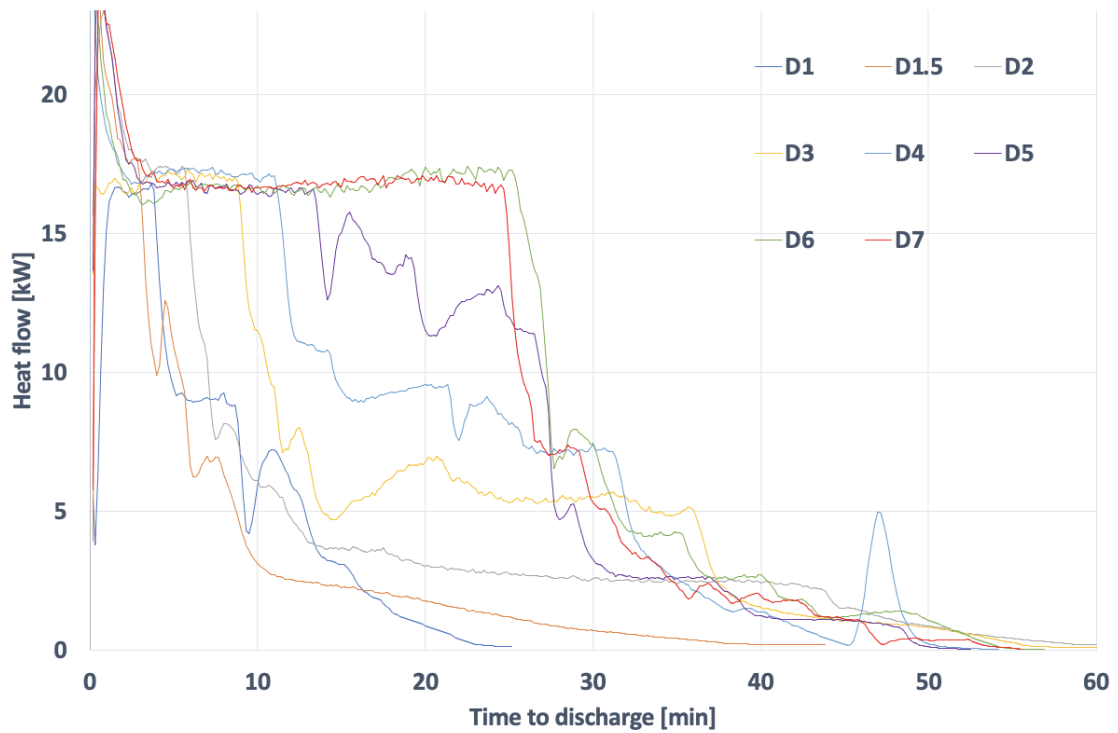


Figure 72: Heat flow during the discharging cycles for the 15 mm configuration for RT-9HC

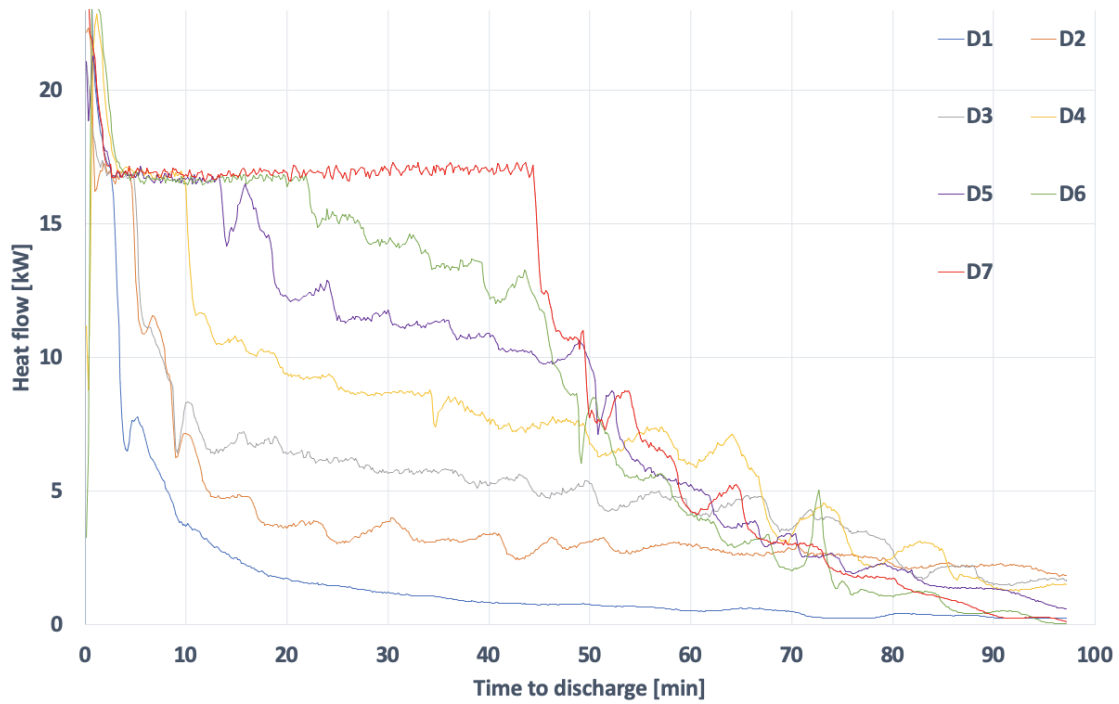


Figure 73: Heat flow during the discharging cycles for the 30 mm configuration for RT-9HC

Figure 74 and 75 below show the cumulative energy discharged during the time of the experiment. Both figures show that the discharging cycles with high inlet CO<sub>2</sub> temperature had the highest cumulative energy discharged, and vice versa. Figure 75 shows that D6 in green had the highest cumulative energy discharged of 8,9 kWh, followed by D7 in red with a value of 8,43 kWh. Figure 75 also shows that D7 in red had the highest cumulative energy discharged with a value of 16,1 kWh, followed by D7 with a value of 14,32 kWh. The points marked on the curves represent the point when 90% of the cumulative energy discharged is achieved in each of D2 in grey and D5 in purple in both configurations. Figure 74 shows that D2 and D5 reach their 90% cumulative energy discharged at 54% and 51% of their total experiment time, with coordination of (39 min, 3,9 kWh) and (27 min, 6,9kWh), respectively. Figure 75 shows that D2 and D5 reach their 90% cumulative energy discharged at 63% and 53% of their total experiment time, with coordination of (104 min, 6,87kWh), and (62 min, 12,2 kWh), respectively.

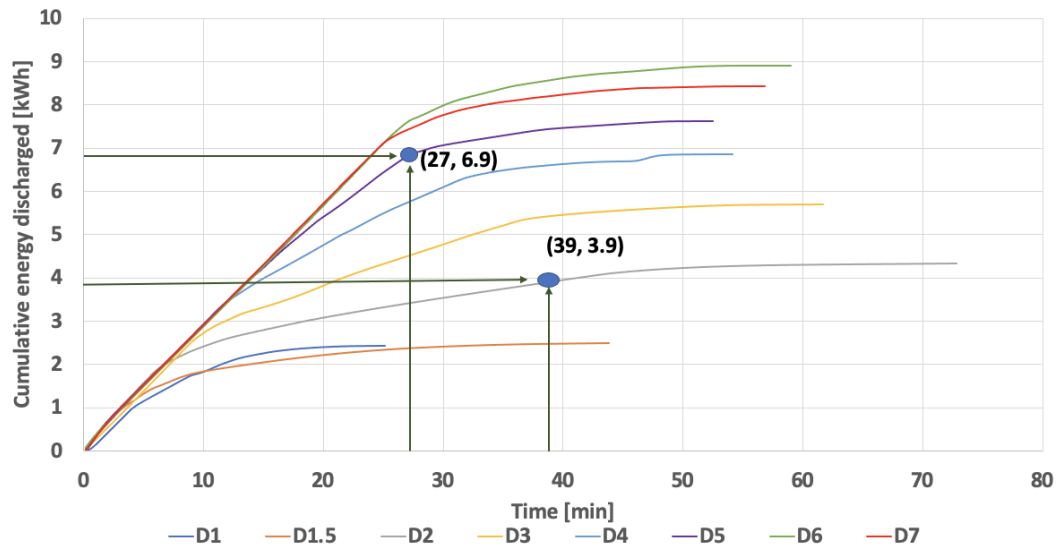


Figure 74: Cumulative energy discharged during the discharging cycles for the 15 mm configuration for RT-9HC

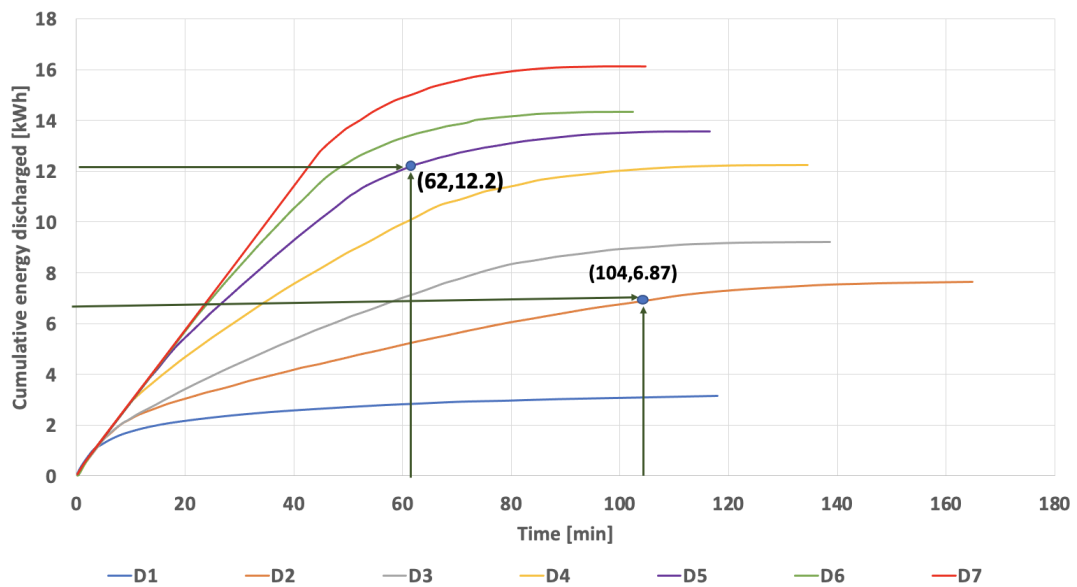


Figure 75: Cumulative energy discharged during the discharging cycles for the 30 mm configuration for RT-9HC

Figure 76 and 77 show the difference in the inlet and outlet CO<sub>2</sub> temperature. This difference in temperature indicates that subcooling happened during the discharging cycles for both configurations. Both figures show a trend with higher subcooling degree for the lower inlet CO<sub>2</sub> temperature, and vice versa. Figure 76 shows that subcooling was between 3 °C and 6 °C between D7 in red, and D1 in blue being the lower and upper boundaries, respectively. Figure 77 shows that subcooling was between 2,5 °C and 4 °C between D7 in red, and D1 in blue being the lower and upper boundaries, respectively.

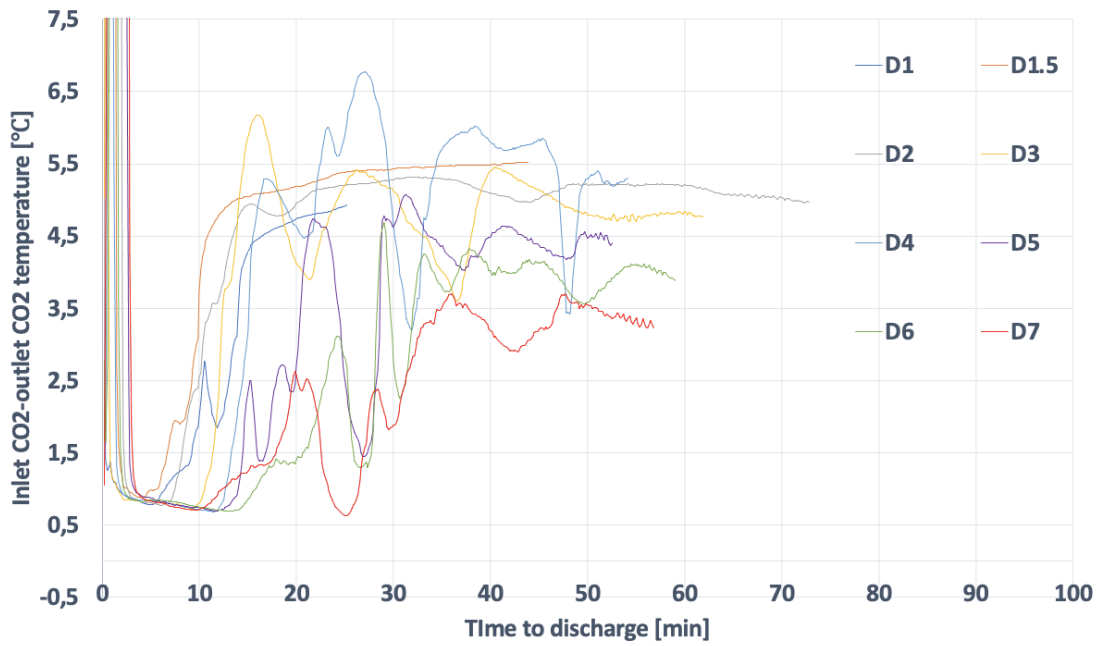


Figure 76: inlet-outlet CO<sub>2</sub> temperature of the 15 mm configuration for RT-9HC

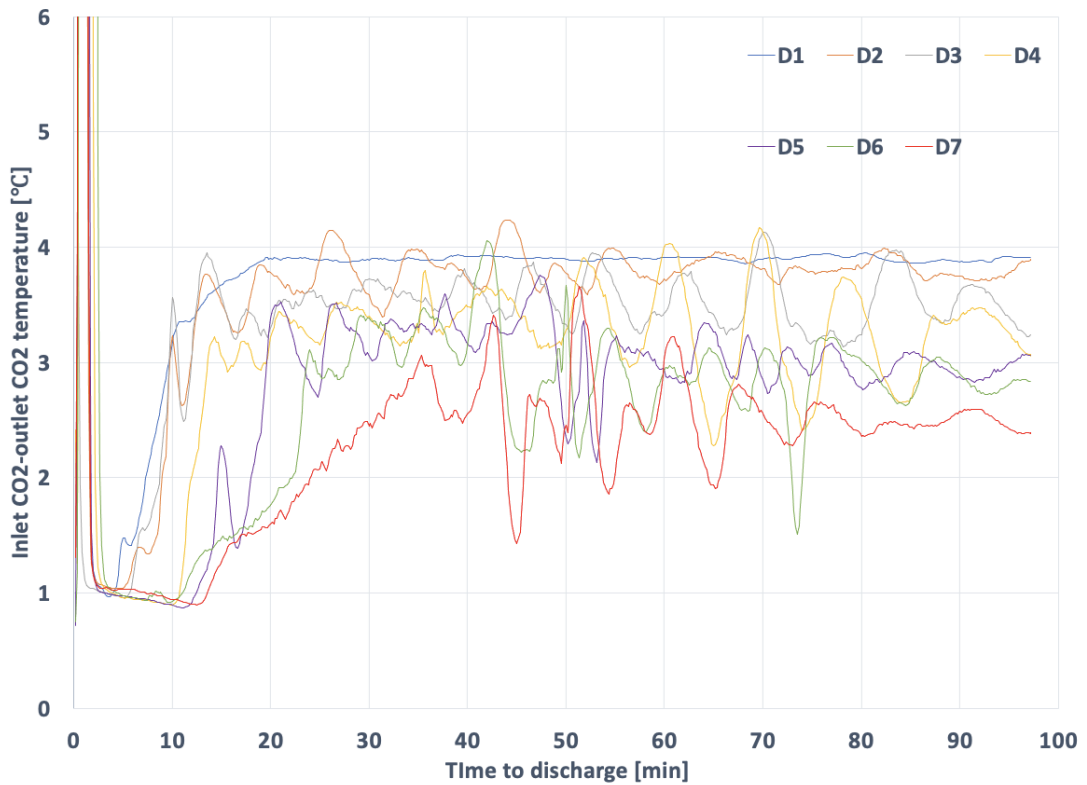


Figure 77: inlet-outlet CO<sub>2</sub> temperature of the 30 mm configuration for RT-9HC

The subcooling is an extra heat that needs to be accounted for to estimate the real total heat extracted from the system. The same argument was made for calculating the heat due to subcooling in the water section. Equation 2 was used by using the specific heat of CO<sub>2</sub> at saturation conditions and 0 °C to be 2,47 [kJ/kgK].



---

	15 mm configuration		30 mm configuration		
	Total discharged energy kWh	Total heat extracted %	Total discharged energy kWh	Total heat extracted %	
D1	2,7	37%	D1	5,36	37%
D1.5	3,3	45%	D2	10,66	73%
D2	5,6	77%	D3	11,49	79%
D3	6,6	91%	D4	14,35	99%
D4	7,7	106%	D5	15,20	105%
D5	8,4	115%	D6	15,77	109%
D6	9,5	131%	D7	17,35	119%
D7	9,1	125%			

Table 31: The total system performance including the subcooling effect for RT-9HC

---

## 6 Discussion

### 6.1 Charging Mode

#### 6.1.1 Water

The start of the charging cycle is considered for all calculations when the average PCM temperature equals 0,1 °C. This was done so all cycles can be compared to each other, having the same starting conditions. This method used of taking the average PCM temperature equals to 0,1 °C to calculate the time to freeze is less accurate for the low mass flow rate of 4 kg min<sup>-1</sup> than for the high mass flow rate of 10 kg min<sup>-1</sup>. This is because the temperature sensors are distributed along the entire plate, and with low mass flow rate it will take longer for the average PCM temperature to drop to 0,1 °C compared with the inlet part of the pillow plate heat exchangers. This means that ice could start forming at the inlet part of the CTES unit faster than the outlet part of the CTES unit as the temperature in the inlet section will drop to 0 °C faster.

The effect of inlet temperature and mass flow rate of CO<sub>2</sub> on the charging cycle time was studied. Table 37 and 38 show that the time to freeze decreased with decreased inlet temperature and increased flow rate of CO<sub>2</sub>. Inlet temperature had more significant effect on the time to freeze than the mass flow rate. Furthermore, increasing the mass flow for the same inlet temperature rate does not have a linear relationship with the freezing time. It was observed that supplying refrigerant at 7 kg min<sup>-1</sup> gives sufficient supply, and further increase to 10 kg min<sup>-1</sup> does not affect the charging time significantly. This can be attributed to the reduced period of superheating when having the mass flow rate set at 7 kg min<sup>-1</sup>.

The pressure drop over the CTES unit was studied in order to have a better estimate of the energy consumption of the refrigeration system if the system is to be scaled up. In a complete refrigeration cycle, the system will have a compressor in the vapor compression cycle as shown in Figure 2. Therefore, the compressor will have to compress this extra pressure drop to maintain the steady state conditions of that system. Consequently, this will consume more energy if the condensation temperature is to be kept the same. In Figures 39 and 40 the pressure drop varies between tests in the range of 0,13 bar and 0,6 bar, which are relatively low values. This pressure drop is mainly due to the turbulent flow inside the plate heat exchangers which leads to a better heat exchange between the PCM and the CO<sub>2</sub>. This pressure drop is mainly important in a full system with the compressors as the total energy consumption can increase when the compressor needs to further compress the difference caused by this pressure drop. Furthermore, it was judged more important to achieve a low charging time rather than low pressure drop as the pressure drop is quite small for the pillow plate heat exchanger. The pressure drop is compensated in this system by the pump which pumps the flow up and increases the pressure.

It can be observed that the average PCM temperature approaches 0 °C temperature difference with the inlet CO<sub>2</sub> temperature as time passes during all charging cycles. However, it was observed that this difference in temperature increases and then decreases during some charging cycles such as C10, C7, and C8 in the 15 mm configuration, and C10 in the 30 mm configuration. The trend shown in Figures 41 and 42 of increasing followed by dropping temperature difference is due to the fact that the inlet CO<sub>2</sub> keeps dropping in temperature until it reaches steady state conditions. At the same time, the average PCM temperature takes time to lower down in temperature to match the inlet CO<sub>2</sub> temperature; hence increasing difference followed by dropping temperature difference. The main difference between Figures 41 and 42 is that the distance between the plates is bigger and therefore the PCM takes longer time to approach zero which gives the inlet CO<sub>2</sub> temperature enough time to drop to the steady state condition before the freezing of the PCM starts. Therefore, the difference is seen to increase and then drop in Figure 41 where as it drops immediately in Figure 42. C10 shown on the top of Figure 42 showing a different trend than the rest of the charging cycles is due to its low flow rate of 4,19 kg min<sup>-1</sup> with a low temperature -10,85, which lead to longer time for the inlet CO<sub>2</sub> temperature to reach the steady state conditions and longer time for the average PCM temperature to reach the inlet CO<sub>2</sub> temperature. This results in a slight increase in the temperature difference followed by a decrease in it. The rest of the cycles are showing a trend where the lower the inlet CO<sub>2</sub> temperature is, the higher the difference in

---

temperature between the inlet CO<sub>2</sub> temperature and the average PCM temperature.

Superheating of the CO<sub>2</sub> was observed in the charging cycles with low inlet CO<sub>2</sub> temperature, and low mass flow rates. Superheating of the CO<sub>2</sub> happens when the CO<sub>2</sub> evaporates completely inside the pillow plates before reaching the outlet, and then continues to exchange sensible heat with the water causing it to increase in temperature and making it superheated. Figures 43 and 45 show how the CO<sub>2</sub> was leaving the pillow plates superheated in the beginning of some charging cycles such as C10, C7, and C8 in both of the configurations as they have low mass flow rate and low inlet CO<sub>2</sub> temperature. As time passes, the superheating gets less until the CO<sub>2</sub> enters and leaves at approximately the same temperature. This is due to dropping heat transfer due to less temperature difference when the growth of ice layers start. This happens when the CO<sub>2</sub> enters and leaves at saturated conditions and only latent heat is absorbed. Furthermore, the trend shown in Figure 43 with an increase in temperature difference followed by a decrease it is caused by a dropping inlet CO<sub>2</sub> temperature as it takes time to reach the steady state conditions while simultaneously the outlet CO<sub>2</sub> temperature is super heated causing this increase in temperature difference. When comparing Figures 41 and 42 with Figures 43 and 45, respectively, the cycles which have the highest temperature difference between the CO<sub>2</sub> inlet and outlet follows the same order and trend as the cycles which have temperature difference between the PCM and inlet CO<sub>2</sub> temperature. This is because the higher the temperature difference between the PCM and the CO<sub>2</sub> the higher the driving force for heat exchange is. High driving forces with low mass flow rate and low inlet temperature of the CO<sub>2</sub> lead to superheating the CO<sub>2</sub> and to an increased difference between the inlet and outlet CO<sub>2</sub> temperature as the CO<sub>2</sub> evaporates before reaching the end of the pillow plates.

The charging cycle is considered to be done when the ice growing on all of the plates touches the ice growing on the next upper and below plate. Therefore, the amount of ice formed for all charging cycles is assumed to be the same for the same configuration. This volume that the ice can fill was calculated by calculating the volume between two pillow plates and then multiplying it by 10 being the number of plates in the system. The result is the equivalent to the total volume of solid PCM formed. Calculating the amount of heat stored in the PCM while charging was done throughout calculating the latent heat stored in the theoretical mass of ice that can be formed. This can be less accurate for some charging cycles as depending on the flow rate and inlet CO<sub>2</sub> temperature, it was observed that slightly more or less ice can form in some charging cycles than the others. This can be attributed due to the way the CO<sub>2</sub> flows inside the pillow plate heat exchangers. A low mass flow rate would lead to a poor distribution of the refrigerant flowing inside the pillow plates. This means that the refrigerant will not cover the entire surface of the pillow plate heat exchangers, leading to less ice formation on the corners of the plates. Figure 78 below shows how the CO<sub>2</sub> flows inside the pillow plate. The weld lines shown in black are the parts where the CO<sub>2</sub> can not flow through. The parts highlighted in red are the parts which can be skipped by the CO<sub>2</sub> when running a low flow rate as demonstrated in the blue lines. This poor distribution of the CO<sub>2</sub> shortcut in the path taken through the heat exchanger by the CO<sub>2</sub> can attribute to the measured lower pressure drop throughout the system.

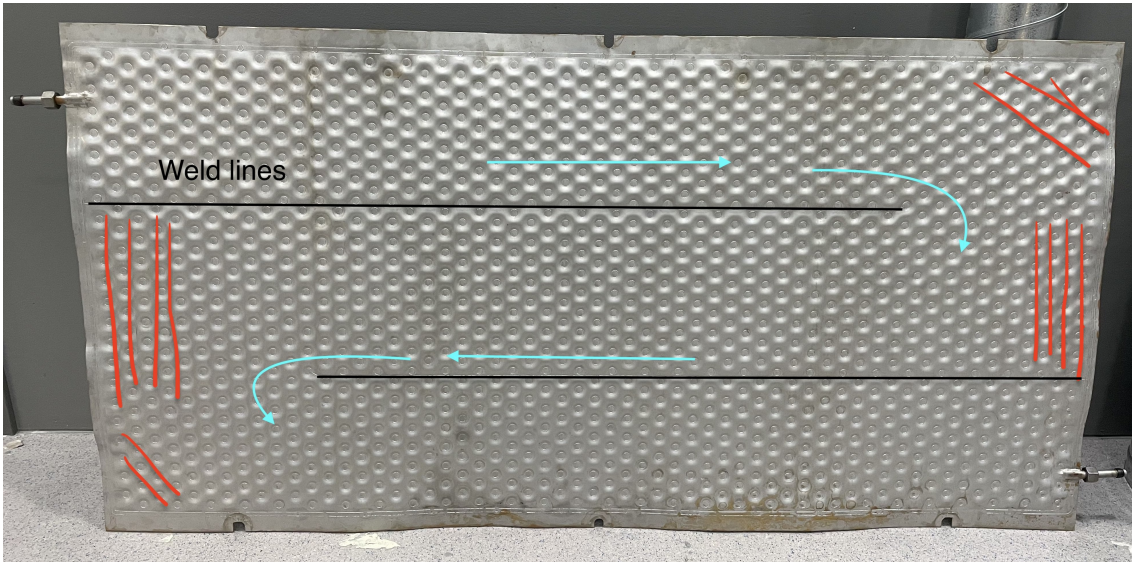


Figure 78: CO<sub>2</sub> path inside the heat exchangers

### 6.1.2 RT-9HC

The inlet conditions were decided based on the findings from the water experiment that the inlet CO<sub>2</sub> temperature had a bigger influence on the charging time than mass flow rate. It was decided to find one optimal flow rate to run the experiment with while varying the inlet CO<sub>2</sub> temperature. The optimal flow rate was chosen by running the experiment with a fixed inlet CO<sub>2</sub> temperature and varying the mass flow rate as shown in tables 12 and 14. It was found that an 8 kg min<sup>-1</sup> mass flow rate charged the unit fastest with the lowest pressure drop compared with the tests that had a similar charging times. Increasing the mass flow rate more had almost no effect on the charging time, and only increased the pressure drop across the system. Increasing the mass flow rate can reduce superheating of the CO<sub>2</sub> going through the plates and increase the turbulent flow which will improve heat transfer up to a certain limit. Afterwards, these effects do not influence heat transfer more, leading to an increased pressure drop without decreasing the charging time. This is shown in Figures 46 and 47.

The effect of the inlet CO<sub>2</sub> temperature on the charging time was shown in Figures 49 and 48. An exponential relationship between the inlet CO<sub>2</sub> temperature and the experiment charging time was observed in both configurations. The lower the inlet CO<sub>2</sub> temperature was, the faster the charging time due to higher driving forces between the PCM and the CO<sub>2</sub>. It is important to notice that when the distance between the plates was shifted from 15 mm to 30 mm, it took more than double the time for the charging to finish given the same inlet CO<sub>2</sub> temperature. For example; at an approximate -20 °C inlet CO<sub>2</sub> temperature, it took 40,5 minutes and 128,8 minutes for charging the PCM to finish for the 15 mm configuration and 30 mm configuration, respectively. Furthermore, the effect of the inlet CO<sub>2</sub> temperature on the pressure drop was shown in Figures 50 and 51. The lower the inlet CO<sub>2</sub> temperature, the higher the pressure drop was following a linear trend in both configurations. This is because the lower the inlet CO<sub>2</sub> temperature is, the higher the driving forces for heat exchange are. This leads to more liquid evaporation inside the plate heat exchangers. Subsequently, a higher gas ratio will lead to faster flow causing the pressure drop to be higher. The values of the pressure drop varied between 0,2 and 0,55 bar which is a low value of pressure drop. This pressure drop was compensated using the pump that increases the system pressure and pump the CO<sub>2</sub> into the plate heat exchangers. The pressure drop is important for a full system with a compressor in a vapor compression cycle to estimate the energy consumption.

The inlet temperature of the CO<sub>2</sub> was found based on the value of the absolute pressure of the inlet CO<sub>2</sub>. This was done due to higher accuracy of the pressure sensor compared with the temperature sensor. Figures 53 and 55 show the results of these findings. Figures 52 and 54 show how the highest the temperature difference between the PCM and the inlet CO<sub>2</sub> was, the faster the charging was

---

done. This is due to higher driving forces to drive the heat exchange between the CO<sub>2</sub> and the PCM. Looking at Figure 55, it is showing how the lower the desired inlet CO<sub>2</sub> temperature was the longer it took it to reach it. This explains why the lower the inlet CO<sub>2</sub> temperature was, the longer it took for the peak to occur in temperature difference between between the inlet CO<sub>2</sub> and the PCM shown in Figure 54.

Superheating was not observed while running the charging modes in the both configurations, which means that the the operation of the charging cycle was run with CO<sub>2</sub> in the two phase region.

Different PCM temperatures were recorded over the different plates locations during the same moment throughout the charging time. This means that the PCM temperature above the top plate dropped faster than the PCM temperature on the bottom plate as shown in Figure 56 and 57. This can be attributed to the maldistribution of the liquid CO<sub>2</sub> into the system. This means more CO<sub>2</sub> flow throughout the top plate compared with the bottom plate. This can be attributed to different reasons such as a higher pressure drop on the top plate which makes more CO<sub>2</sub> flows into it. The higher pressure drop could be due to static height difference between the three plates. The lower the inlet CO<sub>2</sub> temperature, the higher the difference in temperature in the PCM in the three plate locations.

The charging cycle was considered to be finished when when the frozen PCM growing on one plate touches the frozen PCM growing on the neighbouring plate from both sides. Therefore, all the charging cycles are assumed to have the same amount of latent heat capacity.

## 6.2 Discharging Mode

### 6.2.1 Water

The pressure drop during the discharging mode varied between 0,05 bar and 0,34 bar for all cycles with different parameters. In both configurations, cycles with similar flow rates had the same pressure drop across the system with average values of 0,05 bar, 0,15 bar, and 0,26 bar for the 4, 7, 10 kg min<sup>-1</sup> mass flow rate, respectively. In both configurations D12 had an increase of an approximately 0,05 bar in pressure drop compared with the cycles that have the same flow rate. This is due to an increased gas to liquid fraction as more gas can be formed in the evaporator. The higher gas fraction will lead to an increased velocity which can lead to increased turbulent flow leading to higher pressure drop.

The time to complete different discharging cycles was observed to understand how different heat flow rates would affect the discharging time. Tables 24 and 25 show the fastest time for discharging was with D4. This is because in both configurations it was not possible to complete the discharging cycle as it was not possible to extract the latent heat from the system with the given parameters. This is due to the low driving forces between the CO<sub>2</sub> and the ice.

The mean discharge duty for all discharging cycles was calculated to map out different performances with different parameters inputs. Figures 60 and 61 show that the lowest mean discharged duty was for the highest mass flow rate with the lowest inlet CO<sub>2</sub> temperature being D6 discharging cycle. The high mass flow rate with low inlet CO<sub>2</sub> temperature lead to less mean heat transfer than lower mass flow rate with the same inlet CO<sub>2</sub> temperature as the discharging time takes longer. This means that the mean discharged duty was affected by the flow rate and by the inlet temperature of CO<sub>2</sub>.

The heat flow into the system as a function of time was analyzed in order to understand how long the system can operate with high discharge duty. Figures 62 and 63 show that the higher the inlet CO<sub>2</sub> temperature is, the longer the time the discharging cycle maintains a high heat flow. In both figures the average heat flow starts from about 17 kW and decays with time. The 17 kW is limited by the maximum heat input of the two heaters in the glycol system of 18 kW and the efficiency of heat transfer within the glycol circuit itself. The period the heat flow is at its maximum is important because it represents the time the system can provide a high cooling capacity. In addition, both figures show that the system kept the maximum heat flow for approximately the

---

same time in similar running conditions. This is because when the experiment starts the PCM which is ice is touching all the pillow plates from the upper and bottom surface allowing for good thermal contact and low heat transfer resistance. The surface layer of ice melts approximately the same time in both configurations for the same running conditions leading to floating ice into the next upper heat exchanger. The melting ice creates a water layer between the pillow plate surface and the floating ice, which heat needs to be transferred through to reach to the ice. This means that out of the 20 surfaces touching ice the number will drop to 10 surfaces and the rest 10 surfaces will only be in contact with water which has significantly less thermal conductivity than ice as shown in table 9. This will lead to a lower heat transfer efficiency and hence the decay in the heat flow into the CTES unit. The main difference between Figures 62 and 63 is that the decay takes longer in the 30 mm configuration than the 15 mm configuration which is due to having more ice. This means that the system operates with low performance for a longer time in the 30 mm configuration compared with the 15 mm configuration. However, both configurations operate with high heat flow for approximately the same time when comparing similar conditions.

The cumulative discharged energy after each discharging cycle was calculated in order to calculate how much energy was extracted from the system compared with the total energy that is theoretically stored in the system. Figures 64 and 65 show that the higher the inlet CO<sub>2</sub> temperature is, the higher the total cumulative energy discharged is. This is because the main driving forces in heat exchange is temperature difference between the two fluids. Therefore, higher driving forces lead to higher heat exchange rate for longer times. The top three curves in both figures are D10, D11, and D12 which have the highest flow rate followed by D8, D7 and D9 followed by D5, D6 and D4 which have 7 kg min<sup>-1</sup> and 4 kg min<sup>-1</sup> average flow rate, respectively.

Subcooling happens when the outlet temperature of the CO<sub>2</sub> drops below the inlet CO<sub>2</sub> temperature into the CTES unit. This happens when the CO<sub>2</sub> condenses before leaving the pillow plates while still having a higher temperature than the PCM which generates enough driving forces for sensible heat to be exchanged with the ice. This results in further lowering down the CO<sub>2</sub> temperature and hence subcooling the CO<sub>2</sub>. Both figures 66 and 67 show that the CO<sub>2</sub> leaving the CTES unit was always subcooled. Furthermore, figures D8, D11, and D5 had the lowest amount of subcooling with a temperature difference of less than 3 °C. These three discharging cycles were also the best performing cycles in terms of energy extraction when comparing them with their respective flow rates. CO<sub>2</sub> was subcooled the most in discharging cycles D4 and D7 with an approximation of 5 °C in both configurations. The degree of subcooling seems to be more affected with the mass flow rate than the inlet CO<sub>2</sub> temperature, as the figures show that the highest amount of subcooling for the same inlet CO<sub>2</sub> temperature happened for the 4 kg min<sup>-1</sup> mass flow rate, followed by the 10 kg min<sup>-1</sup>, and finally the lowest amount of subcooling was for the 7 kg min<sup>-1</sup> mass flow rate. The system efficiency in terms of heat extraction was better for the 15 mm configuration in a sense that more energy was extracted compared to the theoretical maximum capacity. However, the total energy extraction was more in the 30 mm configuration.

The thermal energy input into the CTES unit was compared with the thermal energy output of the CTES unit to understand the efficiency of different charging cycles. Table 26 shows that in general the amount of energy stored is higher than the amount of energy extracted in most cases. Higher energy percentage is extracted in the 15 mm configuration than the 30 mm configuration when comparing similar running conditions. This can be attributed to better thermal contact for more time during the cycle for the shorter distance. D11 performed best in both cases in terms of the energy extracted with 111% and 82% utilization of heat capacity in the 15 mm, 30 mm configuration respectively. The 111% can be the result of extracting sensible heat of the PCM as the ice can be subcooled and therefore has more stored energy than the latent heat of forming ice. The same applies for all cycles which has more than 100% extraction percentage. The lowest amount of energy extraction was with D4 which has the lowest flow rate and lowest inlet CO<sub>2</sub> temperature. What is further shown is that the group D5, D8, and D11 performed best in both configurations in terms of energy extracted when comparing them with the discharging cycles of the same flow rate and different CO<sub>2</sub> inlet temperature. The very low extraction of energy of 27% in D4 with the 30 mm configuration is due to the fact that the ice didn't melt entirely as the driving forces between the CO<sub>2</sub> and the PCM was not sufficient to extract heat from the ice.

There could be many reasons for the difference in the input and extracted energy from the CTES

---

unit such as un-melted ice which floats through the system. In addition, the refrigerant distribution inside the pillow plate was leaving some corners uncovered as shown in Figure 78. This consequently leads to less ice formation than the theoretically assumed one as this is true for all of the pillow plates. Furthermore, the heat sensors installed on three of the heat exchangers created an obstacle for the ice to float into the upper heat exchanger. This means that the ice could end up floating between the cables connecting the temperature sensors to the electric cabinet without touching any plate heat exchanger. This results in lower heat exchange between the PCM and the CO<sub>2</sub> as the water has lower thermal conductivity than ice. In addition, the top layer of ice float to the surface of the water as soon as the surface in contact with the heat exchanger is melted and therefore that makes an entire block of latent heat lost. Also, the ice is surrounded by water and some of the ice could melt due to heat exchange with the water. This is because some of the water after the charging cycle could be higher than 0 °C and therefore it will exchange heat with the ice and melt it.

### 6.2.2 RT-9HC

Choosing the parameters to run the experiment with followed a procedure where the optimal flow rate was first found by setting the inlet CO<sub>2</sub> temperature to 0 °C and running the experiment with varying mass flow rates. The optimal mass flow rate was chosen based on the cycle that had the highest amount of energy extracted from the system. The mass flow rates which were chosen were 5 kg min<sup>-1</sup> with 99,5 % total heat extracted and 7 kg min<sup>-1</sup> with 84,2 % total heat extracted for the 15 mm configuration and 30 mm configuration, respectively. The experiment was further run using the same mass flow rate for each configuration, while varying the inlet CO<sub>2</sub> temperature as shown in Tables 24 30.

The discharging time was affected by increasing the inlet CO<sub>2</sub> temperature, due to higher driving forces for the heat exchange to happen between the CO<sub>2</sub> and the PCM. The decrease in the discharging time stops after D5 with inlet CO<sub>2</sub> temperature of 1,3 °C for the 15 mm configuration as shown in Figure 68. The discharge time for the 30 mm configuration stops to decrease after D6 where it is fastest 102,33 minutes, followed by D7 where it is approximately the same 104,67 minutes as shown in Figure 69. This can be due to system limitations such as the time it takes to transfer the heat between the refrigerant and the PCM. Meaning that it requires much higher temperature difference to achieve faster charging cycles.

The mean discharged duty was calculated to map out the difference in performance for the different input parameters. Figure 70 shows that each of D5, D6, and D7 have similar mean discharge duty value around 9 kW. Figure 71 shows a linear trend of increasing mean discharged duty with increasing inlet CO<sub>2</sub> temperature. The more clear linear trend in the 30 mm configuration can be attributed to longer experiment time resulting in more data and more accurate average values.

The heat flow into the system over the length of the discharging cycle was calculated to understand how long the system can operate with different capacities. The cycles with higher inlet CO<sub>2</sub> temperature hold the maximum heat capacity which is around 17 kW longer than the cycles having lower inlet CO<sub>2</sub> temperatures. Figure 72 shows that each of D6 and D7 hold the maximum heat capacity for similar time around 25 minutes followed by D5 which holds the maximum heat capacity for around 14 minutes. D5 and D6 had a very similar inlet CO<sub>2</sub> temperatures 1,3 °C and 1,5 °C, respectively. However, D5 was able to hold the maximum heat capacity for slightly more than half of D6, this could mean that there is a threshold between these two temperatures. Figure 73 shows D7 in red holding the maximum heat flow for around 44 minutes, followed by D6 in green holding the maximum heat flow for around 22 minutes. D6 and D7 have approximately 1 °C difference in temperature, however, D7 was able to hold the maximum heat capacity for twice as long, indicating that a threshold can also be present here. This shows how the performance of the system can differ over small changes in inlet CO<sub>2</sub> temperature. The heat flow into the system over the discharging cycle shows how the system can respond given different conditions, for example, the system can provide cooling with high efficiency for longer when the return temperature is similar to conditions such like D7. Furthermore, the lower the temperature difference between the PCM and the refrigerant, the shorter the load peak the refrigeration system can handle.

The cumulative energy discharged during the experiment time was analysed in order to understand the development of the energy extraction over time. Figure 74 and 75 show a trend with an increasing energy discharged that flattens out after a certain part of the experiment. The points where 90% of the cumulative energy discharged was achieved in each of D2 and D5 are marked on the above mentioned figures. For the 15 mm configuration D2 and D5 reached 90% of the cumulative energy after 54% and 51% of the total experiment time. For the 30 mm configuration D2 and D5 reached 90% of the cumulative energy discharged after 63% and 53% of the total experiment time. The mean discharged duty was recalculated for the above mentioned discharging cycles while including the time up until they reached 90% of the total cumulative energy discharged. As a result, the mean discharged duty was significantly increased. Table 32 shows the new calculated mean discharged rate for D2 and D5 in both configurations along with how much it increased compared with the previously calculated one.

Discharging cycle	Mean discharged duty (kW)			
	15 mm configuration	% increase	30 mm configuration	% increase
D2	6,0	168%	4,0	143%
D5	15,1	174%	11,8	169%

Table 32: Mean discharged duty in periods up to 90% of the total discharged energy for the RT-9HC

The above results show that one operating strategy for the system is to run different cycles up until it reaches 90% of the system capacity. This will be more efficient when the system is designed to respond to short and sharp peaks. Furthermore, the temperature difference between the PCM and the refrigerant to be used shouldn't be less than 6 °C as this seems to be the limit for this system to operate properly.

Subcooling was also occurring in this part of the experiment as it was explained in the water section. Figures 76 and 77 show that subcooling occurred in all discharging cycles with values between 3 °C and 6 °C for the 15 mm configuration, and between 2,5 °C and 4 °C for the 30 mm configuration. The cycles with higher inlet CO<sub>2</sub> temperatures such as D7 had the lowest amount of subcooling, while the highest amount of subcooling occurred in the cycles with low inlet CO<sub>2</sub> temperature such as D1. This is due to lower amount of inlet CO<sub>2</sub> gas in the lower inlet CO<sub>2</sub> temperature cycles than higher inlet CO<sub>2</sub> temperature given that they have the same mass flow rate. This will lead to faster condensation of the available gas, and then it will be further subcooled with the available sensible heat. Since the subcooling represents an extra heat unaccounted for, the total energy extracted from the system was recalculated as shown in table 31. The discharging cycles with total heat extracted more than 100% means that the PCM was first melted, and then further warmed up by sensible heat from the refrigerant leading to more than 100% energy extraction. This is because the total energy extracted is only measured against the total amount of latent heat stored in the system. The table shows that D6 was the best performing discharging cycle for the 15 mm configuration in terms of energy extraction with 131 % total heat extracted. D7 was the discharging cycle with highest total heat extracted 119% for the 30 mm configuration. Both these cycles are considered to have high inlet CO<sub>2</sub> temperature.

## 7 Conclusion

The CTES test unit is designed to be used in an industrial application to assist with the refrigeration cycle. The CTES consists of a sealed tank filled with PCM and a stack of 10 pillow plate heat exchangers with possibility to change the distance between the plates. The experiment were run with 15 mm and 30 mm distance between the plates. For each configuration, multiple running modes were run to map out the performance of the system for different parameters. The main two parameters which were changed are the inlet CO<sub>2</sub> temperature and the mass flow rate into the system. The experiment consisted of charging and discharging cycles which dictate solidifying and melting the PCM. The PCMs used were water and RT-9HC with melting temperature of 0 °C and -9,7 °C. The inlet temperature and the mass flow rate of the CO<sub>2</sub> were changed simultaneously



---

in the water experiment, whereas the RT-9HC experiments were run with fixed optimal flow rate and varying inlet CO<sub>2</sub> temperatures. The following findings were observed after performing the experiment:

- The CTES unit filled with water as the PCM had a storage capacity of 12,16 kW and 24,32 kW for the 15 mm and 30 mm configurations, respectively.
- The CTES unit filled with RT-9HC as the PCM had a storage capacity of 7,27kW and 14,54 kW for the 15 mm and 30 mm configurations, respectively.
- Higher mass flow rate in both modes lead to higher pressure drop which could increase the energy consumption of the system. At the same time, higher mass flow rate leads to sufficient refrigerant supply to support an efficient heat transfer process between the PCM and the refrigerant meaning more energy extraction from the system and faster charging cycles. This can outweigh the disadvantage of the small pressure drop.
- Higher difference between the inlet CO<sub>2</sub> temperature and the PCM caused faster charging or discharging cycles as it creates higher driving forces which lead to better heat transfer efficiency in the pillow plates heat exchangers.
- Higher inlet CO<sub>2</sub> temperature in the discharging mode leads to better performance in terms of periods of high heat flow, and the amount of energy extracted from the system.
- the system is sensitive to inlet CO<sub>2</sub> temperature and 1 °C can make a huge difference over the system efficiency and performance.
- A minimum temperature difference of 6 K is needed between the PCM and the refrigerant to generate enough driving forces to be able to extract latent heat.

From the water part it was shown that the charging and discharging cycles take time for the CO<sub>2</sub> to reach the set point temperature, which represents a significant part of the experiment especially in the 15 mm configuration. This is because the ice can be largely melted or formed before the system reaches steady state conditions, which can make it less accurate to compare with the 30 mm configuration results. There is a balance between the mass flow rate and the inlet CO<sub>2</sub> temperature which gives optimal results in both of the charging mode and the discharging mode. Discharging mode has a high importance as it represents how the system will perform when it is needed to release the stored energy. Each of D10, D11, and D12, which have the highest inlet CO<sub>2</sub> steady state temperature of 10 °C and steady state flow rates of 4, 7, and 10 kg min<sup>-1</sup>, respectively, show promising results as operating conditions in the discharging mode in both configurations in terms of the extracted energy and the time of high heat flow into the system.

In both configurations the amount of energy stored was higher than the amount of energy released for most discharging cycles. The 15 mm configuration shows more promising results in terms of the percentage of energy extracted compared to the 30 mm results. However, the 30 mm configuration has a bigger latent heat capacity and can operate with reduced capacity for a longer time. This can be utilized depending on the type of demand the system is expected to respond to, or the application the CTES system will be integrated into. This means that if the refrigeration system has high peak but short refrigeration demands, which can only be satisfied by the periods of high heat flow into the CTES, then the 15 mm configuration can be better suited. However, if the refrigeration system have lower peaks, or long high peaks followed by lower peaks, then the 30 mm configuration can be more useful, as the demand can be fulfilled using the CTES unit for a longer time.

Water and RT-9HC are both showing good potentials when used at the right conditions. Both PCMs can be used within the CTES unit to respond to different applications. Water as PCM can be integrated into a system supplying cooling to fluids between 6 °C and 10 °C. This can be utilized for example in fruits and vegetables cooling, or space cooling. The lower melting temperature of the RT-9HC can make the system be integrated into cooling systems responding to lower cooling requirements between -4 °C and 4 °C. This makes it possible for it to be integrated with refrigeration systems.

---

## 8 Further Work

- The geometric configuration of the system can be further manipulated by installing fins throughout the heat exchangers. This could lead to faster charging results and better performance in the discharging cycles especially with the ones having lower mass flow rates and lower inlet CO<sub>2</sub> temperatures as more surface area of the heat exchangers will be in contact with the ice.
- Adding a third heater to increase the upper limit of the heating input of the current glycol cycle to see the effect on the cumulative energy discharged into the system.
- More experiments need to be done to better understand the points of threshold. This means that more experiments to be done to understand the minimum temperature difference needed for the system to extract the latent heat capacity from the PCM.
- If the system is to be integrated with refrigeration system to provide cooling below -4 °C, a PCM with a lower melting temperature than the RT-9HC needs to be used. This is because a minimum temperature difference of 6 K between the refrigerant and the PCM is needed to provide sufficient driving forces for the latent heat to be extracted from the solid PCM. Therefore, integrating the RT-9HC to provide cooling for applications lower than -4 °C will not be possible as heat will not be extracted from the system.

---

## Bibliography

- [1] Mark MacCracken. Thermal energy storage in sustainable buildings. *ASHRAE Journal*, 46(9):S39, 2004.
- [2] Behzad Rismanchi, Rahman Saidur, G BoroumandJazi, and Shamsuddin Ahmed. Energy, exergy and environmental analysis of cold thermal energy storage (ctes) systems. *Renewable and sustainable energy reviews*, 16(8):5741–5746, 2012.
- [3] Yongjun Sun, Shengwei Wang, Fu Xiao, and Diance Gao. Peak load shifting control using different cold thermal energy storage facilities in commercial buildings: A review. *Energy conversion and management*, 71:101–114, 2013.
- [4] Atul Sharma, A Shukla, CR Chen, and Tsung-Nan Wu. Development of phase change materials (pcms) for low temperature energy storage applications. *Sustainable Energy Technologies and Assessments*, 7:17–21, 2014.
- [5] Mahmood Mastani Joybari, Fariborz Haghighat, Jeff Moffat, and Paul Sra. Heat and cold storage using phase change materials in domestic refrigeration systems: The state-of-the-art review. *Energy and Buildings*, 106:111–124, 2015.
- [6] E Oró, A De Gracia, Albert Castell, Mohammed M Farid, and Luisa F Cabeza. Review on phase change materials (pcms) for cold thermal energy storage applications. *Applied Energy*, 99:513–533, 2012.
- [7] Håkon Selvnes, Yosr Allouche, Raluca Iolanda Manescu, and Armin Hafner. Review on cold thermal energy storage applied to refrigeration systems using phase change materials. *Thermal Science and Engineering Progress*, page 100807, 2020.
- [8] Alberto Cavallini. Properties of co2 as a refrigerant. In *European Seminar-CO2 as a refrigerant: theoretical and design aspects*, 2004.
- [9] Paulus C Tjiang and Sylvia H Sutanto. The efficiency of the carnot cycle with arbitrary gas equations of state. *European journal of physics*, 27(4):719, 2006.
- [10] Animesh Pal, Kutub Uddin, Kyaw Thu, and Bidyut Baran Saha. *Environmental assessment and characteristics of next generation refrigerants*. PhD thesis, Kyushu University, 2018.
- [11] Petter Nekså. Natural gas liquefaction process fundamentals. University Lecture, 2020.
- [12] Arne Fredheim.
- [13] Klaus D Timmerhaus and Thomas M Flynn. *Cryogenic process engineering*. Springer Science & Business Media, 2013.
- [14] James M Calm and David A Didion. Trade-offs in refrigerant selections: past, present, and future. *International Journal of Refrigeration*, 21(4):308–321, 1998.
- [15] Simon Pinnock, Michael D Hurley, Keith P Shine, Timothy J Wallington, and Timothy J Smyth. Radiative forcing of climate by hydrochlorofluorocarbons and hydrofluorocarbons. *Journal of Geophysical Research: Atmospheres*, 100(D11):23227–23238, 1995.
- [16] Trygve M. Eikevik. Heat pumping processes and systems, chapter 4, working fluids. University Lecture, 2000.
- [17] Paride Gullo, Brian Elmegaard, and Giovanni Cortella. Energy and environmental performance assessment of r744 booster supermarket refrigeration systems operating in warm climates. *International Journal of Refrigeration*, 64:61–79, 2016.
- [18] Armin Hafner and Petter Nekså. Integrated co2 solutions for supermarkets. 2018.
- [19] Sergio Giroto, Silvia Minetto, and Petter Nekså. Commercial refrigeration system using co2 as the refrigerant. *International journal of refrigeration*, 27(7):717–723, 2004.

- 
- [20] Armin Hafner. Co2 as a working fluid. University Lecture, 2020.
- [21] Marco Astolfi. Technical options for organic rankine cycle systems. In *Organic Rankine Cycle (ORC) Power Systems*, pages 67–89. Elsevier, 2017.
- [22] Brian T Austin and K Sumathy. Transcritical carbon dioxide heat pump systems: A review. *Renewable and Sustainable Energy Reviews*, 15(8):4013–4029, 2011.
- [23] Yitai Ma, Zhongyan Liu, and Hua Tian. A review of transcritical carbon dioxide heat pump and refrigeration cycles. *Energy*, 55:156–172, 2013.
- [24] Atul Sharma, V Veer Tyagi, CR Chen, and Dharam Buddhi. Review on thermal energy storage with phase change materials and applications. *Renewable and Sustainable energy reviews*, 13(2):318–345, 2009.
- [25] Zainul Abidin and Kaveh Rajab Khalilpour. Single and polystorage technologies for renewable-based hybrid energy systems. In *Polygeneration with Polystorage for Chemical and Energy Hubs*, pages 77–131. Elsevier, 2019.
- [26] Pramod B Salunkhe et al. Investigations on latent heat storage materials for solar water and space heating applications. *Journal of Energy Storage*, 12:243–260, 2017.
- [27] Jan Skovajsa, Martin Koláček, and Martin Zálešák. Phase change material based accumulation panels in combination with renewable energy sources and thermoelectric cooling. *Energies*, 10:152, 01 2017.
- [28] Ibrahim Dincer and Marc Rosen. *Thermal energy storage: systems and applications*. John Wiley & Sons, 2002.
- [29] hakon Selvnes. Termiske kuldager for co2 anlegg:forste maleresultater. Presentation, 2020.
- [30] Lavinia Socaciu, Angela PLEȘA, Paula UNGUREȘAN, and Oana Giurgiu. Review on phase change materials for building applications. *Leonardo Electronic Journal of Practices and Technologies*, 25:179–194, 2014.
- [31] Kinga Pielichowska and Krzysztof Pielichowski. Phase change materials for thermal energy storage. *Progress in materials science*, 65:67–123, 2014.
- [32] Ali Fallahi, Gert Guldentops, Mingjiang Tao, Sergio Granados-Focil, and Steven Van Dessel. Review on solid-solid phase change materials for thermal energy storage: Molecular structure and thermal properties. *Applied Thermal Engineering*, 127:1427–1441, 2017.
- [33] Kavendra A Thakare and AG Bhawe. Review on latent heat storage and problems associated with phase change materials. *International Journal of Research in Engineering and Technology*, 4(10):176–182, 2015.
- [34] Shin Yiing Kee, Yamuna Munusamy, and Kok Seng Ong. Review of solar water heaters incorporating solid-liquid organic phase change materials as thermal storage. *Applied Thermal Engineering*, 131:455–471, 2018.
- [35] G Raam Dheep and A Sreekumar. Influence of nanomaterials on properties of latent heat solar thermal energy storage materials—a review. *Energy Conversion and Management*, 83:133–148, 2014.
- [36] C Veerakumar and A Sreekumar. Phase change material based cold thermal energy storage: Materials, techniques and applications—a review. *international journal of refrigeration*, 67:271–289, 2016.
- [37] Dan Zhou, Chang-Ying Zhao, and Yuan Tian. Review on thermal energy storage with phase change materials (pcms) in building applications. *Applied energy*, 92:593–605, 2012.
- [38] Suhanyaa S Magendran, Fahad Saleem Ahmed Khan, NM Mubarak, Mahesh Vaka, Rashmi Walvekar, Mohammad Khalid, EC Abdullah, Sabzoi Nizamuddin, and Rama Rao Karri. Synthesis of organic phase change materials (pcm) for energy storage applications: A review. *Nano-Structures & Nano-Objects*, 20:100399, 2019.

- 
- [39] Li-Wu Fan, Xin Fang, Xiao Wang, Yi Zeng, Yu-Qi Xiao, Zi-Tao Yu, Xu Xu, Ya-Cai Hu, and Ke-Fa Cen. Effects of various carbon nanofillers on the thermal conductivity and energy storage properties of paraffin-based nanocomposite phase change materials. *Applied Energy*, 110:163–172, 2013.
- [40] Bo He and Fredrik Setterwall. Technical grade paraffin waxes as phase change materials for cool thermal storage and cool storage systems capital cost estimation. *Energy conversion and management*, 43(13):1709–1723, 2002.
- [41] Nihal Sarier and Emel Onder. Organic phase change materials and their textile applications: an overview. *Thermochimica Acta*, 540:7–60, 2012.
- [42] Zhengbin He, Qian Wan, Zhenyu Wang, Jiali Zhang, and Songlin Yi. The numerical simulation and experimental study of heat release in a heat storage system with various diameters of aluminum tubes. *Heliyon*, 5(10):e02651, 2019.
- [43] M Fatih Demirbas. Thermal energy storage and phase change materials: an overview. *Energy Sources, Part B: Economics, Planning, and Policy*, 1(1):85–95, 2006.
- [44] Akio Saito. Recent advances in research on cold thermal energy storage. *International Journal of Refrigeration*, 25(2):177–189, 2002.
- [45] D Feldman, D Banu, D Hawes, and E Ghanbari. Obtaining an energy storing building material by direct incorporation of an organic phase change material in gypsum wallboard. *Solar energy materials*, 22(2-3):231–242, 1991.
- [46] D Feldman, MM Shapiro, D Banu, and CJ Fuks. Fatty acids and their mixtures as phase-change materials for thermal energy storage. *Solar energy materials*, 18(3-4):201–216, 1989.
- [47] S Dutt Sharma and Kazunobu Sagara. Latent heat storage materials and systems: a review. *International Journal of Green Energy*, 2(1):1–56, 2005.
- [48] PA Prabhu, NN Shinde, and PS Patil. Review of phase change materials for thermal energy storage applications. *Int. J. Eng. Res. Appl*, 2:871–875, 2012.
- [49] D Feldman, MM Shapiro, and D Banu. Organic phase change materials for thermal energy storage. *Solar energy materials*, 13(1):1–10, 1986.
- [50] Shamseldin A Mohamed, Fahad A Al-Sulaiman, Nasiru I Ibrahim, Md Hasan Zahir, Amir Al-Ahmed, R Saidur, BS Yılbaş, and AZ Sahin. A review on current status and challenges of inorganic phase change materials for thermal energy storage systems. *Renewable and Sustainable Energy Reviews*, 70:1072–1089, 2017.
- [51] F Bruno, M Belusko, M Liu, and NHS Tay. Using solid-liquid phase change materials (pcms) in thermal energy storage systems. In *Advances in thermal energy storage systems*, pages 201–246. Elsevier, 2015.
- [52] Annabelle Joulin, Zohir Younsi, Laurent Zalewski, Stéphane Lassue, Daniel R Rouse, and Jean-Paul Cavrot. Experimental and numerical investigation of a phase change material: thermal-energy storage and release. *Applied Energy*, 88(7):2454–2462, 2011.
- [53] Ning Xie, Zhaowen Huang, Zigeng Luo, Xuenong Gao, Yutang Fang, and Zhengguo Zhang. Inorganic salt hydrate for thermal energy storage. *Applied Sciences*, 7(12):1317, 2017.
- [54] Tumirah Khadiran, Mohd Zobir Hussein, Zulkarnain Zainal, and Rafeadah Rusli. Advanced energy storage materials for building applications and their thermal performance characterization: A review. *Renewable and Sustainable energy reviews*, 57:916–928, 2016.
- [55] Maria Telkes. Thermal energy storage in salt hydrates. *Solar Energy Materials*, 2(4):381–393, 1980.
- [56] Peng Hu, Da-Jie Lu, Xiang-Yu Fan, Xi Zhou, and Ze-Shao Chen. Phase change performance of sodium acetate trihydrate with aln nanoparticles and cmc. *Solar energy materials and solar cells*, 95(9):2645–2649, 2011.
-

- 
- [57] BML Garay Ramirez, Christ Glorieux, E San Martin Martinez, and JJA Flores Cuautle. Tuning of thermal properties of sodium acetate trihydrate by blending with polymer and silver nanoparticles. *Applied thermal engineering*, 62(2):838–844, 2014.
- [58] Zeinab Kazemi and Sayed Majid Mortazavi. A new method of application of hydrated salts on textiles to achieve thermoregulating properties. *Thermochimica Acta*, 589:56–62, 2014.
- [59] Saito Akio, Utaka Yoshio, Okawa Seiji, Matsuzawa Kazuyuki, and Tamaki Atsushi. Fundamental research on the supercooling phenomenon on heat transfer surfaces—investigation of an effect of characteristics of surface and cooling rate on a freezing temperature of supercooled water. *International Journal of heat and mass transfer*, 33(8):1697–1709, 1990.
- [60] GA Lane, G Warner, P Hartwick, and H Rossow. Macro-encapsulation of pcm. *Report No. oro/5117-8, Dow Chemical Company, Midland, Michigan*, 152, 1978.
- [61] GA Lane and HE Rossow. Encapsulation of heat of fusion storage materials. In *Proceedings of 2nd southeastern conference on application of solar energy*, pages 442–50, 1976.
- [62] Dipak R Biswas. Thermal energy storage using sodium sulfate decahydrate and water. 1975.
- [63] R Naumann and H-H Emons. Results of thermal analysis for investigation of salt hydrates as latent heat-storage materials. *Journal of Thermal Analysis*, 35(3):1009–1031, 1989.
- [64] A Abhat. Low temperature latent heat thermal energy storage: heat storage materials. *Solar energy*, 30(4):313–332, 1983.
- [65] Harald Mehling and Luisa F Cabeza. *Heat and cold storage with PCM*, volume 308. Springer, 2008.
- [66] Vineet Veer Tyagi and DPCM Buddhi. Pcm thermal storage in buildings: a state of art. *Renewable and sustainable energy reviews*, 11(6):1146–1166, 2007.
- [67] Johannes P Kotzé, Theodor W Von Backström, and Paul J Erens. High temperature thermal energy storage utilizing metallic phase change materials and metallic heat transfer fluids. *Journal of solar energy engineering*, 135(3), 2013.
- [68] David Gonzalez-Nino, Lauren M Boteler, Dimeji Ibitayo, Nicholas R Jankowski, Damian Urciuoli, Iain M Kierzewski, and Pedro O Quintero. Experimental evaluation of metallic phase change materials for thermal transient mitigation. *International Journal of Heat and Mass Transfer*, 116:512–519, 2018.
- [69] Ming Liu, Wasim Saman, and Frank Bruno. Review on storage materials and thermal performance enhancement techniques for high temperature phase change thermal storage systems. *Renewable and Sustainable Energy Reviews*, 16(4):2118–2132, 2012.
- [70] Haoshan Ge, Haiyan Li, Shengfu Mei, and Jing Liu. Low melting point liquid metal as a new class of phase change material: An emerging frontier in energy area. *Renewable and Sustainable Energy Reviews*, 21:331–346, 2013.
- [71] Belen Zalba, Jose Ma Marin, Luisa F Cabeza, and Harald Mehling. Review on thermal energy storage with phase change: materials, heat transfer analysis and applications. *Applied thermal engineering*, 23(3):251–283, 2003.
- [72] P Kauranen, K Peippo, and PD Lund. An organic pcm storage system with adjustable melting temperature. *Solar Energy*, 46(5):275–278, 1991.
- [73] Luisa F Cabeza, Albert Castell, C de Barreneche, A De Gracia, and AI Fernández. Materials used as pcm in thermal energy storage in buildings: A review. *Renewable and Sustainable Energy Reviews*, 15(3):1675–1695, 2011.
- [74] Murat M Kenisarin. High-temperature phase change materials for thermal energy storage. *Renewable and sustainable energy reviews*, 14(3):955–970, 2010.
-

- 
- [75] He Bo, E Mari Gustafsson, and Fredrik Setterwall. Tetradecane and hexadecane binary mixtures as phase change materials (pcms) for cool storage in district cooling systems. *Energy*, 24(12):1015–1028, 1999.
- [76] Jing-Hua Li, Gui-en Zhang, and Jin-Yun Wang. Investigation of a eutectic mixture of sodium acetate trihydrate and urea as latent heat storage. *Solar Energy*, 47(6):443–445, 1991.
- [77] XQ Zhai, XL Wang, T Wang, and RZ Wang. A review on phase change cold storage in air-conditioning system: Materials and applications. *Renewable and Sustainable Energy Reviews*, 22:108–120, 2013.
- [78] Chen Zeshao, Ge Xinshi, and Gu Yuqing. Measurement of thermophysical properties, 1991.
- [79] Zhang Yinping and Jiang Yi. A simple method, the-history method, of determining the heat of fusion, specific heat and thermal conductivity of phase-change materials. *Measurement Science and Technology*, 10(3):201, 1999.
- [80] LC Chow, JK Zhong, and JE Beam. Thermal conductivity enhancement for phase change storage media. *International Communications in Heat and Mass Transfer*, 23(1):91–100, 1996.
- [81] Mohammed M Farid, Amar M Khudhair, Siddique Ali K Razack, and Said Al-Hallaj. A review on phase change energy storage: materials and applications. *Energy conversion and management*, 45(9-10):1597–1615, 2004.
- [82] Atyah Najjar and Afif Hasan. Modeling of greenhouse with pcm energy storage. *Energy Conversion and Management*, 49(11):3338–3342, 2008.
- [83] SM Hasnain. Review on sustainable thermal energy storage technologies, part i: heat storage materials and techniques. *Energy conversion and management*, 39(11):1127–1138, 1998.
- [84] IM Bugaje. Enhancing the thermal response of latent heat storage systems. *International journal of energy research*, 21(9):759–766, 1997.
- [85] Yaxue Lin, Yuting Jia, Guruprasad Alva, and Guiyin Fang. Review on thermal conductivity enhancement, thermal properties and applications of phase change materials in thermal energy storage. *Renewable and sustainable energy reviews*, 82:2730–2742, 2018.
- [86] Huanzhi Zhang, Xiaodong Wang, and Dezhen Wu. Silica encapsulation of n-octadecane via sol-gel process: a novel microencapsulated phase-change material with enhanced thermal conductivity and performance. *Journal of colloid and interface science*, 343(1):246–255, 2010.
- [87] MA Kibria, MR Anisur, MH Mahfuz, Rahman Saidur, and IHSC Metselaar. A review on thermophysical properties of nanoparticle dispersed phase change materials. *Energy Conversion and Management*, 95:69–89, 2015.
- [88] JM Khodadadi, Liwu Fan, and Hasan Babaei. Thermal conductivity enhancement of nanostructure-based colloidal suspensions utilized as phase change materials for thermal energy storage: a review. *Renewable and Sustainable Energy Reviews*, 24:418–444, 2013.
- [89] MNA Hawlader, MS Uddin, and Mya Mya Khin. Microencapsulated pcm thermal-energy storage system. *Applied energy*, 74(1-2):195–202, 2003.
- [90] Pramod B Salunkhe and Prashant S Shembekar. A review on effect of phase change material encapsulation on the thermal performance of a system. *Renewable and sustainable energy reviews*, 16(8):5603–5616, 2012.
- [91] Yanio E Milian, Andrea Gutierrez, Mario Grageda, and Svetlana Ushak. A review on encapsulation techniques for inorganic phase change materials and the influence on their thermophysical properties. *Renewable and Sustainable Energy Reviews*, 73:983–999, 2017.
- [92] Hee W Ryu, Sung W Woo, Byung C Shin, and Sang D Kim. Prevention of supercooling and stabilization of inorganic salt hydrates as latent heat storage materials. *Solar energy materials and solar cells*, 27(2):161–172, 1992.
-

- 
- [93] Luisa F Cabeza, Gustav Svensson, Stefan Hiebler, and Harald Mehling. Thermal performance of sodium acetate trihydrate thickened with different materials as phase change energy storage material. *Applied Thermal Engineering*, 23(13):1697–1704, 2003.
- [94] Gang Li, Binbin Zhang, Xiang Li, Yuan Zhou, Qingguo Sun, and Qiang Yun. The preparation, characterization and modification of a new phase change material:  $\text{CaCl}_2 \cdot 6\text{H}_2\text{O}-\text{MgCl}_2 \cdot 6\text{H}_2\text{O}$  eutectic hydrate salt. *Solar energy materials and solar cells*, 126:51–55, 2014.
- [95] Anastasia Efimova, Sebastian Pinnau, Matthias Mischke, Cornelia Breittkopf, Michael Ruck, and Peer Schmidt. Development of salt hydrate eutectics as latent heat storage for air conditioning and cooling. *Thermochimica Acta*, 575:276–278, 2014.
- [96] Binjian Nie, Anabel Palacios, Boyang Zou, Jiaxu Liu, Tongtong Zhang, and Yunren Li. Review on phase change materials for cold thermal energy storage applications. *Renewable and Sustainable Energy Reviews*, 134:110340, 2020.
- [97] N Beupere, U Soupremanien, and L Zalewski. Nucleation triggering methods in supercooled phase change materials (pcm), a review. *Thermochimica Acta*, 670:184–201, 2018.
- [98] Omid Ghahramani Zarajabad and Rouhollah Ahmadi. Numerical investigation of different pcm volume on cold thermal energy storage system. *Journal of Energy Storage*, 17:515–524, 2018.
- [99] Hussein Akeiber, Payam Nejat, Muhd Zaimi Abd Majid, Mazlan A Wahid, Fatemeh Jomehzadeh, Iman Zeynali Famileh, John Kaiser Calautit, Ben Richard Hughes, and Sheikh Ahmad Zaki. A review on phase change material (pcm) for sustainable passive cooling in building envelopes. *Renewable and Sustainable Energy Reviews*, 60:1470–1497, 2016.
- [100] AC Marques, GF Davies, GG Maidment, JA Evans, and ID Wood. Novel design and performance enhancement of domestic refrigerators with thermal storage. *Applied Thermal Engineering*, 63(2):511–519, 2014.
- [101] Binjian Nie, Xiaohui She, Zheng Du, Chunping Xie, Yongliang Li, Zhubing He, and Yulong Ding. System performance and economic assessment of a thermal energy storage based air-conditioning unit for transport applications. *Applied Energy*, 251:113254, 2019.
- [102] Rob Farrington and John Rugh. Impact of vehicle air-conditioning on fuel economy, tailpipe emissions, and electric vehicle range. Technical report, National Renewable Energy Lab., Golden, CO (US), 2000.
- [103] Gabriele Comodi, Francesco Carducci, Balamurugan Nagarajan, and Alessandro Romagnoli. Application of cold thermal energy storage (ctes) for building demand management in hot climates. *Applied thermal engineering*, 103:1186–1195, 2016.
- [104] Motoi Yamaha and Shinya Misaki. The evaluation of peak shaving by a thermal storage system using phase-change materials in air distribution systems. *Hvac&R Research*, 12(S3):861–869, 2006.
- [105] Xiaoqin Sun, Quan Zhang, Mario A Medina, Yingjun Liu, and Shuguang Liao. A study on the use of phase change materials (pcms) in combination with a natural cold source for space cooling in telecommunications base stations (tbss) in china. *Applied Energy*, 117:95–103, 2014.
- [106] Dongliang Zhao and Gang Tan. Experimental evaluation of a prototype thermoelectric system integrated with pcm (phase change material) for space cooling. *Energy*, 68:658–666, 2014.
- [107] Ahmed Aljehani, Siddique Ali K Razack, Ludwig Nitsche, and Said Al-Hallaj. Design and optimization of a hybrid air conditioning system with thermal energy storage using phase change composite. *Energy Conversion and Management*, 169:404–418, 2018.
- [108] Sašo Medved and Ciril Arkar. Correlation between the local climate and the free-cooling potential of latent heat storage. *Energy and Buildings*, 40(4):429–437, 2008.
-



- 
- [109] C Arkar and S Medved. Free cooling of a building using pcm heat storage integrated into the ventilation system. *Solar energy*, 81(9):1078–1087, 2007.
- [110] Alvaro De Gracia, Lidia Navarro, Albert Castell, Álvaro Ruiz-Pardo, Servando Álvarez, and Luisa F Cabeza. Thermal analysis of a ventilated facade with pcm for cooling applications. *Energy and buildings*, 65:508–515, 2013.
- [111] Reza Barzin, John JJ Chen, Brent R Young, and Mohammed M Farid. Application of pcm energy storage in combination with night ventilation for space cooling. *Applied Energy*, 158:412–421, 2015.
- [112] Ming Liu, Wasim Saman, and Frank Bruno. Development of a novel refrigeration system for refrigerated trucks incorporating phase change material. *Applied Energy*, 92:336–342, 2012.
- [113] K Azzouz, Denis Leducq, and D Gobin. Performance enhancement of a household refrigerator by addition of latent heat storage. *International Journal of Refrigeration*, 31(5):892–901, 2008.
- [114] G Alevay Kilic, Enver Yalcin, and Ahmet Alper Aydm. Experimental analysis of a cold store integrated with phase change material: a case study. *Bulgarian Chemical Communications*, 48:195–198, 2016.
- [115] R Elarem, S Mellouli, E Abhilash, and A Jemni. Performance analysis of a household refrigerator integrating a pcm heat exchanger. *Applied Thermal Engineering*, 125:1320–1333, 2017.
- [116] David Smith and Leigh Sparks. Temperature controlled supply chains. *Food supply chain management*, 1(1):179–198, 2004.
- [117] Mashud Ahmed, Oliver Meade, and Mario A Medina. Reducing heat transfer across the insulated walls of refrigerated truck trailers by the application of phase change materials. *Energy Conversion and Management*, 51(3):383–392, 2010.
- [118] Benedetta Copertaro, Paolo Principi, and Roberto Fioretti. Thermal performance analysis of pcm in refrigerated container envelopes in the italian context—numerical modeling and validation. *Applied thermal engineering*, 102:873–881, 2016.
- [119] Our job: temperature control. <http://www.sofrigam.com>. Accessed: 2020-12-14.
- [120] Phase change material pcm manufacturers for air conditioning, electronics cooling. <http://www.teappcm.com>. Accessed: 2020-12-14.
- [121] Jisoo Jeon, Jung-Hun Lee, Jungki Seo, Su-Gwang Jeong, and Sumin Kim. Application of pcm thermal energy storage system to reduce building energy consumption. *Journal of thermal analysis and calorimetry*, 111(1):279–288, 2013.
- [122] Ruben Baetens, Bjørn Petter Jelle, and Arild Gustavsen. Phase change materials for building applications: A state-of-the-art review. *Energy and buildings*, 42(9):1361–1368, 2010.
- [123] Michal Pomianowski, Per Heiselberg, and Yinping Zhang. Review of thermal energy storage technologies based on pcm application in buildings. *Energy and Buildings*, 67:56–69, 2013.
- [124] Conrad Voelker, Oliver Kornadt, and Milan Ostry. Temperature reduction due to the application of phase change materials. *Energy and Buildings*, 40(5):937–944, 2008.
- [125] Frédéric Kuznik and Joseph Virgone. Experimental assessment of a phase change material for wall building use. *Applied energy*, 86(10):2038–2046, 2009.
- [126] Albert Castell, Ingrid Martorell, M Medrano, G Pérez, and Luisa F Cabeza. Experimental study of using pcm in brick constructive solutions for passive cooling. *Energy and Buildings*, 42(4):534–540, 2010.
- [127] Gang Li, Yunho Hwang, Reinhard Radermacher, and Ho-Hwan Chun. Review of cold storage materials for subzero applications. *Energy*, 51:1–17, 2013.
-

- 
- [128] Yehu Lu, Fanru Wei, Dandan Lai, Wen Shi, Faming Wang, Chuansi Gao, and Guowen Song. A novel personal cooling system (pcs) incorporated with phase change materials (pcms) and ventilation fans: an investigation on its cooling efficiency. *Journal of thermal biology*, 52:137–146, 2015.
- [129] Anja Royne, Christopher J Dey, and David R Mills. Cooling of photovoltaic cells under concentrated illumination: a critical review. *Solar energy materials and solar cells*, 86(4):451–483, 2005.
- [130] SA Nada, DH El-Nagar, and HMS Hussein. Improving the thermal regulation and efficiency enhancement of pcm-integrated pv modules using nano particles. *Energy conversion and management*, 166:735–743, 2018.
- [131] Shankar Krishnan, Suresh V Garimella, and Sukhvinder S Kang. A novel hybrid heat sink using phase change materials for transient thermal management of electronics. *IEEE Transactions on Components and Packaging Technologies*, 28(2):281–289, 2005.
- [132] M Piper, A Olenberg, JM Tran, and EY Kenig. Determination of the geometric design parameters of pillow-plate heat exchangers. *Applied Thermal Engineering*, 91:1168–1175, 2015.
- [133] Julian M Tran, Mark Piper, Eugeny Y Kenig, and Stephan Scholl. Pillow-plate heat exchangers: Fundamental characteristics. In *Innovative Heat Exchangers*, pages 233–245. Springer, 2018.
- [134] M Piper, A Zibart, E Djakow, R Springer, W Homberg, and EY Kenig. Heat transfer enhancement in pillow-plate heat exchangers with dimpled surfaces: A numerical study. *Applied Thermal Engineering*, 153:142–146, 2019.
- [135] Hans-Jörg Bart and Stephan Scholl. *Innovative heat exchangers*. Springer, 2017.
- [136] Ice - thermal properties. <https://www.engineeringtoolbox.com/ice-thermal-properties-d576.html>.
- [137] Rubitherm Technologies GmbH. Pcm rt-line.
- [138] Rubitherm Technologies GmbH. Pcm rt-line.

---

## 9 Appendices

### 9.1 Draft of a Conference Paper

# Experimental Investigation of a Cold Thermal Energy Storage System for Industrial Application

Saleh SAKKA AMINI<sup>1\*</sup>,

<sup>1</sup> Norwegian University of Science and Technology (NTNU), Department of Energy and Process Engineering,  
Trondheim, NO-7034, Norway  
Contact Information (+47-40594892, Salehs@stud.ntnu.no)

## ABSTRACT

This report presents the results of experimental investigations about the performance of a CTES system that is designed to be integrated in an industrial NH<sub>3</sub>/CO<sub>2</sub> cascade refrigeration system for peak shaving purposes. The CTES consists of a sealed tank filled with PCM and a stack of 10 pillow plate heat exchangers with possibility to change the distance between the plates. The refrigerant used in this experiment was CO<sub>2</sub>. The experiment consisted of charging and discharging cycles which dictate solidifying and melting the PCM. During these cycles, each of the inlet CO<sub>2</sub> temperature and flow rate into the plate heat exchangers were varied in order to map out the system performance for two different configurations being 15 mm and 30 mm distance between the plate heat exchangers. The PCMs used were water and RT-9HC having 0 °C melting temperature and -9,7 °C, respectively. The CTES unit filled with water as the PCM had a storage capacity of 12,16 kW and 24,32 kW for the 15 mm and 30 mm configurations, respectively. The CTES unit filled with RT-9HC as the PCM had a storage capacity of 7,27 kW and 14,54 kW for the 15 mm and 30 mm configurations, respectively. Both PCMs proved to be efficient under the right conditions of the refrigerant flow rate and its inlet temperature and can be used for peak shaving purposes. Water can be used as the PCM when the system is to be integrated to provide cooling between 6 ° and 10 °C. The RT-9HC as a PCM can be integrated with refrigeration system to provide cooling between -4 °C and 4 °C.

## 1. INTRODUCTION

The increase in greenhouse gas emissions resulting from growing energy consumption rates is pushing industry to integrate more energy friendly and efficient solutions (4). Thermal energy consumption is high among different types of industries, and the energy demand for different processes fluctuates throughout the day and throughout the year (5). This can lead to energy waste and the need for bigger equipment to cover the range of this fluctuation (7). Integrating thermal energy storage with these systems is a key factor that can level the difference between the supply and demand of energy. Refrigeration is an energy demanding process with a significant difference in peak and normal time demands. Therefore integrating cold thermal energy storage in refrigeration systems can improve the performance and reliability of the refrigeration systems allowing it to meet peak time demands without increasing the load on the chillers. Cold thermal energy storage uses phase change materials to store the energy during off-peak time and uses this energy later during peak demands leading to saving energy and reducing costs (6). A cold thermal energy storage unit which uses phase change material as a storage medium for thermal energy is being investigated in this work. The unit is to be integrated in a NH<sub>3</sub>/CO<sub>2</sub> cascade refrigerant system for food processing plant. The refrigerant used in this setup is CO<sub>2</sub> due to its potentials in refrigeration cycles, being environmentally friendly, and safe refrigerant (2). The experiment consists of charging cycle where the latent heat is stored by solidifying the PCM, and discharging cycle where the latent heat is extracted out by melting the PCM. Two different PCMs were experimented with which are water and RT-9HC. The charging and discharging cycles were run multiple times with different parameters to try to figure out how changing these parameters affect the system, and to map the running parameters that lead to optimal performance. These parameters are the flow rate of the refrigerant, the temperature of the refrigerant, and the system geometrical configuration. This report shows how the system performed when changing the previously mentioned parameters among the explanation of the different results. This report first presents a literature review of refrigeration, thermal energy storage, and phase change materials. Second, this report provides a description for the experimental setup followed by the methods and procedures followed in this work. Third, the results of this work are shown followed by a discussion and a conclusion explaining the findings of this work. Finally some suggestions for future work are presented.

## 2. EXPERIMENT DESIGN

The following experimental set up is a prototype of a CTES system that is planned to be used on an industrial scale. The system consists of the CTES unit which is an insulated welded box of stainless steel filled with liquid PCM. First, water was used as the phase change material in order to study the general performance of the system, then it was replaced with RT-9HC which is an organic PCM. The latent heat is stored by freezing the PCM and released by melting it depending on whether the system is charging or discharging. Figure 1 below shows the path the  $CO_2$  follows during charging and discharging modes. During the charging mode, the valves V4, and V6 are closed while V7 and V5 are kept open. During the discharging mode, the valves V5 and V7 are kept closed while V4 and V6 are kept open. The closing and opening of the valves is done manually before starting charging or discharging of the CTES unit.

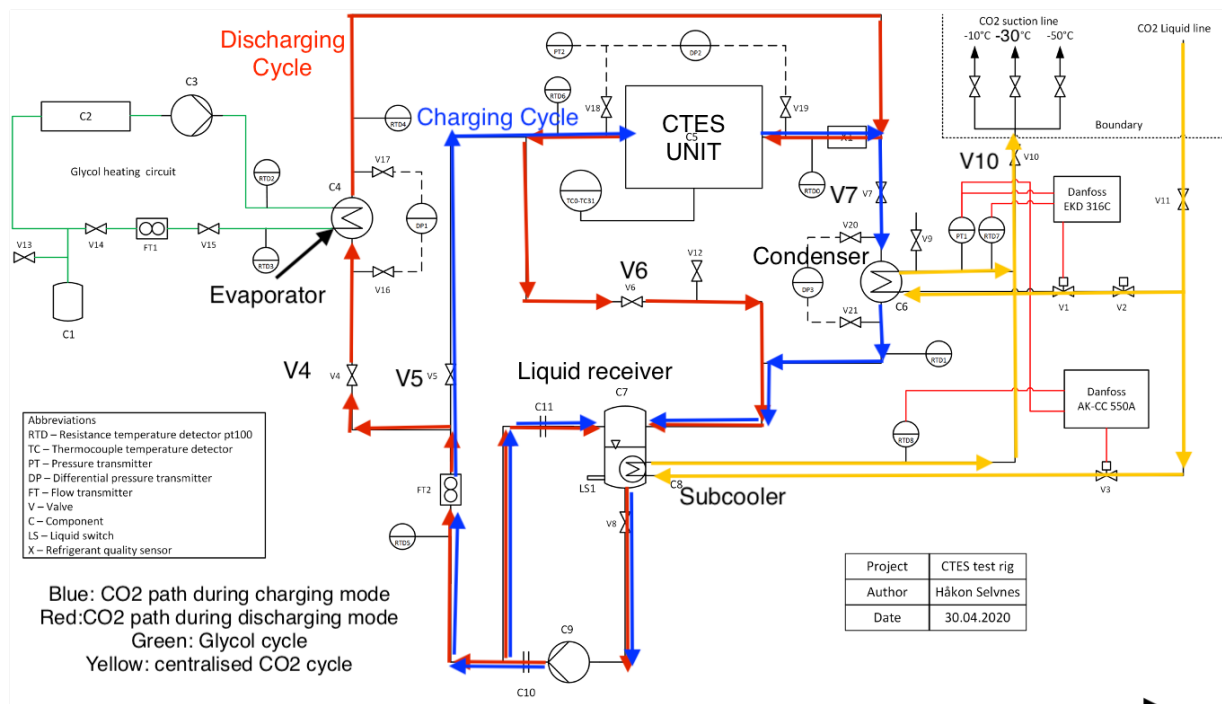


**Figure 1: Diagram of the experimental setup**

The CTES unit is connected to the main  $CO_2$  circuit, which is pump-circulated. Furthermore, the system has an evaporator which is connected to a glycol circuit acting as the heat source. The set up is also connected to a condenser which is connected to a separate centralized  $CO_2$  refrigeration cycle acting as the the heat sink to the CTES system. The set up is also connected to a liquid receiver to store the refrigerant circulating in the CTES system being also  $CO_2$ . The liquid receiver is cooled by the centralized  $CO_2$  system to keep the refrigerant temperature and pressure low all the time. In addition, the system is connected to a pump which controls the flow rate of the  $CO_2$  inside the CTES system by changing its frequency between 35 Hz and 50 Hz. The pump pumps the flow towards the CTES unit or the evaporator depending on the valves arrangement that are set based on the system operating mode. The exchange of heat between the the PCM in the CTES unit and the rest of the system happens through a set of ten pillow plates heat exchangers that are immersed in the PCM and distributed vertically above each other with equal distance between the plates. The plates are connected together using a manifold at the inlet and the outlet. This causes the refrigerant to flow into the manifold and then gets distributed throughout all the ten pillow plates heat exchangers. These plates connect the CTES unit with the rest of the equipment in the system such as the evaporator and the condenser. The system contains temperature, pressure, flow, and phase sensors that are distributed along the system to allow for the control and analyse of the system. Figures 2 below shows the CTES prototype.

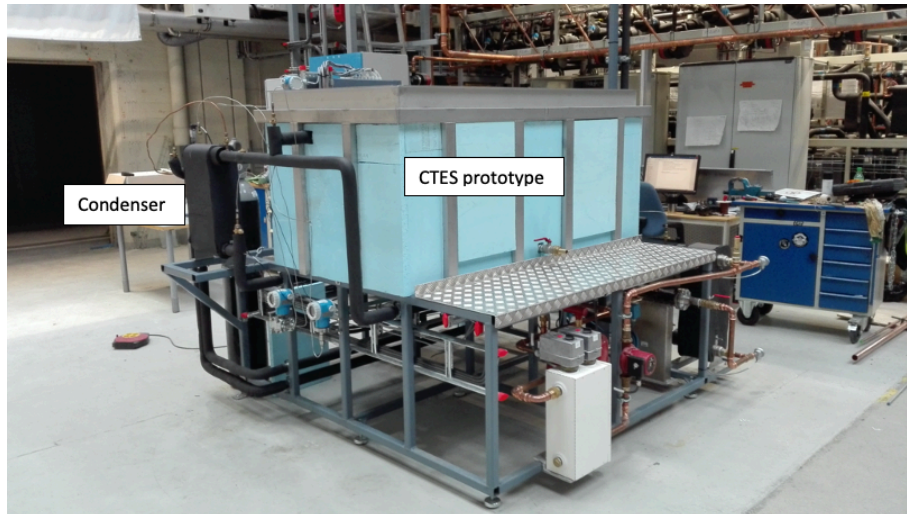


**Figure 2: CTES system with the condenser.**

The system is designed to work in two modes which are charging and discharging. During charging mode, the latent heat is stored by freezing the PCM inside the CTES. This entails that the CO<sub>2</sub> will flow inside the plate heat exchangers as a liquid and flow out mainly as a gas. This mode utilises the pillow plate heat exchangers as evaporators for the internal CO<sub>2</sub> system. After the CO<sub>2</sub> has evaporated, it leaves the pillow plate heat exchangers and goes into the condenser where it condenses back to liquid. The condensed CO<sub>2</sub> flows into the liquid receiver, which then goes out of the liquid receiver to the pump located one floor below the test unit. The pump pumps the cold CO<sub>2</sub> up towards the test unit and the cycle starts again. The heat flows from the PCM into the CO<sub>2</sub> during this mode.

During discharging mode the inlet and outlet of the pillow plate heat exchangers are switched, and the PCM is melted to extract the stored latent heat from it. This entails that the CO<sub>2</sub> will flow inside the pillow plate exchangers as a gas and flow out as a liquid. This mode utilises the pillow plate heat exchangers as a condenser for the internal CO<sub>2</sub> system. After the CO<sub>2</sub> has exchanged heat with the solid PCM and has condensed, it flows out of the pillow plate heat exchangers and it goes into the liquid receiver. The CO<sub>2</sub> flows out of the liquid receiver and goes down into the pump where it is pumped up to go inside the evaporator as a liquid. In the evaporator, the liquid CO<sub>2</sub> exchanges heat with the glycol circuit leaving it in gas phase at approximately the same temperature as the inlet temperature. The CO<sub>2</sub> then flows inside the pillow plate heat exchangers as a heat resource to extract the heat from the solid PCM. The cycle continues and it repeats itself again. The heat flows from the centralised CO<sub>2</sub> into the PCM during this mode.

The experiment used two different PCMs which are water and the organic RT-9HC. First water was used, and then it was replaced with RT-9HC. Tables 1 and 2 show the properties of these two PCMs.

Property	water	Ice
Density at 0°C [g/cm <sup>3</sup> ]	1	0,916
Thermal conductivity [W/m.K]	0,56	2,22
specific heat [kJ/kg.K]	4.217	2,050
Specific latent heat of fusion [kJ/kg]	334	334

**Table 1: Properties of water and ice**  
(too)

Property	solid	liquid
Density at -15°C [kg/l]	0,88	0,77
Thermal conductivity [W/m.K]	0,2	0,2
specific heat [kJ/kg.K]	2	2
Specific latent heat of fusion [kJ/kg]	208	208
phase change temperature °C	-9,7	-9,7

**Table 2: Properties of RT-9HC solid and liquid phases**  
(GmbH)

### 3. RESULTS AND DISCUSSION

#### 3.1 Charging cycle

The effect of inlet temperature and mass flow rate of CO<sub>2</sub> on the charging cycle time was studied. The time to freeze decreased with decreased inlet temperature and increased flow rate of CO<sub>2</sub>. Inlet temperature had more significant effect on the time to freeze than the mass flow rate. Furthermore, increasing the mass flow for the same inlet temperature rate does not have a linear relationship with the freezing time. It was observed that supplying refrigerant at 7 kg min<sup>-1</sup> gives sufficient supply, and further increase to 10 kg min<sup>-1</sup> does not affect the charging time significantly. This can be attributed to the reduced period of superheating when having the mass flow rate set at 7 kg min<sup>-1</sup>. The charging cycles were performed according to a chosen parameters of inlet temperature and mass flow rate of CO<sub>2</sub>. Figures 3a and 3b show the time to finish the charging cycles for the 15 mm configuration and the 30 mm configuration, respectively. The time to freeze is shown from the moment the average PCM temperature in the CTES unit equals 0,1 °C. Both figures show the same trend which is shorter charging times with lower inlet CO<sub>2</sub> temperatures. Furthermore, both figures are showing that mass flow rate has less effect on charging time, and it is the inlet CO<sub>2</sub> temperature that influences the charging time the most. Figure 3a shows that the fastest charging cycle being 27,6 minutes was recorded for C11 with an average inlet CO<sub>2</sub> temperature of -11,38°C. Figure 3b below shows that the fastest charging cycle being 28,5 minutes was recorded for C8 with an average inlet temperature of -8,71 °C.

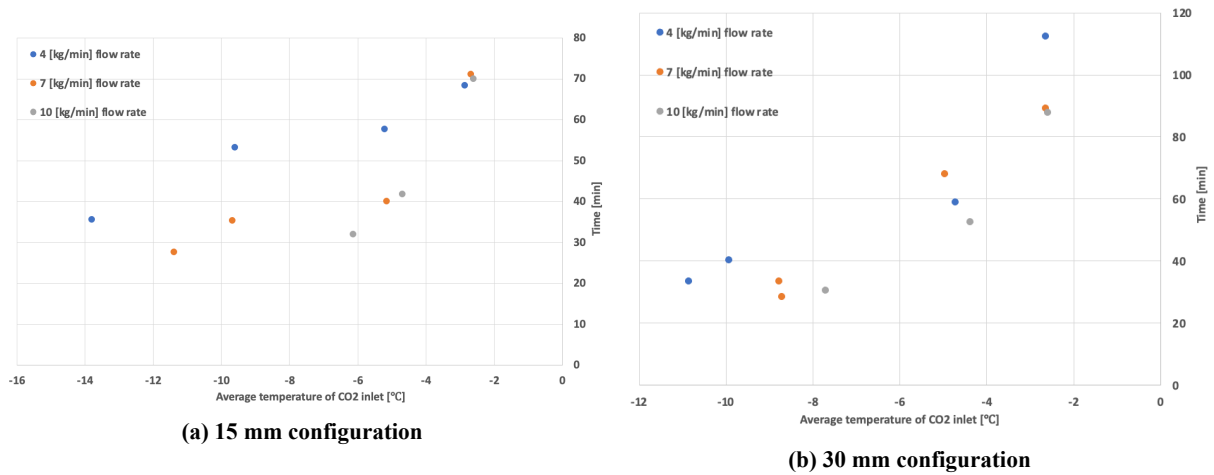


**Figure 3: Time to complete the charging process for different inlet CO<sub>2</sub> temperatures with respect to their flow rate**

#### RT-9HC

The experiments using the RT-9HC were run following a fixed inlet flow rate and varied inlet CO<sub>2</sub> temperatures. The effect of the inlet CO<sub>2</sub> temperature on the charging time is shown in Figures 4b and 4a. An exponential relationship between the inlet CO<sub>2</sub> temperature and the experiment charging time was observed in both configurations. The lower

the inlet CO<sub>2</sub> temperature was, the faster the charging time due to higher driving forces between the PCM and the CO<sub>2</sub>. It is important to notice that when the distance between the plates was shifted from 15 mm to 30 mm, it took more than double the time for the charging to finish given the same inlet CO<sub>2</sub> temperature. For example; at an approximate -20°C inlet CO<sub>2</sub> temperature, it took 40,5 minutes and 128,8 minutes for charging the PCM to finish for the 15 mm configuration and 30 mm configuration, respectively. Figures 4a and 4b below show the charging time for the different average inlet CO<sub>2</sub> temperature for the 15 mm and 30 mm configurations, respectively. Both figures show an exponential decrease of the charging time with a dropping inlet CO<sub>2</sub> temperature. Figure 4a shows the shortest charging time to be 35,8 min with an average inlet CO<sub>2</sub> temperature of -21,76 °C. Figure 4b shows the shortest charging time to be 97,2 min with an average inlet CO<sub>2</sub> temperature of -22,76 °C.

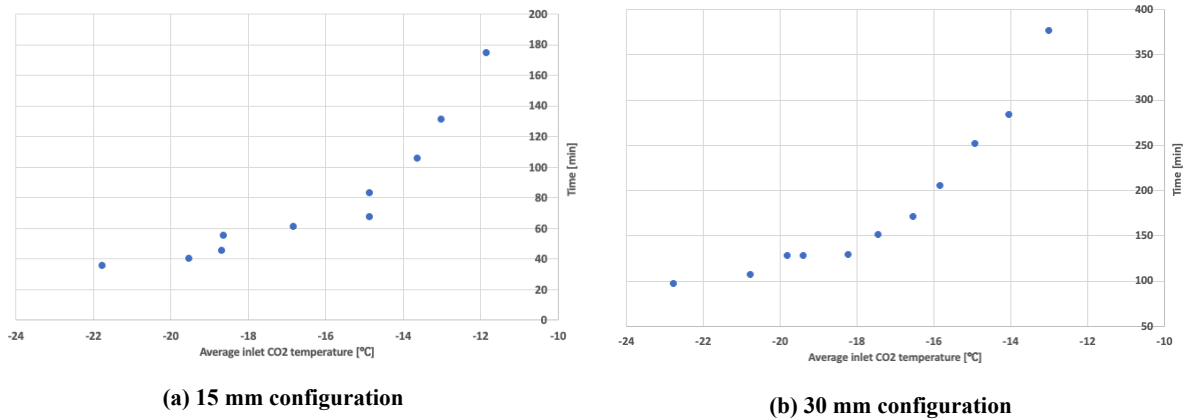


Figure 4: Charging time vs inlet CO<sub>2</sub> temperature for the 15 mm and 30 mm configurations

### 3.2 Discharging cycle

#### Water

The discharging mode was run after the charging mode when the latent heat storage had full capacity which is equivalent to 12,16 kW and 24,32 kW for the 15 mm and 30 mm configurations, respectively. Tables 3 and 4 show the values calculated for the heat extracted from the system due to the heat input from the glycol cycle. The specific heat of the glycol/water mixture of 30 % concentration is 3,85 kJ/kg.K. Table 3 below shows the highest mean discharge duty calculated to be 9,02 kW for the D12 discharging cycle with high mass flow rate and high mean inlet CO<sub>2</sub> temperature. Comparing this mean discharge duty with the mean discharging duty of the discharging cycles with the same mass flow rate shows that it is 14,1% higher than D9 mean discharge duty of 7,91 kW with inlet CO<sub>2</sub> temperature of 6,6 °C, and 89,5% higher than D6 mean discharge duty of 4,76 kW with inlet CO<sub>2</sub> temperature of 4,9 °C. This shows how increasing the inlet CO<sub>2</sub> temperature increased the mean discharge duty. Table below shows the highest mean discharge duty for D12 as well to be 10,67 kW. Comparing this mean discharge duty with the mean discharging duty of the discharging cycles with the same mass flow rate shows that it is 80,1% higher than D9 mean discharge duty of 5,93 kW with inlet CO<sub>2</sub> temperature of 6,74 °C, and 262,9% higher than D6 mean discharge duty of 2,94 kW and inlet CO<sub>2</sub> temperature of 5,08 °C. Both Tables 3 and 4 show that the lowest mean discharged duty was for the highest mass flow rate with the lowest inlet CO<sub>2</sub> temperature being D6 discharging cycle. The high mass flow rate with low inlet CO<sub>2</sub> temperature lead to less mean heat transfer than lower mass flow rate with the same inlet CO<sub>2</sub> temperature as the discharging time takes longer. This means that the mean discharged duty was affected by the flow rate and by the inlet temperature of CO<sub>2</sub>.



	Time to discharge min	CO <sub>2</sub> inlet temperature °C	Mass flow rate of CO <sub>2</sub> kg min <sup>-1</sup>	Mean discharge duty kW	Heat extracted kWh
D4	44,33	4,60	4,04	7,18	5,8
D5	89,17	4,86	7,05	5,31	9,2
D6	69,83	4,88	9,90	4,76	7,5
D7	89,67	6,47	4,03	6,32	10,5
D8	94,17	6,51	7,08	6,30	11,1
D9	64,50	6,62	9,76	7,91	10,4
D10	82,33	8,79	4,06	8,42	12,4
D11	97,33	8,49	7,04	7,68	13,5
D12	72,05	8,60	9,52	9,02	12,5

**Table 3: Results of the discharging tests for the 15 mm configurations for water**

	Time to discharge min	CO <sub>2</sub> inlet temperature °C	Mass flow rate of CO <sub>2</sub> kg min <sup>-1</sup>	Mean discharge duty kW	Heat extracted kWh
D4	89,83	4,99	4,30	3,80	6,6
D5	189,67	5,02	7,05	4,09	13,8
D6	157,00	5,08	9,98	2,94	9,7
D7	179,50	7,13	4,04	4,16	13,3
D8	178,33	6,87	7,11	5,37	16,8
D9	135,17	6,74	9,69	5,93	15,1
D10	131,67	9,71	3,92	8,00	18,3
D11	120,50	9,33	6,56	9,56	19,9
D12	93,17	8,93	9,29	10,67	18,1

**Table 4: Results of the discharging tests for the 30 mm configurations for water**

### RT-9HC

The experiment was further carried based on an optimal flow rate and varied inlet CO<sub>2</sub> temperatures. Tables 5 and 6 show the results obtained following these discharging cycles. The discharging time was affected by increasing the inlet CO<sub>2</sub> temperature, due to higher driving forces for the heat exchange to happen between the CO<sub>2</sub> and the PCM. The decrease in the discharging time stops after D5 with inlet CO<sub>2</sub> temperature of 1,3 °C for the 15 mm configuration as shown in Table 5. The discharge time for the 30 mm configuration stops to decrease after D6 where it is fastest 102,33 minutes, followed by D7 where it is approximately the same 104,67 minutes as shown in Table 6. This can be due to system limitations such as the time it takes to transfer the heat between the refrigerant and the PCM. Meaning that it requires much higher temperature difference to achieve faster charging cycles. The mean discharged duty was calculated to map out the difference in performance for the different input parameters. Table 5 shows that each of D5, D6, and D7 have similar mean discharge duty value around 9 kW. Table 6 shows trend of increasing mean discharged duty with increasing inlet CO<sub>2</sub> temperature. The more clear trend in the 30 mm configuration can be attributed to longer experiment time resulting in more data and more accurate average values.

	Time to discharge min	CO <sub>2</sub> inlet temperature °C	Mean discharge duty kW	Heat extracted kWh	Total heat extracted %
D1	25,17	-7,3	5,80	2,7	37%
D1.5	43,83	-4,1	3,43	3,3	45%
D2	72,83	-3,8	3,57	5,6	77%
D3	61,83	-2,6	5,54	6,6	91%
D4	54,17	-0,9	7,59	7,7	106%
D5	52,50	1,3	8,72	8,4	115%
D6	59,00	1,5	9,05	9,5	131%
D7	56,83	4,0	8,91	9,1	125%

**Table 5: Results obtained from performing the discharging cycles for the 15 mm configurations for the RT-9HC**

	Time to discharge min	CO <sub>2</sub> inlet temperature °C	Mean discharge duty kW	Heat extracted kWh	Total heat extracted %
D1	118,00	-5,80	1,60	5,36	37%
D2	164,83	-3,94	2,78	10,66	73%
D3	138,67	-2,05	3,99	11,49	79%
D4	134,50	-0,13	5,46	14,35	99%
D5	116,50	1,53	6,98	15,20	105%
D6	102,33	3,43	8,40	15,77	109%
D7	104,67	4,36	9,24	17,35	119%

**Table 6: Results obtained from performing the discharging cycles for the 30 mm configurations for the RT-9HC**

#### 4. CONCLUSIONS

The CTES test unit is designed to be used in an industrial application to assist with the refrigeration cycle. The CTES consists of a sealed tank filled with PCM and a stack of 10 pillow plate heat exchangers with possibility to change the distance between the plates. The experiment were run with 15 mm and 30 mm distance between the plates. For each configuration, multiple running modes were run to map out the performance of the system for different parameters. The main two parameters which were changed are the inlet CO<sub>2</sub> temperature and the mass flow rate into the system. The experiment consisted of charging and discharging cycles which dictate solidifying and melting the PCM. The PCMs used were water and RT-9HC with melting temperature of 0 °C and -9,7 °C. The inlet temperature and the mass flow rate of the CO<sub>2</sub> were changed simultaneously in the water experiment, whereas the RT-9HC experiments were run with fixed optimal flow rate and varying inlet CO<sub>2</sub> temperatures. The following findings were observed after performing the experiment:

- The CTES unit filled with water as the PCM had a storage capacity of 12,16 kW and 24,32 kW for the 15 mm and 30 mm configurations, respectively.
- The CTES unit filled with RT-9HC as the PCM had a storage capacity of 7,27kW and 14,54 kW for the 15 mm and 30 mm configurations, respectively.
- Higher mass flow rate in both modes lead to higher pressure drop which could increase the energy consumption of the system. At the same time, higher mass flow rate leads to sufficient refrigerant supply to support an efficient heat transfer process between the PCM and the refrigerant meaning more energy extraction from the system and faster charging cycles. This can outweigh the disadvantage of the small pressure drop.
- Higher difference between the inlet CO<sub>2</sub> temperature and the PCM caused faster charging or discharging cycles as it creates higher driving forces which lead to better heat transfer efficiency in the pillow plates heat exchangers.
- Higher inlet CO<sub>2</sub> temperature in the discharging mode leads to better performance in terms of periods of high heat flow, and the amount of energy extracted from the system.

- the system is sensitive to inlet CO<sub>2</sub> temperature and 1°C can make a huge difference over the system efficiency and performance.
- A minimum temperature difference of 6 K is needed between the PCM and the refrigerant to generate enough driving forces to be able to extract latent heat.

From the water part it was shown that the charging and discharging cycles take time for the CO<sub>2</sub> to reach the set point temperature, which represents a significant part of the experiment especially in the 15 mm configuration. This is because the ice can be largely melted or formed before the system reaches steady state conditions, which can make it less accurate to compare with the 30 mm configuration results. There is a balance between the mass flow rate and the inlet CO<sub>2</sub> temperature which gives optimal results in both of the charging mode and the discharging mode. Discharging mode has a high importance as it represents how the system will perform when it is needed to release the stored energy. Each of D10, D11, and D12, which have the highest inlet CO<sub>2</sub> steady state temperature of 10 °C and steady state flow rates of 4, 7, and 10 kg min<sup>-1</sup>, respectively, show promising results as operating conditions in the discharging mode in both configurations in terms of the extracted energy and the time of high heat flow into the system.

In both configurations the amount of energy stored was higher than the amount of energy released for most discharging cycles. The 15 mm configuration shows more promising results in terms of the percentage of energy extracted compared to the 30 mm results. However, the 30 mm configuration has a bigger latent heat capacity and can operate with reduced capacity for a longer time. This can be utilized depending on the type of demand the system is expected to respond to, or the application the CTES system will be integrated into. This means that if the refrigeration system has high peak but short refrigeration demands, which can only be satisfied by the periods of high heat flow into the CTES, then the 15 mm configuration can be better suited. However, if the refrigeration system have lower peaks, or long high peaks followed by lower peaks, then the 30 mm configuration can be more useful, as the demand can be fulfilled using the CTES unit for a longer time.

Water and RT-9HC are both showing good potentials when used at the right conditions. Both PCMs can be used within the CTES unit to respond to different applications. Water as PCM can be integrated into a system supplying cooling to fluids between 6°C and 10°C. This can be utilized for example in fruits and vegetables cooling, or space cooling. The lower melting temperature of the RT-9HC can make the system be integrated into cooling systems responding to lower cooling requirements between -4°C and 4°C. This makes it possible for it to be integrated with refrigeration systems.

## REFERENCES

- [too] Ice - thermal properties. <https://www.engineeringtoolbox.com/ice-thermal-properties-d576.html>.
- [2] Cavallini, A. (2004). Properties of co2 as a refrigerant. In *European Seminar-CO2 as a refrigerant: theoretical and design aspects*.
- [GmbH] GmbH, R. T. Pcm rt-line.
- [4] MacCracken, M. (2004). Thermal energy storage in sustainable buildings. *ASHRAE Journal*, 46(9):S39.
- [5] Rismanchi, B., Saidur, R., BoroumandJazi, G., and Ahmed, S. (2012). Energy, exergy and environmental analysis of cold thermal energy storage (ctes) systems. *Renewable and sustainable energy reviews*, 16(8):5741–5746.
- [6] Sharma, A., Shukla, A., Chen, C., and Wu, T.-N. (2014). Development of phase change materials (pcms) for low temperature energy storage applications. *Sustainable Energy Technologies and Assessments*, 7:17–21.
- [7] Sun, Y., Wang, S., Xiao, F., and Gao, D. (2013). Peak load shifting control using different cold thermal energy storage facilities in commercial buildings: A review. *Energy conversion and management*, 71:101–114.

## ACKNOWLEDGEMENT

I would like to thank Dr. Armin Hafner for making this project possible and for his guidance throughout the project, PhD candidate Håkon Selvnes for his guidance through each stage of the process, and finally the Norwegian University of Science and technology for making this work possible.

---

## 9.2 Safety Document

# Risk Assessment Report

## Plate cold thermal energy storage (CTES)

Prosjektnavn	Plate cold thermal energy storage (CTES)
Apparatur	Cold Thermal Energy Storage (CTES) plate test rig
Enhet	EPT-Kuldeteknikk
Apparaturansvarlig	Håkon Selvnes
Prosjektleder	Armin Hafner
HMS-koordinator	Morten Grønli
HMS-ansvarlig (linjeleder)	Terese Løvås
Plassering	VATL
Romnummer	C159A
Risikovurdering utført av	Håkon Selvnes, Armin Hafner, Morten Grønli

### Approval:

Apparatur kort (UNIT CARD) valid for:	
Forsøk pågår kort (EXPERIMENT IN PROGRESS) valid for:	

Rolle	Navn	Dato	Signatur
Prosjektleder	Armin Hafner		
HMS koordinator	Morten Grønli		
HMS ansvarlig (linjeleder)	Terese Løvås		

---

## TABLE OF CONTENTS

1	INTRODUCTION.....	2
2	RISK MANAGEMENT IN THE PROJECT.....	2
3	DESCRIPTIONS OF EXPERIMENTAL SETUP .....	3
3.1	Process and Instrumentation. Diagram (PID) and list of components.....	3
3.2	Drawings and photos describing the setup.....	5
4	EVACUATION FROM THE EXPERIMENTAL AREA .....	9
5	WARNING.....	9
5.1	Before experiments .....	9
5.2	Abnormal situation .....	9
6	ASSESSMENT OF TECHNICAL SAFETY .....	10
6.1	HAZOP .....	10
6.2	Flammable, reactive and pressurized substances and gas .....	10
6.3	Pressurized equipment .....	11
6.4	Effects on the environment (emissions, noise, temperature, vibration, smell).....	11
6.5	Radiation .....	11
6.6	Chemicals.....	11
6.7	Electrical safety (deviations from the norms/standards).....	11
7	ASSESSMENT OF OPERATIONAL SAFETY .....	12
7.1	Operation procedure and emergency shutdown procedure.....	12
7.2	Training of operators .....	12
7.3	Technical modifications .....	12
7.4	Personal protective equipment .....	12
7.5	General Safety.....	12
7.6	Safety equipment.....	13
7.7	Special actions.....	13
8	QUANTIFYING OF RISK - RISK MATRIX .....	14
9	REGULATIONS AND GUIDELINES.....	15

## 1 INTRODUCTION

The unit is intended to work as a flexible thermal energy storage directly connected to the CO<sub>2</sub> circuit of industrial refrigeration systems. The unit consists of a welded container made of stainless steel supported by a frame of steel square tube, as well as a lid with handles to cover the unit. The test facility has its own independent oil-free CO<sub>2</sub> circuit, which is cooled by the centralized CO<sub>2</sub> refrigeration system in the basement C050. The rig has an independent heated glycol circuit for heating. In the test rig CO<sub>2</sub> circulates through several heat exchanger plates to solidify or melt the phase change material contained in the tank. The rig is located in room C159A.

## 2 RISK MANAGEMENT IN THE PROJECT

Hovedaktiviteter risikostyring	Nødvendige tiltak, dokumentasjon	DATE
Prosjekt initiering	Prosjekt initiering mal	
Vurdering av teknisk sikkerhet	Prosess-HAZOP Tekniske dokumentasjoner	
Vurdering av driftssikkerhet	Prosedyre-HAZOP Opplæringsplan for operatører	
Sluttvurdering, kvalitetssikring	Utstedelse av apparaturkort Utstedelse av forsøk pågår kort	

### 3 DESCRIPTIONS OF EXPERIMENTAL SETUP

#### 3.1 Process and Instrumentation. Diagram (PID) and list of components.

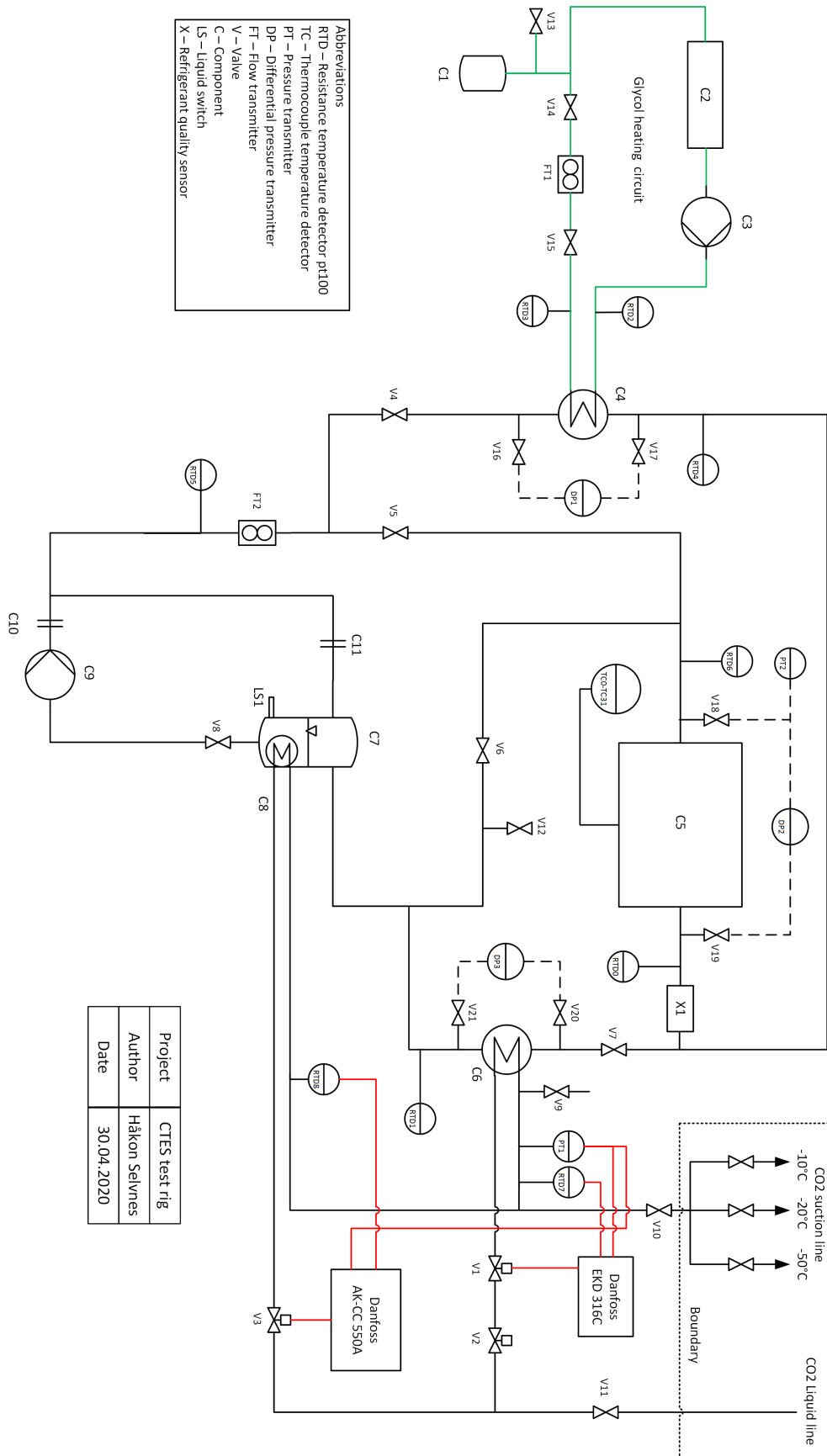


**Figure 1.** Process and Instrumentation Diagram (PID)



<b>Bill of material (BOM)</b>			
<b>PID TAG NO.</b>	<b>TEMP RANGE/ MAX PRESSURE</b>	<b>PROPERTIES (MECHANICAL/ELECTRICAL)</b>	<b>DESCRIPTION</b>
C1	70°C / 3 bar	18 L	A-flex glycol expansion vessel
C2	-- /4 bar	9 kW, 400 V	2 x 9 kW immersion heaters w/thermostatic control 0-50°C
C3	-- /10 bar	230 V	Grundfos UPS25-125 glycol circulation pump
C4	-196 to 225°C / 122 bar		Alfa Laval CBXP112 Brazed plate heat exchanger. Glycol / CO2 evaporator
C5	-- /100 bar	Stainless steel	Skala fabrikk prototype cold thermal energy storage unit
C6	-196 to 225°C / 90 bar		Alfa Laval CBXP52 Brazed plate heat exchanger. CO2 condenser / CO2 evaporator
C7	-50 to 120°C / 60 bar	67 L	Frigomec Klimal CO2 liquid receiver
C8	90°C / 82 bar	14 m spiral, 1/4"	Subcooler coil around C7.
C9	-50°C to +30°C / 52 bar	Test pressure 78 bar	Hermetic CO2 refrigerant pump CAMh 2/4
C10	-- / --	Diameter 6,60 mm	Max flow orifice
C11	-- / --	Diameter 6,00 mm	Min flow orifice
V1	-40 to 60°C / 140 bar	5/8" x 5/8" solder connections	Danfoss CCMT-2 Electronic expansion valve
V2	-40 to +120°C / 60 bar	5/8" x 5/8" solder connections	ALCO 2-Way Solenoid valve 200 RH6, normally closed
V3	-60 to 60°C / 90 bar	3/8" x 1/2" solder connections	Danfoss AKVH 10-3 Electronic expansion valve
V4	-40 to 150°C / 52 bar	3/4" x 3/4" solder connections	Refrigera R744 ball valve
V5	-40 to 150°C / 52 bar	3/4" x 3/4" solder connections	Refrigera R744 ball valve
V6	-40 to 150°C / 52 bar	3/4" x 3/4" solder connections	Refrigera R744 ball valve
V7	-40 to 150°C / 52 bar	3/4" x 3/4" solder connections	Refrigera R744 ball valve
V8	-40 to 150°C / 52 bar	1.5/8" x 1.5/8" solder connections	Refrigera R744 ball valve
V9	-40 to 150° / 120 bar	3/8" solder x 1/4" SAE thread	Refrigera R744 service access valve
V10	-40 to 150°C / 52 bar	3/4" x 3/4" solder connections	Refrigera R744 ball valve
V11	-40 to 150°C / 52 bar	3/4" x 3/4" solder connections	Refrigera R744 ball valve
V12	-- /52 bar	Inlet 1/2" NPT, outlet 1" GAS	Refrigera safety valve w/piped outlet set pressure 52 bar
V13	-- / 2.5 bar	3/4" threaded connection	Wilco Presco safety valve, opening pressure 2.5 bar
V14	-20 to 150°C / 32 bar	1" x 1" threaded connection	CIM ball valve
V15	-20 to 150°C / 32 bar	1" x 1" threaded connection	CIM ball valve
V16	-40 to 150° / 120 bar	3/8" solder x 1/4" SAE thread	Refrigera R744 service access valve
V17	-40 to 150° / 120 bar	3/8" solder x 1/4" SAE thread	Refrigera R744 service access valve
V18	-40 to 150° / 120 bar	3/8" solder x 1/4" SAE thread	Refrigera R744 service access valve
V19	-40 to 150° / 120 bar	3/8" solder x 1/4" SAE thread	Refrigera R744 service access valve
V20	-40 to 150° / 120 bar	3/8" solder x 1/4" SAE thread	Refrigera R744 service access valve
V21	-40 to 150° / 120 bar	3/8" solder x 1/4" SAE thread	Refrigera R744 service access valve
LS1	-55 to 30°C / 150 bar	3/4" NPT thread	HB products HBSC2 CO2 liquid switch
RTD0	-50 to 250°C / --	3.0 mm probe	RS PRO Platinum Resistance Thermometer Pt100 Industrial Sensor Probe, Class B
RTD1	-50 to 250°C / --	3.0 mm probe	RS PRO Platinum Resistance Thermometer Pt100 Industrial Sensor Probe, Class B
RTD2	-50 to 250°C / --	3.0 mm probe	RS PRO Platinum Resistance Thermometer Pt100 Industrial Sensor Probe, Class B
RTD3	-50 to 250°C / --	3.0 mm probe	RS PRO Platinum Resistance Thermometer Pt100 Industrial Sensor Probe, Class B
RTD4	-50 to 250°C / --	3.0 mm probe	RS PRO Platinum Resistance Thermometer Pt100 Industrial Sensor Probe, Class B
RTD5	-50 to 250°C / --	3.0 mm probe	RS PRO Platinum Resistance Thermometer Pt100 Industrial Sensor Probe, Class B
RTD6	-50 to 250°C / --	3.0 mm probe	RS PRO Platinum Resistance Thermometer Pt100 Industrial Sensor Probe, Class B
RTD7	-70 to 180°C / --	IP67, 2.5 m cable	Danfoss AKS 21A Pt1000 temperature detector
RTD8	-50 to 100°C / --	IP67, 3.5 m cable	Danfoss AKS 11 Pt1000 temperature detector
PT1	-50 to 85°C / 354 bar	3/8" BSP connection	Danfoss AKS 2050 Pressure transmitter
PT2	-40 to 125°C / 1050 bar	4 to 20 mA signal	Endress + Hauser Cerabar S PMP71 pressure transmitter, 0 to 100 bar
DP1	-40 to 85°C / 630 bar	4 to 20 mA signal	Endress + Hauser Deltabar S PMD75 differential pressure transmitter, 0 to 3 bar
DP2	-40 to 85°C / 630 bar	4 to 20 mA signal	Endress + Hauser Deltabar S PMD75 differential pressure transmitter, 0 to 3 bar
DP3	-40 to 85°C / 630 bar	4 to 20 mA signal	Endress + Hauser Deltabar S PMD75 differential pressure transmitter, 0 to 3 bar
FT1	-50 to 210°C / 40 bar	DN25 / PN40 connections	Rheonik Coriolis RHM15 mass flow transmitter, 4 to 80 kg/min
FT2	-50 to 210°C / 340 bar	1/2" G female thread connection	Rheonik Coriolis RHM060 mass flow transmitter, 0.5 to 10 kg/min
TC0 to TC31	-270 to 370°C / --	Wire Ga. 0.30	WATLOW thermocouple type T
X1	-60 to 80°C / 100 bar	DN20 / IP65 / 4 to 20 mA signal	HB Products HBX vapor quality sensor

**Table 1:** List of components

### 3.2 Drawings and photos describing the setup.

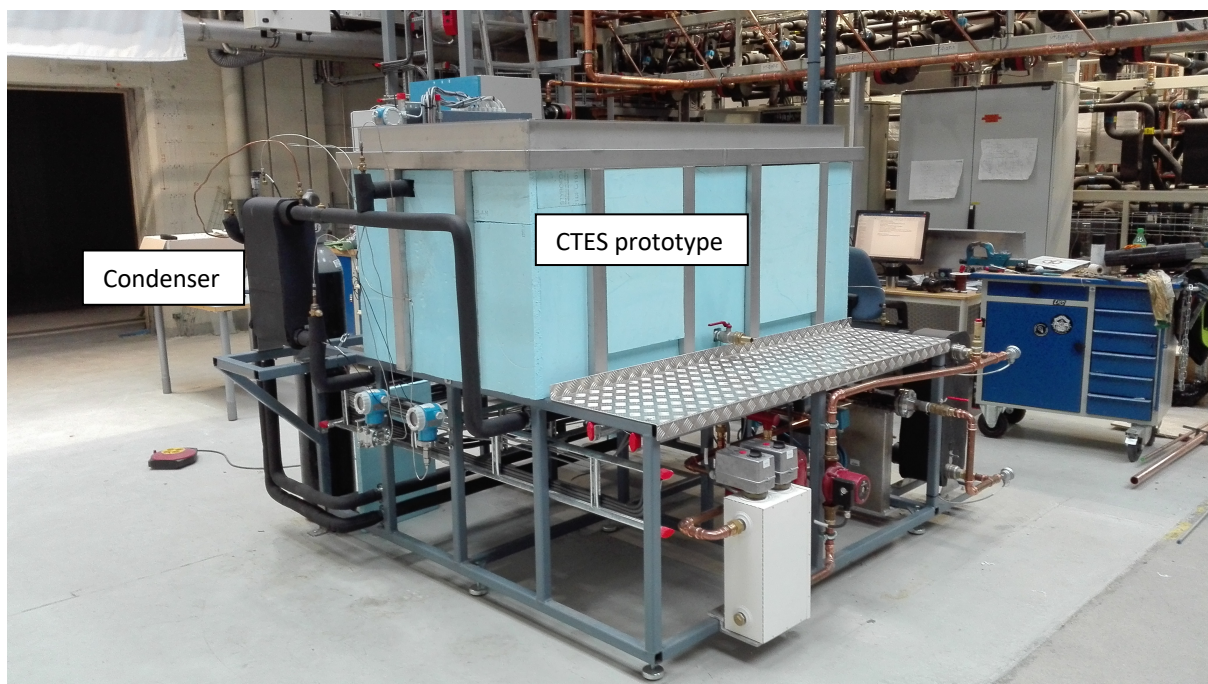


**Figure 2:** CTES unit

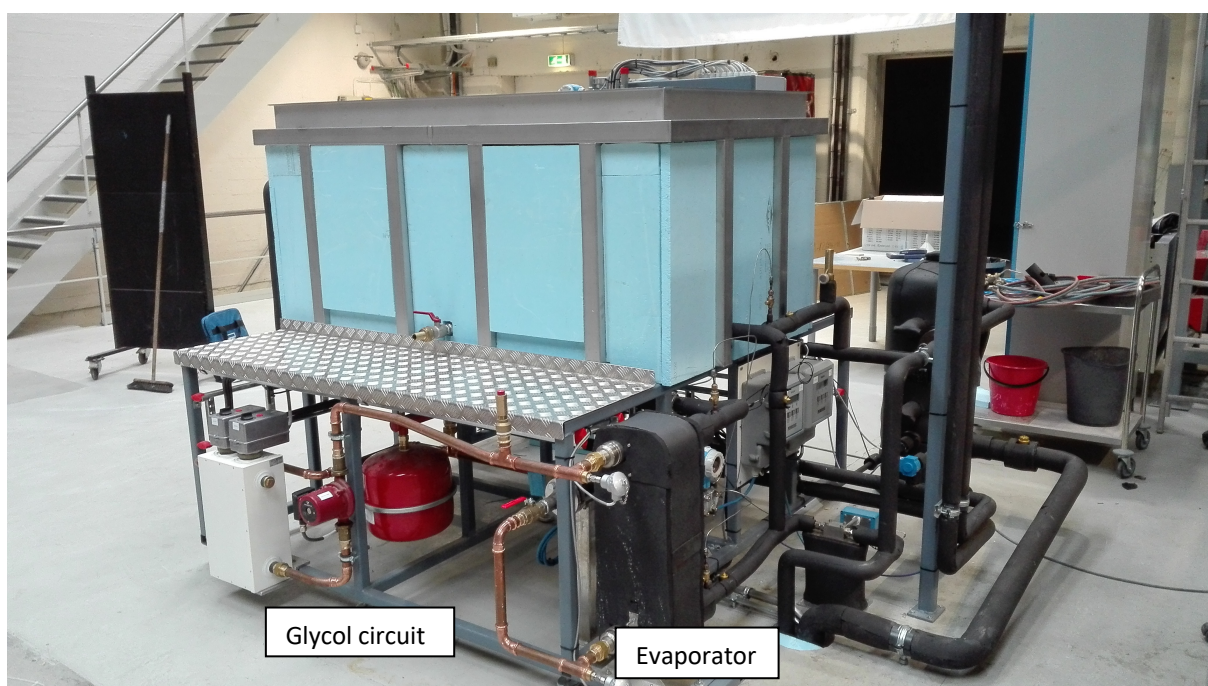


**Figure 3:** CTES unit, with glycol circuit indicated

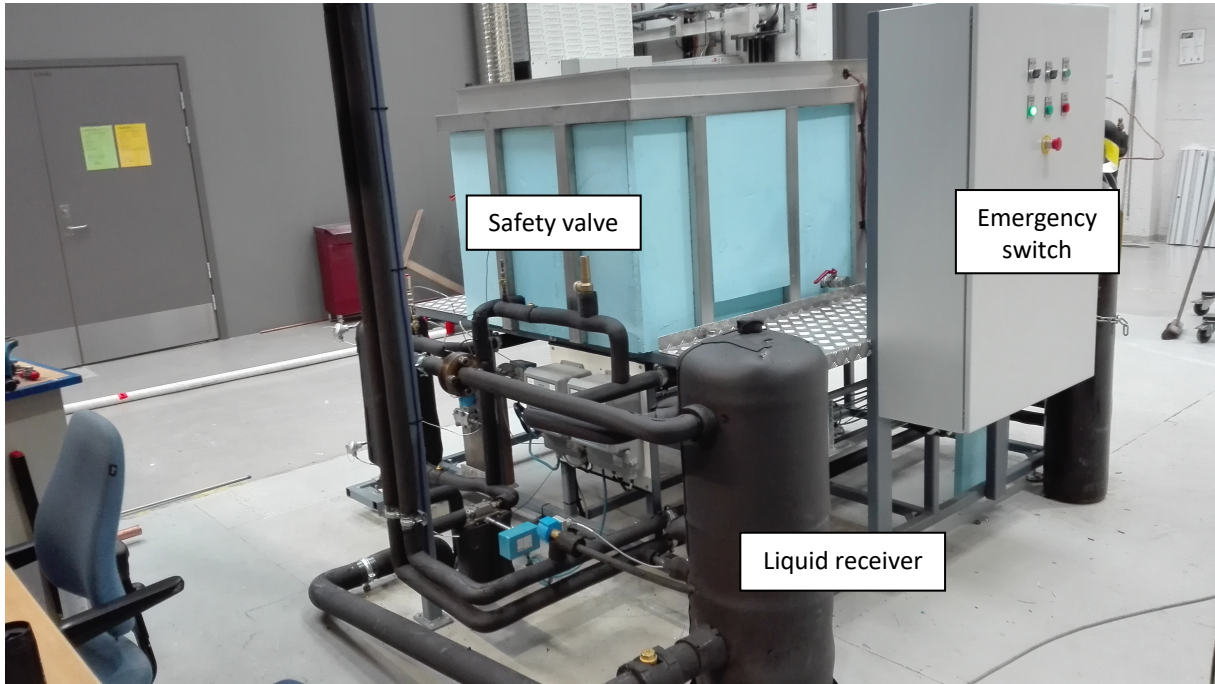


Figure 2: CTES unit with electrical cabinet, emergency switch and liquid receiver

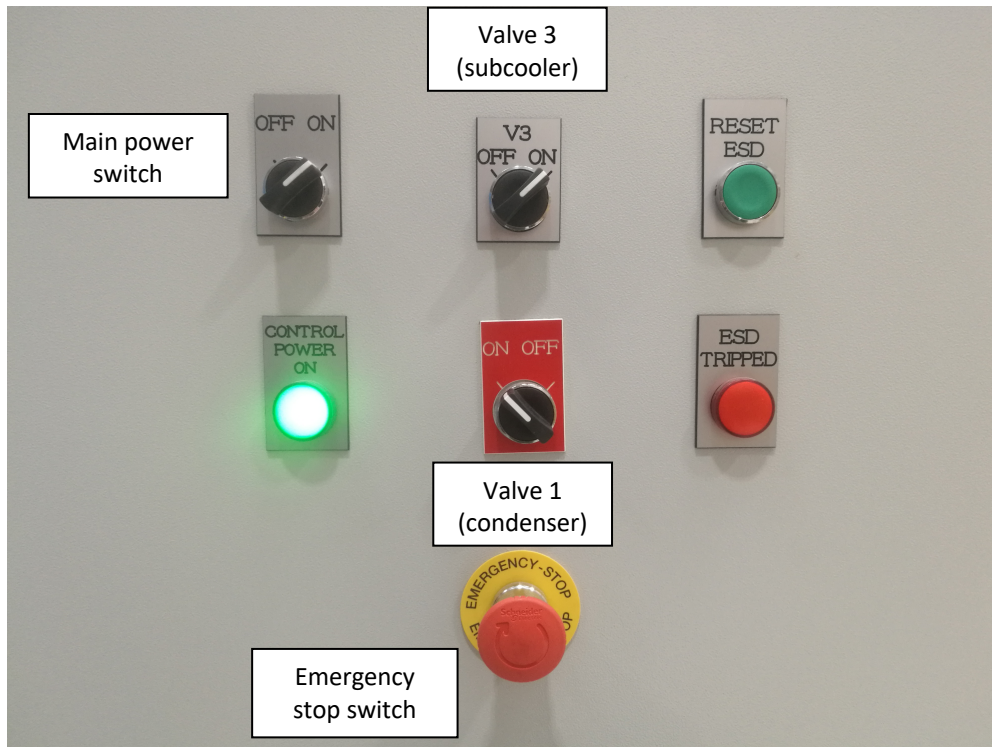
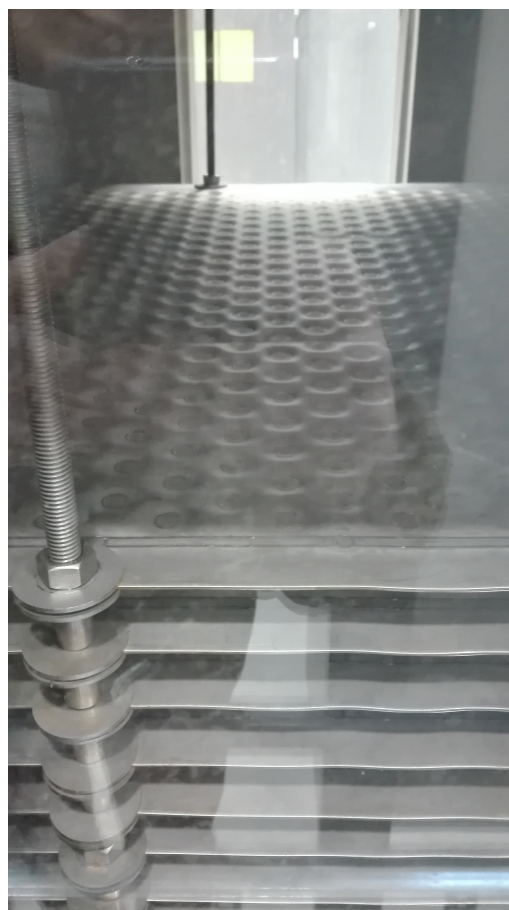


Figure 5: Switches and control on electrical cabinet



**Figure 6:** Discharge line from refrigerant safety valve



**Figure 7:** Pillow plates



**Figure 8:** CO2 hermetic pump in basement

## 4 EVACUATION OF THE EXPERIMENTAL AREA

Evacuate at signal from the alarm system or local gas alarm with its own local alert with sound and light outside the room in question, see 6.2.

Evacuation from the test area takes place through the marked emergency exits to the assembly point (corner of Old Chemistry Kjelhuset or parking 1a-b.)

### Action on rig before evacuation:

- Power off the electrical supply by the emergency stop switches (shown in Figure 5).
- Evacuate area and follow site emergency plan. In case there is the slightest possibility of a large CO<sub>2</sub> leakage, inspect and evacuate the cellar floor.

## 5 WARNING

### 5.1 Before experiments

Send an e-mail with information about the planned experiment to:

[iept-experiments@ivt.ntnu.no](mailto:iept-experiments@ivt.ntnu.no)

### The e-mail must include the following information:

- Name of responsible person
- Experimental setup/rig
- Start Experiments (date and time)
- Stop Experiments (date and time)

You must get the approval back from the laboratory management before starting up. All running experiments are notified in the activity calendar for the lab to be sure they are coordinated with other activity.

### 5.2 Abnormal situation

#### **FIRE**

If you are NOT able to extinguish the fire, activate the nearest fire alarm and evacuate area. Be then available for fire brigade and building caretaker to detect fire place.

If possible, notify:

<b>NTNU</b>
Morten Grønli, Mob: 918 97 515
Terese Løvås: Mob: 918 97 007
NTNU – SINTEF Beredskapstelefon 800 80 388

### **GAS ALARM**

If a gas alarm occurs, close gas bottles immediately and ventilate the area. If the level of the gas concentration does not decrease within a reasonable time, activate the fire alarm and evacuate the lab. Designated personnel or fire department checks the leak to determine whether it is possible to seal the leak and ventilate the area in a responsible manner.

Alert Order is in the above paragraph.

### **PERSONAL INJURY**

- Use the first aid kit in the fire / first aid stations
- Shout for help
- Start life-saving first aid
- **CALL 113** if there is any doubt whether there is a serious injury

### **OTHER ABNORMAL SITUATIONS**

You will find the reporting form for non-conformance on:  
<https://innsida.ntnu.no/wiki/-/wiki/Norsk/Melde+HMS-avvik>

## **6 ASSESSMENT OF TECHNICAL SAFETY**

### **6.1 HAZOP**

The experiment set up is divided into the following nodes:

Node 1	R744
Node 2	Secondary fluids
Node 3	Phase change material

**Attachments:** HAZOP (Attachment A)

**Conclusion:** Safeguards and recommendations from the HAZOP have been considered.

### **6.2 Flammable, reactive and pressurized substances and gas**

Are there any flammable, reactive and pressurized substances and gases in use?

YES	Explosion document must be made and/or documented pressure test
-----	---

**Attachments:** Pressure test

**Conclusion:** Pressure test has been made in accordance with the norm EN 13445 part 5/ Forskrift om trykkpåkjent utstyr.

### 6.3 Pressurized equipment

Is any pressurized equipment in use?

YES	The equipment must undergo pressure tests in accordance with the norms and be documented
-----	--

**Attachments:** Pressure test (Attachment B)

**Conclusion:** Pressure test has been made in accordance with the norm EN 13445 part 5/ Forskrift om trykkpåkjent utstyr.

On the glycol side a leak test was done, without any further pressure test.

A leak test was done on the container where the phase change material is contained

### 6.4 Effects on the environment (emissions, noise, temperature, vibration, smell)

Will the experiments generate emission of smoke, gas, odour or unusual waste?

Is there a need for a discharge permit, extraordinary measures?

NO	Negligible environmental impact
----	---------------------------------

**Attachments:** None

**Conclusion:** Some noise is expected, but it is not expected to be high enough to be considered as harmful.

### 6.5 Radiation

NO	No radiation sources in the experiment
----	--

**Attachments:** None

**Conclusion:** -

### 6.6 Chemicals

Will any chemicals or other harmful substances be used in the experiments? Describe how the chemicals should be handled (stored, disposed, etc.) Evaluate the risk according to safety datasheets, MSDS. Is there a need for protective actions given in the operational procedure?

YES	Do a risk assessment of the use.
-----	----------------------------------

**Attachments:** Glycol Safety Datasheet (Attachment E)

Phase change material Safety Datasheet (Attachment F)

**Conclusion:** Glycol, phase change material and carbon dioxide are not hazardous.

### 6.7 Electrical safety (deviations from the norms/standards)

NO	<p>No deviations from the norms/standards.</p> <ul style="list-style-type: none"> <li>The electrical cabinets must be locked, and only electrical operators can make use of them.</li> <li>Only the electrical operators can reactivate the system if the emergency switch locks.</li> </ul>
----	--

**Attachments:** None



**Conclusion:** The safety guidelines are given by the norms and regulations.

## 7 ASSESSMENT OF OPERATIONAL SAFETY

Ensure that the procedures cover all identified risk factors that must be taken care of. Ensure that the operators and technical performance have enough expertise.

### 7.1 Operation procedure and emergency shutdown procedure

The operating procedure is a checklist that must be filled out for each experiment. Emergency procedure should attempt to set the experiment set up in a harmless state by unforeseen events.

**Attachments:** Procedure for running experiments (Attachment C)

**Emergency shutdown procedure:** Power off the electrical supply and press the emergency stop switch (shown in Figure 5)

### 7.2 Training of operators

A document showing the training plan for operators.

**Attachments:** Training program for operators (Attachment D)

### 7.3 Technical modifications

- Technical modifications made by the operator:
  - None
- Technical modifications that must be made by technical staff:
  - Modification of pressurised equipment.
  - Replacement of components.
- What technical modifications give a need for a new risk assessment (by changing the risk picture)?
  - Modification of pressurized equipment or emergency stop switch modified.
  - Introducing new phase change material with different chemical properties

### 7.4 Personal protective equipment

- Use insulating gloves when there is opportunity for contact with hot/cold surfaces.
- Use safety glasses when approaching any pressurized equipment.

### 7.5 General Safety

- The area around the staging attempts shielded.
- Gantry crane and truck driving should not take place close to the experiment.
- Gas cylinders shall be placed in an approved carrier with shut-off valve within easy reach.
- Components at the test rig at dangerous temperatures must be properly isolated.
- Coolant containing parts must be checked before system start-up (tighten connectors, check damages in tubes ...).
- Switch off when limiting value (pressure, temperature) is exceeded.
- Safeguarding of the construction through safety valves, temperature switch, etc.
- Check and retighten screwed joints continuously.

- The electrical cabinets must be locked, and only electrical operators can make use of them.
- Only the electrical operators can reactivate the system if the emergency switch locks.

### **7.6 Safety equipment**

- Warning signs: see the Regulations on Safety signs and signalling in the workplace.

### **7.7 Special actions**

- Accompaniment is required when charging CO<sub>2</sub> or opening parts of a system that may have contained liquid CO<sub>2</sub>.

## 8 QUANTIFYING OF RISK - RISK MATRIX

The risk matrix will provide visualization and an overview of activity risks so that management and users get the most complete picture of risk factors.

IDnr	Activity-event	Probability	Consequence	RV
1	Freeze burns	1	B	B1
2	Warm fluid scald	1	C	C1
3	Electrocution	1	E	E1
4	Contusion	1	C	C2
5	Explosion	1	E	E1
6	Asphyxiation	1	E	E1

**Conclusion:** The probability of these risks has been considered after applying the safety measures.

<b>CONSEQUENCES</b>	Catastrophic	<b>E1</b>	<b>E2</b>	<b>E3</b>	<b>E4</b>	<b>E5</b>
	Major	<b>D1</b>	<b>D2</b>	<b>D3</b>	<b>D4</b>	<b>D5</b>
	Moderate	<b>C1</b>	<b>C2</b>	<b>C3</b>	<b>C4</b>	<b>C5</b>
	Minor	<b>B1</b>	<b>B2</b>	<b>B3</b>	<b>B4</b>	<b>B5</b>
	Insignificant	<b>A1</b>	<b>A2</b>	<b>A3</b>	<b>A4</b>	<b>A5</b>
		Rare	Unlikely	Possible	Likely	Almost
		<b>PROBABILITY</b>				

Table 8. Risk's Matrix

COLOUR	DESCRIPTION
Red	Unacceptable risk Action has to be taken to reduce risk
Yellow	Assessment area. Actions has to be considered
Green	Acceptable risk. Action can be taken based on other criteria

Table 9. The principle of the acceptance criterion. Explanation of the colors used in the matrix

## 9 REGULATIONS AND GUIDELINES

Se: <http://www.arbeidstilsynet.no/regelverk/index.html>

- Lov om tilsyn med elektriske anlegg og elektrisk utstyr (1929)
- Arbeidsmiljøloven
- Forskrift om systematisk helse-, miljø- og sikkerhetsarbeid (HMS Internkontrollforskrift)
- Forskrift om sikkerhet ved arbeid og drift av elektriske anlegg (FSE 2006)
- Forskrift om elektriske forsyningsanlegg (FEF 2006)
- Forskrift om utstyr og sikkerhetssystem til bruk i eksplosjonsfarlig område NEK 420
- Forskrift om håndtering av brannfarlig, reaksjonsfarlig og trykksatt stoff samt utstyr og anlegg som benyttes ved håndteringen
- Forskrift om Håndtering av eksplosjonsfarlig stoff
- Forskrift om bruk av arbeidsutstyr.
- Forskrift om Arbeidsplasser og arbeidslokaler
- Forskrift om Bruk av personlig verneutstyr på arbeidsplassen
- Forskrift om Helse og sikkerhet i eksplosjonsfarlige atmosfærer
- Forskrift om Høytrykksspuling
- Forskrift om Maskiner
- Forskrift om Sikkerhetsskiltning og signalgivning på arbeidsplassen
- Forskrift om Stillaser, stiger og arbeid på tak m.m.
- Forskrift om Sveising, termisk skjæring, termisk sprøyting, kullbuemeisling, lodding og sliping (varmt arbeid)
- Forskrift om Tekniske innretninger
- Forskrift om Tungt og ensformig arbeid
- Forskrift om Vern mot eksponering for kjemikalier på arbeidsplassen (Kjemikalieforskriften)
- Forskrift om Vern mot kunstig optisk stråling på arbeidsplassen
- Forskrift om Vern mot mekaniske vibrasjoner
- Forskrift om Vern mot støy på arbeidsplassen
- Directive 2014/68/EU of the European Parliament and of the Council of 15 May 2014 on the Harmonization of the Laws of the Member States Relating to the Making Available on the Market of Pressure Equipment.

Veiledninger fra arbeidstilsynet

Se: <http://www.arbeidstilsynet.no/regelverk/veiledninger.html>

# Attachment to Risk Assessment report

## Plate cold thermal energy storage (CTES)

<b>Prosjektnavn</b>	Plate cold thermal energy storage (CTES)
<b>Apparatur</b>	Cold Thermal Energy Storage (CTES) plate test rig
<b>Enhet</b>	EPT-Kuldeteknikk
<b>Apparaturansvarlig</b>	Håkon Selvnes
<b>Prosjektleder</b>	Armin Hafner
<b>HMS-koordinator</b>	Morten Grønli
<b>HMS-ansvarlig (linjeleder)</b>	Terese Løvås
<b>Plassering</b>	VATL
<b>Romnummer</b>	C159A
<b>Risikovurdering utført av</b>	Håkon Selvnes, Armin Hafner, Malte Brunner, Morten Grønli

## **TABLE OF CONTENTS**

ATTACHMENT A: HAZOP TEMPLATE

ATTACHMENT B: TEST CERTIFICATE FOR LOCAL PRESSURE TESTING

ATTACHMENT C: PROCEDURE FOR RUNNING EXPERIMENTS

ATTACHMENT D: TRAINING OF OPERATORS

ATTACHMENT E: OPERATING MODES CHECKLIST

APPARATURKORT / UNITCARD

FORSØK PÅGÅR / EXPERIMENT IN PROGRESS

ATTACHMENT F: GLYCOL SAFETY DATASHEET

**ATTACHMENT A: HAZOP TEMPLATE**

Ref. Number (Part – Node)	Part	PID tag	Node
1	Evaporator	C4	CO <sub>2</sub>
2	CTES-unit	C5	Secondary fluids
3	Condenser	C8	Phase change material
4	Valve	V1 – V21	
5	CO <sub>2</sub> pump	C9	
6	Receiver	C7	
7	Subcooler heat exchanger	C8	
8	Glycol heater	C2	
9	Glycol pump	C3	
10	Glycol expansion vessel	C1	

Project: Plate cold thermal energy storage (CTES) Node: 1 (CO <sub>2</sub> )						
Ref	Guideword	Causes	Consequence	Safeguards/ Recommendations	Action	Date/Sign
1-6	Sink of pressure	Leakage of CO <sub>2</sub>	Not optimal functioning	Regular maintenance and visual inspection of equipment. Pressure sensors to detect leakages. Observation of gas bubbles in CTES tank	Detect leakage	
1-6	Fluctuating mass flow	Leakage Fluctuating work pump	Not optimal functioning	Pressure sensors to detect leakages. Check pump operation	Detect leakage	
5	No revolutions	No current. No voltage. Liquid switch in receiver tripped	Temporary malfunction System not operating	Check connections and power to frequency converter. Check liquid level in receiver	Contact technicians Reset liquid switch	
1/2 /3/ 4/6	Corrosion / erosion	Refrigerant contamination	CO <sub>2</sub> leakage	Regular maintenance and visual checks	Detect leakage. Change part if needed.	
2	No freezing of PCM	No flow of CO <sub>2</sub> through unit. Incorrect pressure.	Charging process not working	Check mass flow of CO <sub>2</sub> . Pump function. Correct suction temperature of centralized unit	Check mass flow sensor FT2. Change to correct suction temperature of centralized unit	
6	High pressure in receiver	Subcooler not working during standstill	Discharge of high-pressure CO <sub>2</sub> through safety valve	Check operation of centralized CO <sub>2</sub> system. Check operation of expansion valve in subcooler	Inspect valve settings and setpoint of controller AK CC-550A	

Project: Plate cold thermal energy storage (CTES) Node: 2 (Secondary fluids)						
Ref	Guideword	Causes	Conseq.	Safeguards/ Recommendations	Action	Date/Sign
1/8 -10	Low glycol flow rate	Valves partially closed / blocked. Pump off	No evaporation of CO2 in the evaporator. Freezing of glycol	Regular check of flow rates and inspect valves in glycol circuit before start	Check glycol pump status Open valves completely	
1/8 -10	Fluctuating glycol flow rate	Air trapped Low glycol charge	No optimal control / functioning	Purge of the air in the highest parts of the loop. Micro bubble filter installed.	Manually air the system Check filling of glycol	
1/8 -10	Overpressure glycol system	Pipe obstruction. Valves closed	Damage of the tank/tubing Discharge of safety valve	Regular maintenance and system check. Valves at both ends of tube must never be closed at the same time.	Open valves completely	
1/8 -10	Over-temp. Glycol system	Incorrect temperature limit in electric heaters or number of heaters in operation.	Overheating and discharge of safety valve	Check temperature limit and status of the electric heaters Check thermostat setting		
1/8 -10	Under-temp. Glycol system	Incorrect number of electric heaters in operation	Freezing of the glycol.	Check temperature limit and status of the electric heaters. Check thermostat setting		

Project: Plate cold thermal energy storage (CTES) Node: 3 (Phase change material)						
Ref	Guideword	Causes	Conseq.	Safeguards/ Recommendations	Action	Date/Sign
2	Low level of phase change material	Leakage through joints in container or drain valves.	No thermal buffer for operating the system, loss of valuable material.	Inspect and take note of liquid level before running each test. Visually check for leaks underneath the container.	Shut drain valves when filling new material.	



**ATTACHMENT B: TEST CERTIFICATE FOR LOCAL PRESSURE TESTING**

Trykkpåkjent utstyr:	Sammenstilling av rørsystem og komponenter i testrigg
Benyttes i rigg:	Cold Thermal Energy Storage (CTES) plate test rig
Design trykk for utstyr (bara):	52 bar
Maksimum tillatt trykk (bara): (i.e. burst pressure om kjent)	52 bar (sikkerhetsventilens settpunkt)
Maksimum driftstrykk i denne rigg:	50 bar

**Prøvetrykket skal fastlegges i følge standarden og med hensyn til maksimum tillatt trykk.**

Prøvetrykk (bara):	75
X maksimum driftstrykk: I følge standard	1,43
Test medium:	Nitrogen
Temperatur (°C)	25
Start tid:	Trykk (bara):
Slutt tid:	Trykk (bara):
Maksimum driftstrykk i denne rigg:	50 bar

Eventuelle repetisjoner fra atm. trykk til maksimum prøvetrykk:.....

Test trykket, dato for testing og maksimum tillatt driftstrykk skal markers på (skilt eller innslått)

---





 Sted og dato

---

 Signatur

## ATTACHMENT C: PROCEDURE FOR RUNNING EXPERIMENTS

<b>Prosjekt</b> Plate cold thermal energy storage (CTES)	<b>Dato</b>	<b>Signatur</b>
<b>Apparatur</b> Cold Thermal Energy Storage (CTES) plate test rig		
<b>Prosjektleder</b> Armin Hafner		

	<b>Conditions for the experiment:</b>	<b>Completed</b>
	Experiments should be run in normal working hours, 08:00-16:00 during wintertime and 08.00-15.00 during summertime. Experiments outside normal working hours shall be approved.	
	One person must always be present while running experiments and should be approved as an experimental leader. This person must have completed the training as described in Attachment D: Training of operators	
	An early warning is given according to the lab rules, and accepted by authorized personnel. Report all experimental activity to: <a href="mailto:lept-experiments@ivt.ntnu.no">lept-experiments@ivt.ntnu.no</a>	
	Be sure that everyone taking part of the experiment is wearing the necessary protecting equipment and is aware of the shutdown procedure and escape routes a	
	<b>Preparations</b>	<b>Carried out</b>
	Post the "Experiment in progress" sign.	
	<p><i>Start-up procedure</i></p> <ol style="list-style-type: none"> <li>1. Check that the electric cabinet is energised. This is indicated if the main power switch is in ON position, and the green light labelled with "Control Power ON" is illuminated (see Figure 5 in Risk Assessment report). If the cabinet is not energized, please inform the responsible of the system before taking any further step.</li> <li>2. Verify that the valve to the correct suction line is open to the centralized CO2 system (i.e. Advansor basement unit in room C050). The centralized unit has three suction levels, -10°C, -25°C and -50°C. These can be chosen by opening/closing a manual valve on the suction line. Contact a technician and modify if needed.</li> <li>3. Run LabVIEW <ol style="list-style-type: none"> <li>a. Click the LabVIEW-icon  on the Desktop.</li> <li>b. Select "CTES.lvproj" in the Project Window. If not shown under recent projects it can be found in the folder "Desktop/CTES/Program/"</li> <li>c. In the Project Explorer select "My Computer → VI → Main_1.vi". One window will appear.</li> <li>d. Select where to log the data file by selecting the browse icon . Select the folder Documents/CTES_log_data, and write in a suitable name for the file.</li> <li>e. Run the program by selecting the white arrow  in the upper left corner.</li> <li>f. Activate the logging function by clicking the logging button . Select a "Logspeed" (5 sec. is recommended). After the</li> </ol> </li> </ol>	



LOG button is pressed, a \*.data file will be created in the folder "C:\Documents\CTES\_log\_data". The name of the file has the following format: daymonthyear\_hourminutesecond.data. The selected name of the datafile will be first, then the time parameter secondly.

#### **Routine for charging mode**

- g. Set the valves of the CO<sub>2</sub> circuit on the test rig according the charging mode in Attachment E: Operation modes checklist.
- h. Open valve 2 by pressing the "Valve 2 (magnetic valve)" button in the Labview program. This should now become green.
- i. Activate the superheat controller EKD 316C that controls the CCMT-2 expansion valve by turning the valve 1 switch to the ON position (see Fig. 5 in the Risk Assessment Report). In addition, the internal ON signal must be active in the controller. This can be done by operating the EKA 164A display. Hold the upper button for a few seconds to enter the menu. Press the upper button until you reach r12. Push the middle button and change the setting from OFF to ON by pressing the upper button. This is normally active and turning the switch on the cabinet is enough.
- j. Activate the CO<sub>2</sub> pump via the Labview program by selecting the "CO<sub>2</sub> pump" button. The button should now become green. Set the frequency of the pump between 35 Hz to 60 Hz, this is the operating range of the pump motor. This can be done either by writing in the frequency manually, or by operating the slider in the program by selecting and dragging the indicator. If a lower mass flow is required in the test, valve 5 can be used to throttle the flow. Bear in mind that the valve should never be fully closed.
- k. If required by the test, activate the subcooler by turning the V3 switch to the ON position on the electrical cabinet (see Fig. 5 in the Risk Assessment Report).

#### **Routine for discharging mode**

- l. Set the valves of the CO<sub>2</sub> circuit on the test rig according the discharging mode in Attachment E: Operation modes checklist.
- m. Manually select the circulation rate of the glycol pump by turning the white selector on the pump. The pump has three speed settings; approximately 19.5 kg/min, 31 kg/min and 48 kg/min.
- n. Verify that the thermostat on the electric heater is set to the correct temperature between 0 and 50°C. Be aware that setting the thermostat temperature too high might give too high pressure in the CO<sub>2</sub> circuit.
- o. Activate one or both heaters in Labview according to the heating demand.
- p. Activate the CO<sub>2</sub> pump via the Labview program by selecting the "CO<sub>2</sub> pump" button. The button should now become green. Set the frequency of the pump between 35 Hz to 60 Hz, this is

	<p>the operating range of the pump motor. This can be done either by writing in the frequency manually, or by operating the slider in the program by selecting and dragging the indicator. If a lower mass flow is required in the test, valve 4 can be used to throttle the flow. Bear in mind that the valve should never be fully closed.</p> <p>q. If required by the test, activate the subcooler by turning the V3 switch to the ON position on the electrical cabinet (see Fig. 5 in the Risk Assessment Report).</p>	
	<p><b>During the experiment</b></p>	
	<p><i>Control of temperature, pressure e.g.</i></p>	
	<ol style="list-style-type: none"> <li>1. LabVIEW. Observe and control continually the parameters in the main window, i.e massflow rates, pressures and temperatures. Pay close attention to the pressure reading of pressure transmitter 1, this value must never exceed 52 bar during and experiment. This is the set pressure of the safety valve, and it will discharge at pressures above this limit.</li> <li>2. The temperature of the glycol sucked by the pumps should not exceed 40 °C and must not fall under the freezing point of the glycol (<math>\approx -13</math> °C). This temperature can be actively maintained in a safe range by setting activating the heaters and setting the thermostat in the proper range in Labview.</li> <li>3. Visually observe the melting and freezing of the ice/water in the CTES tank.</li> <li>4. Towards the end of the discharge experiment, pay especially close attention to the pressure in the test rig. As the ice is melted and temperature of the water in the CTES unit is increasing, the pressure in the test rig also increases. Adjust the temperature of heaters and/or the number of heaters in operation.</li> </ol>	
	<p><b>End of experiment</b></p>	
	<p><i>Shut down procedure</i></p>	
	<ol style="list-style-type: none"> <li>1. LabVIEW. <ol style="list-style-type: none"> <li>a. Deactivate the CO2 pump by setting the frequency to zero and then deactivate the CO2 pump button. Wait for the frequency to reach zero before deactivating the CO2 pump</li> <li>b. Deactivate the heaters if they have been active.</li> <li>c. Deactivate the glycol pump if it has been active.</li> <li>d. Deactivate the logging function by selecting the LOGGING  button.</li> <li>e. Select the stop button  in the upper-left corner of the Main Window to stop the LabVIEW program.</li> <li>f. Close Labview by selecting the cross in the upper-right corner in the Main Window.</li> </ol> </li> <li>2. If it has been deactivated during an experiment, activate the subcooler by turning the V3 switch on the electric cabinet to the ON position (see Fig. 5 in the Risk Assessment Report).</li> </ol>	
	<p><b>Notes</b></p>	
	<ul style="list-style-type: none"> <li>• Verify when closing a valve in the refrigerant loop that there is no possibility of trapping liquid in the tube. In case liquid could be trapped,</li> </ul>	

	<p>please vent it through the closest service valve. Inform the responsible of the system to proceed with the venting.</p> <ul style="list-style-type: none"> <li>To prevent the expansion of trapped glycol, never close valves on both ends of tubes. Valve V14 and V15 on both sides of the mass flow meter FT01 must always be fully open.</li> </ul>	
	<b>Additional recommendations</b>	
	<ul style="list-style-type: none"> <li>Remove all obstructions/barriers/signs around the experiment.</li> <li><b>Tidy and clean-up work areas.</b></li> <li>Return equipment and systems back to their normal operation settings.</li> </ul>	
	<b>To reflect on before the next experiment and experience useful for others</b>	
	Was the experiment completed as planned and on scheduled in professional terms?	
	Was the competence which was needed for security and completion of the experiment available to you?	
	Do you have any information/ knowledge from the experiment that you should document and share with fellow colleagues?	

**Operator(s):**

Navn	Dato	Signatur
Håkon Selvnes		
Malte Brunner		

**ATTACHMENT D: TRAINING OF OPERATORS**

<b>Prosjekt</b> Plate cold thermal energy storage (CTES)	<b>Dato</b>	<b>Signatur</b>
<b>Apparatur</b> Cold Thermal Energy Storage (CTES) plate test rig		
<b>Prosjektleder</b> Armin Hafner	08.07.19	

	<b>Knowledge about EPT LAB in general</b>	
	Lab <ul style="list-style-type: none"> <li>• Access</li> <li>• Routines and rules</li> <li>• Working hour</li> </ul>	
	Knowledge about the evacuation procedures	
	Activity calendar for the Lab	
	Early warning, <a href="mailto:iept-experiments@ivt.ntnu.no">iept-experiments@ivt.ntnu.no</a>	
	<b>Knowledge about the experiments</b>	
	Procedures for the experiments	
	Emergency shutdown	
	Nearest fire and first aid station	
	Knowledge of health effects of CO <sub>2</sub> and glycol	
	Safety datasheets for CO <sub>2</sub> and glycol	

I hereby declare that I have read and understood the regulatory requirements has received appropriate training to run this experiment and are aware of my personal responsibility by working in EPT laboratories.

**Operator(s):**

<b>Navn</b>	<b>Dato</b>	<b>Signatur</b>
Håkon Selvnes		
Malte Brunner		

**ATTACHMENT E: OPERATING MODES CHECKLIST**

O	Open
I	Closed

**Valves for charging mode**

Valve	Position	√
V-4	I	
V-5	O	
V-6	I	
V-7	O	

**Valves for discharging mode**

Valve	Position	√
V-4	O	
V-5	I	
V-6	O	
V-7	I	

All other valves except for the ones specified here must be in the *open* position.

## APPARATURKORT / UNITCARD

**Dette kortet SKAL henges godt synlig på apparaturen!**  
***This card MUST be posted on a visible place on the unit!***

<b>Apparatur (Unit)</b> Cold Thermal Energy Storage (CTES) plate test rig	
<b>Prosjektleder (Project Leader)</b> Armin Hafner	<b>Telefon mobil/privat (Phone no. mobile/private)</b> 92857730
<b>Apparaturansvarlig (Unit Responsible)</b> Håkon Selvnes	<b>Telefon mobil/privat (Phone no. mobile/private)</b> 47096502
<b>Sikkerhetsrisikoer (Safety hazards)</b> <ul style="list-style-type: none"><li>- Freeze burns</li><li>- Warm fluid scald</li><li>- Electrocutation</li><li>- Contusion</li></ul>	
<b>Sikkerhetsregler (Safety rules)</b> <ul style="list-style-type: none"><li>- It is mandatory to use of eye protection in the rig zone</li><li>- Use gloves when there is opportunity for contact with hot/cold surfaces</li><li>- Gas cylinders shall be placed in an approved carrier with shut-off valve within easy reach.</li><li>- Switch off when limiting value (pressure, temperature) is exceeded.</li><li>- Warning signs see the Regulations on Safety signs and signalling in the workplace.</li><li>- Accompaniment is required when charging CO<sub>2</sub> or opening parts of a system that may have contained liquid CO<sub>2</sub>.</li></ul>	
<b>Nødstop prosedyre (Emergency shutdown)</b> <ul style="list-style-type: none"><li>- Press the emergency stop switch.</li><li>- Evacuate area and follow site emergency plan.</li></ul>	

**Her finner du (Here you will find):**

<b>Prosedyrer (Procedures)</b>	In the folder on the door of the electrical cabinet
<b>Bruksanvisning (Users manual)</b>	In the folder on the door of the electrical cabinet

**Nærmeste (Nearest)**

<b>Brannslukningsapparat (Fire extinguisher)</b>	Right side of the nearest door
<b>Førstehjelpsskap (First aid cabinet)</b>	Right side of the nearest door

NTNU  
Institutt for energi og prosessteknikk

Dato

---

Signert

---



# FORSØK PÅGÅR / EXPERIMENT IN PROGRESS

**Dette kortet SKAL henges opp før forsøk kan starte!**  
***This card MUST be posted on the unit before the experiment startup!***

<b>Apparatur (Unit)</b> Cold Thermal Energy Storage (CTES) plate test rig	
<b>Prosjektleder (Project Leader)</b> Armin Hafner	<b>Telefon mobil/privat (Phone no. mobile/private)</b> 92857730
<b>Apparaturansvarlig (Unit Responsible)</b> Håkon Selvnes	<b>Telefon mobil/privat (Phone no. mobile/private)</b> 47096502
<b>Godkjente operatører (Approved Operators)</b>	<b>Telefon mobil/privat (Phone no. mobile/private)</b>
<b>Prosjekt (Project)</b> Plate cold thermal energy storage (CTES)	
<b>Forsøksstid / Experimental time (start - stop)</b>	
<b>Kort beskrivelse av forsøket og relaterte farer (Short description of the experiment and related hazards)</b> <p>The experimental test rig uses pump-circulated CO<sub>2</sub> to freeze/melt water/ice in a cold thermal energy storage (CTES) unit. The experiments consist of storing energy in the ice by evaporating CO<sub>2</sub> through heat exchanger plates immersed in water in the CTES unit. The energy is recovered by circulating CO<sub>2</sub> gas through the plates and condensing the CO<sub>2</sub>. Heat is provided by an independent glycol circuit and cooling of the rig is provided by the centralized CO<sub>2</sub> refrigeration unit in C050.</p> <p>Main hazards:</p> <ul style="list-style-type: none"><li>- Freeze burns</li><li>- Warm fluid scald</li><li>- Electrocutation</li></ul>	

**NTNU**  
**Institutt for energi og prosessteknikk**

**Dato**

---

**Signert**

---